

Universiteit
Leiden
The Netherlands

Mind the gap : gas and dust in planet-forming disks

Marel, N.

Citation
Marel, N. (2015, September 29). *Mind the gap : gas and dust in planet-forming disks*. *PhD Thesis*. Retrieved from https://hdl.handle.net/1887/35579

Version:	Not Applicable (or Unknown)
License:	Licence agreement concerning inclusion of doctoral thesis in the Institutional Repository of the University of Leiden
Downloaded from:	https://hdl.handle.net/1887/35579

Note: To cite this publication please use the final published version (if applicable).

Cover Page



Universiteit Leiden



The handle http://hdl.handle.net/1887/35579 holds various files of this Leiden University dissertation

Author: Marel, Nienke van der
Title: Mind the gap : gas and dust in planet-forming disks
Issue Date: 2015-09-29

Mind the gap:
gas and dust in planet-forming disks

Mind the gap:
gas and dust in planet-forming disks

Proefschrift

ter verkrijging van
de graad van Doctor aan de Universiteit Leiden,
op gezag van Rector Magnificus prof.mr. C.J.J.M. Stolker,
volgens besluit van het College voor Promoties
te verdedigen op dinsdag 29 september 2015
klokke 13.45 uur

door

Nienke van der Marel

geboren te Groningen, Nederland
in 1986

Promotiecommissie

Promotors:	Prof. dr. E. F. van Dishoeck	
	Prof. dr. C. P. Dullemond	
Overige leden:	Prof. dr. I. A. G. Snellen	
	Prof. dr. G. A. Blake	California Institute for Technology
	Prof. dr. J. P. Williams	University of Hawaii
	Prof. dr. A. Natta	Dublin Institute for Advanced Studies
	Dr. M. R. Hogerheijde	
	Prof. dr. H. J. A. Röttgering	

ISBN: 978-94-6259-807-2

Cover design by Floris van der Marel and Killian K.M. Poolmans

To my grandmother Dolly
who never lost passion and interest
for the world around her

'Live as if you were to die tomorrow
Learn as if you were to live forever'
–Mahatma Gandhi

Contents

1 Introduction **1**
- 1.1 Stars, disks and planets . . . 4
  - 1.1.1 Star formation . . . 4
  - 1.1.2 Planet formation . . . 5
  - 1.1.3 Protoplanetary disks . . . 5
  - 1.1.4 Transition disks . . . 7
- 1.2 Disk processes . . . 9
  - 1.2.1 Dust evolution . . . 9
  - 1.2.2 Disk dynamics and dust trapping . . . 10
  - 1.2.3 Planetesimal and planet formation . . . 11
  - 1.2.4 Disk dispersion and photoevaporation . . . 12
- 1.3 Observations . . . 12
  - 1.3.1 SEDs . . . 12
  - 1.3.2 Gas observations . . . 14
  - 1.3.3 Millimeter observations . . . 16
  - 1.3.4 Infrared observations . . . 18
- 1.4 This thesis . . . 18
- 1.5 Outlook . . . 20

2 A major asymmetric dust trap in Oph IRS 48 **23**
- 2.1 Main article . . . 25
- 2.2 Supplementary Materials . . . 29
  - 2.2.1 IRS48 . . . 29
  - 2.2.2 ALMA observations . . . 29
  - 2.2.3 Morphology of the continuum emission . . . 31
  - 2.2.4 Dust mass . . . 33
  - 2.2.5 CO 6-5 lines . . . 34
  - 2.2.6 Dust trapping . . . 36
  - 2.2.7 Model of the IRS 48 dust trap . . . 37
  - 2.2.8 Alternative scenarios . . . 39

3 A concentration of centimeter-sized grains in Oph IRS 48 **43**
- 3.1 Introduction . . . 45
- 3.2 Observations . . . 46
- 3.3 Results . . . 46
- 3.4 Discussion and summary . . . 49

4 Testing particle trapping in transition disks **53**
- 4.1 Introduction . . . 55
- 4.2 Targets and observations . . . 55
- 4.3 Data analysis . . . 57
  - 4.3.1 Visibilities and disk morphology . . . 57
  - 4.3.2 Spectral index . . . 58
- 4.4 Theoretical predictions of particle trapping . . . 61

4.5 Discussion . . . 62
4.A Uncertainties of azimuthal variations of spectral index . . . 63
4.B Imaginary part of the visibilities . . . 65
4.C Residual maps . . . 65

5 Gas structure inside dust cavities of transition disks: Oph IRS 48 67
5.1 Introduction . . . 69
5.2 Observations and data reduction . . . 70
5.3 Results . . . 71
5.3.1 Integrated intensity maps . . . 71
5.3.2 Channel maps . . . 73
5.3.3 Total spectrum and $C^{17}O$ . . . 74
5.3.4 A cut through the major axis of the disk . . . 74
5.4 Analysis . . . 74
5.4.1 Disk structure . . . 77
5.4.2 Physical-chemical modeling . . . 80
5.4.3 Comparison to observations . . . 81
5.4.4 How well is the 20 AU radius determined? . . . 84
5.4.5 Prediction for the CO isotopologue lines . . . 84
5.5 Discussion . . . 86
5.5.1 The gas mass and surface density profile . . . 86
5.5.2 The gas surface density at the dust trap . . . 88
5.5.3 Consequences of the gas mass for a companion . . . 88
5.6 Conclusions . . . 89

6 Gas density drops inside dust cavities of transitional disks 91
6.1 Introduction . . . 93
6.2 Data . . . 95
6.2.1 Observational details . . . 95
6.2.2 Continuum and line maps . . . 96
6.3 Method . . . 99
6.3.1 Modeling . . . 99
6.3.2 DALI . . . 100
6.3.3 Approach . . . 100
6.4 Results . . . 104
6.4.1 Results of individual targets . . . 107
6.5 Discussion . . . 112
6.5.1 Implications of gas density drop . . . 112
6.5.2 Cavity size and dust distribution . . . 113
6.6 Conclusions . . . 114
6.A Channel maps . . . 115

7 Resolved gas cavities in transitional disks inferred from CO isotopologues 119
7.1 Introduction . . . 121
7.2 Data . . . 125
7.2.1 Observational details . . . 125
7.2.2 Continuum and line maps . . . 125
7.3 Modeling . . . 126
7.3.1 Physical model . . . 126
7.3.2 Model fitting approach . . . 126

7.4 Results . . . 128
7.4.1 Results of individual targets . . . 128
7.4.2 A gradual drop . . . 133
7.4.3 Isotopologue selective photodissociation . . . 135
7.5 Discussion . . . 135
7.6 Conclusions . . . 137
7.A Dust model DoAr44 . . . 138
7.B Channel maps . . . 139
7.C Additional models . . . 140

8 Warm formaldehyde in Oph IRS 48 143
8.1 Introduction . . . 145
8.2 Observations . . . 146
8.3 Results . . . 147
8.4 Model . . . 148
8.4.1 Physical structure . . . 148
8.4.2 Results . . . 153
8.5 Discussion . . . 157
8.5.1 Origin of the H_2CO emission . . . 157
8.5.2 Comparison with chemical models . . . 159
8.5.3 Comparison of upper limits with other observations . . . 160
8.5.4 Predictions of line strengths of other transitions . . . 161
8.6 Conclusions . . . 162

9 The (w)hole survey: transition disk candidates from the Spitzer catalogs 165
9.1 Introduction . . . 167
9.2 Observations . . . 169
9.2.1 Target selection . . . 169
9.2.2 Additional photometry . . . 170
9.2.3 Submillimeter observations . . . 172
9.2.4 Herschel observations . . . 173
9.2.5 Spectroscopy . . . 173
9.3 Results . . . 174
9.3.1 Stellar parameters . . . 174
9.3.2 Photometry . . . 180
9.3.3 Disk parameters . . . 180
9.4 Modeling . . . 182
9.4.1 Approach . . . 182
9.4.2 Results . . . 183
9.5 Discussion . . . 188
9.5.1 Comparison of cavity radii with literature values . . . 188
9.5.2 Binaries . . . 189
9.5.3 Accretion . . . 190
9.5.4 Evaluation of color criteria . . . 191
9.5.5 Comparison with Cieza survey . . . 191
9.5.6 Evolution . . . 194
9.5.7 Inner disk . . . 196
9.5.8 Cavity radii and exoplanets . . . 196
9.6 Summary . . . 197

9.A Sample 197
9.B Flux tables 216

Bibliography **221**

Nederlandse samenvatting **231**

List of publications **237**

Curriculum Vitae **239**

Acknowledgements **241**

1

Introduction

"We live in a universe whose age we can't quite compute, surrounded by stars whose distances we don't altogether know, filled with matter we can't identify, operating in conformance with physical laws whose properties we don't truly understand." - Bill Bryson: 'A short history of nearly everything'

Since the beginning of humanity, people have looked up to the sky and wondered where they come from. Both religion and philosophy played a major role to explain everything we saw that we could not understand. Observing the motions and phenomena in the sky within the human perspective gives only a limited view on what is going on in the Universe. It is then even harder to imagine that there is a link between the Earth we live on, the Sun that rises and sets every day and the twinkling dots in the night sky. The major question throughout history is the place of humans (and their home planet) within the Universe: from Aristarchos who suggested for the first time that the Sun was the center of the Universe instead of the Earth, to Galileo's discovery of moons orbiting Jupiter, to William Herschel defining the Sun as an ordinary star somewhere in the outer parts of the Milky Way, to exoplanets not quite following the 'perfect' configuration of our Solar System. With time, ideologies and philosophical theories were replaced by science and empirical research. Even now, new discoveries are constantly overtaken by the understanding at that time, creating new problems and challenges for scientists to be solved and new ideas to be explored.

One of the most remarkable revolutions was the idea that stars and planets do not live forever, but that they must be born, live and die. The main trigger for this idea was the discovery of nuclear fusion as the main fuel of stars in the beginning of the 20th century, which implies directly that there has to be a beginning and end of the fueling process. The Solar Nebular Hypothesis was already proposed in the 18th century by Emanuel Swedenborg and further developed by Immanuel Kant. This theory contributed to the idea that stars and planets are formed at some stage. It is surprising that the idea of an infinite, unchanging Universe was taken for granted for such a long time, while evidence of birth and death is all around us in every day life. The main reason is again the limitation of the human perspective: the spatial and temporal scales in which things happen in the Universe go beyond our imagination. Even if we put numbers and units to these scales, it is difficult to put a feeling to what it is really like in the Universe. As a consequence, astronomy was for a long time driven by the development of physics itself.

With the technological innovations and the exponential increase of new telescopes and instruments at wavelengths outside the optical regime in the second half of the 20th century, observations did not only confirm or disprove theories, but started to drive new theories. The dawn of every new telescope revealed new objects, new structures, new prospects for our understanding of the Universe. The insight in formation of young stars, disks and planets has been revolutionized by telescopes such as *IRAS*, *Spitzer* and *Herschel* in the infrared, and JCMT, IRAM, APEX and SMA in the (sub)millimeter, where these objects are shining the brightest.

Of particular interest for this thesis are the protoplanetary disks, and the processes leading to the formation of planets in these disks. Disks can be seen as flattened, rotating structures of gas and dust around protostars, which evolve through viscous accretion to gas-poor debris disks. Transition disks, the disks with cleared-out inner dust cavities, are the prime targets of this study. The major questions that we aim to answer in this thesis are the following. What is the structure of the gas in transition disks? What is the clearing mechanism, the origin of dust cavities? How do recently formed planets sculpt their surrounding disk? How can small dust grains grow into larger pebbles and planetesimals, the start of planet formation? What can gas observations tell us about physical processes in disks? In general: what is the role of

transition disks in the planet formation process?

The arrival of ALMA, the Atacama Large Millimeter/submillimeter Array, is another revolution in answering these questions. ALMA is an array of 66 antennas operating at (sub)millimeter wavelengths, built at the Chajnantor plateau in the Atacama desert at 5000 m altitude in Chile. ALMA is an international partnership of ESO, NSF (USA) and NINS (Japan), together with NRC (Canada), NSC and ASIAA (Taiwan), and KASI (Republic of Korea), in cooperation with the Republic of Chile. When finished, the antennas will be equipped with 10 receivers ranging from 30 to 950 GHz (0.3 millimeter up to 1 cm) and placed in configurations with baselines up to 16 kilometer, resulting in spatial resolutions at the mas level. Both the sensitivity and spatial resolution exceed the pioneering millimeter interferometers by two orders of magnitude. Of particular importance for this thesis are the high frequency Band 9 receivers operating at 690 GHz (Baryshev et al. 2015), developed by NOVA (the Netherlands Research School for Astronomy) and SRON (Netherlands Institute for Space Research). ALMA started operations in 2011 with a partially completed array of 16 antennas and 4 receivers with baselines up to 400 meter (0.2" resolution at the highest frequency) and has gradually increased its capacities in the following years. ALMA allows us to zoom in deeper on the birth of planets than any other telescope before, unraveling more questions than we could ever have imagined in the wonder about our origin.

1.1 Stars, disks and planets

1.1.1 Star formation

Stars and planets are ubiquitous in the universe and their formation process has been the subject of decades of study (see reviews e.g. Shu et al. 1987; Williams & Cieza 2011; Armitage 2011; André et al. 2014; Raymond et al. 2014; Helled et al. 2014). Planets are thought to form in protoplanetary disks of gas and dust around young low-mass and intermediate mass (<8 $M_\odot$) protostars (see Figure 1.1 for an evolutionary sequence). These disks are a natural consequence of star formation. A star is formed by gravitational collapse of a molecular cloud, where the conservation of angular momentum ensures the spin up of material leading to a flattened, rotating structure around the star, called a *'disk'*. The cloud mass is dominated by the gas with a typical gas-to-dust ratio of 100. In the early phases of evolution the disk is surrounded and fed by the protostellar envelope (*embedded disk*) and simultaneously depositing material onto the still forming star for a period of a few 10^5 years (Evans et al. 2009; Dunham et al. 2014). After this, a period of several Myr years starts in which the disk disperses its material, through viscous accretion inside the disk and stellar winds at the disk surface. Since the bulk of the disk mass is in the gas, the gas dominates the dynamical processes in the disk. By some critical point, the disk has lost a large fraction of its gas mass and accretion onto the star has come to an end. Some, if not all planets in the system may already have formed at this stage. The star continues its evolutionary path towards the main sequence until hydrogen fusion starts; by this time the star and its surrounding planets have several billion relaxing years ahead of them until the star has run out of its nuclear fuel. Although the formation of high-mass stars (>8 $M_\odot$) likely follows more or less the same sequence of events, the physical processes behind it are less well understood due to the destructive consequences of their much higher radiation fields.

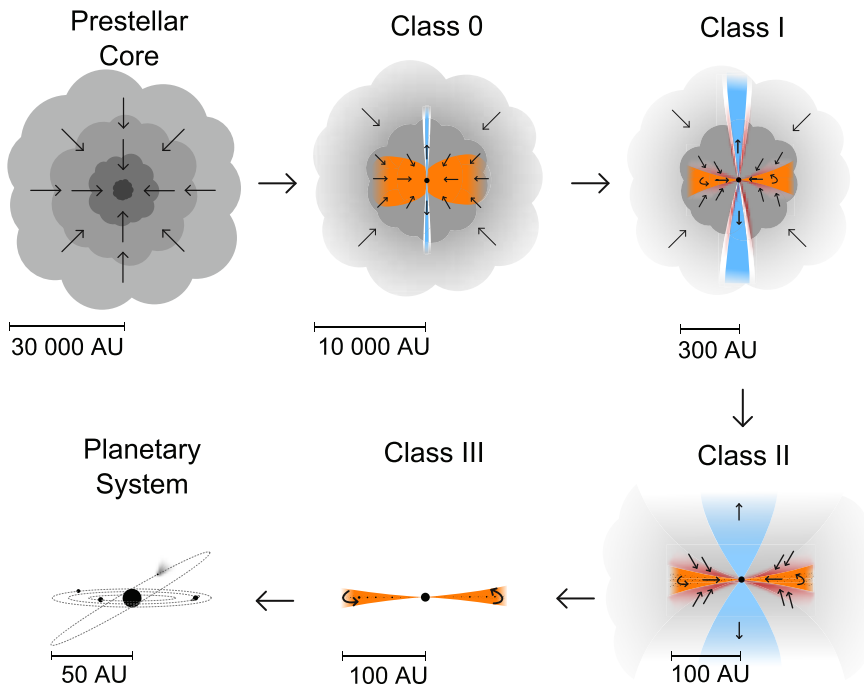


Figure 1.1: *The evolutionary process of star and planet formation. A prestellar core collapses to a protostar still embedded in its envelope. Material keeps falling in and a rotating disk forms around the star. Molecular outflows and accretion remove the envelope material, until only a disk remains. The disk evolves from a massive gas-rich to a gas-poor debris disk, ending as a planetary system. Figure by Magnus Persson.*

1.1.2 Planet formation

One of the many open questions is when and how the formation of planets fit into this story. Current statistical studies of exoplanets suggest that most stars in the Milky Way (and perhaps the Universe) hosts at least one planet (Batalha 2014). This conclusion raises the question whether planets are just a natural by-product of disk evolution and star formation. Since the construction of a planet is a long-lasting process taking up millions of years (see Section 1.2), we have to study the structure of their birth cradles, the protoplanetary disks, in order to learn more about the relevant physical processes. This thesis focuses on the structure of the gas and dust in disks, which is now possible due to the sensitivity and spatial resolution of ALMA, which started operations only a few years ago. Interestingly, the Solar Nebular Hypothesis was proposed long before astronomers could prove the presence of circumstellar disks around other stars and study how planets form inside these disks.

1.1.3 Protoplanetary disks

The objects that are now known as young stars with circumstellar disks were originally identified through optical observations as pre-main sequence stars that were thought to be in the

middle of their formation; the presence of disks was not confirmed until several decades later. The main characteristics of this new class of stars pointing to their pre-main sequence status were e.g. their systematically higher brightness compared to main sequence stars of the same spectral type; their overabundance inside dark clouds; and strong optical emission lines such as the hydrogen Balmer lines (e.g. Hα) and Ca II (Joy 1945; Herbig 1957). They were called T Tauri stars and their massive, bright equivalents the Herbig Ae/Be stars. The latter were recognized early on as equivalent to T Tauri stars (Herbig 1960), with the distinct difference that the star is of earlier type and illuminates a reflection nebula, which is a natural consequence of the star being brighter.

Initially the T Tauri/Herbig stars were thus not even known to have disks. T Tauri stars often show emission excess in the UV with respect to the stellar photosphere, which is not so evident in Herbig stars. At this stage, two types of T Tauri stars were known: *classical* (CTTS) and *weak-line* (WTTS or NTTS: naked TTS), referring to the emission strength and width of the Hα line. In addition WTTS show strong X-ray emission (e.g. Walter & Kuhi 1981) and much less UV excess. The first evidence for dust grains surrounding these stars was found through additional emission excess above the photosphere in the infrared up to 5 μm (Mendoza V. 1966). However, the pieces of the puzzle were not put together until the suggestion of a self-luminous viscous accretion disk model to explain the nature of both of these types of excess emission (Lynden-Bell & Pringle 1974; Kenyon & Hartmann 1987). This was also the time that both UV and far infrared data became available through the *International Ultraviolet Explorer (IUE)* and the *InfraRed Astronomical Satellite (IRAS)* in 1978 and 1983, respectively. The bright infrared emission with optically visible stars proved that the dust grains could not be distributed in a spherical shell, as this would result in much higher optical extinction. Therefore the emission had to originate from a physically thin structure: a disk. Another piece of evidence for disks was found through optical spectroscopy showing only the blue-shifted component of forbidden line emission: the red-shifted emission is obscured by an occulting disk (e.g. Edwards et al. 1987; Bertout 1989). The recognition and understanding of disks has thus always been strongly driven by new observational facilities, just as this thesis is largely driven by ALMA.

Remarkably, one of the main reasons that T Tauri and Herbig stars were even recognized as a signature of protostellar evolution, is their similarity to high mass counterparts seen in short-lived (and thus recently formed) OB associations, whereas the high-mass star formation process itself remains much less understood. The Herbig stars were studied largely separately from T Tauri stars due to their bright nature and thus easy observability. This terminology splits up the pre-main sequence stars in different categories, whereas they are likely just similar in nature, albeit with a different spectral type and mass, and thus a different evolutionary pace. In this thesis we study several disks for a range of spectral types from A-type Herbig to M-type T Tauri stars.

In the decades after the discovery of circumstellar disks through excess emission, they were successfully imaged: the nearby β Pic debris disk in scattered light (Smith & Terrile 1984), the 'proplyds' (acronym for protoplanetary disks seen in silhouette against a bright HII region) in Orion with the *Hubble Space Telescope* (O'Dell et al. 1993) and the millimeter continuum and CO line images showing Keplerian rotation (e.g. Sargent & Beckwith 1987). Accretion was related to UV excess and optical line emission (Kenyon & Hartmann 1987). With the availability of infrared data from *IRAS* and *Infrared Space Observatory (ISO)* an evolutionary sequence in the path of planet formation was proposed (Adams et al. 1987): from the disks deeply embedded in their envelope (Class I), to the young stars with a bright accreting disk (Class II or CTTS), to the pre-main sequence stars with only weak disk and accretion signatures (Class III or WTTS).

This classification (Lada classification) relies on the infrared part of the Spectral Energy Distribution or SED: the (spatially unresolved) photometric spectrum from optical to millimeter wavelengths. Dust grains are heated by the star and by viscous heating, and emit primarily through thermal emission. As the dust temperature in a disk (or envelope) largely depends on the distance from the central heating source, this results in a broad continuous excess above the stellar photosphere at infrared and longer wavelengths due to the range of temperature in the disk. Disk emission is clearly distinct from envelope emission because a spherical envelope obscures a much larger fraction of the emission originating from the protostar. With the *Spitzer Space Telescope* complete samples of young stellar objects in nearby star-forming regions were constructed. From the complete survey of star-forming regions it was possible to compute statistics and derive typical time scales of the different stages in the star and disk evolution process, which were compared to evolutionary models (e.g. Evans et al. 2009). Disks around young stars were found to be a common feature. At the same time the number of discovered exoplanets was steadily growing, giving more and more evidence that planets around stars are ubiquitous.

1.1.4 Transition disks

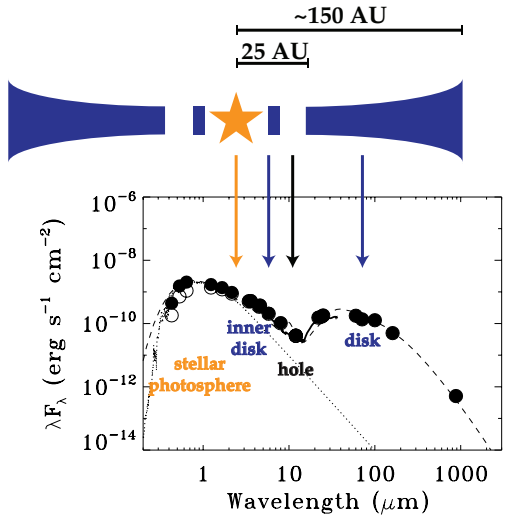


Figure 1.2: *Spectral Energy Distribution of a transition disk, showing the different components of the system and their emitting wavelengths. The stellar photosphere emits as a blackbody in optical to near-infrared wavelengths, an inner disk is recognized as near-infrared excess above the photosphere due to hot dust grains, the hole is seen as a dip in the mid-infrared, while the bulk of the dust in the outer disk emits in far-infrared up to millimeter wavelengths.*

One of the main questions in this evolutionary process is the transformation of the massive, gas-rich circumstellar Class II disks towards the tenuous Class III debris disks with planets. During this crucial transition the material from the disk is accreted onto the star, dispersed into the interstellar medium and possibly merged into planets, although planet formation could also start at an earlier stage. The transition is thought to be rapid, due to the small amount of disks with properties in between Class II and III (or between CTTS and WTTS). The discovery of disks with a dip in the mid infrared excess in the SED through *IRAS* photometry

was interpreted as a sign of inner holes or dust clearing (Strom et al. 1989). This group of disks were named 'transition disks' (see Figure 1.2), although it remains unclear whether all disks go through a 'transition disk phase'. Several other disks with cleared inner cavities were identified 10-15 years later through dips in their Spitzer IRS spectra (5-35 μm) (Forrest et al. 2004; Calvet et al. 2005; Brown et al. 2007).

In this transitional phase a range of processes were thought to be responsible for the appearance of a cavity (see also next section): (1) grain growth, where dust grains inside the cavity have grown to larger sizes that do not emit sufficiently at the observed wavelength; (2) photoevaporative clearing, where the stellar UV heats gas to temperatures above the escape speed, resulting in a photoevaporative wind that clears the disk from the inside out; (3) certain instabilities leading to dust concentrations in the outer disk; (4) companion clearing, where either a planet or a star carves a gap in the dust and gas in their orbit.

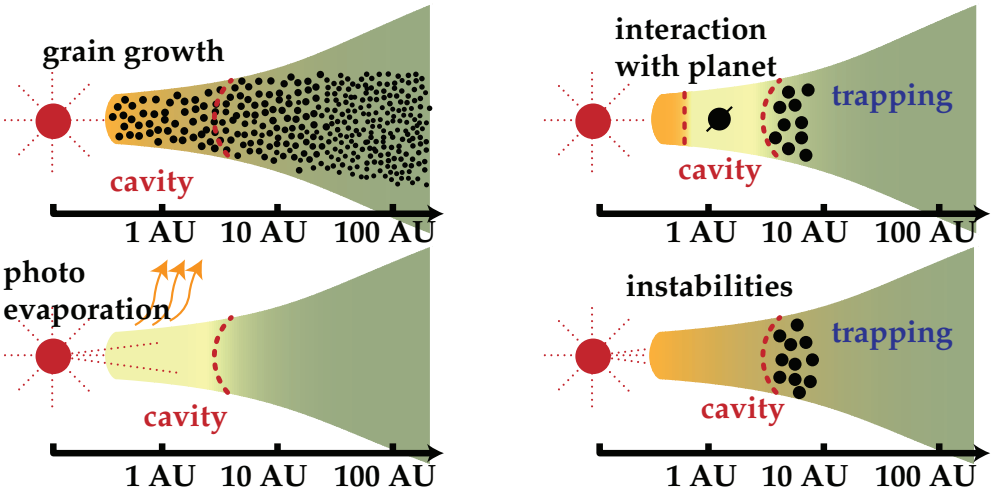


Figure 1.3: *Cavity clearing mechanisms in dust (black dots) and gas (yellow).* **Top left:** *increased grain growth inside the cavity, while the gas density remains unchanged compared with the original disk.* **Bottom left:** *photoevaporative clearing, with both the gas and dust cleared simultaneously from the inside out.* **Top right:** *clearing by a companion, in which the gas density inside the cavity drops and the large dust particles get trapped at the edge.* **Bottom right:** *instabilities due to e.g. viscosity or entropy gradients create a dust trap, the gas density remains unchanged. Figure based on cartoon by Simon Bruderer.*

The discovery of transition disks thus opened up an interesting possibility of studying the most important disk evolution processes for understanding planet formation. Most observational studies of transition disks have focused on the dust distribution in these disks, while the key for distinguishing between the mechanisms lies in the gas, which is predicted to be different in all cases (see Figure 1.3): the gas density is unaffected by grain growth and certain instabilities, is cleared completely by photoevaporation from the inside out and is reduced in case of companion clearing depending on the companion mass and disk viscosity (Lubow & D'Angelo 2006; Crida et al. 2006; Pinilla et al. 2012a).

Early observations have revealed evidence for the presence of warm atomic and molecular gas inside dust cavities from optical and infrared observations (e.g. Najita et al. 2003; Acke & van den Ancker 2004; Salyk et al. 2007; Pontoppidan et al. 2008). However, measurements of the bulk of the molecular material inside the dust cavity was not possible until the arrival

of ALMA. In this thesis we quantify the gas distribution directly with resolved ALMA observations of several transition disks in order to answer the questions of their underlying clearing mechanism and their role in planet formation and disk evolution.

1.2 Disk processes

With a large range of observations of the planet birth cradles, the step towards solving the puzzle of planet formation itself appears to be close, but this could not be further from reality: although increasingly sophisticated evolution models explain a large range of disk properties and physical processes, planet formation itself remains a mystery, as any theory that has been developed so far ultimately breaks down when compared to the actual time scales and exoplanet properties. Transition disks are promising candidates with active planet formation. The spatially resolved ALMA observations of gas and dust presented in this thesis can be compared directly with physical disk processes to get a better understanding of their role in disk evolution.

1.2.1 Dust evolution

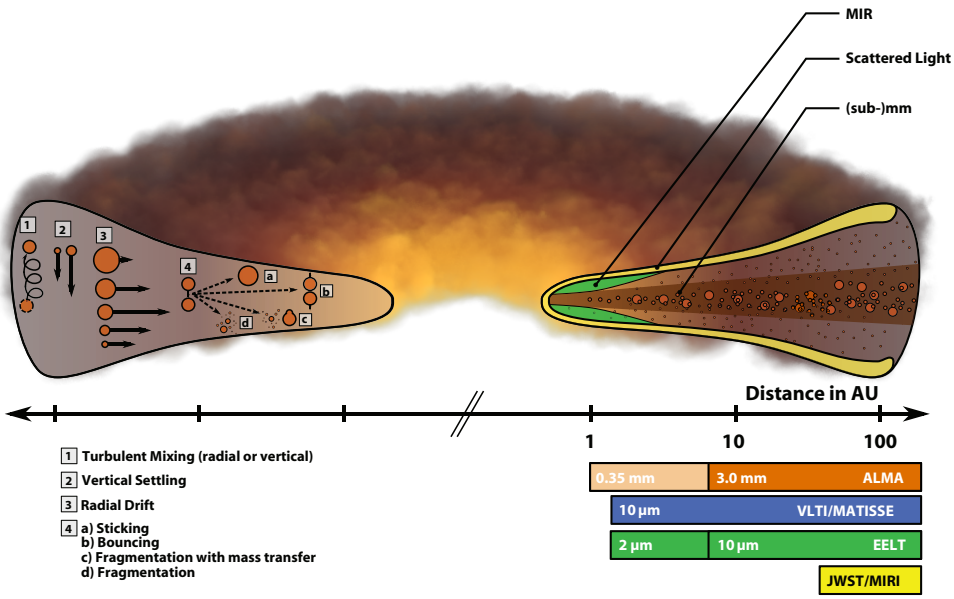


Figure 1.4: *Dust processes in the disk. The left part shows the physical processes affecting the dust grains in the disk, as described in the text. The right part shows which section of the disk is observed at different wavelengths, as discussed in Section 2.3. Figure taken from Testi et al. (2014).*

The starting point of planet formation lies in the evolution of dust grains: the growth of small (sub)micron-sized particles, which are present in the interstellar medium (ISM), to centimeter-sized pebbles, planetesimals and beyond. Several physical processes are involved in grain growth in disks, which need to be taken into account in models. Dust grains can grow by collisions, followed by either coagulation or fragmentation, depending on the relative

velocities (which in turn are affected by turbulence, drift, mixing and location in the disk) and the grain stickiness (composition, icy layers and fluffiness or shape). Dust evolution requires numerical modeling, with constraints on the collision outcomes set by laboratory experiments (Blum & Wurm 2008). Dust growth models show that ISM grains can indeed efficiently grow to millimeter sizes within 10^5 year time scales (Brauer et al. 2008). However, growth is stymied by several processes, including fragmentation and drift.

The most important issue is the presence of gas in the disk, which prevents dust particles from moving freely: they experience a drag force (depending on their physical size) when they move relative to the gas. One of the consequences is vertical settling: larger dust particles settle to the midplane of the disk due to damping of the drag force, although turbulent mixing partially opposes the effect. The vertical structure of dust particles is thus an equilibrium between settling and mixing (e.g. Dullemond & Dominik 2004). Another consequence is the *radial drift problem* (Whipple 1972; Weidenschilling 1977). Dust and gas orbit in Keplerian motion in a protoplanetary disk, due to gravitational and centrifugal forces. However, the gas feels an additional pressure force, due to the outward pointing pressure gradient in the disk, resulting in slightly sub-Keplerian velocities of the gas. This causes a head-wind or friction for the dust particles, which consequently lose angular momentum and spiral inwards on short time scales: typically 100 years for a one-meter-sized object at 1 AU or a millimeter-sized dust grain at 100 AU, since the efficiency of this phenomenon depends on the dust particle size and orbital time scale. This 'meter-size-barrier' prevents particles to grow to larger pebbles, which is a crucial first step in planet formation. Radial drift also predicts that larger grains are radially more concentrated than the gas in a protoplanetary disk.

If the drift barrier can be overcome, the fragmentation barrier limits dust to grow beyond 1 meter in the outer disk. Fragmentation occurs when larger particles collide with relatively high velocities (Brauer et al. 2008). In principle this problem can be overcome when additional dust growth mechanisms such as sweep-up and mass transfer are included (Xie et al. 2010; Windmark et al. 2012). However, the radial drift problem can not be solved by dust processes alone.

1.2.2 Disk dynamics and dust trapping

A possible way to overcome the radial drift problem is to trap dust particles in so-called *pressure bumps* in the gas. A local region of high pressure in the outer disk provides a negative pressure gradient outwards, reversing the drift direction and effectively trapping the dust particles (Whipple 1972). Anti-cyclonic vortices in disks were suggested first to act as pressure bumps (Barge & Sommeria 1995; Klahr & Henning 1997).

Vortices result from hydrodynamical processes such as Rossby-wave and baroclinic instabilities in a disk (Lovelace et al. 1999; Klahr & Bodenheimer 2003). Several other physical processes in a disk can create dust traps: the most well-known are the density bumps at the edges of gaps cleared by planets (Zhu et al. 2011; Pinilla et al. 2012a, and Figure 1.5) and the edges of so-called dead zones. Dead zones are regions of low ionization in the disk in which the MRI angular momentum transport does not work (MRI is magnetorotational instability). They can form spontaneously in between cosmic or UV-ray ionized low-density outer regions and collisionally ionized warm high-density inner regions of disks (Varnière & Tagger 2006; Regály et al. 2012). These and other processes are described in more detail in Armitage (2011). The planet-gap scenario is interesting as it returns to the original question of what causes the clearing of a transition disk. However, as an explanation of the planet formation scenario it creates a chicken and egg problem: if a dust trap is required to grow particles and form planets, where does the first planet that has made the dust trap come from?

1.2.3 Planetesimal and planet formation

In general, a radial pressure trap would result in a ring of millimeter-sized particles, while an azimuthal maximum such as seen in a vortex would result in an asymmetric millimeter-dust distribution (Wolf & Klahr 2002; Regály et al. 2012; Birnstiel et al. 2013). In this thesis we present the first clear observational evidence for such a dust trap in the Oph IRS 48 disk. Other transition disks imaged by ALMA show asymmetric dust distributions (Casassus et al. 2013; Pérez et al. 2014). Trapping depends on the particle size, so smaller particles are predicted to spread further throughout the disk and continue to flow inwards through the gap. This radial segregation of small vs large particles is also referred to as dust filtration (Rice et al. 2006). On the other hand, larger centimeter-sized dust particles are expected to be even further concentrated in a dust trap, either radially or azimuthally. This is indeed found for the dust trap in IRS 48 as well.

Time-dependent dust evolution models show that dust not only gets trapped but also grows more efficiently inside these traps, as fragmentation is lower due to a decrease in relative velocities (Brauer et al. 2008). Growth continues up to planetesimal sizes, which can then grow further to rocky planets through runaway or orderly growth, as their own gravitational field starts to attract planetesimals in their surroundings. Once a rocky planet of >10 Earth masses has been formed, the *core accretion* model predicts the formation of a gas giant, where the planet accretes gas from the disk. This implies that the rocky core needs to be formed before the gas disk has dissipated. Alternatively *gravitational instability* can result in disk fragmentation and quick gas giant formation (e.g. Helled et al. 2014). Both models have difficulties explaining the observed exoplanets and their orbital radii, also due to the expected migration of planets through the disk-planet torques.

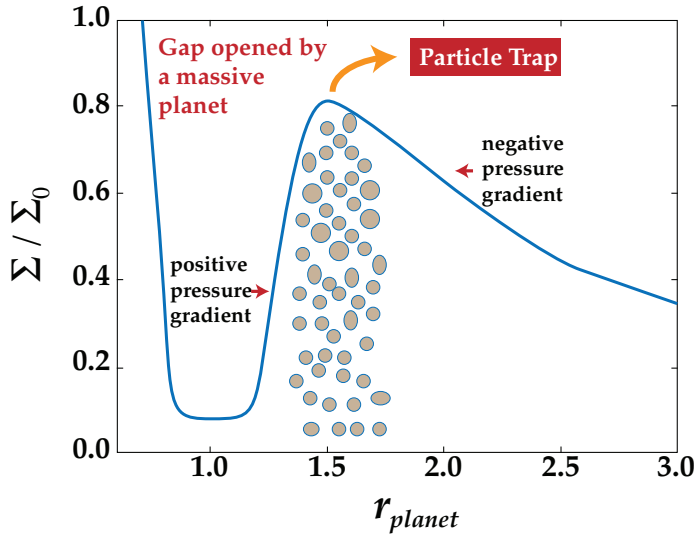


Figure 1.5: *Cartoon of a radial pressure bump, induced by a planet. The gas surface density is lowered at the location of the planet, resulting in a pressure maximum at the edge of the gap, where the milimeter dust gets trapped. Figure by Paola Pinilla.*

1.2.4 Disk dispersion and photoevaporation

Although planet formation is one of the major drivers for disk studies, it is not the main reason why disks disappear: observations of both the Solar System and exoplanets show that planets contain only $\lesssim$1% of the initial disk mass. Instead, the main mechanisms for disk dissipation are accretion onto the star and photoevaporation (Hollenbach et al. 2000; Gorti et al. 2009; Alexander et al. 2014): stellar and interstellar high energy radiation (UV and/or X-rays) heats the disk surface to higher temperatures, up to the point where the thermal energy exceeds the gravitational binding energy and the heated gas escapes as a photoevaporative wind. Disk dispersal by photoevaporation becomes important when the accretion rate from the disk onto the star drops below the photoevaporation rate: at that point the material in the inner part of the disk is no longer replenished by the outer disk and will disappear from the inside out on time scales of $\sim 10^5$ years. Transition disks with cleared out cavities have been suggested to be caused by photoevaporation, but disks with large cavities (R >20 AU) which are still strongly accreting cannot be explained by photoevaporation models only (Owen & Clarke 2012).

1.3 Observations

Disk theories are developed from a theoretical point of view, in attempts to explain planet formation, and directly driven by disk observations. New observations provide better constraints but also raise new questions: the measurement of millimeter fluxes in disks confirmed larger particles in disks than in the ISM (Beckwith & Sargent 1991) but set the challenge of solving the radial drift problem; the discovery of the stellar companion of CoKu Tau 4 solved the question of its large cavity (Ireland & Kraus 2008) but binarity could not explain other transition disks; scattered light imaging confirmed a gap in the small dust grains in some disks but did not reveal a cavity in others (e.g. Follette et al. 2013); large cavity sizes were confirmed by millimeter interferometry observations (Andrews et al. 2011), but they were generally too large to match with exoplanet orbital radii (planet clearing mechanism) or photoevaporation models. This thesis combines the results of several of the studies mentioned above with new ALMA data and resolves some of the issues.

1.3.1 SEDs

One of the difficulties of disk observations is their low mass (only a fraction of the cloud mass) and thus total flux and their angular size: due to the distances of the nearby star-forming regions of ~100-200 pc, disks are typically only a few arcseconds in size. Their detection and identification was relatively easy when the first infrared observations became available through *IRAS* photometry in the 1980s. However, resolving disks was only possible for the proplyds in silhouette against a bright background until the arrival of the first millimeter interferometers in the early 2000s. Fortunately, even SEDs consisting of unresolved photometry fluxes provide important information on the structure of the dust disk, especially transition disks. As the dip in the mid infrared part of the SED is the main signature of a transition disk, the *Spitzer Space Telescope* with a wavelength range from 3.6 up to 70 μm was by far the most important tool to recognize and study transition disks. All nearby star forming regions were observed in the Cores to Disks (c2d) and Gould Belt *Spitzer* programs, and several transition disks were discovered by observations with the *Spitzer* IRS spectrograph 5-35 μm range.

Disk structure in the SED The SED of a transition disk consists of signatures of the stellar photosphere in the optical/near-infared, accretion in the UV, the presence of an inner dust

disk in the near-infrared and the outer dust disk at wavelengths from mid-infrared up to millimeter emission (Figure 1.2). The continuum emission at long wavelengths probes the cold, optically thin millimeter-sized dust. Some disks have a strong near-infrared excess while others do not, implying systems with and without an optically thick inner disk. Espaillat et al. (2007) interpret the existence of these two types of systems as an evolutionary effect and name them pre-transitional and transitional, respectively, as clearing by a companion would first just clear a gap and later remove the inner disk entirely. However, as the clearing mechanism is unknown for most disks and as material needs to continue to flow through the gap to explain the accretion onto the star, one needs to be careful with interpreting this observational difference as a real evolutionary sequence. Hence the term pre-transitional disk will not be used in this work.

Identifying transition disks A transition disk is often identified in the SED by comparison with a representative disk (usually the median SED of disks in the well-studied Taurus star forming region): typically the excess between 5 and 20 μm is lower in a transition disk while the SEDs are similar at longer wavelengths. A problem of photometry is confusion: the large beam size of *IRAS* could contain multiple young stellar objects, as they are often grouped together, leading to overestimating the excess emission and the false presence of a mid-infrared deficit. The *Spitzer* beam was better at the longest wavelengths where the beam is largest, with a 70 μm beam size of 15", similar to single dish submillimeter observations. Photometry of the *Herschel* telescope with a 4 times larger mirror has revealed cases of *Spitzer* confusion of objects at 70 μm (Ribas et al. 2013).

With the large surveys from *Spitzer*, several criteria of infrared colors have been developed in order to select transition disk candidates from surveys, which have been tested against sources with full IRS spectra available (e.g. Brown et al. 2007; Hernández et al. 2007; Cieza et al. 2010; Merín et al. 2010). In this thesis we present a study of a large transition disk candidate sample, using color criteria on the *Spitzer* catalogs.

Modeling transition disks For a proper assessment of the disk structure and its cavity, SED modeling with a radiative transfer code is required, such as RADMC, MCFOST and McMAX (Dullemond & Dominik 2004; Pinte et al. 2006; Min et al. 2009). These codes calculate the expected dust emission based on a given 2D density structure by computing the dust temperature at all locations in the disk from the scattering and absorption of photons from a central star. The density structure of a transition disk is usually assumed to be a radially decreasing surface density law with a sharp cavity in the inner part of the disk and, if required by near-infrared excess, an inner disk close to the star (see Figure 1.6). The vertical structure (flaring or settling) is either calculated from hydrostatic equilibrium or parametrized. The vertical structure is particularly important. A flaring disk intercepts more radiation in the outer part of the disk, while a high scale height in the inner disk and at the wall edge can cast a shadow on the outer disk, lowering the temperature and thus the emission at far-infrared and longer wavelengths. Dust opacities are a key ingredient for any radiative transfer model and require assumptions about the dust composition and grain size distribution. Silicate and polyaromatic hydrocarbon (PAH) features that are sometimes seen in the mid-infrared spectrum set constraints on the dust composition (e.g. Kessler-Silacci et al. 2006). Transition disks have been successfully fit with SED modeling, in particular those SEDs for which IRS spectra with fluxes between 5-35 μm were available (Brown et al. 2007; Merín et al. 2010). Using millimeter interferometry (see Section 1.3.3), dust cavity sizes were confirmed to be within a factor of two of the results from SED modeling (Brown et al. 2009; Andrews et al. 2011). Degeneracies in SED modeling exist, especially in the vertical structure and amount

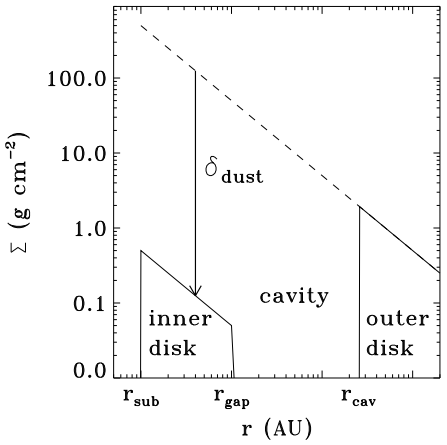


Figure 1.6: *Typical dust density structure for modeling a transition disk.*

of dust in the inner disk, which influence the derived cavity size.

Time domain studies of SEDs have shown so-called 'seesaw' variability in some transition disks where the slope of the infrared spectrum changes with time on time scales of weeks up to years. This suggests changes in the inner disk structure with time although it remains unclear what causes this behaviour (Muzerolle et al. 2009; Espaillat et al. 2011).

1.3.2 Gas observations

Whereas the dust distribution in disks has been studied to great detail, observational constraints on the gas distribution are rather limited, while the gas is considered to be dominating the disk properties such as mass and dynamical processes. In particular, the clearing mechanisms for transition disks described above have similar effects on the dust distribution, while the gas is affected in completely different ways and provides thus a way to distinguish between them (see Figure 1.3). Photoevaporation removes the gas and dust simultaneously, a companion would lower the gas density and trap the millimeter-sized dust at the edge and instabilities (and grain growth) would not significantly change the gas density inside the cavity at all. In particular, in case of a companion, planet-disk interaction models have shown that knowing the depth and shape of the gas gap could set constraints on the disk viscosity and planet mass (Crida et al. 2006; Pinilla et al. 2012a). Measuring the gas density inside and outside the dust cavity is thus a crucial step in understanding the transition disks, which is the main topic of this thesis.

Molecular line observations The reasons for the limited amount of gas observations to date are the low line sensitivity compared to continuum sensitivity for most instruments, confusion with surrounding envelope material (for single dish observations) and lack of direct density tracers. While the bulk of the gas mass is in H_2, its molecular lines cannot be used as mass tracer due to its lack of dipole moment. CO (with its isotopologues ^{13}CO and C^{18}O) is the second most abundant molecule in the gas and has been detected in several disks (e.g. Dutrey et al. 1997; Dent et al. 2005). The proper interpretation of CO as column density tracer is

challenging. CO rotational emission cannot be translated directly into mass for several reasons. First, the ^{12}CO and ^{13}CO lines are usually optically thick. Second, the gas temperature is decoupled from the dust temperature, especially in the higher layers in the disk. Third, the CO abundance is not constant with respect to H_2: in the surface layers CO is photodissociated by stellar radiation; in the mid-plane the CO freezes out onto the dust grains due to the low temperatures; and the chemical formation/destruction of CO depends strongly on the local density, temperature and radiation conditions (van Zadelhoff et al. 2001; Woitke et al. 2009). Even though the gas motion is Keplerian, the line-of-sight velocity is confused by contributions from different parts of the disk and it is almost impossible to derive mass information from unresolved spectra alone. Spatially resolved observations in combination with a physical-chemical modeling tool for proper interpretation of the emission are thus required for study of the gas density distribution.

The physical-chemical modeling tool developed for the purpose of interpreting molecular line emission in disks and in particular transition disks in this thesis is DALI (Dust And LInes) (Bruderer et al. 2012; Bruderer 2013). The DALI code first solves the dust radiative transfer in 2D for a given density structure and stellar radiation field. With the derived dust temperatures as starting point, the heating-cooling balance of the gas and chemistry are solved simultaneously to determine the gas temperature, molecular abundances and molecular excitation. All effects discussed above are thus taken into account. Special attention is paid to the chemistry and heating inside the dust-free cavities (Jonkheid et al. 2006). The resulting CO abundance in the disk in combination with the gas temperature determine the intensity and profile of the CO line emission in the final step, the ray tracer. The code is summarized in Figure 1.7. For CO isotopologues it was shown that isotope-selective photodissociation plays an important role: without the inclusion of this effect the column density based on C^{18}O observations can be severely underestimated (Miotello et al. 2014). In this thesis we have used DALI to analyze the gas structure in several transition disks.

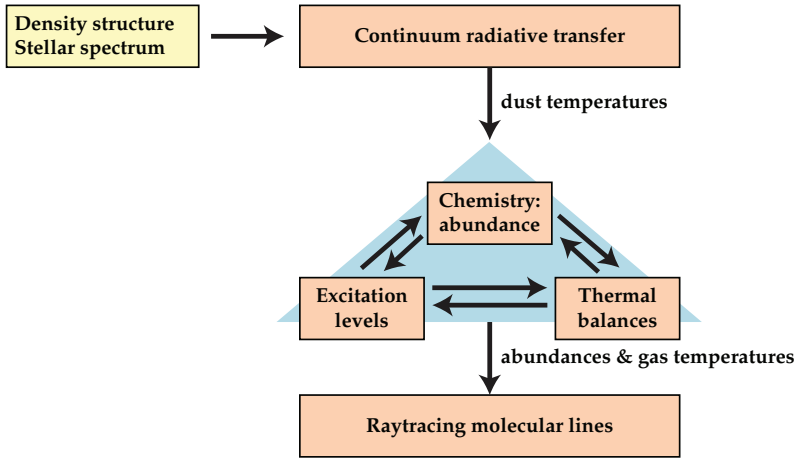


Figure 1.7: *DALI modeling structure. The input of the model is a 2D density structure and a stellar spectrum. Using dust radiative transfer (based on RADMC), the dust temperatures are calculated. DALI then solves the heating-cooling balance of the gas to determine molecular abundances, temperatures and excitation before raytracing spectra and spectral line cubes.*

A similar modeling code is ProDiMo (Protoplanetary Disk Modeling), which was developed to interpret infrared lines observed with Herschel (Woitke et al. 2009), and has a

comparable approach as DALI. Other codes to interpret gas line emission are e.g. ANDES (Akimkin et al. 2013) and the code developed by Gorti & Hollenbach (2004).

Gas inside the cavity The presence of accretion in the majority of the transition disks suggests that some gas must still be present inside the dust cavities. This gas is hotter than in the outer disk and can be traced by ro-vibrational and atomic lines, which can reveal the presence and kinematics of molecules, but no global density information. Ro-vibrational CO line observations at 4.7μm of several bright transition disks reveal Keplerian gas down to radii smaller than the dust cavity radius using the spectroastrometry technique for e.g. Oph IRS 48, SR 21 and HD135344B (Pontoppidan et al. 2008; Brown et al. 2012a), which are key targets in this thesis. For other disks, the CO line observations are often single-peaked, consistent with a photoevaporative wind (Bast et al. 2011; Brown et al. 2013), previously seen in [Ne II] line emission (Pascucci et al. 2007; Lahuis et al. 2007). However, although these results are promising, they do not indisputably reveal the gas surface density structure and thus the mechanism responsible for the transition disk. The ALMA observations presented in this thesis reveal deep drops in the gas density inside the dust cavity, where the gas cavity is smaller than the dust cavity, hinting directly at the presence of embedded planets. The proper interpretation was possible due to the use of the DALI model.

Disk chemistry The chemical composition of planet atmospheres is related to the chemical composition of the disk. Emission originating from the outer disk from simple molecules such as HCO^+, CS, HCN, CN, H_2CO, N_2H^+ and H_2O have been detected in several disks in rotational line emission (Dutrey et al. 1997; Thi et al. 2004; Dent et al. 2005; Öberg et al. 2011; Hogerheijde et al. 2011, e.g.). Herschel observations reveal the presence of high J H_2O, CO, [O I], OH, CH^+ and [C II] lines originating from the hot surface layers of the disk (Meeus et al. 2012; Fedele et al. 2013). An interesting aspect is that the chemical complexity is observed to be higher for T Tauri stars compared to Herbig stars despite their lower stellar brightness: the larger FUV luminosities of the Herbig stars leads to more efficient photodissociation of molecules. Complex organic molecules in disks form the building blocks of life on planets. However, the chemical variation in disks detected to date is rather low: apart from the simple molecules mentioned above, slightly more complex molecules c-C_3H_2 (Qi et al. 2013a) and CH_3CN (Öberg et al. 2015) have only recently been detected in transition disks by ALMA. This is surprising, as the presence of a cavity allows a view into the normally hidden midplane composition. Many complex molecules are expected to be formed and locked up in ices in a disk, but the directly UV irradiated wall in a transition disk should result in increased photodesorption of these ices (Cleeves et al. 2011).

1.3.3 Millimeter observations

Interferometry Resolved imaging of the dust continuum at (sub)millimeter wavelengths in the pre-ALMA era has confirmed the presence of dust cavities in about two dozen transition disks with large cavities of 15-75 AU (~0.15-0.65" at 120 pc) to date (e.g Piétu et al. 2006; Brown et al. 2009; Isella et al. 2010a; Andrews et al. 2011; Williams & Cieza 2011). Interferometric arrays such as the PdBI, CARMA and SMA have been used to resolve the structure down to $\sim$ 0.3" diameter resolution. The millimeter images of these SED-selected transition disks show a ring-like morphology, confirming the deficit of dust inside the cavity. In some cases hints of asymmetries were seen, but the signal-to-noise of the images was too poor to conclude whether these asymmetries were significant. Even though their significance was debatable, these asymmetries were already suggested to originate from vortices (Regály et al.

2012). The quality of the images was also low because of the limited u, v-coverage (spatial scales) of the observations, due to the small number of antennas. With the larger number of antennas of ALMA the issues of sensitivity and u, v-coverage are largely resolved for imaging these disks.

The analysis of the pre-ALMA data, using radiative transfer codes, was performed on the interferometric visibilities, which show a Bessel function in case of a ring, where the first "null" (crossing of zero) is a measure of the ring size. The basic modeling structure was a surface density with a sharp dust cavity wall with cavity radii of ∼15-75 AU and an empty dust gap, but the dynamic range of the images was limited and the inner disk was set by the SED with all its caveats. Alternative models suggested that a smooth cavity wall fits equally well (Isella et al. 2012) and that some dust may still be present inside the gap (Isella et al. 2010a; Mathews et al. 2012). For some disks it was already known that gas was present inside the cavities as well (e.g. Pontoppidan et al. 2008).

It is important to recognize that modeling disk structure was (and is) not dictated by theoretical models of disk clearing mechanisms, but by a simple parametrization based directly on the observations with limited parameter space due to the large number of uncertainties, both in the data and in the modeling assumptions. However, the deep millimeter cavities could rule out grain growth in the inner part of the disk as a transition disk mechanism: although grain growth in the inner part of the disk results in a dip in the SED, the grains do not grow sufficiently large to stop emitting at millimeter wavelengths (Birnstiel et al. 2012). Interferometric imaging was very time expensive; multiple nights in different array configuration were required to cover sufficient spatial scales and the sensitivity was limited to observations of the brightest disks. With the large number of antennas of ALMA it is now possible to get high S/N images of the millimeter-dust structure within hours.

Dust opacity Millimeter continuum emission is usually optically thin and originates from the cold outer disk. The dust opacity κ_ν represents the level of warm dust emissivity per unit mass, depending on composition, porosity and size distribution $n(a)$ of the dust grains. In general $\kappa_\nu \sim \nu^\beta$, where the spectral index β is sensitive to the maximum particle size in $n(a)$ (Draine 2006). The small dust grains in the interstellar medium have a typical value of $\beta \sim 1.7$. For a dusty disk with a power-law size distribution and a maximum grain size of ∼1 millimeter this results in β values lower than 1. At a specific observing wavelength $\lambda_{\rm obs}$, the emission is sensitive to dust particles up to $3\lambda_{\rm obs}$. Although β can not be measured directly, in the Rayleigh-Jeans tail of the SED (where the dust is optically thin), the spectral slope α_{mm} given by $F_\nu \sim \nu^{\alpha_{mm}}$ can be used to derive β using $\beta \approx \alpha_{mm} - 2$. The observational parameter α_{mm} can thus be used as a probe of dust growth.

Observing dust growth The detection of multi-wavelength millimeter emission with low values of β has confirmed dust growth up to at least millimeter-sized grains in protoplanetary disks as the start of planet formation (e.g. Beckwith & Sargent 1991; Andrews & Williams 2005, 2007a; Rodmann et al. 2006; Lommen et al. 2009; Ricci et al. 2010a,b). Dust evolution models predict that in absence of pressure maxima the continuum emission will be radially concentrated due to the radial drift (Birnstiel & Andrews 2014). This has been observed several protoplanetary disks in spatially resolved millimeter observations, indicating a radially increasing spectral slope $\beta(r)$ (Guilloteau et al. 2011; Pérez et al. 2012). The global value of β in transition disks is higher than in normal disks due to the removal of large grains inside the cavity (Pinilla et al. 2014). However, dust growth inside pressure bumps would reveal a local decrease of β in spatially resolved observations at the pressure maximum (Birnstiel et al.

2013). This effect is studied in this thesis for three transition disks using ALMA and VLA observations.

1.3.4 Infrared observations

Infrared imaging has been used to probe the small dust grains in the hot surface layers of the inner part of the disk. The brighter Herbig disks are most suitable for these observations, although some T Tauri stars have been imaged as well. Scattered light or polarimetric imaging in the near-infrared is a particularly useful tool for high spatial resolution images. Polarimetric imaging of transition disks has been done with VLT/NACO (e.g. Quanz et al. 2011; Garufi et al. 2013) and in the SEEDS survey with Subaru/HiCIAO (e.g. Thalmann et al. 2010; Muto et al. 2012; Follette et al. 2013) in H and K bands. These observations have revealed a large variety of features in the small dust distribution: spiral arms, warps, gaps and dips. Remarkably, the dust gap seen at infrared wavelengths, if present, is often smaller than the millimeter-dust cavity. In some cases no gap is seen, although it could simply be smaller than the mask that is used to block the stellar light. Future observations with SPHERE and GPI are expected to reveal even more detail, at < 0.1" spatial resolution. Dust filtration/trapping by a planetary companion has been suggested as a possible reason for the discrepancy between the millimeter/micrometer-sized dust grain cavities (Dong et al. 2012; de Juan Ovelar et al. 2013).

At longer infrared wavelengths the thermal radiation of the cavity wall dominates the dust emission. Mid-infrared imaging with e.g. the VLT/VISIR instrument has resolved dust cavities of several bright transition disks (Geers et al. 2007; Maaskant et al. 2013), including IRS 48, which is used in this thesis as a comparison between small grains and large millimeter grains seen by ALMA. Infrared interferometry with VLTI and the Keck Interferometer provides only limited imaging due to the low u, v-coverage, but by modeling the visibilities it was found that the gaps of a handful of transition disks were indeed largely depleted of dust (Olofsson et al. 2011) and evidence was found for a smooth rather than sharp cavity edge (Mulders et al. 2013).

The combination of infrared and millimeter observations and theoretical models in the last decade have thus shown several hints for dust trapping in transition disks. However, it was not until spatially resolved observations of gas and dust became available with ALMA that clear evidence for dust trapping was found.

1.4 This thesis

The advent of ALMA has revolutionized our view on transition disks, giving unprecedented spatial resolution and sensitivity in (sub)millimeter observations. For the first time, the sensitivity is sufficient to resolve the dust *and* the gas at high S/N, connecting the dots in the complex framework of transition disks. The main questions we aim to answer in this thesis are: What is the gas density structure inside transition disk cavities? What does that tell us about their origin and the properties of any embedded planets? Can we find observational evidence for dust trapping in these disks? What can statistical studies of a broad sample of transition disks tell us about their role in evolution?

In the ALMA Early Science Cycles we requested CO line observations at high spatial resolution (~ 0.25") of several famous transition disks in order to constrain the clearing mechanism. The disks were selected based on previous SMA dust continuum observations and VLT CRIRES CO observations, already indicating the presence of gas inside the dust cavity, which

could now finally be quantified through ALMA CO rotational line observations and the modeling program DALI. The first disk studied was Oph IRS 48, a Herbig star in the star forming region Ophiuchus (d=120 pc) with a known micrometer-dust ring at 55 AU from mid-infrared observations. PAHs are found inside this dust cavity and a hot CO gas ring is seen at 30 AU. Subsequently a sample of 7 other disks have been observed and modeled to draw more general conclusions.

- In Chapter 2, the discovery of an azimuthally asymmetric dust trap in IRS 48 is presented through ALMA Band 9 observations of the 690 GHz continuum and the ^{12}CO 6–5 lines. The azimuthal asymmetry came as a total surprise, as the millimeter-dust continuum was only a by-product of the requested line observations. The millimeter-sized dust shows peanut-shaped emission on one side of the disk at 60 AU radius, in contrast with the CO and the mid-infrared emission which are consistent with ring-like emission. The system could be modeled as a disk with a vortex, caused by a Rossby-wave instability of a radial pressure bump generated by a massive planet.

- Chapter 3 and 4 continue the exploration of the dust trap scenario: the concentration of dust grains inside the IRS 48 dust trap is confirmed through spatially resolved VLA observations of centimeter grains. Chapter 4 presents spectral index variations in SR 21 and HD135344B from 345 and 690 GHz ALMA observations, which are compared with dust evolution models to test the validity of the trapping model for these transition disks.

- In Chapter 5, the ^{12}CO 6-5 observations of IRS 48 are modeled in more detail using the physical-chemical modeling code DALI. The gas disk is found to have two drops in the density distribution: one within 20 AU and one within 60 AU, suggesting the presence of multiple planets.

- In Chapter 6 ALMA Early Science observations of six other well studied transition disks are analyzed with DALI to derive the gas and dust density structures. The dust surface density and in particular the cavity size is constrained by a simultaneous fit of the SED and the 690 GHz continuum visibilities. The density drop of the dust inside the cavity is at least a factor of 1000 for all disks. Assuming a gas-to-dust ratio of 100 in the outer disk, the ^{12}CO 6–5 line data are fit using the same surface density model, but with different drops in the gas density inside the cavity. For five of the disks, the drop in gas density is found to be less deep than the drop in dust density, which is consistent with the planet clearing scenario.

- Chapter 7 continues the analysis of gas inside cavities through spatially resolved ^{13}CO and C^{18}O observations of four disks: IRS 48, DoAr 44, SR 21 and HD 135344B. The last two disks were also part of the ^{12}CO analysis of Chapter 6. The CO isotopologues suffer less from optical depth and are more direct column density tracers. For three of these disks, the CO observations clearly show gas cavities smaller than the dust cavities, which is a direct hint of clearing by planets. The observations are compared with the outcome of planet-disk interaction models to estimate the mass of the embedded planets. Also, in this analysis the isotope-selective CO photodissociation model is applied, resulting in a more robust derivation of the disk mass through C^{18}O emission.

- Chapter 8 zooms in on the chemistry in IRS 48. We present the discovery of warm H_2CO in the IRS 48 disk from ALMA observations and set an upper limit on the abundance of this molecule with respect to H_2 of 10^{-8}. Upper limits for several other complex molecules are derived and found to be consistent with full chemical models.

- Finally, in the last chapter, a large SED survey of 200 *Spitzer*-selected transition disk candidates is presented. The candidates are selected using color criteria derived by Merín et al. (2010) from the *Spitzer* catalogs and spectroscopy of nearby star-forming regions. SEDs are constructed from optical, 2MASS and *Spitzer* photometry, complemented by new *WISE*, *Herschel* and (sub)millimeter data. Spectral types are derived from a large optical spectroscopy program. Using RADMC modeling, the SEDs are modeled to infer the cavity sizes. The survey has resulted in at least 70 new candidate transition disks with large inner cavities, that can be followed up by ALMA observations.

Each chapter ends with its conclusions based on the presented data. Overall the main conclusions from this thesis are:

- The first unambiguous evidence for a dust trap in a transition disk has been found through combined micrometer, millimeter and centimeter observations (Chapter 2,3). This discovery confirms theoretical predictions that have been made in the last three decades. This conclusion is strengthened by spatial variations in the millimeter spectral index (Chapter 4).
- All transition disks that have been studied with CO observations in this thesis show that gas is present inside the dust cavity. The gas cavity is smaller than the dust cavity and the gas density drops by a factor of 100-1000. This indicates that planets are embedded in these disks which have cleared their orbit and trapped the millimeter dust in a ring around it (Chapter 5,6,7).
- Color criteria provide a robust method to select good transition disk candidates with large dust cavities from *Spitzer* catalogs (Chapter 9).

1.5 Outlook

ALMA has revolutionized our view of transition disks, making a direct connection with dust trapping models and zooming in on the gas structure inside the dust cavities. The observations presented in this study were taken in ALMA Early Science, with baselines of less than 1 kilometer. In the coming years observations will be taken with very long baselines up to 10-15 kilometers, providing spatial resolution of milliarcseconds, such as shown in the astonishing image of dust rings in the HL Tau disk (ALMA Partnership et al. 2015).

Observing other transition disks at such high resolution will allow us to measure the gas structure to much better detail, constraining the shape of the gaps to the precision of theoretical disk models and resolving dust and gas cavities as small as a few AU. Direct detection of planets inside disks remains challenging, but has been done in a few cases (Huélamo et al. 2011; Kraus & Ireland 2012; Quanz et al. 2013; Reggiani et al. 2014; Quanz 2015). Measuring the shape of the gas cavity will allow us to determine properties of embedded planets indirectly, leading to the earliest view on these recently formed planets. The high spatial resolution will allow the detection of circumplanetary disks as well, another indirect method of detecting planets in a disk. ALMA also has the sensitivity to observe less massive transition disks, so the sample is no longer restricted to the brightest known disks studied so far. Measuring cavities down to a few AU radius and disk masses down to less than a Jupiter mass means a much more complete picture of transition disks, which will give us a better understanding of their origin. Are multiple mechanisms responsible for the cavities? Are there different classes of transition disks? What role do transition disks play in the disk dispersion process?

Multi-wavelength observations of the dust continuum at high spatial resolution will give further constraints on dust growth in disks, by measuring spectral index variations as a function of position in the disk. The Band 9 observations that were used in this thesis to show spectral index variations have the limitation that the dust is likely optically thick at this wavelength. With the longer baselines of ALMA, high spatial resolution can be achieved also at longer wavelengths where the dust becomes optically thin. The ongoing Disks@EVLA key program will observe 66 disks at centimeter wavelengths, which can be compared directly with millimeter observations. The multi-wavelength approach provides information on dust grain sizes in disks, which is crucial for dust evolution theories and understanding the start of planet formation.

Large disk surveys of Class II and Class III objects with ALMA in gas and dust may finally connect the link between the gas-rich primordial disks and gas-poor debris disks: ALMA observations of a handful of bright debris disks have already revealed that gas is still present in some of these disks, possibly second-generation gas due to icy planetesimal collisions (e.g. Kóspál et al. 2013; Dent et al. 2014). Perhaps transition disks and debris disks are more closely linked than previously thought.

Finally, the ALMA sensitivity will increase further, and some complex molecules are expected to be detected in disks in the coming years (Öberg et al. 2015). Knowing the chemical composition of disks will answer important questions about the composition of exoplanet atmospheres and, ultimately, the origin of life.

Other telescopes and instruments will also contribute to an even better understanding of transition disks. The VLT SPHERE instrument has just started operations, creating beautiful scattered light images of the small dust grains in disks at less than 0.1" resolution that can be compared directly to the millimeter dust in ALMA observations. Infrared spectroscopic observations with future facilities such as the *James Webb Space Telescope*, the *European Extremely Large Telescope* and the *Thirty Meter Telescope* will zoom in on the hot inner regions of disks, providing even more information on the gas dynamics close to star where planets are expected to form.

2

A major asymmetric dust trap in Oph IRS 48

van der Marel, N.; van Dishoeck, E. F.; Bruderer, S.; Birnstiel, T.; Pinilla, P.; Dullemond, C. P.; van Kempen, T. A.; Schmalzl, M.; Brown, J. M.; Herczeg, G. J.; Mathews, G. S.; Geers, V. *A Major Asymmetric Dust Trap in a Transition Disk.* 2013, Science, 340, 1199V

Abstract

The statistics of discovered exoplanets suggest that planets form efficiently. However, there are fundamental unsolved problems, such as excessive inward drift of particles in protoplanetary disks during planet formation. Recent theories invoke dust traps to overcome this problem. We report the detection of a dust trap in the disk around the star Oph IRS 48 using observations from the Atacama Large Millimeter/submillimeter Array (ALMA). The 0.44-millimeter-wavelength continuum map shows high-contrast crescent-shaped emission on one side of the star originating from millimeter-sized grains, whereas both the mid-infrared image (micrometer-sized dust) and the gas traced by the CO 6-5 rotational line suggest rings centered on the star. The difference in distribution of big grains versus small grains/gas can be modeled with a vortex-shaped dust trap triggered by a companion.

2.1 Main article

Although the ubiquity of planets is confirmed almost daily by detections of new exoplanets (Batalha et al. 2013), the exact formation mechanism of planetary systems in disks of gas and dust around young stars remains a long-standing problem in astrophysics (Armitage 2011). In the standard core-accretion picture, dust grains must grow from submicrometer sizes to rocky cores of ~10 M_{Earth} within the ~10 million year lifetime of the circumstellar disk. However, this growth process is stymied by what is usually called the radial drift and fragmentation barrier: Particles of intermediate size (~1 m at 1 AU, or ~1 mm at 50 AU from the star) acquire high drift velocities toward the star with respect to the gas (Whipple 1972; Weidenschilling 1977). This leads to two major problems for further growth (Brauer et al. 2008): First, high-velocity collisions between particles with different drift velocities cause fragmentation. Second, even if particles avoid this fragmentation, they will rapidly drift inward and thus be lost into the star before they have time to grow to planetesimal size. This radial drift barrier is one of the most persistent issues in planet formation theories. A possible solution is dust trapping in so-called pressure bumps: local pressure maxima where the dust piles up. One example of such a pressure bump is an anticyclonic vortex which can trap dust particles in the azimuthal direction (Barge & Sommeria 1995; Klahr & Henning 1997; Birnstiel et al. 2013; Casassus et al. 2013).

Using the Atacama Large Millimeter/submillimeter Array (ALMA), we report a highly asymmetric concentration of millimeter-sized dust grains on one side of the disk of the star Oph IRS 48 in the 0.44 millimeter (685 GHz) continuum emission (Figure 2.1). We argue that this can be understood in the framework of dust trapping in a large anticyclonic vortex in the disk. The young A-type star Oph IRS 48 [distance ~ 120 pc] has a well-studied disk with a large inner cavity (a deficit of dust in the inner disk region), a so-called transition disk. Mid-infrared imaging at 18.7 μm reveals a disk ring in the small dust grain (size ~50 μm) emission at an inclination of ~50°, peaking at 55 AU radius or 0.46 arcsec from the star (Geers et al. 2007). Spatially resolved observations of the 4.7 μm CO line, tracing 200 to 1000 K gas, show a ring of emission at 30 AU radius and no warm gas in the central cavity (Brown et al. 2012a). This led to the proposal of a large planet clearing its orbital path as a potential cause of the central cavity.

Although these observations provide information about the inner disk dynamics, they do not address the bulk cold disk material accessible in the millimeter regime. The highly asymmetric crescent-shaped dust structure revealed by the 0.44-mm ALMA continuum (Figure 2.1) traces emission from millimeter-sized dust grains and is located between 45 and 80 AU (± 9 AU) from the star. The azimuthal extent is less than one third of the ring with no detected flux at a 3σ level (2.4 mJy per beam) in the northern part (Figure 2.3). The peak emission has a very high signal-to-noise ratio of ~390 and the contrast with the upper limit on the opposite side of the ring is at least a factor of 130. The complete absence of dust emission in the north of IRS 48 and resulting high contrast make the crescent-shaped feature more extreme than earlier dust asymmetries (Andrews et al. 2011; Casassus et al. 2013). The spectral slope α of the millimeter fluxes F_ν (0.44 mm combined with fluxes at lower frequencies ν (see Section 2.2) is only 2.67 ± 0.25 ($F_\nu \propto \nu^\alpha$), suggesting that millimeter-sized grains (Draine 2006) dominate the 0.44 mm continuum emission. However, the gas traced by the ^{12}CO 6-5 line from the same ALMA data set indicates a Keplerian disk profile characteristic of a gas disk with an inner cavity around the central star (Figure 2.1). ^{12}CO 6-5 emission is detected down to a 20 AU radius, which is consistent with the hot CO ring at 30 AU (see Section 2.2). This indicates that there is indeed still some CO inside the dust hole, with a significant drop of the gas surface density inside of ~25 ± 5 AU. The simultaneous ALMA line and continuum

observations leave no doubt about the relative position of gas and dust.

The observations thus indicate that large millimeter-sized grains are distributed in an asymmetric structure, but that the small micrometer-sized grains are spread throughout the ring. To our knowledge, the only known mechanism that could generate this separation in the distribution of the large and small grains is a long-lived gas pressure bump in the radial and azimuthal direction. The reason that dust particles get trapped in pressure bumps is their drift with respect to the gas in the direction of the gas pressure gradient: $v_{\rm dust} - v_{\rm gas} \propto \Delta p$ (Whipple 1972; Weidenschilling 1977), where $v_{\rm dust}$ and $v_{\rm gas}$ are the dust and gas velocities and p is the pressure. In protoplanetary disks without vortices this gradient typically points inward, so dust particles experience the above-mentioned rapid radial drift issue. If, however, there exists (for whatever reason) a local maximum of the gas pressure in the disk (i.e. where $\Delta p_{\rm gas} = 0$ and $\Delta p^2_{\rm gas} < 0$), then particles would converge toward this point and remain trapped there (Whipple 1972; Weidenschilling 1977), avoiding both inward drift and destructive collisions (see Section 2.2). Because small dust particles are strongly coupled to the gas they will be substantially less concentrated toward the pressure maximum along the azimuthal direction than large particles. Various mechanisms have been proposed that could produce a local pressure maximum in disks, for instance when there is a "dead zone" (Regály et al. 2012)) or a substellar companion or planet (Draine 2006; Pinilla et al. 2012a) in the disk, hindering accretion. Until recently, however, the presence of such dust pressure traps was purely speculative, because pre-ALMA observations did not have the spatial resolution and sensitivity necessary to constrain the distribution of gas and dust required for testing dust trapping models (Williams & Cieza 2011).

Although vortices in models have an azimuthal gas contrast up to only a factor of a few (Regály et al. 2012; Lovelace et al. 1999; de Val-Borro et al. 2007), models predict that even a very minor pressure variation in the gas ring will trap the dust efficiently, leading to a strong lopsided azimuthal asymmetry in the dust ring if the vortex is long-lived. A gas contrast of only 10% can create a dust contrast of 100 for large dust particles in $\sim 10^5$ years (Birnstiel et al. 2013), so a long-lived azimuthal pressure bump can readily explain the observed high asymmetry in the dust structure of IRS 48. Vortices created by planets have been shown to survive over at least 10^5 years (Meheut et al. 2013). Even though these vortices tend to diffuse at longer timescales, $\sim 10^5$ years is enough time to create strong dust concentrations that remain even if the vortex disappears. It takes millions of years to even out these dust concentrations completely (Birnstiel et al. 2013). More generally, vortices are expected to be long-lived if they have an elongation (an aspect ratio of arc length over width) of at least 4 (Lesur & Papaloizou 2009). The accumulated dust in IRS 48 has an elongation of ~3.1 (± 0.6).

We present a detailed numerical model (see Section 2.2), showing the feasibility of our proposed scenario (Figure 2.2). Given the central cavity in the Oph IRS 48 disk, we propose a substellar companion as the cause of the inner cavity which also creates a long-lived ring of enhanced pressure outside the planetary orbit. The gas densities inside the cavity are decreased with the level depending on the companion's mass and the disk viscosity (Crida et al. 2006; Dodson-Robinson & Salyk 2011). The drop of the gas surface density at ~25 ± 5 AU in combination with the shape and steep radial drop of the millimeter dust emission at 45 AU suggests that this substellar companion is located between the star and dust trap around ~20 AU, and has a mass of at least 10 $M_{\rm Jup}$ (Pinilla et al. 2012a). The presented model with these parameters shows that the radial overdensity at the edge of the cavity is Rossby unstable, leading to the production of an anti-cyclonic vortex (see Section 2.2). Dust accumulation in this pressure bump results in the spatial separation between the gas and the millimeter dust emission (Pinilla et al. 2012a; Zhu et al. 2012). Other than the hole, the high gas velocities

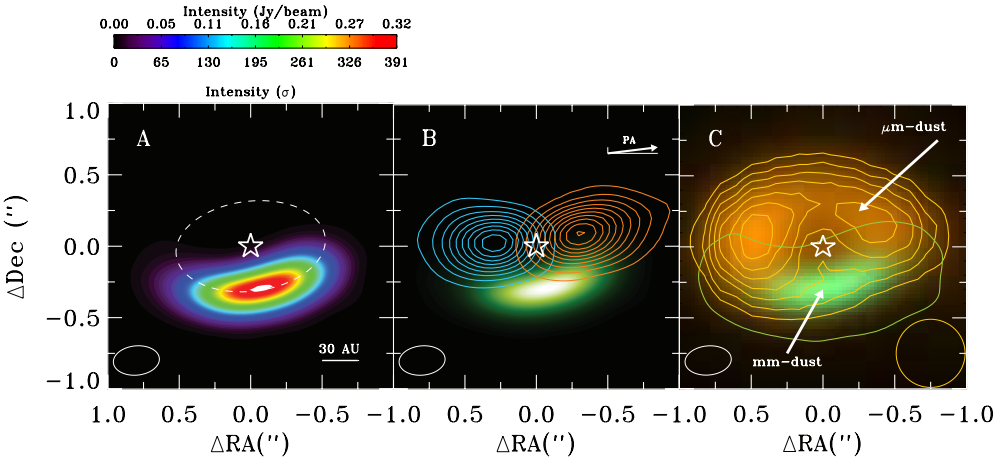


Figure 2.1: *IRS 48 dust and gas observations. The inclined disk around IRS 48 as observed with ALMA Band 9 observations, centered on the star (white star symbol). The ALMA beam during the observations is 0.32" × 0.21" and is indicated with a white ellipse in the lower left corner.* **A)** *The 0.44-mm (685 GHz) continuum emission expressed both in flux density and relative to the root mean square (rms) level (σ = 0.82 mJy per beam). The 63 AU radius is indicated by a dashed ellipse.* **B)** *The integrated CO 6-5 emission over the highest velocities in contours (6,12,...,60σ_{CO} levels, σ_{CO} = 0.34 Jy km s^{-1}): integrated over -3 to 0.8 km s^{-1} (blue) and 8.3 to 12 km s^{-1} (red), showing a symmetric gas disk with Keplerian rotation at an inclination i = 50°. The green background shows the 0.44 millimeter continuum. The position angle is indicated in the upper right corner.* **C)** *The Very Large Telescope Imager and Spectrometer for the mid-infrared (VISIR) 18.7-μm emission in orange contours (36 to 120σ_{VISIR} levels in steps of 12σ_{VISIR}, σ_{VISIR} = 0.2 Jy arcsec^{-2}) and orange colors, overlayed on the 0.44 millimeter continuum in green colors and the 5σ contour line in green. The VISIR beam size is 0.48" in diameter and is indicated with an orange circle in the bottom right corner.*

are symmetric in the east and west and consistent with Keplerian motion around a 2 $M_\odot$ star (see Figure 2.1). Any gas density variation along the azimuthal direction cannot be observed directly in the CO 6-5 observations, due to high line optical depth within the disk and foreground absorption, but $C^{17}O$ data are not inconsistent with a full gas ring (see Section 2.2). Regardless of the formation mechanism, the ALMA observations clearly show a concentration of dust grains within a small region of the disk. The total measured dust emission corresponds to 9 M_{Earth}, assuming a dust temperature of 60 K. The millimeter observations confirm dust growth up to a maximum grain size of a_{max} = 4 mm. Including larger grains, the dust mass could be a factor of $\sqrt{a_{max}(mm)/4}$ larger (see Section 2.2). The mass is similar to the full disk dust masses found in other young disks (Andrews & Williams 2005). This amount of large dust in a small area will favour grain growth up to ~1 m size until the fragmentation barrier (Brauer et al. 2008). Further growth to planetesimal sizes is possible when additional mechanisms such as the sweeping-up of small particles by larger seeds and bouncing effects including mass-transfer are considered (Xie et al. 2010; Windmark et al. 2012). Because these closely formed planetesimals will scatter and disperse along the ring on short time scales, it is not possible to continue growth and form a planetary core with regular orderly growth models within ~10 million years at this large distance from the star. On the other hand, the dust trap could initiate the formation of a Kuiper Belt around IRS 48 such as that found in our own solar system at comparable radii (Jewitt & Luu 2000). The dust trap as a "Kuiper Belt object factory" is analogous to a "planet factory" at smaller radii around other stars, where both

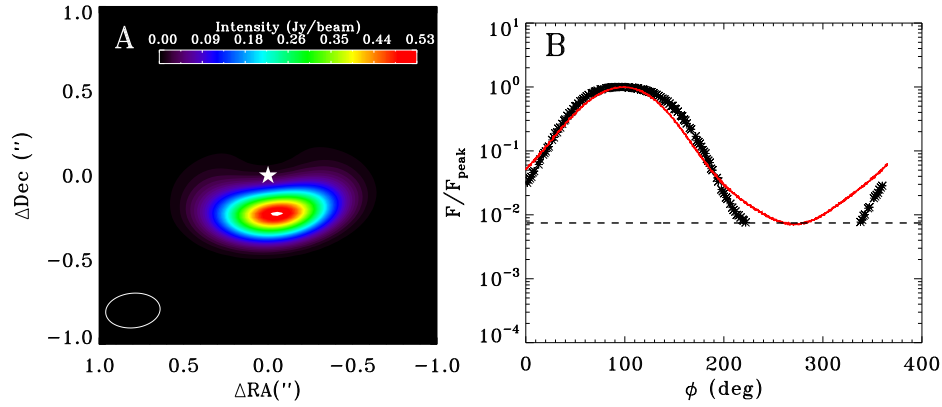


Figure 2.2: *Model of the dust asymmetry.* **A)** *Simulated ALMA Band 9 dust continuum images at 0.44 millimeter (685 GHz) for our model using the dust trapping scenario (Birnstiel et al. 2013). Details of the model and model parameters are derived based on the IRS 48 properties (see Section 2.2). The high azimuthal contrast is similar to that found in the data.* **B)** *Normalized logarithmic azimuthal cut at the peak emission radius through the dust ring of the observations (black) and the ALMA-simulated model (red), showing the large contrast in the millimeter dust density between the maximum and the opposite side of the ring. The (normalized) 3σ upper limit of the ALMA data is indicated with a dashed line. The data points below the normalized 3σ level have been removed for clarity.*

the fragmentation barrier is higher and the collisional growth is faster (Brauer et al. 2008). Thus, the possibility of dust trapping as the start of core formation could help to explain the observations of massive planets at smaller radii around A-stars such as found in HR 8799 (Marois et al. 2008) and beta Pictoris (Lagrange et al. 2010). Dust asymmetries have been hinted at in other disks by SubMillimeter Array (SMA) observations (Andrews et al. 2011) and are clearly seen in earlier ALMA observations (Meheut et al. 2013). The low image fidelity of the SMA data (low sensitivity and spatial sampling) and the lower contrast leave room for multiple interpretations, although a relation to vortices has been hinted at (Meheut et al. 2013). In contrast, the ALMA observations of IRS 48 with their unprecedented spatial resolution and sensitivity show a contrast of at least 130 in the continuum along the ring, with no indications of a highly asymmetric small dust/gas distribution. Alternative scenarios are discussed to be less likely (see Section 2.2). A long-lived azimuthal gas pressure bump triggered by a companion, followed by particle trapping, appears to be the most viable scenario that could produce this. The key feature is the observed separation between big and small dust grains/gas, which is a direct consequence of the dust trapping model.

2.2 Supplementary Materials

2.2.1 IRS48

The A0 star IRS 48 a.k.a. WLY 2-48 (J2000 RA=16 27 37.18, Dec=-24 30 35.3) is located in the ρ Ophiuchi star formation region at a distance of 120 parsec (Loinard et al. 2008). A ring-like structure peaking at ~55 AU radius was found by spatially resolved 18.7 μm imaging of the dust continuum with the Very Large Telescope (VLT)-VISIR instrument (Geers et al. 2007). The 18.7 μm emission is dominated by the thermal dust emission of small grains (~50 μm) and is merely tracing the surface layer of the disk which is irradiated directly by the star, since thermal dust emission is very optically thick at this wavelength (Draine 2006). The 18.7 μm image appears to be brighter in the north (Figure 2.1, Geers et al. 2007). This is due to the inclination of the disk, with our line of sight directly to the inner wall. The near (southern) part of the inner wall is hidden by the intervening body of the disk itself (Dullemond & Monnier 2010). The bright peak at 55 AU radius implies a large scale height of the disk. The inner radius of the small grain disk is not constrained by the VISIR image, as the inner 20-55 AU may sit in the shadow of an inner disk and may thus not be heated enough to emit brightly at 18.7 μm.

Interferometric imaging with the SubMillimeter Array (SMA) in the very extended configuration at 0.85 mm (345 GHz) revealed a single elliptical structure, that was modeled with a hole size of only 13 AU (Brown et al. 2012b). Without the simultaneous dust and gas observations available with ALMA, the SMA dust continuum was modeled as if centered on the star rather than offset. Since the gas line kinematics allow a very precise determination of the stellar position, the combined ALMA observations of line and continuum within the same dataset is crucial for accurate interpretation. The crescent-shaped structure is expected to be similar at 345 GHz: when the continuum as found in the ALMA observations is convolved with the beam from the SMA observations, the result is indeed the same shape as found in the SMA image.

Previous information on the gas in the IRS 48 disk comes from VLT-CRIRES spectra of the CO ro-vibrational transition at 4.7 μm clearly showing extended CO emission (Brown et al. 2012a). Modeling of its extent and position is compatible with a hot gas ring at ~30 AU radius in Keplerian rotation around the young A star. However, the lack of hot CO emission inside 30 AU may be due to a lack of excitation of the vibrationally excited level and does not imply a lack of colder gas inside the hole, which could exist due to shielding of an inner disk. Given the fact that polycyclic aromatic hydrocarbons (PAHs) are still abundant inside the dust hole (Geers et al. 2007), a complete absence of molecular gas would be unlikely, especially since accretion is ongoing (Salyk et al. 2013).

2.2.2 ALMA observations

The ALMA observations of IRS 48 were taken using Band 9 in Early Science Cycle 0 using the extended configuration. Data were taken on June 6th and July 17th 2012 in three execution blocks of 1.7 hours each (one on June 6th and two on July 17th). Between these three execution blocks, 18 to 21 antennas were used with baselines up to 390 meter. The average precipitable water vapor (PWV) levels during the executions were 0.50, 0.34 and 0.17 mm respectively. The spectral setup consisted of four spectral windows, centered at 674.00 , 678.84, 691.47 and 693.88 GHz. This setup was meant to target the $C^{17}O$ J=6-5, CN J=6-5, ^{12}CO J=6-5, and $H^{13}CO^+$ J=8-7 transitions. Each spectral window consists of 3840 channels, a channel separation of 488 kHz and thus a bandwidth of 1875 MHz. The resulting velocity res-

olution is 0.21 km s^{-1} using a reference of 690 GHz. The astrometric accuracy of the ALMA data is measured to be on average ~30 milliarcseconds.

Reduction and calibration of the data was done using the Common Astronomy Software Application (CASA) version 3.4. The bandpass was calibrated using quasar 3c279 and fluxes were calibrated against Titan. For Titan, the flux calibration was done using only the shortest ~30% of the baselines, since Titan was resolved out at longer baselines. For the second execution block taken on July 17th, the original bandpass and flux calibrators were quasar J1924-292 and asteroid Juno respectively. Both sources are significantly weaker than 3c279 and Titan. As such, after thorough comparison of the calibration solutions of the first execution block, as well the applications on the gain calibrators over both executions taken that night, the solutions of 3c279 and Titan were preferred over the solutions of J1924-292 and Juno.

The gains were calibrated using at first the solutions of quasars J1625-254 and J1733-130, which were observed at 12 minute intervals. It was found that using just J1625-254 resulted in the best solution. After applying the gain solutions, it was found that the resulting amplitudes and phases of IRS 48 were dominated by short-term (10 minutes or less) phase fluctuations. The calibration was improved by calibrating these fluctuations on the continuum of IRS 48 itself. This resulted in a net gain of 40% in S/N. As the continuum of IRS 48 is resolved, the unselfcalibrated continuum solution served as the model for this self-calibration. No changes in shape larger than 5% were seen as a result of this self-calibration. In the end the overall calibration uncertainty is less than 20%.

The continuum emission from IRS 48 was extracted from the total coverage by combining the line-free channels from all four spectral windows, flagging the edge channels and the channels containing the strong CO 6-5 emission. No other areas containing lines were flagged as no other strong lines were identified. The total bandwidth of the continuum is ~6.5 GHz, with a mean frequency of 684.55 GHz.

The image conversion of the continuum and line data was done using natural weighting, providing a synthesized beam of 0.32" × 0.21" at a position angle of 96°. For the cleaning of the continuum an elliptical cleaning mask around the continuum shape was used, derived from the unselfcalibrated continuum shape, padded by half a beam at the 3σ level of the unselfcalibrated image. For the lines, a rectangular cleaning mask centered on the detected emission peaks was used was used, extending 0.24" in all directions to cover most assumed emission. This mask was applied and changed adaptively to the emission of each channel and each peak with emission larger than 3σ in the various iterations of cleaning of the dataset. For the weaker lines, the final mask of the ^{12}CO cleaning was used. The rms noise level is 0.82 mJy/beam for the continuum and ~18 mJy/beam per 1 km s^{-1} bin for the line data. This noise level is measured in a region between 2 and 5" from the central source position, avoiding any contamination from the disk emission. The continuum shows isotropic noise levels in all areas of the primary beam and no systematic effects. The total continuum flux is 950 mJy. To confirm that the dust trap is not an artifact of the reduction steps, different sizes and shapes of clean masks were compared to the result seen in the main paper. This was done both on the selfcalibrated and the unselfcalibrated image, with no structural differences seen. From the comparison we conclude that no more than 2% of the presented noise level can be attributed to the choice of calibration methods, much lower than the overall calibration uncertainty.

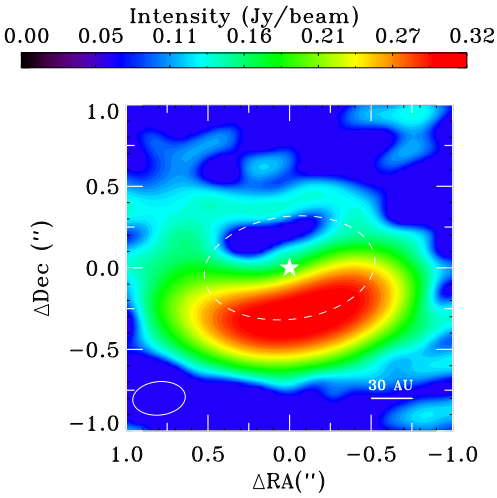


Figure 2.3: *The 0.44 millimeter (685 GHz) continuum emission of IRS 48 as observed with ALMA Band 9 observations, in exponential color scale to show the dynamic range of the image and the high contrast between north and south. Positive values from 0 to 390σ (σ = 0.82 mJy/beam) are shown with blue through red, while negative values from 0 to -4σ are shown with blue, violet, and black. The image is centered on the star (white star symbol). The ALMA beam is indicated with a filled white ellipse in the lower left corner. White and black contours indicate the 2, 3, 10 and 100σ rms levels.*

2.2.3 Morphology of the continuum emission

The extent of the dust trap was estimated by a simple surface density profile of the dust emission, assuming a fourth power Gaussian-like distribution in radial and azimuthal direction:

$$\Sigma(R) = \Sigma_R e^{\frac{-(R-R_c)^4}{2R_w^4}} \tag{2.1}$$

$$\Sigma(\phi) = \Sigma_\phi e^{\frac{-(\phi-\phi_c)^4}{2\phi_w^4}} \tag{2.2}$$

with R_w and R_c the half-width and center in the radial direction and ϕ_w and ϕ_c the half-width and center in azimuthal direction. The full profile $\Sigma(R,\phi) = \Sigma(R) \cdot \Sigma(\phi)$ and the normalization constant product $\Sigma_R \cdot \Sigma_\phi$ is chosen such as to match the scale of the observations. These high power profiles are required to match the steep rise in both radial and azimuthal direction and broad peak in the data. Although the arc is only just resolved in the radial direction, it can not be infinitesimally thin considering the high total dust continuum flux of 950 mJy and a typical dust temperature of 60 K. The temperature is based on a generic radiative transfer calculation of a transition disk with a dust hole around an A-type star. Applying the inclination of i=50°, position angle of 97°(measured from the CO data; North to East) and the central position (derived from the CO Keplerian model described below) and convolving the total surface density model with the ALMA beam from the observations, the best fit to the continuum data was found for R_c = 63 (± 8) AU, Rw = 18 (± 2) AU, ϕ_c = 95°(± 10°) and ϕ_w= 50°(± 5°). The main uncertainty arises from the uncertainties in the stellar position (~0.05"). Defining the extent of the profile as $2R_w$ and $2\phi_w$, the dust extends from ~45 - 80 (± 9) AU and covers in the azimuthal direction an arc length of ~100°, less than a third of the disk ring. As discussed

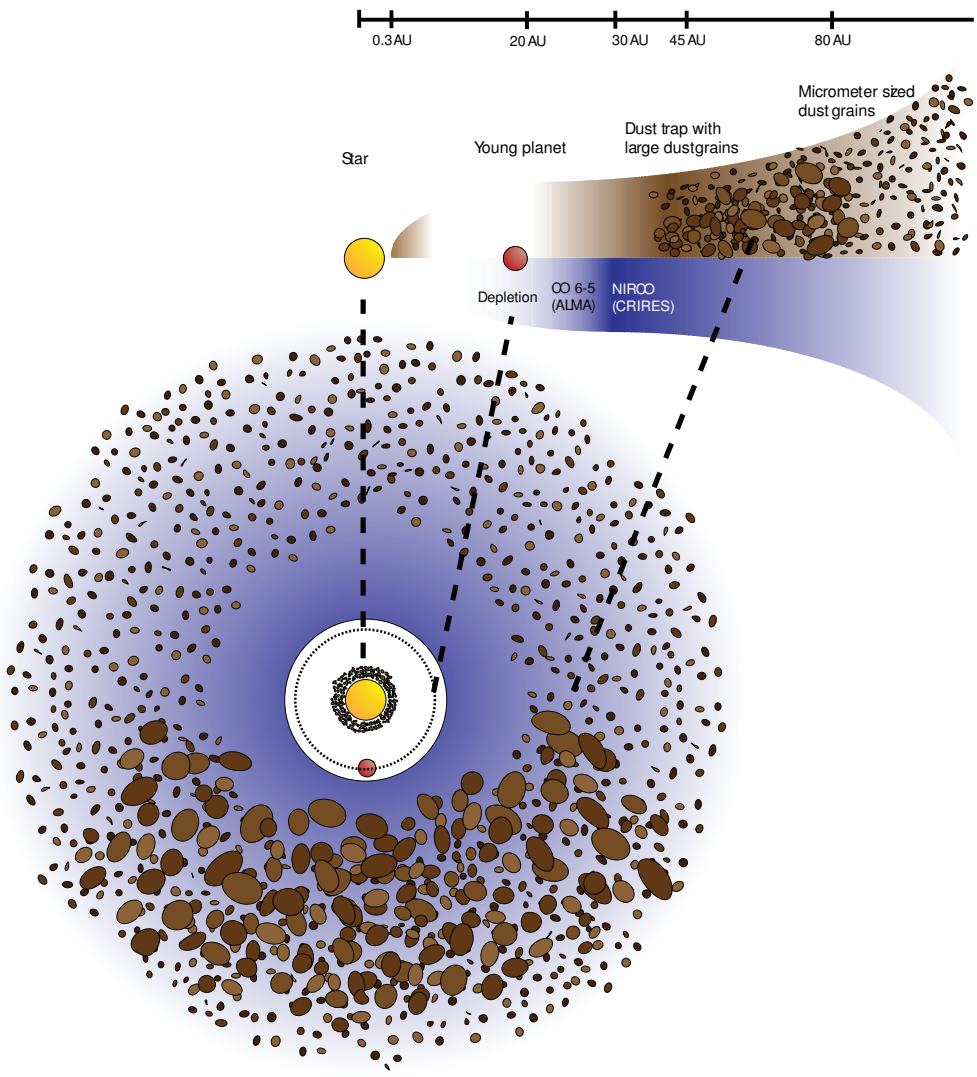


Figure 2.4: *Cartoon of the proposed disk structure of IRS 48. The brown spots represent the large and small grains as traced by the 0.44 millimeter ALMA continuum and VISIR 18.7 micrometer emission, the large grains concentrated in the dust trap in the south. The blue represents the gas surface density as traced by CO 6-5 and fundamental rovibrational CO line as observed by CRIRES, with a gas hole carved out by the planet at 15-20 AU.*

in the main text, these characteristics of the dust emission make this source very different from what has been observed before (Casassus et al. 2013; Andrews et al. 2011; Williams & Cieza 2011). The elongation (aspect ratio of arc length over width) of an arc is defined as:

$$e = \frac{R_c \phi_w [\mathrm{rad}]}{R_w} \tag{2.3}$$

The elongation of our dust trap is ~3.1 (± 0.6) with the derived parameters. If the dust trap is entirely coincident with the gas vortex, this elongation indicates whether the vortex is long-lived: in general vortices are expected to be long-lived if they have an elongation of at least 4 (Lesur & Papaloizou 2009).

The high north/south contrast is shown in Figure 2.3; although a narrow 2σ emission (σ = 0.82 mJy/beam) arc indicates some dust emission in the north, this is not sufficient to measure the contrast. However, this image demonstrates that the emission in the south (390σ peak emission) is at least a factor 130 higher than in the north.

The radial structure of this disk is as follows (see Figure 2.4): the gas shows a surface density decrease around ~25 ± 5 AU, whereas the dust inner rim is at least 45 AU away from the star. The model presented later in the Supplement confines the location of the companion to 15-20 AU, although it is possible that multiple companions are present. While the large dust grains are azimuthally concentrated, the smaller micrometer-sized grains traced by 18.7 μm continuum imaging extend over the full ring (Meheut et al. 2013). The small grains could be either following the gas, only depleted in the inner most region by the companion (Crida & Morbidelli 2007), or be distributed along a dust ring around 55 AU. The ALMA continuum data were overlayed on the VISIR 18.7 μm (Figure 2.1C) by aligning their central positions, determined by the CO Keplerian velocity profile for the ALMA line data and by the VISIR PAH images (taken to be centered on the star) for the 18.7 μm image. The 18.7 μm image and PAH images were taken in sequence so the relative alignment errors are small.

2.2.4 Dust mass

The continuum flux of the dust emission can be written as

$$F_\nu \propto \Omega \times B_\nu(T_{\rm dust}) \times \left(1 - e^{-\tau_\nu}\right) \tag{2.4}$$

with solid angle $\Omega = A/d^2$ with A emission area, d distance and τ_ν the opacity. The area of the continuum emission seen in the ALMA images is $A = \pi((R_c + R_w)^2 - (R_c - R_w)^2) \times 2\phi_w/360^\circ \times cos(i) = 2544AU^2$, using the estimates derived in the previous section. The dust temperature is estimated to be ~ 60 K at a radius of 60 AU. For the total flux density of 950 mJy at 685 GHz, we obtain τ_{685GHz} = 0.43. Flux loss due to larger scale emission was measured to be less than 20% for the 230 and 345 GHz emission for spatial scales >100 AU (Brown et al. 2012b). For the ALMA data, the spatial filtering occurs for >500 AU, so flux loss by spatial filtering will be even less than 20%. The opacity is defined as $\tau_\nu = \rho_{\rm dust}\kappa_\nu s$ with $\rho_{\rm dust}$ the dust density (g cm^{-3}), κ_ν the dust mass opacity (cm^2 g^{-1}) and s the length of the slab along the line of sight. Therefore the dust mass $M_{\rm dust}$ can be calculated as:

$$M_{\rm dust} = As\rho_{\rm dust} = A\frac{\tau_\nu}{\kappa_\nu} \tag{2.5}$$

For 685 GHz and a dust temperature of 60 K, the Rayleigh-Jeans limit is justified and the slope of the (sub)millimeter emission $\alpha(F_\nu \propto \nu^\alpha)$ can be directly related to the power-law index of the dust opacity $\kappa_\nu \propto \nu^\beta$, where $\alpha = 2 + \beta$. The value of β is estimated by making a power law fit to the (sub)millimeter fluxes at 230, 345 and 685 GHz (50, 160 and 950 mJy (Brown et al. 2012b), the 685 GHz flux density derived in this work) and we obtain β = 0.67 ± 0.25. This low value of $\beta \ll \beta_{\rm ISM} \approx 1.7$ is indicative of grain growth (Draine 2006). Since dust grains larger than ~ 3λ do not contribute to the opacity, dust growth can be confirmed up to a grain size of at least 4 millimeter due to the detected dust emission at 1.3 mm. For a dust-size distribution $N(a) \sim a^{-3.5}$ and amorphous silicate spheres, the dust mass opacity

is approximately (Draine 2006) $\kappa_{685GHz} = 9/\sqrt{a_{\rm max}[mm]}$ cm^2 g^{-1} (valid for $a_{\rm max} \geq 1$ mm). We thus obtain a dust mass of

$$M_{\rm dust} = 4.5 \times \sqrt{a_{\rm max}[mm]} M_{\rm Earth} \tag{2.6}$$

With $a_{\rm max} > 4$ mm this yields a lower limit of the dust mass of 9 $M_{\rm Earth}$. This mass does not include larger bodies (boulders or planetesimals).

2.2.5 CO 6-5 lines

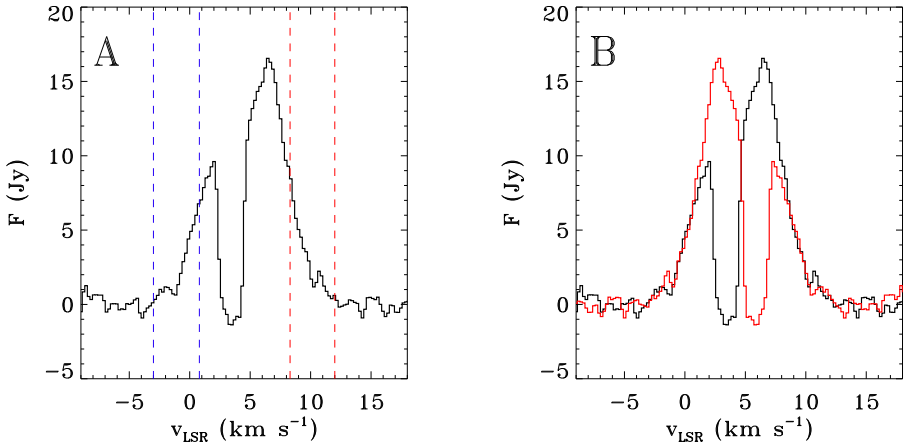


Figure 2.5: *Full ^{12}CO 6-5 spectrum integrated over the entire disk area. The profile is distorted by absorption features from foreground clouds around 3.5 km s^{-1}.* **A)** *The velocity limits used for the integrated contour map in Figure 2.1 are indicated by blue and red dashed lines for the blue-shifted and red-shifted emission, respectively. The limits are taken at -3, +0.8, +8.3 and +12 km s^{-1}.* **B)** *The spectrum is folded over the source velocity of 4.55 km s^{-1}, showing that the spectrum is symmetric, as expected for a Keplerian disk.*

The ^{12}CO 6-5 line (E_U = 116 K) is detected throughout most of the disk of IRS 48 with an rms level of 47 mJy in 0.21 km s^{-1} velocity channels and a peak S/N of ~45. Figure 2.5 shows the flux profile over the entire region of the disk. The profile shows a strong absorption feature around 3.5 km s^{-1}, caused by foreground clouds also seen in C^{18}O 3-2 observations (van Kempen et al. 2009). The Local Standard of Rest source velocity is derived from the symmetry of the ^{12}CO 6-5 profile as 4.55 km s^{-1}. Due to the small offset of the foreground cloud velocity compared to the disk velocity, the red-shifted emission of the disk appears to be stronger than the blue-shifted emission. Inspection of the high velocity channels shows that the profile is in fact symmetric, as expected from a Keplerian disk. Folding the full spectrum over the source velocity of 4.55 km s^{-1} also shows this symmetry (Figure 2.5B). Furthermore, the red velocity channels that are not contaminated by the foreground absorption extend within the region of dust continuum emission.

In order to derive the inner radius $R_{\rm in}$ of the gas hole, the kinematics of the CO 6-5 line were studied. The fastest gas detected in the line wings agrees both kinematically and spatially with a location at 20 AU. The maximum detected velocities are -3 and 12 km s^{-1} or ± 7.5 km s^{-1} from the source velocity. The emission in these channels has a separation of 0.33", in

agreement with gas at 20 AU in Keplerian rotation around a 2 $M_\odot$ star at an inclination of 50°. The non-detection of faster gas in both the line wings and strongly decreased emission at the central position at any velocity imply a significant drop in surface density in the inner 20 AU. This is slightly interior to the hot CO gas ring at 30 AU detected at 4.7 μm (Brown et al. 2012a). The CRIRES observations trace much warmer gas which must by illuminated by the central star but the general kinematics are in good agreement with the gas seen by ALMA.

Due to the foreground absorption in the ^{12}CO 6-5 line around the source velocity (Figure 2.5), this emission does not reveal a full gas ring: emission is missing in the north and south part of the disk. However, the small dust grains, that are coupled to the gas, show emission both in the north and south as well as east and west (Figure 2.1C and Geers et al. 2007). Similarly, the near infrared CRIRES lines (Brown et al. 2012a) show hot gas emission also to the north and south of the star. Both observations are consistent with the presence of gas along the entire ring.

The ^{12}CO 6-5 line is likely optically thick, so deviations from a symmetric full outer disk (including azimuthal density variations) can not be traced directly from these ^{12}CO observations. Optically thin C^{17}O 6-5 emission shows significant detections (4-6σ, σ = 25 mJy/beam) in the eastern and western parts of the disk. In the north and south C^{17}O 6-5 emission is not detected, but this can be understood by limb brightening due to the inclination of the source, where emission on the sides of the disk appears up to twice as bright as in the north and south. The C^{17}O 6-5 observations are thus also not inconsistent with gas along the entire ring.

Integrating over the channels with significant C^{17}O detections (962 mJy km s^{-1}) and calculating the mass for an average gas temperature between 50 and 200 K, we find a total gas mass between 1.3 and 1.8 $M_{\rm Jup}$. The integrated flux $F_{\rm int}$ is related to the number of C^{17}O molecules $N_{C^{17}O}$ by

$$F_{\rm int} = \frac{N_{C^{17}O} f_T T_{65} hc}{4\pi d^2} \tag{2.7}$$

with $f_T = 13e^{-113.3K/T}/Q(T)$ the fraction of molecules in J=6, $Q(T)$ the partition function, A_{65} the Einstein A coefficient of the 6-5 transition and d the distance. This is converted into gas mass (assuming all is in H_2) by

$$M = N_{C^{17}O} m_{H_2} X_{H_2/^{12}CO} X_{^{12}CO/C^{17}O} \tag{2.8}$$

with X the relative abundances (2500 for ^{12}CO/C^{17}O, 1.2·10^4 for H$_2$/^{12}CO) and m_{H_2} the mass of a H_2 molecule (3.35·10^{-24} g).

For comparison, the dust mass of 9 $M_{\rm Earth}$ derived from the millimeter-sized dust suggests a gas mass of 900 $M_{\rm Earth}$ = 2.8 $M_{\rm Jup}$ assuming that this dust was originally smeared out over the entire disk with a standard gas/dust mass ratio of 100. No overdensity at the central location of the dust trap is detected in the C^{17}O emission, but the high dust continuum emission makes weak C^{17}O emission more difficult to observe there. The gas mass of 1.3-1.8 $M_{\rm Jup}$ that is seen even outside the dust trap proves that there is a lot of gas along the disk ring, even without the (undetected) gas emission at the location of the dust trap. An overdensity of a factor 100 at the dust trap location compared to the east and west would make the total disk mass as high as ~0.1 $M_\odot$ and the implied gas/dust ratio of ~ 10^4, which is very unrealistic (Williams & Cieza 2011). Moreover, such a high gas mass should have readily been detected in C^{17}O even in the south. A gas density contrast within a factor of a few in the dust trap compared with the east and west can not be ruled out, however. Alternatively, if the emission in the east or west was the only location with a high gas overdensity, the dust would have been trapped at that location.

Altogether, the data can be modeled with a full gas ring with possible azimuthal density

variations. The amount of variation cannot be constrained by the current data set.

2.2.6 Dust trapping

Trapping of dust particles has been proposed as a solution for the radial drift and fragmentation barrier. Dust trapping is a natural consequence of pressure gradients, since particles tend to drift with respect to the gas in the direction of the pressure gradient. In its simplest form one could have an axisymmetric disk with a mass accumulation at some radius, leading to a ringlike pressure trap along the radial direction with $dp_{\rm gas}(r)/dr = 0$ and $d^2p_{\rm gas}(r)/dr^2 < 0$ (Whipple 1972; Brauer et al. 2008; Kretke & Lin 2007; Johansen et al. 2009). In a radial pressure bump, where the pressure gradient is zero, the drift velocity vanishes for particles of all sizes, so that not only the drift barrier but also destructive collisions can be avoided. The presence of a massive planet has been demonstrated to create radial pressure bumps due to a reduction of the gas surface density in the inner part of the disk (Pinilla et al. 2012a). By combining two-dimensional hydrodynamic gas simulations using FARGO (Masset 2000) with coagulation/fragmentation dust evolution models (Birnstiel et al. 2010), it has been shown that dust grains converge toward these ring like pressure bumps and grow efficiently (Pinilla et al. 2012b). The efficiency of the dust trapping (the largest produced grain size) and the location of the dust depend on the planet orbit, planet mass and (for planet mass $< 5\ M_{\rm Jup}$) the turbulence in the disk. For planets of more than $5\ M_{\rm Jup}$, the pressure bump and therefore also the dust can be located at distances of more than twice the star-planet separation (Pinilla et al. 2012a). The gas accumulation at the outer edge of the cavity depends on the planet mass and disk viscosity (Crida et al. 2006).

If the overdensity at the outer edge of the cavity is high enough, it becomes Rossby unstable (de Val-Borro et al. 2007; Lyra et al. 2009) and forms vortices that could be long-lived, $\sim 10^5$ years (Meheut et al. 2013). A vortex is defined as a gas region where the perturbed velocity spins around a center. In case of an overdensity created by a planet, the Rossby instability creates anticyclonic vortices (super-Keplerian motion at the inner and sub-Keplerian motion at the outer radius). Such a vortex acts as a long-lived non-axisymmetric pressure bump and can trap dust in the azimuthal direction along the ring (Birnstiel et al. 2013). The azimuthal location of the dust trap is tied to variations in the gas density rather than the planet location, because the material in the outer disk only sees the planet as an orbital ring as it is moving much faster than the outer disk. The density contrast in the dust can become significantly larger than the contrast in the gas, depending on the coupling of the dust to the gas summarized in the Stokes number:

$$\mathrm{St} = \frac{\rho_s a}{\rho_{\rm gas} c_s \sqrt{8/\pi}} \Omega_k \tag{2.9}$$

where ρ_s is the intrinsic dust density (density of the material out of which the dust is made), a the particle radius, $\rho_{\rm gas}$ the local gas mass volume density, c_s the vertical isothermal sound speed and Ω_k the Keplerian rotation rate. Particles with $\mathrm{St} \ll 1$ are strongly coupled to the gas and move along with the gas, while particles with $\mathrm{St} \gg 1$ move with their own velocity i.e. Keplerian velocity. In pressure maxima gas moves with Keplerian velocity, so there is no friction any more between gas and dust and as a consequence particles naturally get stuck in the pressure maximum.

The trapping is, however, never perfect, because even small amounts of turbulence will, to some extent, counteract the converging motion of the dust particles. As a result, in a steady state situation, small dust particles will be substantially less strongly concentrated toward the trapping point than large particles. In the case of IRS 48 it is possible that the small grains,

traced by the 18.7 μm emission, are still radially trapped (although not azimuthally), but since the inner radius of the 18.7 μm emission can not be constrained this possibility can not be confirmed.

For estimating the mass and location of the planet in the IRS 48 disk, we use the Hill radius r_H, defined as $r_H = r_p(M_p/3M_*)^{1/3}$ where r_p is the orbital radius of the planet. The outer edge of a gas cavity created by a planet is expected to be at most at 5 r_H (Dodson-Robinson & Salyk 2011) whereas the location where the gas pressure bump forms - hence dust accumulates - is ~10 r_H for planets with $M_p > 5M_{\rm Jup}$ (Pinilla et al. 2012a). In the case of IRS 48, with a gas hole edge at ~25 AU and a dust trap peaking at ~63 AU with the inner edge at ~45 AU, these approximate relations can not reproduce the large gas-dust separation exactly, but it indicates that the mass of the companion, likely located at 17-20 AU, has to be more massive than 10 $M_{\rm Jup}$.

2.2.7 Model of the IRS 48 dust trap

A model is presented in Figure 2.2 reproducing the high azimuthal contrast in the dust trap in IRS 48. The gas surface density features a cavity carved out by a companion. For the disk-planet interaction process, we use the two-dimensional hydrodynamical code FARGO (Masset 2000). The FARGO simulations are done considering a single planet in a fixed orbit (no migration effects are taken into account) to study the resulting gas density distribution when a massive planet carves a cavity in a disk. The used parameters are: stellar mass $M_{\rm star} = 2M_\odot$, companion mass $M_p = 10M_{\rm Jup}$, companion orbital radius r_p = 20 AU and turbulence $\alpha_t = 10^{-4}$. The initial gas surface density profile in FARGO was taken as a power-law with $\Sigma_0 = 1.35 \cdot 10^{-4} M_{\rm star}/r_p^2$ = 3.0 g cm^{-2}. This number is based on the estimated gas mass of the IRS 48 disk, assuming a gas/dust ratio of 100 with the gas distributed over the entire disk, but it turns out that the gas mass of the disk does not matter much for the nature of the vortex. For the vertical disk structure, we use an aspect ratio h/r (height over radius) = 0.05 at r_p and a flaring disk with a flaring index of 0.25. The radial dust temperature structure was based on a generic radiative transfer calculation of a transition disk with a dust hole around an A-type star. The gravitational potential is smoothed around the planet by ϵ = 0.5 r_H (r_H is the Hill radius of the planet). The inner boundary conditions are non-reflecting. FARGO uses a fixed grid in cylindrical coordinates (r, ϕ). The number of pixels n in each direction is $n_r \times n_\phi$ = [512, 757]. The radial grid is logarithmically spaced. The radial boundaries are $r_{\rm in} = 0.1 r_p$ and $r_{\rm out}$ = 7.5 r_p.

These simulations show that a 10 $M_{\rm Jup}$ planet at 20 AU creates a Rossby unstable radial pressure bump that becomes a vortex within 10^3 year (Figure 2.6). The vortex continuously evolves (there is no steady-state solution) but it does not disappear for at least 10^5 years, which is sufficient to trap the dust efficiently. Recent work (Meheut et al. 2012) shows that vortices in 3D simulations decay quickly compared to 2D observations when the origin of the Rossby instability disappears, but that there is no decay when the pressure gradient is sustained. Since the planet sustains the Rossby unstable overdensity, this is not an issue in our case. Therefore, the long lifetime of 2D vortices is well justified. The azimuthal gas contrast of the vortex at the outer edge of the cavity could reach values of 2-3 (Figure 2.6).

The dust evolution and resulting dust distribution is calculated separately from the FARGO simulations because it is computationally expensive to do simulations of gas and dust evolution with grain growth simultaneously. We can not use the FARGO output directly because vortices are dynamical objects, whose shape varies with time. The FARGO simulations demonstrate that vortices survive long enough and have high enough gas contrast to trap particles and model the observations. The radial gas disk profile from the FARGO simulations

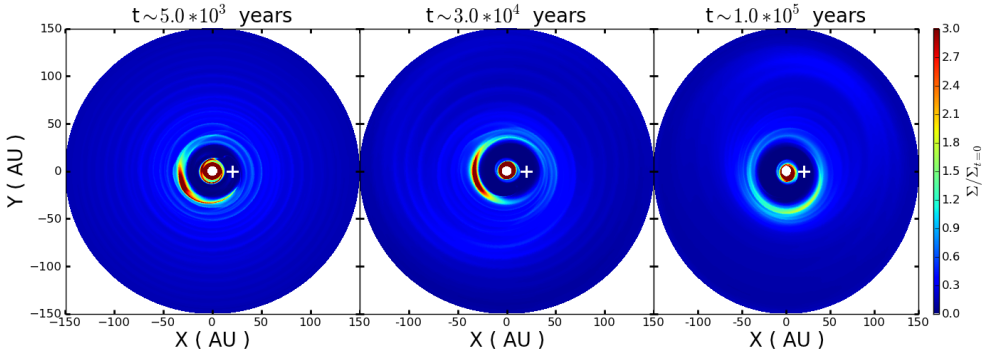


Figure 2.6: *Three snapshots in time of the resulting gas surface density of a disk with a 10 $M_{\rm Jup}$ companion at 20 AU after 1200 companion orbits, simulated with FARGO hydrodynamical code. The companion is indicated with a white cross. The gas surface density was used to model the trapped dust in pressure bumps (Figure 2.7B), to simulate the observed dust trap around IRS 48 (Figure 2.2).*

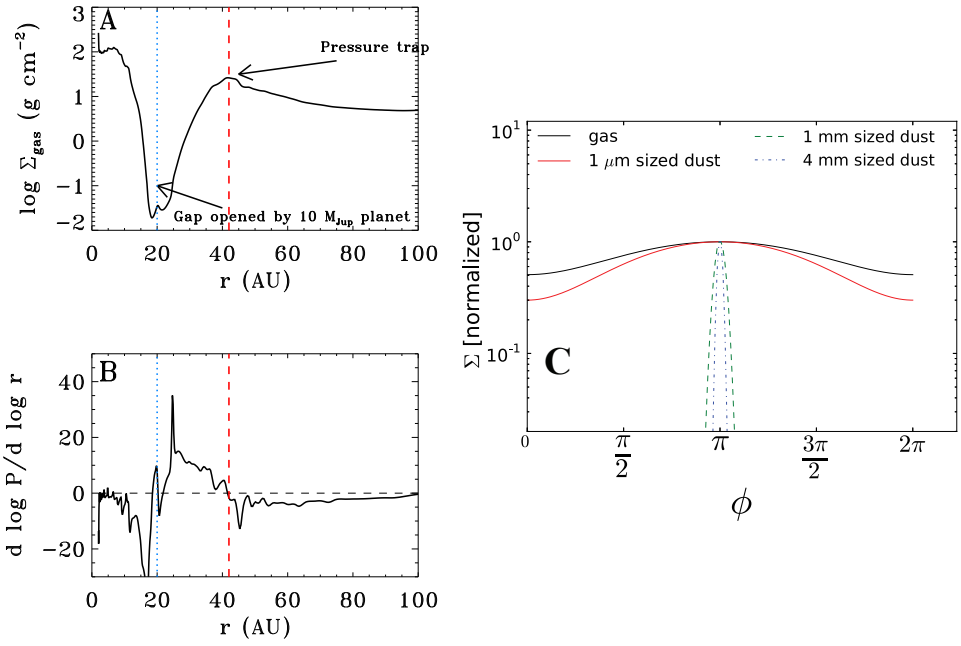


Figure 2.7: *In both A and B, the blue dotted line indicates the location of the planet, the red dashed line the point of zero pressure gradient where the dust gets trapped.* **A)** *The radial gas surface density $\Sigma_{\rm gas}$ after running >1000 orbits (~0.1 Myr) with a 10 $M_{\rm Jup}$ planet at 20 AU in the model disk.* **B)** *The pressure gradient dlog P/dlog r corresponding to the gas surface density profile in A). The grey dashed horizontal line shows where the pressure gradient equals zero.* **C)** *The azimuthal profile of the gas density (black line) versus the large dust grain density (blue) and small dust grain density (red) in the model (Birnstiel et al. 2013). The contrast in the large dust is significantly higher than in the gas.*

(Figure 2.7A) is used as the initial condition for the dust evolution model. The dust evolution code (Masset 2000) is run on this profile, simulating the growth, fragmentation and radial transport of dust to calculate the radial size distribution. For the dust evolution, we consider a grid of grain size from 1 μm to 10 cm and an intrinsic dust density $\rho_s = 0.8$ g cm^{-3}.

To study the azimuthal asymmetry, we now redistribute at each radius the dust using a sinusoidal perturbation (Birnstiel et al. 2013) with a gas contrast of 3, as a steady-state solution based on the vortex in the FARGO simulations described above. The size distribution from the radial profile is distributed azimuthally at each radius using the analytical solution for the gas contrast (Birnstiel et al. 2013). This leads to a weak over-density of micrometer-sized grains, but a very strong overdensity of millimeter-sized grains (see Figure 2.7C).

The resulting grain size distribution as function of radius and azimuth was used to calculate the opacities and the resulting continuum intensity maps, assuming low optical depth and spherical magnesium-iron-silicate grains (Henning et al. 1999). The resulting continuum emission is imaged using CASA (v3.4.0) using the same configurations as in the actual ALMA observations. The final image (Figure 2.2A) shows that the dust trap created by this model has the same morphology and high azimuthal contrast as observed in IRS 48 (Figure 2.2B). The model does not predict the exact same radial extent as the dust trap in IRS 48: the model trap is somewhat closer to the star and narrower in the radial direction. The peak emission is also higher than in the observational data. A more massive companion or placement at a larger radius would increase the radius of the dust trap, but also moves the gas hole edge too far out. A more complex system with multiple companions may solve this problem.

2.2.8 Alternative scenarios

The highly asymmetric dust structure in the Oph IRS 48 disk can be explained by a vortex dust trapping model (Figure 2.2 and associated discussion), with the vortex formed from a pressure bump created by a substellar companion. In this section, we discuss other scenarios that could potentially lead to this kind of asymmetry and explain why they are less likely based on the available observations.

Alternative origin of the pressure bump

The vortex is induced by a Rossby instability of a radial pressure bump, independent of its origin. In this work we present a pressure bump generated by a gas density gradient. Although photoevaporation (Alexander et al. 2006b) could also create a cavity with an overdensity at the edge, photoevaporative clearing is unlikely in the case of IRS 48 as it still has an accretion rate of $\sim 10^{-8} M_{\odot} yr^{-1}$ (Salyk et al. 2013), much higher than typical EUV photoevaporation rates ($\sim 10^{-10} M_{\odot} yr^{-1}$) (Alexander et al. 2006b). In any case, the large hole radii observed for IRS 48 put this source outside the cases that can be reproduced by photoevaporation only (Owen et al. 2011). A pressure bump could also be generated by a viscosity gradient. This gradient exists along the edge of a so-called dead zone: a region of low viscosity below the surface layer of the disk, which occurs if the gas does not have a high enough ionization fraction to enable magnetorotation instabilities that transport the gas. Dead zones form in regions where stellar X-rays and interstellar cosmic rays cannot penetrate and the temperature is not high enough to collisionally ionize the gas, as in the midplane in the inner disk (Gammie 1996). Rossby unstable pressure bumps are formed at the edges of this dead zone (Varnière & Tagger 2006) and the resulting vortices will trap the dust (Regály et al. 2012). The presence of a dead zone can not be excluded from the data presented here, so a dead zone could have formed the unstable pressure bump as well. However, the absence of gas in the inner region of the disk

implies a density gradient that is already sufficiently steep to become a vortex, so a dead zone is not required and we consider this origin less likely.

Gravitational instabilities

If a disk is very massive, gravitational instabilities (Vorobyov & Basu 2008) in the gas could result in the formation of dense gaseous clumps where dust can accumulate. In a rapid cooling scenario, this could lead to direct gas giant planet formation (Boss 1997). Considering the gas-dust separation observed in IRS 48, gravitational instability as a cause of the dust concentration is unlikely, since such an instability would concentrate gas and dust simultaneously. Also the gas and temperature properties of the IRS 48 disk are such that gravitational instability is not expected. The classical criteria for gravitational collapse are (Armitage 2011; Toomre 1964; Gammie 2001): Toomre parameter

$$Q(r) = \frac{c_s(r)\Omega_k(r)}{\pi G \Sigma_{\rm gas}(r)} < 1 \tag{2.10}$$

with vertical isothermal sound speed

$$c_s(r) = \sqrt{\frac{k_B T(r)}{\mu m_p}} \tag{2.11}$$

in combination with fast enough cooling time

$$t_c = \frac{\Sigma_{\rm gas}(r) c_s(r)}{2\sigma T^4(r)} < 3\Omega_k(r)^{-1} \tag{2.12}$$

with k_B the Boltzmann constant, μ the mean molecular mass (μ =2.3), m_p the proton mass, G the gravitational constant and σ the Stefan-Boltzmann constant. Applying the formulae to IRS 48 in combination with the model temperature structure neither of these requirements are met. Although the assumptions here are simple, the temperature structure or the gas surface density would need to change considerably (more than an order of magnitude) to push the criteria to these limits.

Planet collision remnants

If a massive collision happened between two rocky planets, the resulting debris and dust will be first sheared along a ring before it will be turbulently mixed in the radial direction. A single collision is unlikely to have produced the ~9 $M_{\rm Earth}$ of millimeter-sized dust observed here.

Dust clumps in debris disks

Concentrations of large grains have been observed in debris disks, where the dust is produced in situ by planetesimal collisions and is then trapped in clumps through resonances with an existing planet (Wyatt 2003; Lazzaro et al. 1994). This scenario is ruled out here by the large amounts of gas still present in the disk outside 25 AU.

Acknowledgements. We thank M. Benisty and W. Lyra for useful discussions. This paper makes use of the following ALMA data: ADS/JAO.ALMA 2011.0.00635.SSB. ALMA is a partnership of the European Southern Observatory (ESO) (representing its member states), NSF (USA) and National Institutes of Natural Sciences (Japan), together with the National Research Council (Canada) and National Science Council and Academia Sinica Institute of Astronomy and Astrophysics (Taiwan), in cooperation with the Republic of Chile. The Joint ALMA Observatory is operated by ESO, Associated Universities Inc./National Radio Astronomy Observatory, and National Astronomical Observatory of Japan. The data presented here are archived at http://www.alma-allegro.nl/science.

3

A concentration of centimeter-sized grains in Oph IRS 48

van der Marel, N.; Pinilla, P.; J. Tobin; T. van Kempen; S. Andrews; L. Ricci; T. Birnstiel. *A concentration of centimeter-sized grains in the Oph IRS 48 dust trap.* ApJL, in press.

Abstract

Azimuthally asymmetric dust distributions observed with ALMA in transition disks have been interpreted as dust traps. We present VLA Ka band (34 GHz or 0.9 cm) and ALMA Cycle 2 Band 9 (680 GHz or 0.45 mm) observations at 0.2" resolution of the Oph IRS 48 disk, which suggest that larger particles could be more azimuthally concentrated than smaller dust grains, assuming an axisymmetric temperature field or optically thin 680 GHz emission. Fitting an intensity model to both data demonstrates that the azimuthal extent of the millimeter emission is 2.3 ±0.9 times as wide as the centimeter emission, marginally consistent with the particle trapping mechanism under the above assumptions. The 34 GHz continuum image also reveals evidence for ionized gas emission from the star. Both the morphology and the spectral index variations are consistent with an increase of large particles in the center of the trap, but uncertainties remain due to the continuum optical depth at 680 GHz. Particle trapping has been proposed in planet formation models to allow dust particles to grow beyond millimeter sizes in the outer regions of protoplanetary disks. The new observations in the Oph IRS 48 disk provide support for the dust trapping mechanism for centimeter-sized grains, although additional data is required for definitive confirmation.

3.1 Introduction

Studies of transitional disks – protoplanetary disks with inner holes in their dust distribution – are revolutionizing our understanding of planet formation (see review by Espaillat et al. 2014). High spatial resolution ALMA observations reveal not only the dust cavities, but also azimuthal asymmetries (van der Marel et al. 2013; Casassus et al. 2013; Fukagawa et al. 2013; Pérez et al. 2014), and gas still present inside the dust cavities (van der Marel et al. 2013; Casassus et al. 2013; Bruderer et al. 2014; Zhang et al. 2014; van der Marel et al. 2015c; Perez et al. 2015). Dust trapping has been suggested as a solution for the radial drift problem (Whipple 1972; Weidenschilling 1977; Brauer et al. 2008) which prevents dust grains to grow beyond millimeter-sizes in the outer disk. Trapping facilitates the crucial steps in dust growth toward the formation of planetesimals (and therefore planets). As dust continuum emission is dominated by grains with sizes up to 3 times the observing wavelength (Draine 2006), different continuum wavelengths probe different particle sizes. Since particle trapping depends on particle size, disk turbulence, and the pressure gradient profile, multi-wavelength observations are required to confirm the trapping scenario and constrain disk parameters such as viscosity (e.g. Birnstiel et al. 2013, and references therein).

The Oph IRS 48 transition disk exhibits a highly asymmetric structure in the 0.45 mm dust continuum. The continuum emission is generated by millimeter-sized grains gathered in a peanut-shaped structure, spanning less than a third of the disk ring azimuth; the peak of this structure is $> 100\times$ higher than the opposite side of the ring (van der Marel et al. 2013). However, the gas traced by ^{12}CO J=6–5 line emission has an axisymmetric disk distribution down to 20 AU in radius (Bruderer et al. 2014), confirmed by CO isotopologue observations of the same disk (van der Marel et al. 2015b). Likewise, the thermal mid-infrared and near-infrared scattered light emission, tracing small micrometer-sized grains, suggest a ring-like structure although variations along the ring cannot be seen due to high optical depth (Geers et al. 2007; Follette et al. 2015). A separation between large and gas/small grains indicates trapping of the large grains in a pressure trap (Barge & Sommeria 1995; Klahr & Henning 1997; Brauer et al. 2008; Pinilla et al. 2012b). Azimuthal traps may result from vortices, which can be due to instabilities such as the Rossby wave or baroclinic instability (e.g. Lyra & Lin 2013; Raettig et al. 2013; Fung et al. 2014; Flock et al. 2015). A vortex locally increases the gas pressure over a limited radial and azimuthal extent. In the outer disk, millimeter-sized particles will then drift toward this pressure maximum and get trapped in the azimuthal direction (e.g. Ataiee et al. 2013; Zhu & Stone 2014), which can explain the observed features in IRS 48. Inside traps dust particles continue to grow to the maximum grain size permitted by the fragmentation barrier (Birnstiel et al. 2010), which in the outer disk corresponds to centimeter-sizes (e.g. Pinilla et al. 2012b). Further growth to planetesimal sizes can occur by streaming instabilities (Johansen et al. 2009) or by taking mass transfer effects into account (Windmark et al. 2012).

The trapping depends on the particle size: small dust particles are strongly coupled to the gas and thus follow the gas distribution, while larger particles (traced at longer wavelengths) are less coupled and therefore feel the drag force towards the pressure maximum, resulting in a more spatially concentrated distribution of these particles, both radially and azimuthally. Both the trapping concentration and the maximum particle size in the trap are dependent on the turbulence and the gas surface density (Pinilla et al. 2015a). In this paper we present spatially resolved observations of Oph IRS 48 at both millimeter and centimeter wavelengths, taken with the Atacama Large Millimeter/Submillimeter Array (ALMA) and the Karl G. Jansky Very Large Array (VLA). The distributions of dust emission at 450 μm and 0.9 cm are compared and we aim to provide confirmation of the dust trap scenario in a transitional disk.

Section 3.2 describes the observation setup and calibration process, Section 3.3 presents the images and the derived intensity profile and Section 3.4 discusses the interpretation of the different morphologies and possible implications for the dust trapping scenario.

3.2 Observations

Table 3.1: *Image properties*

Array	Freq (GHz)	BW (GHz)	Beam size	Beam PA (°)	Flux (mJy)	Peak (mJy/beam)	Rms (mJy/beam)
ALMA	680	4.7	0.19"×0.15"	79	1000	190	0.6
VLA	34	8.0	0.46"×0.26"	21	251×10^{-3}	138×10^{-3}	3.5×10^{-3}

Observations of Oph IRS 48 at 34 GHz (9 mm) were obtained using the VLA in the CnB and B configurations in January-February 2015 as part of program 14B-115, with baselines ranging from 75 to 8700 m. The spectral windows were configured for a maximum possible continuum bandwidth of 8 GHz centered at 34 GHz (Ka band) in dual polarization, using 64 spectral windows of 128 MHz each, with 3-bit sampling. Due to the low declination, the source was observed in 3 scheduling blocks of 2.75 hours with 1.25 hours on source in each block. The bandpass was calibrated using J1517-2422 (in the third block J1924-2914 was used instead), the absolute flux was calibrated using 3C286 and J1625-2527 was used as gain calibrator, periodically observed every 3 minutes. The pointing was checked on the gain calibrator in X-band every 30 minutes. The calibrated data were concatenated and imaged using Briggs weighting with a robust parameter of 0.5. Deconvolution using CASA imfit reveals that the source is marginally resolved. The flux calibration uncertainty is 10%.

Observations at 680 GHz (440 μm) were obtained using ALMA in Cycle 2 in July 2014 in the C34-3 configuration with Band 9 (Baryshev et al. 2015) as part of program 2013.1.00100.S. The observations were taken in four spectral windows of 1920 channels: three windows have a bandwidth of 937.5 MHz, centered on 661, 659 and 675 GHz, the fourth spectral window was centered on 672 GHz with a bandwidth of 1875 MHz. The total continuum bandwidth was ~4.7 GHz. The flux was calibrated using J1517-243, the bandpass with J1427-4206 and the phase with J1626-2951. The total on-source integration time was 52 minutes. The data were self-calibrated and imaged using Briggs weighting with a robust parameter of 0.5. The flux calibration uncertainty is 20%.

Table 3.1 lists the properties of the images. The astrometric accuracy is set by the calibrators, and is typically $\lesssim$30 mas for these two datasets, which is much smaller than the beam size.

3.3 Results

Figure 3.1 shows images of the dust continuum emission at 680 and 34 GHz. The 680 GHz continuum has a similar asymmetry as observed in van der Marel et al. (2013) in the Band 9 Cycle 0 data, although these new data have improved angular resolution. The 34 GHz continuum emission peaks at the same location, but is much more azimuthally concentrated. This is not a sensitivity effect: when the 680 GHz data are restored with the same cleaning beam as the 34 GHz data, its azimuthal extent is still clearly wider than in the measured 34 GHz data (see Figure 3.1d). The radial width can not be compared due to the vertically

elongated VLA beam shape, which is caused by the low declination of the source with respect to the VLA site, but given the disk geometry, this elongation does not affect constraints on the azimuthal width, the key parameter of interest here. Spatial filtering can be ruled out as an explanation for the different azimuthal extents; these data recover all of the flux found on the shortest baselines from previous VLA observations in the DnC configuration (beam size 3.3×1.3", flux = 252 ±11μJy). Also, we have simulated the ALMA image as if observed by the VLA by sampling the ALMA image on the VLA visibilities (Figure 3.1e) to rule out horizontal spatial filtering. Besides, the largest angular scales recovered by the CnB observation is 5", which is much larger than the disk. Thus, the centimeter-sized dust grains (traced by the 34 GHz continuum) have a narrower azimuthal distribution than the millimeter-sized dust grains (traced by the 690 GHz continuum). The peak brightness temperatures for the 680 GHz and 34 GHz are 31 and 1 K, respectively.

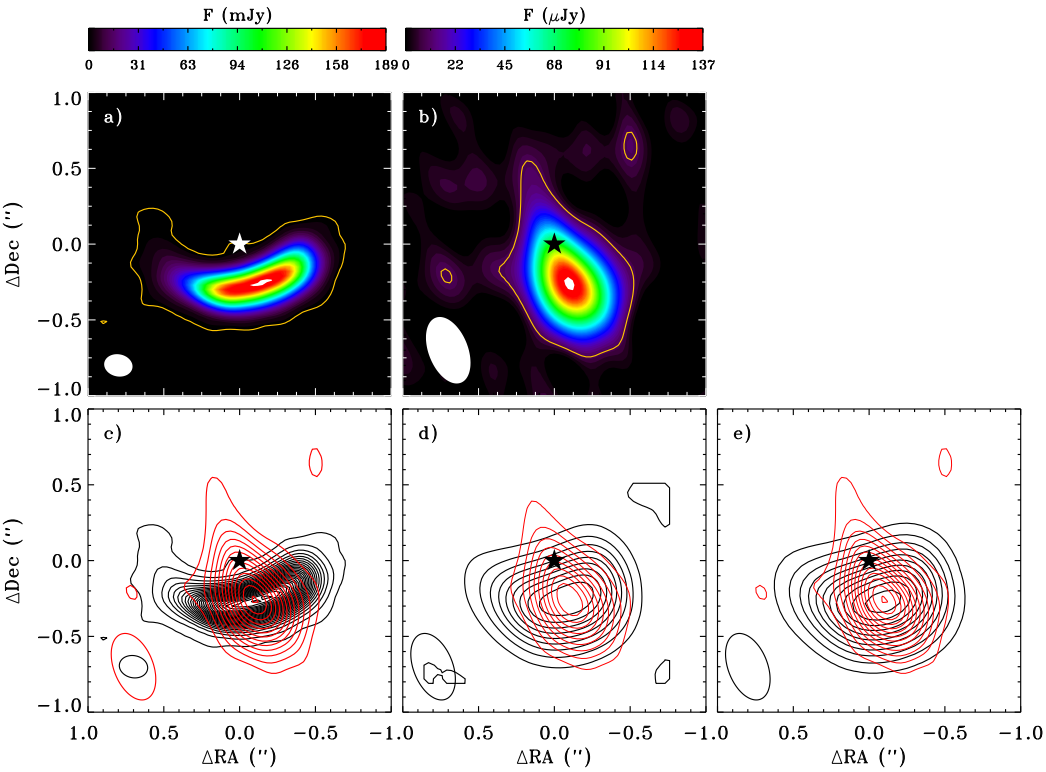


Figure 3.1: *ALMA and VLA observations of dust emission at 680 and 34 GHz of the Oph IRS 48 disk.* **a)** *the 680 GHz image (color scale);* **b)** *the 34 GHz (color scale);* **c)** *the overlay of the 34 GHz contours in red (taken at 3,6,...,39σ, σ=3.5 μJy) on the 680 GHz contours in black (taken at 3,12, 24,...,324σ, with σ=0.6mJy);* **d)** *the overlay of the observed 34 GHz image (red) on the 680 GHz image imaged with the 34 GHz beam (black) in contours taken at 10,20,...,90% of the peak;* **e)** *the overlay of the 680 GHz image as if observed by the VLA (sampled on the VLA visibilities) with the 34 GHz observations taken at 3,6,9,12,...σ, with σ = 3.5μJy. Ellipses indicate the beam size listed in Table 3.1.*

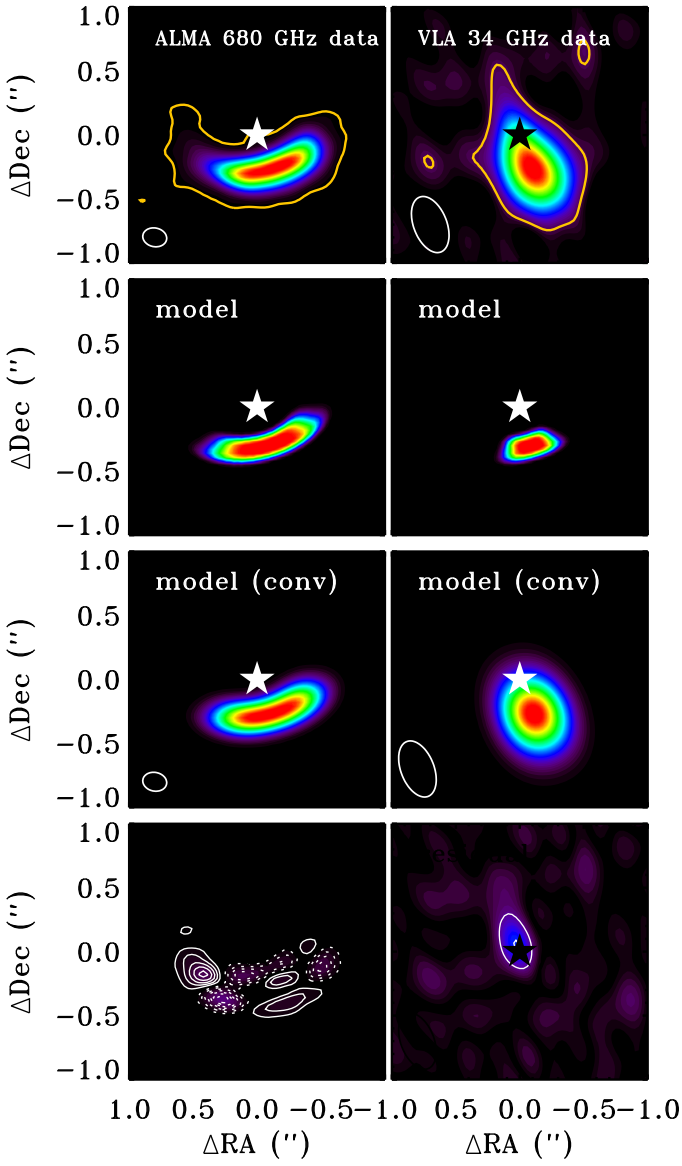


Figure 3.2: *The best fits of the intensity profile given in Equation 1 to the dust continuum for the 680 GHz (left) and 34 GHz (right) data. The top panel shows the data in colorscale (the yellow contour shows the 3σ level), the middle two panels the unconvolved and convolved model and the bottom panel the residual image, with in colors the absolute values of the residual in the color scale of the data and contours at 5σ spacing ($\sigma_{680\mathrm{GHz}}$=0.6 mJy beam^{-1}, $\sigma_{34\mathrm{GHz}}$=3.5 μJy beam^{-1}). Dashed contours indicate negative intensity levels.*

In order to quantify the concentration of the dust grains, the morphology of the continuum image is fit to a two-dimensional 4th power Gaussian intensity profile $I(r,\phi)$ (van der Marel et al. 2013):

$$I(r,\phi) = I_c \exp\left(\frac{-(r-r_c)^4}{2r_w^4}\right)\exp\left(\frac{-(\phi-\phi_c)^4}{2\phi_w^4}\right) \quad (3.1)$$

Previous studies describe azimuthal dust asymmetries due to vortices as regular 2nd power Gaussians (Pérez et al. 2014; Lyra & Lin 2013), but it was found that our data are fitted much better with the 4th power equation. The stellar position was set to $16^h27^m37^s.185$ - 24°30'35.39", taken from a Keplerian model fit to the CO isotopologue data from the same ALMA data set (van der Marel et al. 2015b). The proper motion is negligible compared to the beam size for the period in between these observation sets (~6 months), so they can be overlaid directly. For the fitting we use χ^2 minimization over a grid of ϕ_c, ϕ_w, r_c and r_w with steps of 1 degrees and 1 AU for angle and radius respectively. The fitting is performed in the uv-plane, with the model visibilities sampled onto the observed spatial frequencies. We find the best fit (see Figure 3.2) for r_c=61(± 2) AU, r_w=14(±2) AU, ϕ_c=100(±3)° with ϕ_w=41(±4)° for the 680 GHz and ϕ_w=18(±7)° for the 34 GHz continuum. The area at 680 GHz is smaller than that reported in van der Marel et al. (2013), due to better spatial resolution, although still within the derived error bars. The values and errors for r_c, r_w and ϕ_c are mainly constrained by the ALMA data, as the VLA data did not have sufficient spatial resolution to constrain the error bars. The errors are estimated by rescaling the reduced χ^2 to 1.

The important conclusion is that the azimuthal width of the centimeter emission is 2.3(±0.9) times narrower than the millimeter emission. The aspect ratio of the submillimeter emission is 3.1(±0.6), and >1.4 for the centimeter emission.

The residual of the 680 GHz image still shows significant emission outside the Gaussian fit (peak 25σ), especially at the tail in the east: 15% of the total absolute flux remains in the residual. The intensity equation described by Eqn. 3.1 is clearly not sufficient to describe the detailed structure: additional (vertical) features may be present. The disk is known to have a large scale height (Bruderer et al. 2014), which is not taken into account in the intensity model, while the dust is possibly optically thick at this wavelength and the vertical structure may be relevant. However, as still more than 85% of the structure is recovered by the Gaussian intensity equation and the SNR is very high, the description is sufficient to compare the azimuthal width at the two wavelengths.

The residual of the 34 GHz image clearly shows a point source at the stellar position, with a peak flux of 36 μJy beam^{-1} (10σ). This point source can be either dust emission from an unresolved inner disk, or free-free/synchrotron emission from ionized gas close to the star. Since this emission is not seen in the ALMA data, the spectral index of this emission is <1.3, so dust emission is unlikely. The origin of this emission can be determined using longer wavelength observations (Rodmann et al. 2006; Ubach et al. 2012). The total flux of the dust emission in the dust trap is thus only 216 μJy at 34 GHz.

3.4 Discussion and summary

The difference in azimuthal width between the two continuum images suggests a segregation of particle sizes, where centimeter-sized grains are more azimuthally concentrated than millimeter-sized dust grains. However, optical depth effects can hide a narrow concentration of millimeter-dust grains equivalent to the 34 GHz morphology on top of the apparent millimeter-dust distribution. The optical depth τ_{680GHz} can not be measured independently from the temperature with the available data. The measured brightness temperature at 680

GHz of 31 K (assuming the Planck equation) is only a factor of 2 lower than the calculated physical dust temperature of 60 K (at 60 AU radius in a physical disk model, Bruderer et al. 2014) so the emission is likely not highly optically thick. In order to quantify the optical depth at 680 GHz, we assume that the peak millimeter emission originates from an isothermal area $\Omega_{\rm beam}$ (sr) of the beam size with $T_{\rm dust}$=60 K. This is a conservative limit as τ likely decreases azimuthally outwards. For the peak flux of 189 mJy, τ_{680GHz}=0.5, so the emission is indeed marginally optically thick at 680 GHz. If the dust temperature is much lower than assumed here, the emission becomes fully optically thick and a narrow concentration of millimeter-dust grains could remain hidden. Locally lowering the temperature is possible by shadowing due to an inclined inner disk, such as proposed for HD142527 (Marino et al. 2015) to explain the scattered light emission. For Oph IRS 48, there is no evidence for a local temperature drop, so we propose that the difference in emission originates from a spatial segregation between particles, where the centimeter-sized grains are more concentrated than the millimeter-sized grains. Spatially resolved continuum observations at intermediate wavelengths are required to confirm the dust temperature and optical depth.

Combining the total 34 GHz flux of 216±22 μJy with SMA and disk integrated ALMA observations at 230, 345 and 680 GHz gives a spectral slope $\alpha = 2.84 \pm 0.06 (F_\nu \sim \nu^\alpha)$. The fluxes are 50±7.5, 160±24 and 1000±200 mJy respectively, taken from Brown et al. (2012b) and this work, with the errors dominated by the flux calibration uncertainty. Measuring α independently between 680 and 230 GHz (2.8±0.2) and between 230 and 34 GHz (2.85±0.7) results in the same value within error bars, supporting at most modest optical depth at 680 GHz.

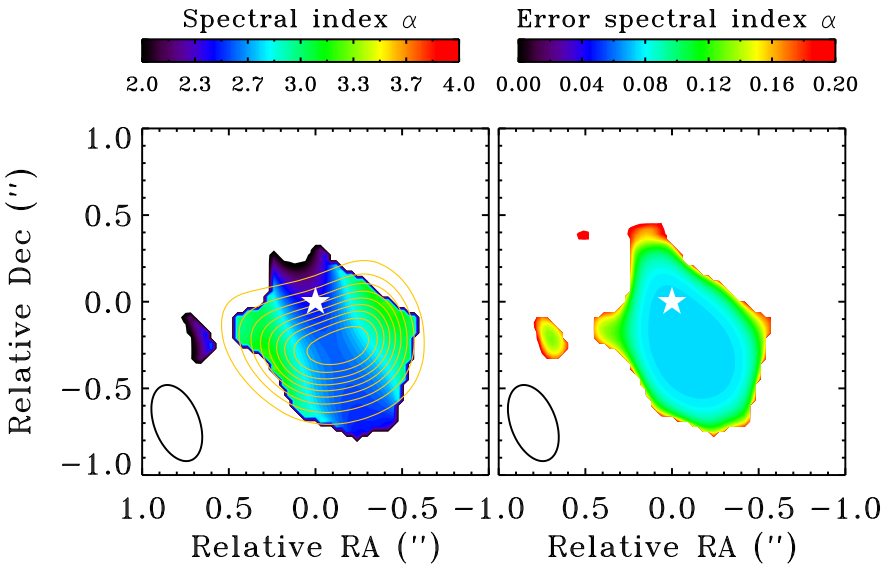


Figure 3.3: *Comparison of the ALMA and VLA data of Oph IRS 48, imaged with the same synthesized beam of 0.46"×0.26" (lower left corner). The left plot shows the spatially resolved spectral index α, using 34 GHz and 680 GHz data. The right plot shows the error on α as function of position. The ALMA data are overlaid in yellow contours with 10,20,...,90% of the peak flux. The spectral index decreases at the peak of the dust emission. Data points where the 34 GHz flux density is less than 2σ ($\sigma = 3.5\mu$Jy) are excluded.*

As both the VLA and the ALMA data are spatially resolved, the spectral index can be computed as a function of position (see Figure 3.3). For this figure, the ALMA data were convolved with the same synthesized beam as the VLA observations. The figure shows that α increases from 2.6±0.08 in the center to 3.3±0.15 in the outer wings, similar to the synthetic spectral index map from Birnstiel et al. (2013) of azimuthal trapping. The error in spectral index across the image is calculated based on the S/N, as shown in the right panel of Figure 3.3. Therefore, the decrease of the spectral index at the peak of the dust emission is significant. Due to the flux calibration uncertainty, which is 20% for ALMA Band 9 and 10% for the VLA Ka band observations, the calibration error over the entire image on σ_α is ~ 0.07, but this does not vary with position and therefore it is not included in the error plot.

Analysis of the dust opacity index β ($\tau_\nu \propto \nu^\beta$) is an important tool in constraining the dust particle sizes in the disk. When the dust emission is optically thin ($\tau \ll 1$) and in the Rayleigh-Jeans regime, $\beta = \alpha - 2$, where $\beta < 1$ indicates dust growth to >mm-sized particles (Draine 2006). For IRS 48 the 680 GHz is not optically thin and these assumptions can not be made. Therefore, the dust opacity index thus has to be derived from the optical depth τ_ν itself.

Using $\tau_\nu \propto \nu^\beta$, β can be calculated as a function of position by calculating τ_ν at both frequencies at different positions, assuming $T_{\rm dust}$=60 K and the flux filling the beam. We find $\beta \sim 0.7 \pm 0.1$ in the center and $\beta \sim 1.3 \pm 0.3$ in the outer parts for a uniform temperature. As the continuum peak is likely more optically thick in the center, the emission there traces higher vertical layers where the temperature is higher, implying an even lower β: for $T_{\rm dust}$=200 K in the center, $\beta = 0.6 \pm 0.1$ according to the same calculation. The azimuthal trend in β is thus consistent with increased dust growth (increase of $a_{\rm max}$) or an increase of larger particles in the center (increase of $a_{\rm min}$). On the other hand, if the temperature is in fact as low as 31 K, β would increase in the center. In order to get a uniform β along the entire azimuthal shape (which implies no change in dust growth or size segregation), $T_{\rm dust}$ needs to be as low as 24 K at the center, which is more than a factor of 2 lower than the derived midplane dust temperature (Bruderer et al. 2014), while the optically thick emission likely originates from higher vertical layers with even higher temperatures. Thus, within reasonable azimuthal variations of the temperature, the results hint at variation in β, although some uncertainties remain.

In summary, the centimeter emission provides further support for the dust trapping mechanism in the Oph IRS 48 disk: within the assumptions of the 680 GHz optical depth and the temperature field, the centimeter-sized grains appear to be more concentrated in azimuth than the millimeter-sized grains as predicted in analytical dust models of azimuthal pressure maxima (Birnstiel et al. 2013; Lyra & Lin 2013). Inside the dust trap, grains may have reached centimeter sizes (and perhaps even larger), the first step towards planetesimal and planet formation.

Acknowledgements. We are grateful to E.F. van Dishoeck and M. Schmalzl for useful discussions, to the referee for useful comments and to the VLA staff for their efforts to observe this program after the configuration move. N.M. is supported by the Netherlands Research School for Astronomy (NOVA). J.T. acknowledges support from grant 639.041.439 from the Netherlands Organisation for Scientific Research (NWO). T.B. acknowledges support from NASA Origins of Solar Systems grant NNX12AJ04G. Astrochemistry in Leiden is supported by the Netherlands Research School for Astronomy (NOVA), by a Royal Netherlands Academy of Arts and Sciences (KNAW) professor prize, and by the European Union A-ERC grant 291141 CHEMPLAN. The National Radio Astronomy Observatory is a facility of the National Science Foundation operated under cooperative agreement by Associated Universities, Inc. This paper makes use of the following ALMA data: ADS/JAO.ALMA/2013.1.00100.S. ALMA is a partnership of ESO (representing its member states), NSF (USA) and NINS (Japan), together with NRC (Canada) and NSC and ASIAA (Taiwan), in cooperation with the Republic of Chile. The Joint ALMA Observatory is operated by ESO, AUI/NRAO and NAOJ.

4

Testing particle trapping in transition disks

Pinilla, P.; van der Marel, N.; Pérez, L.M.; van Dishoeck, E.F.; Andrews, S.M.; Birnstiel, T.; Herczeg, G.J.; Pontoppidan, K.M.; van Kempen, T. *Testing particle trapping in transition disks with ALMA.* A&A, in revision.

Abstract

Some protoplanetary disks show evidence of inner dust cavities. Recent observations of gas and dust of these so-called transition disks have given major support to the hypothesis that the origin of such cavities is trapping in pressure bumps. We present new Atacama Large Millimeter/submillimeter Array (ALMA) continuum observations at 336 GHz of two transition disks, SR21 and HD 135344B. In combination with previous ALMA observations from Cycle 0 at 689 GHz, we compare the visibility profiles at the two frequencies and calculate the spectral index ($\alpha_{\rm mm}$). The observations of SR 21 show a clear shift in the visibility nulls, indicating radial variations of the inner edge of the cavity at the two wavelengths. Notable radial variations of the spectral index are also detected for SR 21 with values of $\alpha_{\rm mm} \sim 3.8 - 4.2$ in the inner region ($r \lesssim 35$ AU) and $\alpha_{\rm mm} \sim 2.6 - 3.0$ outside. An axisymmetric ring (*"ring model"*) or a ring with the addition of an azimuthal Gaussian profile, for mimicking a vortex structure (*"vortex model"*), is assumed for fitting the disk morphology. For SR 21, the ring model better fits the emission at 336 GHz, conversely the vortex model better fits the 689 GHz emission. For HD 135344B, neither a significant shift in the null of the visibilities nor radial variations of $\alpha_{\rm mm}$ are detected. Furthermore, for HD 135344B, the vortex model fits both frequencies better than the ring model. However, the azimuthal extent of the vortex increases with wavelength, contrary to model predictions for particle trapping by anticyclonic vortices. For both disks, the azimuthal variations of $\alpha_{\rm mm}$ remain uncertain to confirm azimuthal trapping. The comparison of the current data with a generic model of dust evolution that includes planet-disk interaction suggests that particles in the outer disk of SR 21 have grown to millimetre sizes and have accumulated in a radial pressure bump, whereas with the current resolution there is not clear evidence of radial trapping in HD 135344B, although it cannot be excluded either.

4.1 Introduction

Recent observations of transition disks (disks with inner dust cavities) suggest that their structures may originate from particle trapping in pressure bumps (e.g. van der Marel et al. 2013; Zhang et al. 2014). Particle accumulation in pressure maxima has been suggested to solve the problem of rapid inward drift of particles (e.g. Weidenschilling 1977; Brauer et al. 2008), implying that planetary embryos may form in localised environments (e.g. Klahr & Henning 1997; Johansen et al. 2007). Pressure bumps may occur due to the presence of one or multiple planets in the disk (e.g. Dodson-Robinson & Salyk 2011; Pinilla et al. 2012a, 2015a; Zhu et al. 2012), but other phenomena such as dead zones may also create pressure traps and explain their structures (e.g. Regály et al. 2012; Flock et al. 2015). Observations of transition disks reveal that dust cavities appear to be smaller at shorter wavelengths (e.g. Dong et al. 2012; Garufi et al. 2013). This spatial segregation of small and mm-sized grains is a natural consequence of particle trapping in the planet-disk interaction scenario (e.g. Rice et al. 2006; de Juan Ovelar et al. 2013).

The spectral index $\alpha_{\rm mm}$ ($F_\nu \propto \nu^{\alpha_{\rm mm}}$) provides information on the particle size in protoplanetary disks (see Testi et al. 2014, for a review). For (sub-)micron sized dust, as found in the interstellar medium, $\alpha_{\rm mm}$ is expected to have values of $\gtrsim 3.5 - 4.0$ (e.g. Finkbeiner et al. 1999). When dust grows to millimetre sizes, $\alpha_{\rm mm}$ is expected to decrease (Draine 2006; Ricci et al. 2010b). Radial increases in $\alpha_{\rm mm}$ (on 100 AU scales) have been found for individual disks without cavities (e.g. Guilloteau et al. 2011; Pérez et al. 2012), consistent with radial drift. In contrast, the inner region of transition disks is depleted of large grains, so that $\alpha_{\rm mm}$ would decrease with radius from the central star (Pinilla et al. 2014). However, such radial variations for $\alpha_{\rm mm}$ in transition disk have not been spatially resolved to date.

In this paper, we combine observations from ALMA Cycle 0 at 689 GHz (~450 μm) and Cycle 1 at 336 GHz (~ 870μm) of SR 21 and HD 135344B (also known as SAO 206462) to compare the morphological structures at the two frequencies and calculate $\alpha_{\rm mm}$ throughout the disk. In addition, we compare the results with a generic model of particle trapping and dust growth in a pressure bump induced by an embedded planet, and place the results in the context of other transition disks.

4.2 Targets and observations

SR 21 is a G3 star located in the Ophiuchus star-forming region at a distance of $d = 120$ pc (Loinard et al. 2008). The disk was identified as a transition disk by its mid-infrared SED, with a cavity radius of $\sim$ 18 AU (Brown et al. 2007). Observations with the Submillimeter Array (SMA) at 850 μm confirmed a $\sim$ 35 AU cavity and suggested an azimuthal disk asymmetry (Brown et al. 2009; Andrews et al. 2011), which was much more clearly seen with ALMA observations in Cycle 0 (Pérez et al. 2014). While 450 μm imaging with ALMA shows strong depletion of large mm-sized grains, by a factor of 10^3 or more in the inner region (van der Marel et al. 2015c), H-band scattered light imaging indicates that the small grains are much less depleted, perhaps by as little as a factor of 10 (Follette et al. 2013).

HD 135344B is an F4 star located in the Sco OB2-3 star-forming region at a distance of $d = 140$ pc (van Boekel et al. 2005). A cavity radius of $\sim$ 45 AU was also identified by its SED (Brown et al. 2007) and confirmed by SMA observations (Brown et al. 2009). One of the most intriguing characteristics of this disk is its spiral arms observed in scattered light images (Muto et al. 2012; Garufi et al. 2013). The observations with VLT/NACO did not show signs of a gap in small dust grains down to 28 AU radius (Garufi et al. 2013).

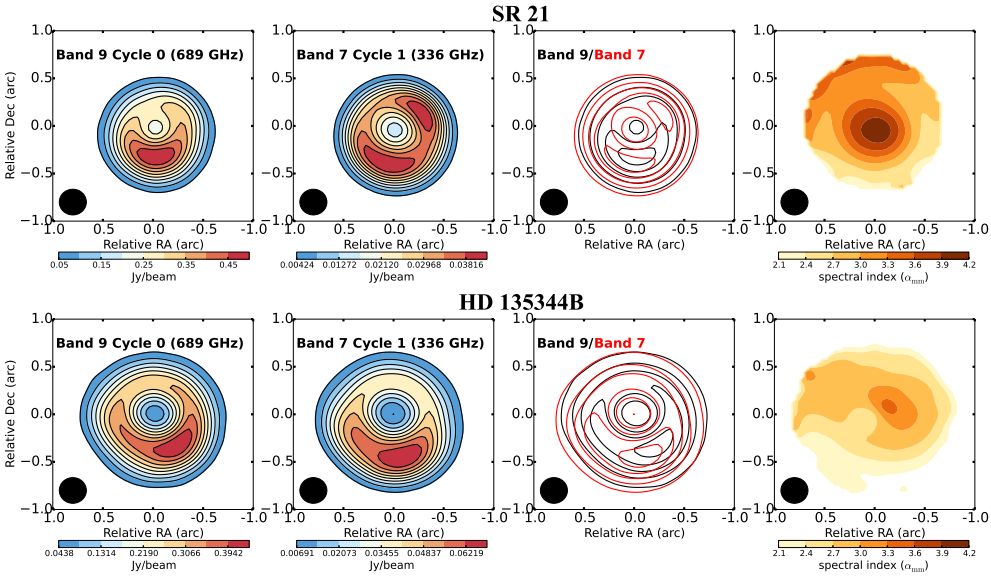


Figure 4.1: *ALMA observations of dust continuum emission for SR 21 (top panels) and HD 135344B (bottom panels). The left columns show the Band 9 (689 GHz) and Band 7 (336 GHz) continuum, with the contour overlaid at 10,20,...,90% of the peak. The third column shows the overlay of the contours with a step of 20% of the peak (black is Band 9, red is Band 7). The right column shows the resolved $\alpha_{\rm mm}$ in colour contours. The beam size is indicated in each plot.*

Table 4.1: *Observation properties*

Target	Band	ν (GHz)	$\Delta\nu$ (GHz)	$F_{\rm peak}$ (mJy)	$F_{\rm total}$ (mJy)	σ (mJy)	Date
SR 21	7	336	3.2	42.4	349	0.08	26/07/2014
	9	689	7.5	500	2877	2.0	18/07/2012
HD 135344B	7	336	3.2	69.1	636	0.13	27/07/2014
	9	689	7.5	438	3360	2.5	05/07/2012

The observations used in this letter are from ALMA Cycle 0 program 2011.0.00724.S (P.I. Pérez) and Cycle 1 program 2012.1.00158.S (P.I. van Dishoeck), taken in Band 9 and Band 7, respectively. The details of the calibration are described in Pérez et al. (2014) and van der Marel et al. (2015b). For both observation sets, the images were obtained using Briggs weighting with a robust parameter of 0.5 and and the beam is set to be the same at both Bands by the post-processing of the images, which is the best possible beam size corresponding to both the Band 7 and Band 9 observations (0.27"). The details of the images are given in Table 4.1.

As the data are taken almost two years apart, the centre of the 2014 data was shifted before overlaying the images to compensate for the proper motion of the stars. The proper motion is -12,-24 mas yr^{-1} for SR 21 (Makarov 2007) and -20,-24 mas yr^{-1} for HD 135344B (Høg et al. 2000). Figure 4.1 shows the continuum maps and their overlay. The shape and contrast of the asymmetry look similar between Band 7 and 9 for HD 135344B. In contrast, SR 21 looks more symmetric in Band 7. There is an azimuthal shift in the continuum overlay for both sources. The position of the gain calibrator (the same for both observations) shifts $\lesssim$0.1 mas, meaning that the azimuthal shift is not due to calibration. With respect to the SMA images in 2006/2007 (Brown et al. 2009), the asymmetries are also shifted.

4.3 Data analysis

4.3.1 Visibilities and disk morphology

The real part of the visibilities at both frequencies is shown in Figure 4.2. These are extracted from the continuum data and deprojected using $i = 15°$ and position angle P.A.=14° for SR 21, and $i = 20°$ and P.A.=63°, as derived in Pontoppidan et al. (2008) and van der Marel et al. (2015c). The data are binned by taking the mean of the available data points in bins of 20 kλ, with a minimum of 5 data points per bin. In Figure 4.2, we show the real part of the visibilities for the two bands. The length of the projected baseline where the visibilities cross zero (the null) indicates the location inner edge of the cavity in a given bandpass (smaller values for the null mean that the cavity inner edge is further out for the same disk properties). The nulls for SR 21 are ~220 kλ at Band 9 and ~250 kλ at Band 7. For HD 135344B the null is almost at the same position at both wavelengths (~190 kλ). The imaginary part of the visibilities are presented in Appendix 4.B.

To fit the visibility profiles and constrain the structure of both disks, we used the same morphological models described in Pérez et al. (2014). One model is a ring-like emission described by $F(r,\theta) = F_R\, e^{-(r-r_R)^2/2\sigma_R^2}$, being r_R the location of the peak of the ring emission, F_R the flux density at r_R, and σ_R the ring width *("ring model")*. The other model assumes a ring together with an azimuthal Gaussian profile to mimic a vortex structure (Lyra & Lin 2013). The vortex is described by $F(r,\theta) = F_V\, e^{-(r-r_V)^2/2\sigma_{r,V}^2} e^{-(\theta-\theta_V)^2/2\sigma_{\theta,V}^2}$, with r_V and θ_V being the radius and P.A. at the peak of the vortex, F_V the flux density at (r_V,θ_V), and $\sigma_{\theta,V}, \sigma_{r,V}$ is the width of the vortex in the radial and azimuthal direction respectively *("vortex model")*. The parameters of the best fit model are found by minimising χ^2 using the same Markov Chain Monte Carlo (MCMC) approach implemented by Pérez et al. (2014). The results are summarised in Table 4.2. The errors from the MCMC calculations are much smaller than the spatial uncertainty from the observations, which is typically $\sim$ 10% of the beam size (i.e. $\sim$3 AU for SR 21 and $\sim$4 for HD 135344B) for the high signal to noise of the data (Table 4.1). For the MCMC calculations, the inclination and P.A. are fixed to the values found by Pérez et al. (2014) for both disks. The model including a vortex did not converge to a physical

Table 4.2: *Best fit parameters the disk morphology models of ring or ring+vortex.*

(a) Ring model

Target	ν (GHz)	χ^2	F_R (μm)	r_R (AU)	σ_R (AU)
SR 21	336	2.07	0.71	41	12
	689	1.39	5.91	36	15
HD 135344B	336	3.75	0.84	61	19
	689	1.18	5.72	60	18

(b) Ring+Vortex model

Target	ν (GHz)	χ^2	F_R (μm)	r_R (AU)	σ_R (AU)	F_V (μm)	r_V (AU)	θ_V ($^\circ$)	$\sigma_{R,V}$ (AU)	$\sigma_{\theta,V}$ (AU)
SR 21	689	1.06	4.72	35	14	4.0	46	178	14	40
HD 135344B	336	1.52	0.70	70	14	0.88	43	172	16	53
	689	1.05	5.24	65	16	7.0	42	194	7.0	47

Notes. All data of Band 9 are identical than Pérez et al. (2014). The parameters for SR 21 in Band 7 of the ring+vortex model are omitted because of the unphysical results. The errors from the MCMC calculations are much smaller than the spatial uncertainty from the observations (and therefore omitted), which is ~ 10% of the beam size (i.e. ~3 AU for SR 21 and ~4 AU for HD 135344B).

solution for SR 21 in Band 7, because the azimuthal extension of the vortex covers more than 2π. In summary, the SR 21 data are best fit with a ring model, while the HD 135344B data are best fit with a vortex model (see Figure 4.2). The residuals obtained by subtracting the best fit model from the data in Band 7 are shown for both targets in Appendix 4.C.

In the case of SR 21, the best-fit model indicates that larger grains, as traced at longer wavelengths by Band 7, are more spatially confined than the smaller grains traced at shorter wavelengths by Band 9 ($\sigma_R \sim 12$ AU at 870 μm vs. $\sigma_R \sim 15$ AU at 450 μm). Furthermore, the peak of emission in the ring is at larger radii in Band 7 than in Band 9 ($r_R \sim 41$ AU at 870 μm vs. $r_R \sim 36$ AU at 450 μm). The location of the inner edge of the cavity at the two frequencies varies from ~ 29 AU in Band 9 to ~ 35 AU in Band 7, which together with the wider ring, is consistent with the shift of the null of the visibilities (Figure 4.2). For HD 135344B, the vortex model is consistently the best-fit model for both wavelengths. The inner edge of the cavity is almost constant in the two bands, as shown in the visibility nulls (Figure 4.2). However, the width of the vortex in both the radial and azimuthal directions is significantly larger in Band 7, and its aspect ratio ($\sigma_{\theta,V}/\sigma_{r,V}$) decreases from 7.1 in Band 9 to 3.3 in Band 7.

4.3.2 Spectral index

The position-dependent spectral index (right panels of Figure 4.1) is calculated using both bands as $\alpha_{\rm mm} = \ln \frac{F_{\nu_{B7}}}{F_{\nu_{B9}}} / \ln \frac{\nu_{B7}}{\nu_{B9}}$. All data with $F < 5\sigma$ are excluded. The dust emission within the cavity is detected at a high level of significance (S/N~ 320σ and ~ 250σ in Band 7, and ~ 120σ and ~ 80σ in Band 9, for SR 21 and HD 135344B, respectively), so $\alpha_{\rm mm}$ can be accurately computed in the cavity separately from the dust ring. The uncertainty of $\alpha_{\rm mm}$ is calculated by error propagation from the observational uncertainty, which includes the calibration uncertainties (~20% and ~10% in Band 9 and 7 respectively) and the noise level or rms (σ) of the observations. With the high signal-to-noise of the data, the uncertainty on the spectral index $\sigma_{\alpha_{\rm mm}}$ at a given position is dominated by the calibration uncertainties

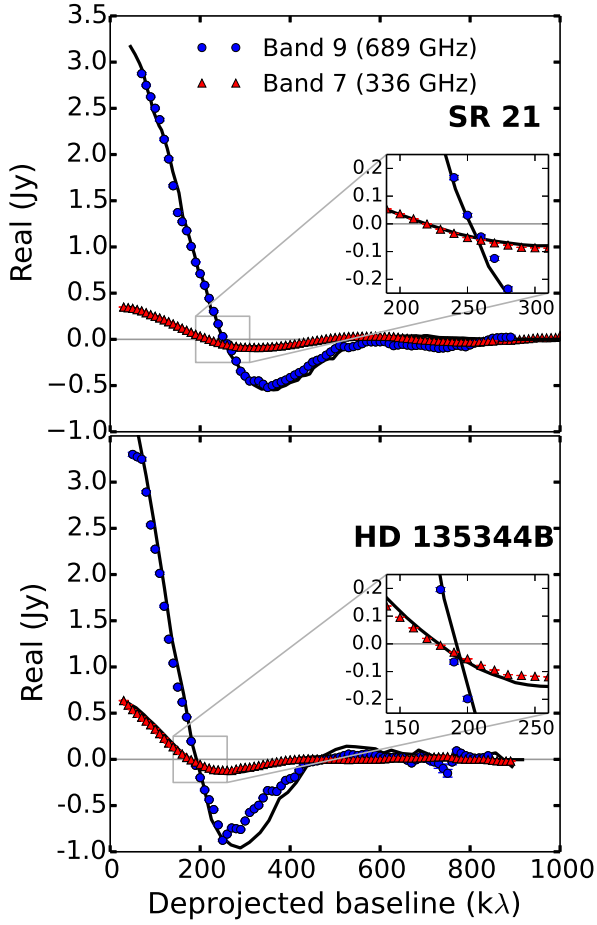


Figure 4.2: *Real part of the visibilities at 689 GHz (~450 μm, Band 9) and at 336 Gz (~870 μm, Band 7) for SR 21 (top panel) and HD 135344B (bottom panel). Note that the plot includes error bars which are of the size of the plotting points. At both wavelengths, the models with the best fit parameters are over-plotted (solid line), which is the ring model in the case of SR 21, and the vortex model for HD 135344B.*

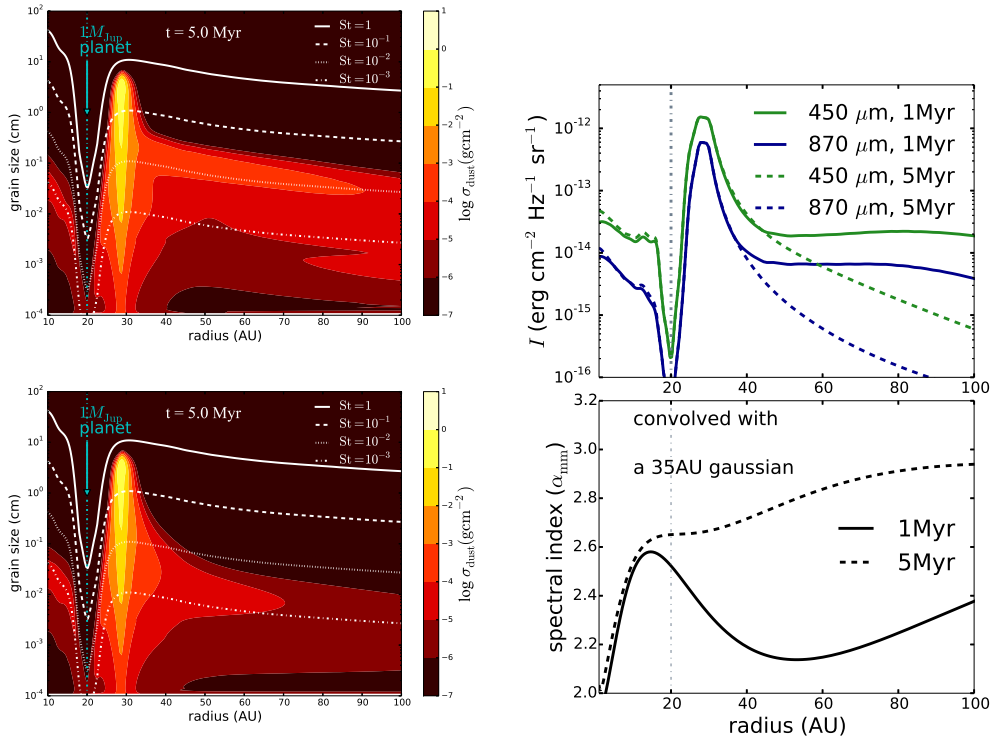


Figure 4.3: Left. *Dust density distribution when* 1 $M_{\rm Jup}$ *is embedded at 20 AU after 1 and 5 Myr of evolution (top and bottom panel respectively). The lines represent particle sizes with different Stokes numbers (St=*$[10^{-3}, 10^{-2}, 10^{-1}, 1]$*), which are proportional to the gas surface density profile.* **Right.** *Top panel: Intensity radial profiles at 450 and 870* μ*m, obtained from the dust density distributions after 1 and 5 Myr of evolution. Bottom panel: radial profile of* $\alpha_{\rm mm}$ *calculated from the intensity profiles at 450 and 870* μ*m, which is convolved a with 35 AU Gaussian beam.*

and approximates to $\approx (\ln \nu_1/\nu_2)^{-1}\sqrt{(0.2^2+0.1^2)} \approx 0.3$, in both cases. However, for the relative spatial changes in $\alpha_{\rm mm}$, the systematic calibration uncertainty does not contribute since it is constant across the field, and changes in $\alpha_{\rm mm}$ inside and outside the dust cavity have high significance with maximum values of $\sigma_{\alpha_{\rm mm}}$ of $\approx$ 0.01. SR 21 shows significant radial variations of $\alpha_{\rm mm}$, with values of $\alpha_{\rm mm} \sim 3.8-4.2$ within ~0.3" radius (~35 AU) and $\alpha_{\rm mm} \sim 2.6-3.0$ outside ($\Delta\alpha_{\rm mm} \gtrsim 120\sigma_{\alpha_{\rm mm}}$). This implies a lack of mm-grains in the inner region ($r \lesssim 35$ AU), and is consistent with accumulation of mm grains in a localised region in the outer disk. For HD 135344B, no significant radial variations for $\alpha_{\rm mm}$ are found, and the values remain within a range of 2.6 – 3.2. Although Figure 4.1 shows azimuthal variations of $\alpha_{\rm mm}$ for both sources, these depend considerably on how the two images are overlaid in the calculation of $\alpha_{\rm mm}$ (see Appendix 4.A), and therefore any azimuthal variation within a range of $\alpha_{\rm mm} \simeq 2.6-3.2$ remains uncertain.

4.4 Theoretical predictions of particle trapping

Dust trapping, in radial and azimuthal pressure bumps, depends on the coupling of the particles to the gas, the pressure gradient, and the disk turbulence. The dimensionless stopping time, Stokes number, quantifies the coupling of the particles and it is defined as $\mathrm{St} = a\rho_s\pi/2\Sigma_g$ (with ρ_s being the volume density of a grain, with typical values of $\sim$ 1g cm^{-3}, Blum & Wurm 2008, and Σ_g the gas surface density). Particles with St $\sim$ 1 preferentially move to the regions of pressure maxima (e.g. Birnstiel et al. 2010; Pinilla et al. 2012a). However, because the gas is turbulent, it is expected that the dust is turbulently mixed by the gas. The dust diffusion prevents the concentration of all the particles with St $\sim$ 1 inside pressure traps. The drift of particles (and hence the trapping) is efficient for particles with St $\gtrsim$ ff$_{\mathrm{visc}}$, where α_{visc} is a dimensionless number that quantifies the disk viscosity (Shakura & Sunyaev 1973). From the combination of radial drift and dust diffusion, it is expected that particles with St $\sim$ 1 are more concentrated at the pressure maximum than St $<$ 1. For example, the models of dust trapping by a vortex predict that larger grains would be more azimuthally concentrated in the centre of the vortex (Birnstiel et al. 2013; Lyra & Lin 2013), as observed in IRS 48 (van der Marel et al. 2015a) and HD 142527 (Casassus et al. 2015).

The left panels of Figure 4.3 show the model predictions for particle trapping triggered by planet-disk interaction. The gas surface density is obtained from hydrodynamical simulations of a 1 M_{Jup} planet embedded in the disk at 20 AU distance from the star as in Pinilla et al. (2012a). The initial gas surface density and temperature are assumed to be a power law, and the disk viscosity is taken to be $\alpha_{\mathrm{visc}} = 10^{-3}$. The dust density distributions are obtained from dust evolution models that include the dynamics and coagulation of dust particles Birnstiel et al. (2010). When a planet opens a gap in the disk, a pressure bump is formed at the outer edge of the gap, and large particles drift to the pressure maximum located in this case at $\sim$ 30 AU. The particle sizes with different Stokes number (St=$[10^{-3}, 10^{-2}, 10^{-1}, 1]$) are shown to illustrate how the radial concentration becomes narrower for particles with higher St. The right panels of Figure 4.3 show the intensity profile at 450 and 870 μm. The emission profile is only slightly narrower at 870 μm since the range of particles sizes that are traced is comparable. Both the dust density distributions and the intensity profiles become narrower at longer times of evolution.

Due to particle trapping, the region close to the planet is empty of mm/cm particles, and therefore α_{mm} is expected to increase close to the location of the gap carved by the planet. Figure. 4.3 also shows the expected radial profiles of α_{mm} calculated from the models at 450 and 870 μm and convolved with a 2D Gaussian profile of 35 AU diameter. In the inner part ($r \lesssim 10$ AU), α_{mm} drops because of the presence of the mm-particles. Because there is no total filtration of particles at the outer edge of the gap, small-grains still flow through the gap and grow again to mm-sizes in the inner region ($r \lesssim 10$ AU). One way to prevent the presence of mm-grains is to increase the mass of the planet, to completely filter all particle sizes (Zhu et al. 2012; Pinilla et al. 2012a, 2015a).

At early times of dust evolution ($\sim$ 1 Myr), mm/cm-grains are still distributed in the entire outer disk ($r \gtrsim 30$ AU) and radial variations of α_{mm} are detected after convolution. This is not the case at 5 Myr, since the concentration of mm/cm particles becomes much narrower compared to the spatial resolution and hence the potential radial variation of α_{mm} is smeared out and is not detected.

4.5 Discussion

With the new ALMA observations of SR 21 and HD 135344B, it is possible to test if radial/azimuthal trapping is the cause of the disk structures (cavities and asymmetries). Observationally, radial trapping can be tested by analysing the location of the null in the real part of the visibilities at different wavelengths, because in the case of trapping, the mm-emission is expected to show a wider ring at shorter wavelengths. Thus, the inner edge of the ring (or dust cavity) should be located closer to the star at shorter wavelengths (Section 4.4). Additional insights can be gained by analysing the wavelength-dependent morphology and the position-dependent spectral index.

SR 21: The current observations of SR 21 at 336 and 689 GHz suggest that the disk morphology at longer wavelengths is better described by a ring than by a vortex. From observations of ^{12}CO, the disk mass of SR 21 has been inferred to be $\sim$ 12 $M_{\rm Jup}$, and the average value of the gas surface density close to the cavity is $\sim$ 80 g cm^{-2} (van der Marel et al. 2015c). Analysis of recent observations of ^{13}CO and C^{18}O of this disk confirmed the disk mass (van der Marel et al. 2015b). Assuming that at each wavelength, particles with a maximum size of $\lesssim 3\lambda$ are traced (e.g. Draine 2006), the observations at Band 7 and 9 traced particles with St $\sim 2.5\times10^{-3} - 5.0\times10^{-3}$ close to the location of the cavity. These particles are expected to be still affected by radial drift and to move toward pressure maxima.

The fact that at a longer wavelength the morphology is better described by a ring than a vortex is in contradiction with model predictions of trapping by a vortex. Thus, the observed azimuthal structure is likely not caused by a vortex. Moreover, to sustain a long-lived vortex, the radial width of the vortex cannot be much higher than the disk scale-height ($\lesssim 2h$, Barranco & Marcus 2005) and the fact that the radial width of the vortex in SR 21 is much larger than the disk scale height ($\sim \times 5\ h$, van der Marel et al. 2015c), as found from the morphology fitting of the Band 9 data (Table 4.2), also disfavours the vortex scenario.

In the radial direction, larger grains traced at 870 μm are more narrowly concentrated than smaller grains traced at 450 μm in SR 21, as demonstrated in the shift of the nulls of the visibilities (see Figure 4.2 and Table 4.2). The narrower concentration of larger grains is in agreement with particle trapping by a radial pressure bump. Further evidence that radial trapping occurs in SR 21 is given by the radial changes of the spectral index $\alpha_{\rm mm}$, which increase outwards, as expected from radial trapping models (Figure 4.3b). The detection of radial variation of $\alpha_{\rm mm}$ with the current resolution suggests that particle trapping in SR 21 have occurred in $\lesssim$ 1 Myr, because at longer times, variations of $\alpha_{\rm mm}$ would not be detected (Figure 4.3b). The discrepancy between the model predictions and the observations for the values of $\alpha_{\rm mm}$ in the inner part of the disk come from the fact that we do not have total filtration of particles in the outer edge of the gap in our model.

Another potential explanation for variations of $\alpha_{\rm mm}$ is high optical depth, in which case the physical temperature is expected to be close to the brightness temperature. To reproduce the observed differences in $\alpha_{\rm mm}$ only by optical depth effects the emission must originate from a small surface area. Assuming that the emission is distributed in a homogeneous ring whose temperature is equal to the highest brightness temperature at the peak of emission obtained at the two frequencies ($T_B \approx$32 K in Band 9 and $\approx$13 K in Band 7), the ring must be very narrow ($\lesssim$3 AU in width), which contradicts the observed spatial extent of the emission in both bands (30-40AU for SR 21 and 60-70AU for HD 135344B, see Table 4.2). Thus, the radial variations of $\alpha_{\rm mm}$ cannot be due to optically thick emission alone. Pérez et al. (2014) demonstrated that the emission at Band 9 is marginally optically thick at the peak of emission, so it can only trace some of the mass surface density, and hence high angular resolution observations at

longer wavelength are necessary to confirm our predictions at the location of the peak.

HD 135344B: In this case, the model with the best fit parameters for the disk morphology at the two wavelength is the vortex model (Table 4.2). The disk mass inferred from ^{12}CO, ^{13}CO, and C^{18}O is $\sim 20\ M_{\rm Jup}$ (van der Marel et al. 2015c,b), and the average value of the gas surface density at the location of the dust cavity is similar to that in SR 21 (~ 80 g cm^{-2}). Therefore, the current observations trace particles with similar Stokes numbers as SR 21.

From the morphological models, the azimuthal width of the vortex increases at longer wavelengths in contradiction with predictions of particle trapping by vortices. Similar as in SR 21 the radial width of the vortex is too large compared to the scale-height of the disk. The origin of the azimuthal asymmetry is inconsistent with a vortex and may be related to the spiral arms observed at scattered light as also suggested by Pérez et al. (2014). In particular the bright spiral in the south coincides with the location of the asymmetry in the millimetre (Garufi et al. 2013; Quanz 2015, see also Appendix 4.C). Indeed, the azimuthal shift of the peak (Figure 4.1, also observed for SR 21) may be related with physical rotation of spiral arms, but higher angular resolution observations are needed to confirm this prediction.

In contrast with SR 21, neither a shift of the null of the visibilities nor radial variations of $\alpha_{\rm mm}$ are detected for HD 135344B, but this does not exclude radial particle trapping. From the model predictions (Section 4.4), the dust density distribution of mm-grains is narrower concentrated at the pressure maximum after 5 Myr than at 1 Myr, and radial variatons in $\alpha_{\rm mm}$ would not be detected with the current resolution (Figure 4.3b). Hence, the fact that radial changes in $\alpha_{\rm mm}$ are not detected for HD 135344B can be related with the fact that any instability (e.g., planet) responsible for the trapping formed earlier (~5 Myr ago) in HD 135344B than in SR 21 (~1 Myr ago). Another possibility is that trapping happens in more refined structures such as spiral arms in gravitationally unstable disks, in which case any variations of $\alpha_{\rm mm}$ remains unresolved (Dipierro et al. 2015).

Besides longer evolution times, other disk and planet parameters, such as planet mass, turbulence, or disk temperature, can also affect the gap shape and thus the radial concentration of mm/cm-sized particles in pressure bumps, leading to a different spatial distribution of small and large grains. High contrast asymmetries have been observed in other transition disks and interpreted as vortices (e.g. Oph IRS 48, van der Marel et al. 2013). Detection of vortices in transition disks may be atypical because several parameters can prevent a vortex from being long-lived, such as strong turbulence or feedback from dust to the gas (e.g. Ataiee et al. 2013; Zhu & Stone 2014; Raettig et al. 2015). Even in the case where a planet originally triggered the formation of the vortex, an eccentric orbit or the presence of addition planets can also lead to its rapid destruction (Ataiee & Pinilla 2015). The current ALMA observations of SR 21 and HD 135344B suggest that anti-cyclonic vortices are not the origin of their low contrast azimuthal asymmetries. Observations at high angular resolution at longer, optically thin, wavelengths, which provide information about the distribution of larger grains, will further constrain the origin of the observed dust structures in transition disks.

4.A Uncertainties of azimuthal variations of spectral index

The calculation of the spectral index ($\alpha_{\rm mm}$) from the observations depends considerably on how the two images are overlapped. To demonstrate that the apparent azimuthal variations remain uncertain, we shifted the alignment of the Band 7 and Band 9 images of SR21 and

HD135344B by the positional uncertainty. Figure 4.4 shows $\alpha_{\rm mm}$ by shifting 20 mas in both vertical and horizontal direction. The only reliable variation of $\alpha_{\rm mm}$ is in the radial direction for SR 21, which remains significant independent of the alignment. In HD 135344B, there is a hint of high values of $\alpha_{\rm mm}$ opposite to the azimuthal asymmetry, that also remains independent of the alignment.

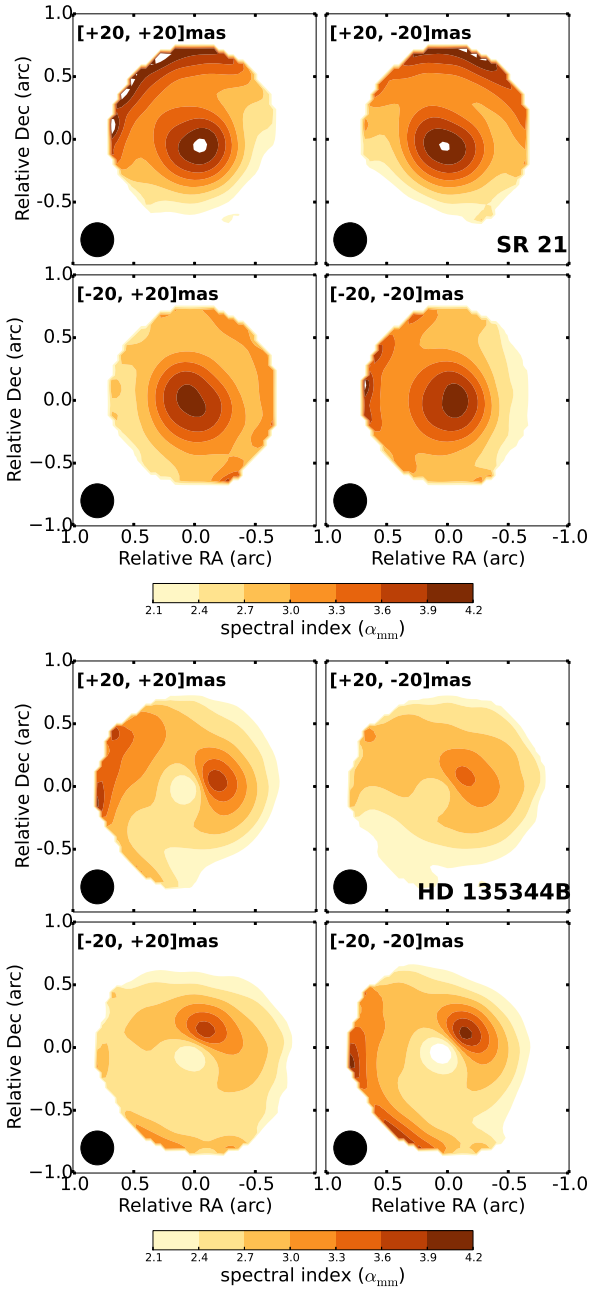


Figure 4.4: *Calculated spectral index ($\alpha_{\rm mm}$) assuming different alignments of the images for SR 21 (upper panel) and HD 135344B (lower panel).*

4.B Imaginary part of the visibilities

Figure 4.5 shows the imaginary part of the visibilities at 689 GHz (~450 μm, Band 9) and at 336 Gz (~870 μm, Band7) for SR 21 and HD 135344B. Non-zero imaginary visibilities indicate the presence of an azimuthal asymmetry (e.g. Isella et al. 2013). For HD 135344B, there are significant variations from zero at both frequencies. For SR 21, the non-zero values are marginal in Band 7, but significant in Band 9 data.

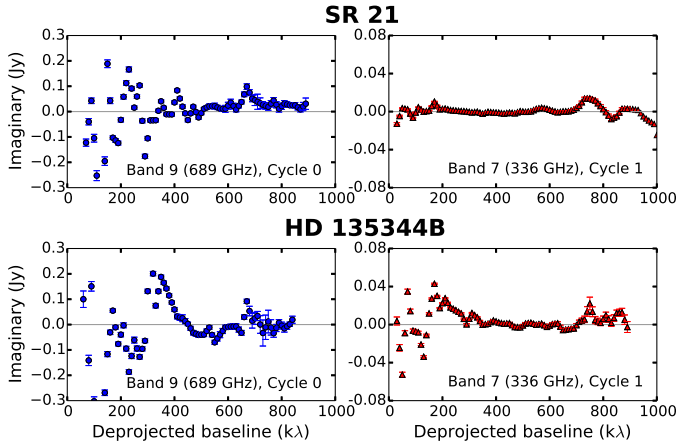


Figure 4.5: *Imaginary part of the visibilities at 689 GHz (~450 μm, Band 9) and at 336 GHz (~870 μm, Band7) for SR 21 (upper panel) and HD 135344B (lower panel).*

4.C Residual maps

Figure 4.6 illustrates the residual maps for both sources after subtracting the best fit models (Table 4.2) to the Band 7 data (336 GHz). For SR 21 the best fit is described by a ring model, whereas for HD 135344B it is a vortex model. The residuals for HD 135344B show a spiral structure as also suggested by Pérez et al. (2014) in Band 9 (689 GHz).

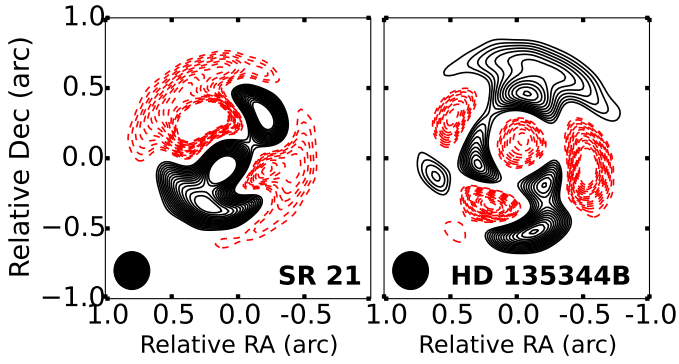


Figure 4.6: *Residual maps after subtracting the best fit models from Table 4.2, contours start at ±3σ and space by 3σ steps.*

Acknowledgements. We are thankful to the anonymous referee who helped to improve the quality of this manuscript. We are grateful to M. Benisty and C. P. Dullemond for fruitful discussions. Astrochemistry in Leiden is supported by the Netherlands Research School for Astronomy (NOVA), by a Royal Netherlands Academy of Arts and Sciences (KNAW) professor prize, and by the European Union A-ERC grant 291141 CHEMPLAN. T. B. acknowledges support from NASA Origins of Solar Systems grant NNX12AJ04G. This paper makes use of the following ALMA data: ADS/JAO.ALMA#2012.1.00158.S and #2011.0.00724.S. ALMA is a partnership of ESO (representing its member states), NSF (USA) and NINS (Japan), together with NRC (Canada) and NSC and ASIAA (Taiwan), in cooperation with the Republic of Chile. The Joint ALMA Observatory is operated by ESO, AUI/NRAO and NAOJ.

5

Gas structure inside dust cavities of transition disks: Oph IRS 48

Bruderer, S.; van der Marel, N.; van Dishoeck, E. F.; van Kempen, T. A. *Gas structure inside dust cavities of transition disks: Ophiuchus IRS 48 observed by ALMA*. 2014, A&A, 562, 26B

Abstract

Transition disks are recognized by the absence of emission of small dust grains inside a radius of up to several 10s of AUs. Due to the lack of angular resolution and sensitivity, the gas content of such dust holes has not yet been determined, but is of importance to constrain the mechanism leading to the dust holes. Transition disks are thought to currently undergo the process of dispersal, setting an end to the giant planet formation process. We present new high-resolution observations with the Atacama Large Millimeter/submillimeter Array (ALMA) of gas lines towards the transition disk Oph IRS 48 previously shown to host a large dust trap. ALMA has detected the $J = 6-5$ line of ^{12}CO and C^{17}O around 690 GHz (434 μm) at a resolution of $\sim$0.25$''$ corresponding to $\sim$30 AU (FWHM). The observed gas lines are used to set constraints on the gas surface density profile. New models of the physical-chemical structure of gas and dust in Oph IRS 48 are developed to reproduce the CO line emission together with the spectral energy distribution (SED) and the VLT-VISIR 18.7 μm dust continuum images. Integrated intensity cuts and the total spectrum from models having different trial gas surface density profiles are compared to observations. The main parameters varied are the drop of gas surface density inside the dust free cavity with a radius of 60 AU and inside the gas depleted innermost 20 AU. Using the derived surface density profiles, predictions for other CO isotopologues are made, which can be tested by future ALMA observations of the object. From the ALMA data we find a total gas mass of the disk of 1.4×10^{-4} M$_\odot$. This gas mass yields a gas-to-dust ratio of $\sim$10, but with considerable uncertainty. Inside 60 AU, the gas surface density drops by a factor of $\sim$12 for an assumed surface density slope of $\gamma = 1$ ($\Sigma \propto r^{-\gamma}$). Inside 20 AU, the gas surface density drops by a factor of at least 110. The drops are measured relative to the extrapolation to small radii of the surface density law at radii >60 AU. The inner radius of the gas disk at 20 AU can be constrained to better than $\pm$5 AU. The derived gas surface density profile points to the clearing of the cavity by one or more massive planet/companion rather than just photoevaporation or grain-growth.

5.1 Introduction

Protoplanetary disks are the cradle for young planets. As the disk evolves from a gas-rich T Tauri disk to a gas-poor debris disk, the disk mass steadily decreases (see Armitage 2011 for a review). The dispersal of the disk sets an end to giant planet formation and thus determines the time-scale of the planet formation process. Detailed understanding of the disk evolution and in particular of the disk dispersal is thus crucial for our understanding how, where, and when planets form. A particular class of protoplanetary disks, called transition disks, is thought to be currently in the stage of dispersal. The dust distribution in transition disks has been studied thoroughly through the spectral energy distribution (SED) from ultraviolet (UV) to millimeter wavelength and in continuum imaging, but still very little is known about the presence and characteristics of the gas in these disks. Here, we use spatially resolved high signal-to-noise gas line observations towards a transition disk to derive the gas structure, and implicitly, determine the origin of the dust holes in this disk.

Transition disks are commonly identified through their SED showing a strong excess over the stellar photosphere at wavelengths $\gtrsim 20\mu$m, but little excess at shorter wavelengths. The deficit of near infrared excess arises from the absence of hot small dust close to the star, suggesting the presence of an inner dust cavity (Strom et al. 1989; Calvet et al. 2002; Brown et al. 2007). Several of these dust holes have been imaged directly in (sub)millimeter interferometric imaging (Piétu et al. 2006; Brown et al. 2009; Andrews et al. 2011; Isella et al. 2012, 2013). Recently, candidates for young planets have been found in cavities of the transition disks T Cha by Huélamo et al. (2011), LkCa 15 by Kraus & Ireland (2012), and HD 100546 by Quanz et al. (2013).

The gas component studied in this work is key to distinguish the different mechanisms proposed for the formation of the dust cavity: grain growth, photo-evaporation and clearing by a planet or substellar companion. Grain growth does not affect the gas density, while photo-evaporation removes gas and dust simultaneously. Clearing by a planet or substellar companion reduces the amount of gas in the cavity depending on the mass of the companion and other parameters (e.g. viscosity, e.g. Zhu et al. 2011; Dodson-Robinson & Salyk 2011; Pinilla et al. 2012a; Mulders et al. 2013; Fung et al. 2014). The planet/companion-disk interaction can also induce perturbations in the gas structure leading to local gas pressure maxima. These pressure maxima can prevent large ($\gtrsim$ mm-sized) dust grains from quickly drifting towards the star before planet formation through dust coagulation and core accretion can take place (e.g. Whipple 1972; Rice et al. 2006; Alexander & Armitage 2007; Garaud 2007; Kretke & Lin 2007; Dzyurkevich et al. 2010; Pinilla et al. 2012a; Birnstiel et al. 2013; Lyra & Lin 2013). Thus, the gas structure in transition disks is of direct importance for planet formation. Moreover, the magnitude of any drop in surface density profile is directly related to the mass of the companion.

Gas line observations towards transition disks have been carried out at near infrared and submillimeter wavelengths. The CO rovibrational emission line at 4.7 μm tracing the several 100 K warm gas from the inner regions of the disk has been detected for several transition disks (Goto et al. 2006; Pontoppidan et al. 2008; van der Plas et al. 2009; Salyk et al. 2009; Brown et al. 2012a, 2013). In contrast, submillimeter observations of the rotational gas lines trace the bulk of the colder gas and are more suitable for constraining the gas mass and distribution inside the cavity (Bruderer 2013). So far, submillimeter observations have suffered from the low angular resolution and sensitivity, barely detected the gas in the outer disk, and did not allow the study of properties of the gas inside the cavity (Dutrey et al. 2008; Lyo et al. 2011). With the Atacama Large Millimeter/submillimeter Array (ALMA[1]) the cold gas in the inner

[1] http://www.almaobservatory.org

regions of transition disks can be imaged for the first time. In this paper, we present a detailed analysis of the gas distribution in the transition disk around the young Herbig star Oph IRS 48, using spatially resolved submillimeter ALMA Band 9 (690 GHz) observations.

Oph IRS 48 (α_{2000} =16^{h}27^{m}37^s.18, δ_{2000} =-24°30′35.3″) is an A0 star located in the ρ Ophiuchi star formation region at a distance of 120 parsec (Loinard et al. 2008; Brown et al. 2012a). The star shows weak accretion signatures (Salyk et al. 2013). A ring-like structure peaking at ~60 AU radius was found by spatially resolved 18.7 μm imaging of the dust continuum (Geers et al. 2007). IRS 48 shows very bright polycyclic aromatic hydrocarbon (PAH) emission centered on the star within this hole. VLT-CRIRES spectra of the 4.7 μm CO line reveal a gas ring with a radius of ~25-35 AU (Brown et al. 2012a). The submillimeter continuum (685 GHz or 0.43 mm) of our ALMA observations was presented in van der Marel et al. (2013). In contrast to the gas and small dust grains, the millimeter dust is concentrated on one side of the disk, with a high azimuthal contrast of >130 compared to the other side. This asymmetric dust distribution was interpreted as a dust trap, triggered by the presence of a substellar companion inside ~20 AU.

In this work we analyze the gas distribution of IRS 48 in detail, using the ALMA observations of ^{12}CO $J = 6-5$ and C^{17}O $J = 6-5$ taken simultaneously with the continuum observations. Using the combined physical-chemical model by Bruderer et al. (2012) and Bruderer (2013), we derive constraints on the drop of the gas surface density profile at a radius of 60 AU, which is the outer radius of the dust cavity, and at ~20 AU, where van der Marel et al. (2013) have identified a gas hole possibly related to a companion situated inside. With the detailed modeling of IRS 48, we also introduce a framework to analyze upcoming ALMA observations of transition disks.

The paper is structured as follows: In Section 5.2 we discuss the observations and data reduction. Section 5.3 presents spectra, integrated intensity maps and channel maps. In Section 5.4, we present detailed models of IRS 48. We first discuss the dust structure derived from the spectral energy distribution and VISIR images and then compare models with different gas surface density profiles to the ALMA observations. Implications of the derived gas mass and gas surface density structure are given in Section 5.5. The paper ends with a conclusions section.

5.2 Observations and data reduction

Band 9 ALMA Cycle 0 observations of IRS 48 were carried out in the extended configuration on June 6th and July 17th 2012 in three execution blocks of 1.7 hours each (one on June 6th and two on July 17th). In these blocks, 18 to 21 antennas were used with baselines up to 390 meter. The average precipitable water vapor (PWV) levels were 0.50, 0.34 and 0.17 mm, respectively. The spectral setup consisted of four spectral windows, centered at 674.00 , 678.84, 691.47 and 693.88 GHz, to target the C^{17}O $J = 6-5$, CN $J = 6_{11/2} - 5_{11/2}$, ^{12}CO $J = 6-5$, and H^{13}CO$^+$ $J = 8-7$ transitions. The CN and H^{13}CO$^+$ lines have however not been detected and are discussed in van der Marel et al. (2014) together with a detection of H_2CO $9_{18} - 8_{17}$. The spectral windows consist of 3840 channels each with a channel separation of 488 kHz and thus a bandwidth of 1875 MHz. The final velocity resolution is 0.21 km s^{-1} using a reference of 690 GHz and the rms noise level is 40 mJy beam^{-1} channel^{-1}. The synthetic beam has a size of 0.32″ × 0.21″ (38 × 25 AU) and a position angle of 96° (east-of-north).

Reduction and calibration of the data was performed using the Common Astronomy Software Application (CASA) v3.4 and is further described in van der Marel et al. (2013).

5.3 Results

5.3.1 Integrated intensity maps

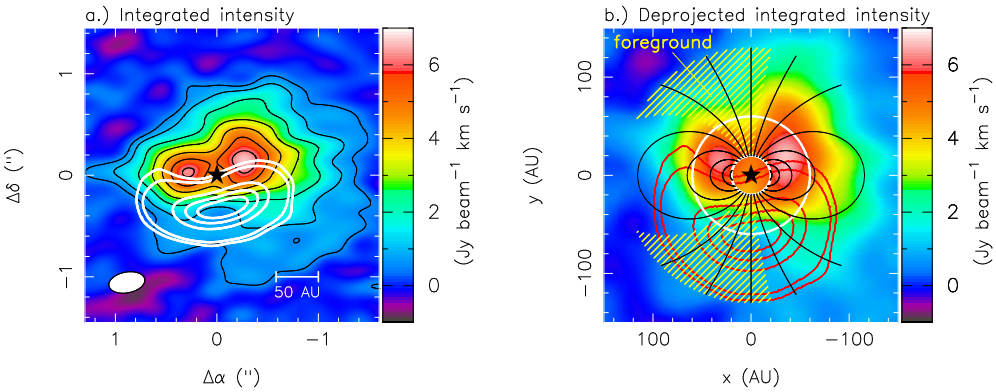


Figure 5.1: *a) Continuum subtracted integrated intensity of ^{12}CO $J = 6-5$ in color. The black contour lines show $5\sigma, 10\sigma, 20\sigma, \ldots$ detections of the line ($1\sigma = 73$ mJy beam^{-1} km s^{-1}), white contour lines represent $5\sigma, 10\sigma, 100\sigma, 200\sigma, 300\sigma$ detections of the continuum ($1\sigma = 0.82$ mJy beam^{-1}). The ALMA beam (FWHM) is indicated in the left lower corner. b) Deprojected continuum subtracted integrated intensity maps of ^{12}CO $J = 6-5$ in color and the continuum with contours ($5\sigma, 10\sigma, 100\sigma, 200\sigma, 300\sigma$ detections). The (x, y)-coordinates are along the major/minor axis of the observed disk. Thick white lines indicated radii of 20 and 60 AU and deprojected isovelocity contours of regions with velocity $\pm1, \pm2, \ldots$ km s^{-1} relative to v_{lsr} towards us. The yellow shaded region indicates positions affected by foreground absorption.*

Figure 5.1a shows the continuum subtracted integrated intensity of the ^{12}CO $J = 6-5$ observation. The continuum emission at the same wavelength (430 μm) is indicated in white contour lines. The strongly lopsided shape of the continuum is interpreted by van der Marel et al. (2013) as large >mm-size dust being trapped by a local pressure maximum due to a long-lived vortex in the gas, induced by a companion situated at a radius <20 AU. The integrated intensity of CO is elongated in the east-west direction and shows a drop at the stellar position. The stellar position (Table 5.1) is determined from the fastest velocity channels where CO emission has been detected. The elongation is due to the inclination of $i = 50°$. At the position of the continuum peak, CO emission is detected, but not particularly strong. This is however not inconsistent with a pressure maximum at this position, because ^{12}CO is likely optically thick and a weak increase of density by less than a factor of 2 is sufficient to trigger dust trapping (Birnstiel et al. 2013; see further discussion in Section 5.5.2).

In Figure 5.1b, the continuum subtracted integrated intensity deprojected for inclination, position angle, and distance is shown. After deprojection, the disk is shown as seen face-on with coordinates (x, y) in AU along the major/minor axis of the observed disk. For the deprojection, the parameters given in Table 5.1 are used. The inclination is determined by Geers et al. (2007) from 18.7 μm dust continuum images to be $i = 48 \pm 8°$. This inclination is confirmed by Brown et al. (2012a) from CO ro-vibrational lines. We use $i = 50°$, which was found to agree best with the channel maps of ^{12}CO (Figure 5.2). Geers et al. (2007) find a position angle of $98 \pm 3°$ (east-of-north) from the 18.7 μm dust continuum images. This is consistent with PA $= 100.3°$ determined from the position of the highest velocity channels where ^{12}CO is detected (Figure 5.2). We overlay deprojected isovelocity contour lines

providing lines with the same velocity towards us. The contour lines are derived assuming a geometrically thin disk in Keplerian rotation around a 2 $M_\odot$ star (Table 5.1). The deprojected map shows weaker emission in the north-east compared to the north-west. The reason for this is absorption by a foreground cloud. The ρ Ophiuchus region has several foreground layers and clouds with a high enough shielding to be abundant in CO (Loren 1989; Boogert et al. 2002; van Kempen et al. 2009). Such cold foreground CO can shield the disk emission. The foreground towards IRS 48 (A_V = 11.5, Brown et al. 2012a) can provide enough line opacity ($\tau >$ few) in ^{12}CO $J = 6-5$ for a cloud with temperatures around 30 K and densities around 3×10^4 cm^{-3}. Foreground absorption usually affects only a narrow velocity range, since they are cold and have small intrinsic line widths. Towards IRS 48, velocities v_{lsr} ~2.0 to ~4.5 km s^{-1} are affected indicated by the yellow shaded region (van Kempen et al. 2009).

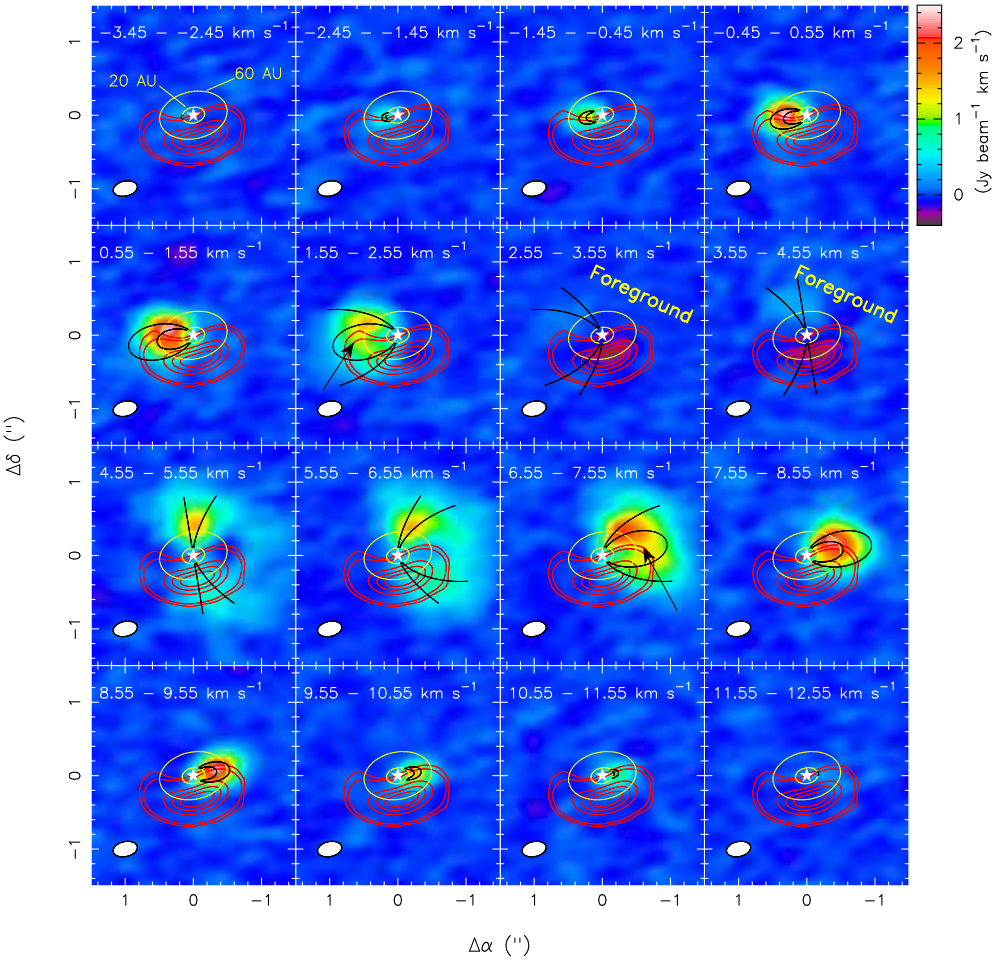


Figure 5.2: *^{12}CO $J = 6-5$ channel map around $v_{source} = 4.55$ km s^{-1}. Channels are binned to 1 km s^{-1}. Black lines show isovelocity contours of the border velocity of each velocity bin assuming Keplerian rotation with parameters in Table 5.1. Channels between 2.55 and 4.55 km s^{-1} are affected by foreground absorption. Black arrows indicate regions with clear deviations from the Keplerian pattern (see Section 5.3.2). Circles indicated radii of 20 and 60 AU. Red contours give the continuum ($5\sigma, 10\sigma, 100\sigma, 200\sigma, 300\sigma$ detections).*

Asymmetries in the east-west direction in the north of the disk ($y \gtrsim 50$ AU in the deprojected map) can thus be explained by foreground absorption. Between $y = -50$ AU and $y = 50$ AU, the disk is less extended in the eastern direction, which cannot be explained by the foreground. An additional foreground layer at $v_{lsr} = 1.5$ km s^{-1} found towards Oph VLA 1623 by Murillo et al. (2013) would help to explain this asymmetry, but it is unclear if this previously unknown layer also extends to IRS 48. The projected distance of IRS 48 to VLA 1623 is ~19′ or 0.7 pc. At $x \lesssim -20$ AU, an asymmetry in north-south direction is outside the region affected by foreground by more than the size of the beam of 20 – 30 AU. For example at $x = -20$ AU, the emission at $y = -60$ AU is about a factor of 3 weaker compared to $y = 60$ AU. At these positions the peak intensities are 1.7 Jy beam^{-1} and 0.7 Jy beam^{-1}, which is stronger than the continuum peak of 0.3 Jy beam^{-1}. Thus, a pure line-to-continuum effect can also not explain this asymmetry. Since also the peak integrated intensity is slightly shifted to the north with respect to the major axis of the disk ($y = 0$ AU), a north-south temperature gradient could be the reason for this asymmetry (see further discussion in Section 5.5.2).

We conclude that some, but not all, of the asymmetries seen in the integrated intensity maps can be attributed to foreground absorption. Least affected by the foreground are regions close to the major axis of the disk.

Table 5.1: *Basic data of Oph IRS 48*

Parameter	Value	Reference
Stellar position	α_{2000} =16^{h}27^{m}37^s.18	B13
	δ_{2000} =-24°30′35.3″	
Distance	120 pc	L08
Inclination	$i = 50°$	G07, B13
Systemic velocity	$v_{lsr} = 4.55$ km s^{-1}	vdM13
Position angle	PA = 100.3° (east-of-north)	G07, B13
Stellar type	$A0^{+4}_{-1}$	B12
Stellar mass	$M_* = 2$ M$_\odot$	B12
Stellar luminosity	14.3 L$_\odot$	B12
Accretion rate	4×10^{-9} M$_\odot$ yr^{-1}	S13

Notes. B13=this work, L08=Loinard et al. (2008), G07=Geers et al. (2007), B12=Brown et al. (2012a), S13=Salyk et al. (2013), vdM13=van der Marel et al. (2013)

5.3.2 Channel maps

Channel maps of ^{12}CO 6 – 5, binned to 1 km s^{-1}, are presented in Figure 5.2. Overlayed on the spectrum are isovelocity contours for the velocity bin, derived in the same way as for Figure 5.1b (Section 5.3.1). The blue part at $v_{lsr} < v_{source} = 4.55$ km s^{-1} shows in the fastest channels with CO detected the expected Keplerian pattern, derived using the parameters in Table 5.1. At slower channels ($v_{lsr} = 1.55 - 2.55$ km s^{-1}) some emission along the major axis of the disk at distances smaller than expected from the Keplerian pattern is found (indicated by black arrows in Figure 5.2). The reason for this slow gas is not clear, but could be related to gas streaming inwards. In our data, this component is only clearly seen at distances >60 AU and it is thus uncertain if it is related to gas streaming towards the star as found by Casassus et al. (2013) for the case of HD 142527. Between $v_{lsr} = 2.55$ and 4.55 km s^{-1}, the emission is completely absorbed by foreground. The red-shifted channels with respect to v_{source} show a Keplerian pattern for channels between $v_{lsr} = 4.55 - 6.55$ km s^{-1} and the fastest channels

($v_{lsr} > 8.55$ km s^{-1}). In between, some emission along the major axis at smaller distances than expected from the Keplerian pattern is found, as for the blue shifted side.

We conclude that the disk for higher velocities and thus for regions closer to the star, follows the expected Keplerian rotation. Deviations from the Keplerian rotation are found at velocities slower than 4 km s^{-1} relative to v_{source} at regions outside ~60 AU.

5.3.3 Total spectrum and $C^{17}O$

The total spectrum extracted from regions with >5σ detections in ^{12}CO is shown in Figure 5.3, together with the spectrum mirrored at v_{source}. Original and mirrored spectrum overlay for velocities faster than ~4 km s^{-1} relative to v_{source}, indicating a symmetric disk close to the protostar. Assuming Keplerian rotation, a velocity shift of 4 km s^{-1} corresponds to radius of $r = \sin(i)^2 GM_*/v^2 \sim 65$ AU. CO is detected out to velocity shifts of ~7 km s^{-1}, corresponding to a radius of ~20 AU. Between $v_{lsr} = 0$ and 2 km s^{-1}, the blue shifted side is weaker than the red shifted side. This could be due to an additional foreground layer (Section 5.3.1).

The emission of $C^{17}O$, observed in parallel with ^{12}CO, is too weak to be detected in a single beam. When integrated over a larger region and binned to 1 km s^{-1} velocity-resolution, it has been detected at a ~4σ level. Only channels with velocity of 3.5 and 4.5 km s^{-1} relative to v_{source} are detected. Only the channel at 4.5 km s^{-1} is detected on both the blue and red side. The largest contribution to this channel is from radii of 60 to 110 AU, assuming Keplerian rotation. The lower panels in Figure 5.3 show spectra extracted from regions where ^{12}CO is detected at a >5σ level in the blue and red part of the spectrum. Indeed, the $C^{17}O$ emission is also only detected on the corresponding side of the spectrum, providing some evidence that the $C^{17}O$ detection is real.

We conclude from the total spectrum that the disk does not show clear signs of asymmetries inside 60 AU. Observations at higher angular resolution or better sensitivity may however reveal asymmetries also in this region. We further conclude that $C^{17}O$ is detected at >60 AU, although at a very weak level.

5.3.4 A cut through the major axis of the disk

The previous sections have shown that a cut through the major axis of the disk is least affected by foreground absorption. In Figure 5.4, the integrated intensity of ^{12}CO along this cut is presented together with the 18.7 μm dust continuum emission observed with VLT-VISIR.

Both the ^{12}CO integrated intensity and 18.7 μm dust continuum emission profiles are double-peaked, with the peaks located symmetrically with respect to the star. The strengths of the peaks are slightly asymmetric with the dust emission ~15 % stronger in the east, while the line emission is about ~10 % stronger in the west. The ^{12}CO emission peaks at a distance of ~35 AU to the star, while the dust emission peaks at ~55 AU. At the positions where the dust emission peaks, no clear break or change in the ^{12}CO emission can be seen. The depletion in the center of the ^{12}CO emission has about the width of one beam.

5.4 Analysis

In order to constrain changes of the gas surface density profile in particular the drop of the gas surface density inside the dust cavity and the inner gas hole, we use the combined physical-chemical model DALI (Dust And LInes) by Bruderer (2013), based on Bruderer et al. (2012).

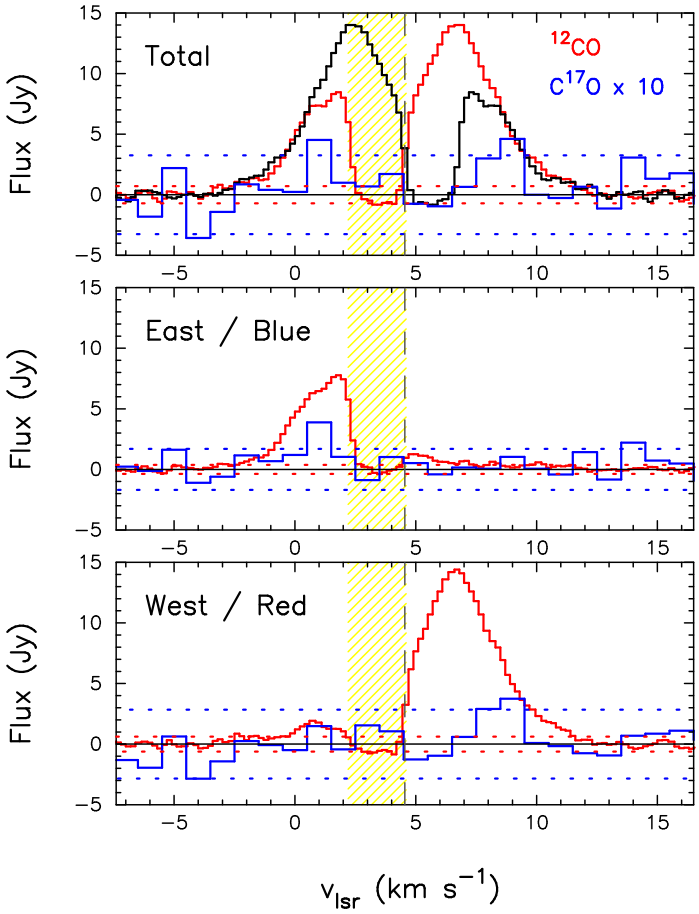


Figure 5.3: *Continuum subtracted spectra of ^{12}CO $J = 6-5$ (red lines) and ^{17}CO $J = 6-5$ (blue lines). The spectra are extracted from regions with $> 5\sigma$ detections in ^{12}CO. The yellow shaded region indicated velocities affected by foreground absorption. The vertical dashed line at 4.55 km s^{-1} gives* v_{source}. *Dotted horizontal lines show the 3σ detection level.* **Top panel:** *Total spectrum. The spectrum of ^{12}CO mirrored on* v_{source} *is given in black line.* **Center panel:** *Spectrum extracted from the east/blue part of the disk.* **Bottom panel:** *Spectrum extracted from the west/red part of the disk.*

The models solve for the dust radiative transfer, the chemical abundance, the molecular excitation and the thermal balance to obtain the gas temperature in a self-consistent way. Such a model is also needed to determine the abundance of CO inside and outside the dust cavity since it is not a priori obvious that CO can survive in the dust-free gas exposed to intense UV radiation from the star. The CO abundance distribution in the disk, together with the gas temperature distribution, determines the intensity and profile of the CO line emission. Spectral image cubes of the line emission are derived from the models and compared to the observations.

The main focus of our modeling are the regions inside the 60 AU radius dust cavity. As discussed in Section 5.3, this region does not show strong signs of asymmetries and we will restrict our analysis to 2d axisymmetric models. Fully 3d models might ultimately be needed to explain e.g. the structure of the outer disk, but they are computationally very demand-

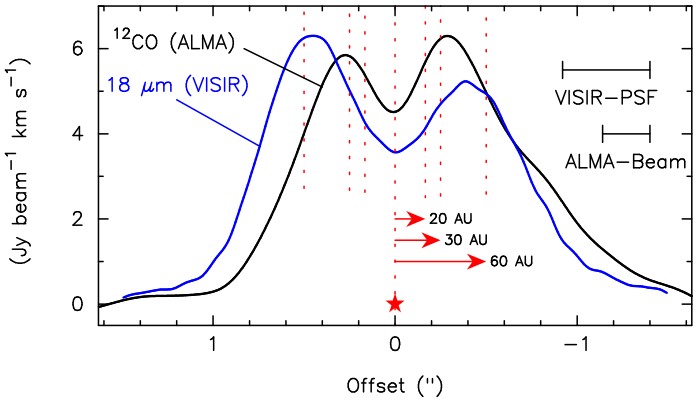


Figure 5.4: *Integrated intensity of ^{12}CO $J = 6-5$ (black line) extracted from a cut through the major axis of the disk ($y = 0$ AU in Figure 5.1b). The 18.7 μm dust emission observed by VLT-VISIR (blue line) has been scaled to the ^{12}CO peak.*

ing. Also, a more detailed analysis will require the additional constraints from optically thin isotopologue emission (Bruderer 2013) which are not yet available.

In this section, we will first discuss the adopted disk structure for our modeling, and then show the physical and chemical structure derived from the models and a comparison of the line emission to the observations.

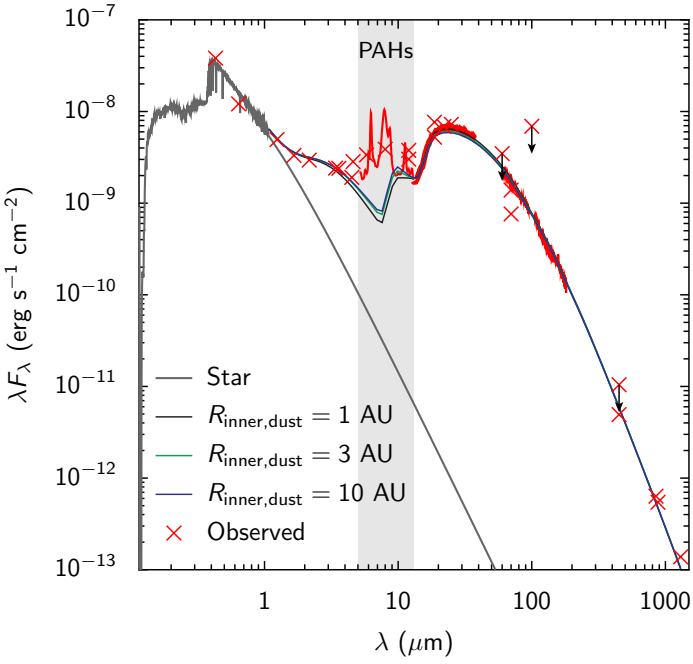


Figure 5.5: *Observed, dereddened SED of IRS 48 (red crosses/lines) compared to models with different extent (outer radius) of the warm dust inner disk ($R_{inner,dust} = 1, 3$ or 10 AU in black, green and blue lines). The stellar SED is shown by a grey line. Wavelengths with PAH emission not used in the SED fitting are indicated by a grey shaded region.*

5.4.1 Disk structure

The dust structure of IRS 48 is derived from the SED and 18.7 μm VLT-VISIR dust continuum image by Geers et al. (2007). The SED is given in Figure 5.5 (Table 5.2). It has been dereddened using a Weingartner & Draine (2001) extinction curve for R_V = 5.5 assuming A_V = 11.5 (Brown et al. 2012a). The stellar SED is derived from the Pickles (1998)-library spectrum for an A0 star with bolometric luminosity 14.3 $L_\odot$. At wavelengths shorter than 1150 Å, this spectrum is extended by FUSE observations towards a star of the same spectral type, scaled for the bolometric luminosity. The dust SED shows excess emission over the stellar emission at near infrared wavelengths (1-5 μm), indicative of warm dust close to the star (<1 AU). The spatial location of this warm dust is not known, but is here attributed to the optically thick inner wall of a dusty inner disk. Other SED fits of IRS 48 (Maaskant et al. 2013) have assigned the near infrared excess to a dust halo around the star. A peculiar feature of the SED are the strong PAH features at 5-12 μm, discussed by Geers et al. 2007. The mid-infrared excess has been spatially resolved by VLT-VISIR at 18.7 μm and comes from a ring located at a radial distance of ~60 AU to the star. The (sub)millimeter continuum is strongly lopsided, but remains marginally optically thin at 450 μm (van der Marel et al. 2013). The peak emission of the submillimeter continuum is located slightly outside 60 AU (Figure 5.1, van der Marel et al. 2013) and in the following we will assume that both the mid-infrared and (sub)millimeter continuum emission come from an outer disk located at a radius >60 AU. The FIR continuum (60-180 μm), observed by Herschel (Fedele et al. 2013), is not spatially resolved and it is unknown whether it is ring-like or lopsided.

For our modeling, we adopt the physical structure suggested by Andrews et al. (2011), as implemented by Bruderer (2013). The surface density profile is assumed to be a power-law and the vertical structure follows a Gaussian distribution (vertically isothermal structure). Given that our data do not constrain the vertical structure and disk models assuming hydrostatic equilibrium overestimate the scale-height (Thi et al. 2013), we feel that such a simple approach is warranted. The outer radius of the disk is not the focus of our work, and we here employ a sharp cut-off in the surface density profile rather than an exponential decrease as in Andrews et al. (2011) and Bruderer (2013).

The parameters of the structure are shown in Table 5.3 and Figure 5.6. The surface density profile follows

$$\Sigma(r) = \Sigma_{60\,\mathrm{AU}} \cdot \left(\frac{r}{60\,\mathrm{AU}}\right)^{-\gamma} \tag{5.1}$$

and is defined by the power-law index γ and a surface density $\Sigma_{60\,\mathrm{AU}}$ at 60 AU. The surface density profile of the outer disk at 60-160 AU is scaled by different factors within the warm dust inner disk inside $R_{\mathrm{inner,dust}} = 1$ AU (δ_{dust}), the gas depleted hole inside 20 AU and the gap between 20-60 AU ($\delta_{20\,\mathrm{AU}}$ and $\delta_{60\,\mathrm{AU}}$). In the radial direction, these regions are defined by the dust sublimation temperature (0.4 AU), the line wings of the ^{12}CO emission (20 AU), and the size of the dust cavity seen in the 18.7 μm dust continuum images and the (sub)millimeter continuum (60 AU). The critical parameter to be studied in this work are the drop of the gas surface density profile at 20 AU ($\delta_{20\,\mathrm{AU}}$) and at 60 AU ($\delta_{60\,\mathrm{AU}}$).

The vertical distribution is defined by a scale-height angle $h_{60\,\mathrm{AU}}$ at 60 AU, such that the scale-height angle follows $h(r) = h_{60\,\mathrm{AU}} \cdot (r/60\,\mathrm{AU})^{\psi}$. We use the same dust opacities as Andrews et al. (2011) consisting of a small (0.005 – 1 μm) and large (0.005 μm - 1 mm) population of dust with a (mass) fraction f in large grains and the scale-height of the large grains reduced by a factor χ. We fix f and χ to the values adopted by Andrews et al. (2011) for other transition disks. A considerably lower value of f is unlikely given the evidence found for grain-growth towards IRS 48 (van der Marel et al. 2013). Since most of the UV opacity,

Table 5.2: *Observed continuum fluxes*

Instrument	Wavelength (μm)	Flux (Jy)	Reference
		Photometry	
NOMAD	0.43	1.60(-5)	Zacharias et al. (2005)
NOMAD	0.64	3.26(-4)	Zacharias et al. (2005)
2MASS	1.24	9.46(-2)	Cutri et al. (2003)
2MASS	1.66	3.05(-1)	Cutri et al. (2003)
2MASS	2.16	6.18(-1)	Cutri et al. (2003)
WISE	3.4	1.29	Wright et al. (2010)
IRAC	3.6	1.41	van Kempen et al. (2009)
IRAC	4.5	1.60	van Kempen et al. (2009)
WISE	4.6	2.45	Wright et al. (2010)
IRAC	5.8	4.06	van Kempen et al. (2009)
IRAC	8.0	6.00	van Kempen et al. (2009)
IRAS	12.0	7.81	Helou & Walker (1988)
WISE	12.0	6.26	Wright et al. (2010)
AKARI	18.7	21.0	Yamamura et al. (2010)
VISIR	18.7	31.8	Geers et al. (2007)
WISE	22.0	36.5	Wright et al. (2010)
IRAS	25.0	46.5	Helou & Walker (1988)
IRAS	60.0	<65.5	Helou & Walker (1988)
MIPS	70.0	17.0	van Kempen et al. (2009)
PACS	70.0	31.0	Fedele et al. (2013)
IRAS	100.0	<225.0	Helou & Walker (1988)
ALMA	450.0	9.50(-1)	van der Marel et al. (2013)
SCUBA	450.0	<1.57	Andrews & Williams (2007a)
SCUBA	850.0	1.80(-1)	Andrews & Williams (2007a)
SMA	880.0	1.60(-1)	Andrews & Williams (2007a)
SMA	1300.0	6.00(-2)	Andrews & Williams (2007a)
		Spectroscopy	
IRS	5.9 – 36.89		McClure et al. (2010)
PACS	60.0 – 73.3 (B1)		Fedele et al. (2013)
	69.8 – 95.0 (B1)		Fedele et al. (2013)
	105.0 – 146.6 (R1)		Fedele et al. (2013)
	139.6 – 180.9 (R2)		Fedele et al. (2013)

Notes. a(b) means $a \times 10^b$

which controls the gas temperature, is due to the small grain population, the scale height factor χ of the larger grains does not affect the line emission much.

In order to constrain the dust structure of IRS 48, we have explored the dependence of the model SED on various parameters (e.g. surface density profile, scale-height function). Here, we disregard wavelengths affected by PAH emission (5-12 μm) and do not attempt to fit the PAH abundance. For the combined physical-chemical model we adopt a PAH abundance of ~10 % of the ISM abundance (5 % PAH-to-dust mass ratio, Draine & Li 2007) derived by comparing the feature-to-continuum ratio provided by Figure 7 in Geers et al. (2006) to the observed strength of the features.

Exploring the model parameters, we find that reproducing the near infrared excess requires an optically thick dusty inner disk. The amount of excess is determined by the surface of optically thick hot dust at the inner edge of this inner disk. This optically thick layer however

Table 5.3: *Parameters of the representative model. The parameters are explained in Section 5.4.1 and shown in Figure 5.6.*

Parameter		
Surface density profile[1]	γ	1.0
	$\Sigma_{60\,\mathrm{AU,gas}}$	3.2×10^{-2} g cm^{-2}
	$\Sigma_{60\,\mathrm{AU,dust}}$	4.0×10^{-3} g cm^{-2}
Radial sizes	Inner warm dust	0.4 – 1 AU
	Gas depleted hole	0.4 – 20 AU
	Dust free cavity	1 – 60 AU
	Outer disk	60 – 160 AU
Scaling of $\Sigma(R)$	Dust, 0.4-1 AU	$\delta_{\mathrm{dust}} = 9\times10^{-4}$
	Gas, 0.4-20 AU	$\delta_{20\,\mathrm{AU}} < 9\times10^{-3}$
	Gas, 20-60 AU	$\delta_{60\,\mathrm{AU}} = 8\times10^{-2}$
Vertical structure	$h_{60\,\mathrm{AU}}$	0.14 radians
	ψ	0.22
Dust settling	f	0.85
	χ	0.2

Notes. [(1)] See Eq. 5.1.

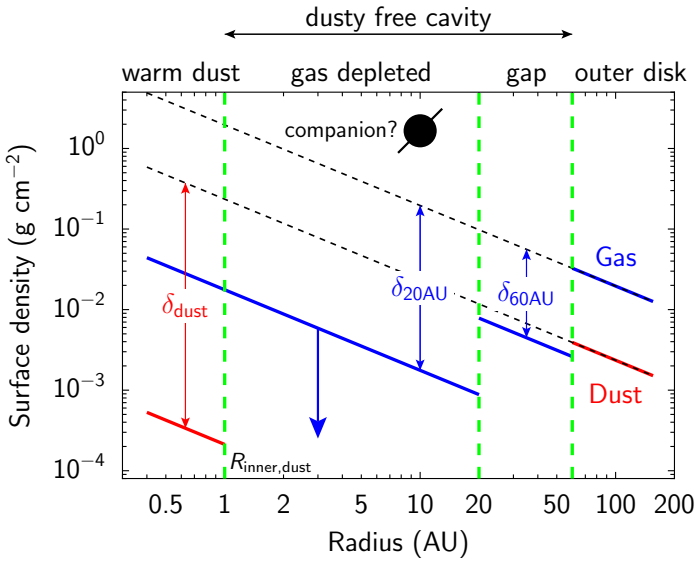


Figure 5.6: *Surface density profile of the representative model. Gas and dust surface density are given in blue and red lines, respectively. The black dashed lines show the gas/dust surface density if there were no cavities (Eq. 5.1). Green dashed lines indicate the outer radii of the inner warm disk, the gas depleted hole, and the dust free cavity (Table 5.3) In the gas depleted hole, only upper limits on the gas surface density profile can be derived from the observations.*

shields the wall of the outer disk at 60 AU and decreases the mid-infrared emission. In order to simultaneously fit the near- and mid-infrared emission, the scale-height of the outer disk needs to be high enough (scale-height angle $h_{60\,\mathrm{AU}} = 0.14$ radians) to intercept direct stellar irradiation. The disk mass is mostly constrained through the optically thin submillimeter emission. Assuming that the submillimeter emitting dust was originally spread out over the

entire disk, the resulting total dust mass is 1.6×10^{-5} $M_\odot$ ($\kappa_{450\,\mu m} = 7.1$ cm^2 g^{-1}). The inner disk mass is with a dust mass of 8×10^{-11} $M_\odot$ much less massive. The dust mass of the inner disk is not well determined because the near infrared emission traces the optically thick inner wall of the inner disk. The 18.7 μm emission of the inner disk is not optically thick and a larger inner disk with a radius of 10 AU and a mass of 1×10^{-9} $M_\odot$ would overproduce the 18.7 μm emission at the stellar position. The submillimeter emission, mapped by ALMA, is not axisymmetric. However, since the dust temperature in the mid-plane remains >50 K out to radii of ~120 AU and the submillimeter emission is optically thin, the submillimeter opacities are not important in determining the dust temperature. Thus, our axisymmetric approach does not alter the derived dust mass much.

Figure 5.7 compares the VLT-VISIR 18.7 μm observations to model images. The observations show a ring-like feature with a depletion at the stellar position and gradients both in east-west and north-south direction. The gradient in north-south direction is also seen in the models and is the result of the disk's scale-height in combination with the inclination. The dust emission at 18.7 μm in the outer disk is optically thick and traces the surface of the disk. Thus, while both near- and far-side of the northern part of the ring is visible to us, only the near-side is visible to us in the south (Dullemond & Monnier 2010) resulting in a north-south asymmetry. Since the inner dusty disk at radii <10 AU is warm enough to emit at 18.7 μm, some constraints on the size of this inner dusty disk can be obtained from the image. If the inner disk has an size of 3 or 10 AU, the emission at the position of the star is too strong. Hence we choose $R_{\rm inner,dust} = 1$ AU. Varying the radius of the inner disk has only a small effect on the SED (Figure 5.5), since the total emission at this wavelength is dominated by the ring at ~60 AU. The reason for the east-west asymmetry is unclear, but could be due to azimuthal changes of the scale-height at the inner disk (Espaillat et al. 2011; Flaherty et al. 2012).

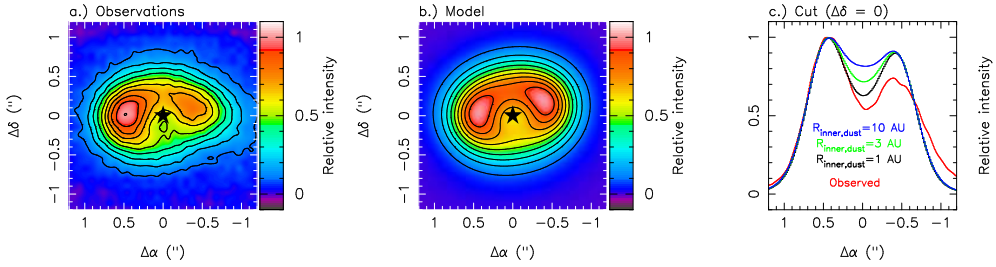


Figure 5.7: Left/center panel: *Observed and modeled VLT-VISIR 18.7 μm image. Contour lines show 10, 20, ... % of the peak emission.* **Right panel:** *Cut through the observed and modeled images ($\Delta\delta = 0$). Red line: observed intensity. Black, green, and blue lines: modeled intensities for different outer radii of the warm dust inner disk ($R_{\rm inner,dust} = 1, 3$ or 10 AU).*

5.4.2 Physical-chemical modeling

Based on the dust structure derived in the previous section, we run the physical-chemical models for different gas surface density profiles. In the following sections we refer to the representative model as that with the gas surface density following the values given in Figure 5.6 and Table 5.3.

Figure 5.8 shows the gas density, CO fractional abundance, gas-temperature ($T_{\rm gas}$) and dust-temperature ($T_{\rm dust}$) of the representative model. In this section we focus on the main fea-

tures of the IRS 48 model, general trends of transition disk models are discussed in Bruderer (2013).

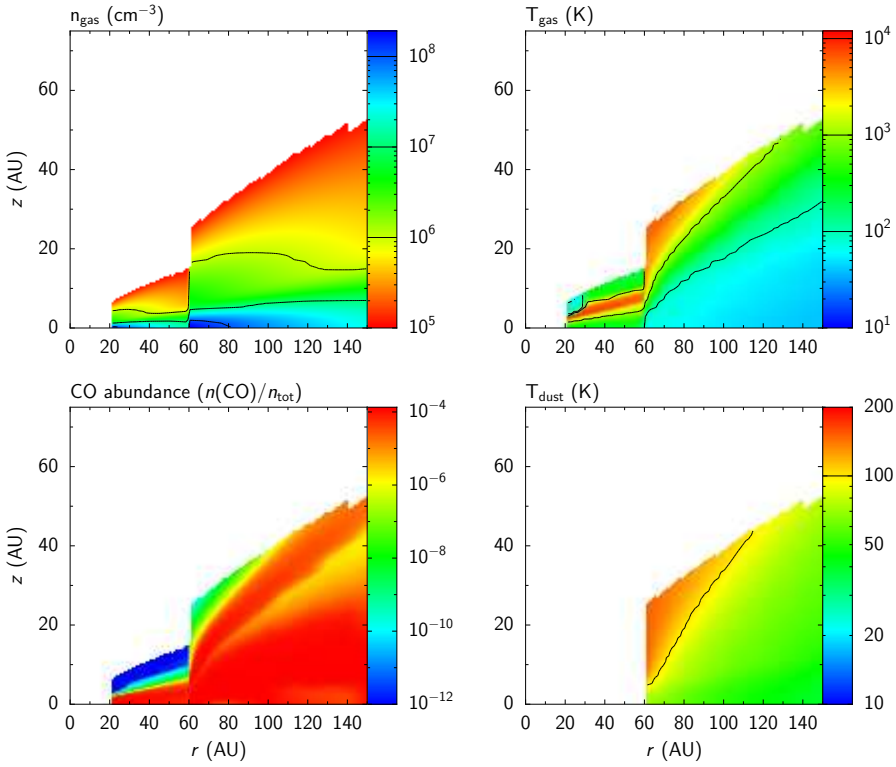


Figure 5.8: *Density structure, gas- and dust-temperature, and CO fractional abundance of the representative model (Table 5.3). Only regions with gas density larger than 10^5 cm^{-3} are shown. The dust temperature is not defined in the dust free cavity. The z-axis is stretched by a factor of two compared to the r-axis.*

Inside the dust cavity at radii <60 AU, the gas density in the mid-plane reaches 2×10^8 cm^{-3}. This is far higher than the critical density of CO 6 – 5 of $\sim 10^5$ cm^{-3} and the observed molecular emission of CO $J = 6-5$ is close to local thermal equilibrium (LTE). Temperatures in the dust cavity are several 1000 K in the upper atmosphere but still above 100 K in the mid-plane and thus high enough to excite CO 6 – 5 with an upper level energy of 115 K. CO is photodissociated in the the upper atmosphere by the intense FUV radiation of the star. Below a narrow C^+/CO transition, carbon is fully bound in CO closer to the mid-plane.

In the outer disk, the gas- and dust temperature close to the mid-plane are well coupled and of order 50 K. At larger heights, the gas temperature decouples from the dust temperature and can reach temperatures of several 1000 K (Bruderer et al. 2012). This hot layer leads to a "warm finger" of CO, where CO formation is initiated by the reaction of C^+ with vibrationally excited H_2 (e.g. Jonkheid et al. 2007).

5.4.3 Comparison to observations

To compare model results with observations and to determine the drop in gas surface density at 20 AU ($\delta_{20\,\mathrm{AU}}$) and at 60 AU ($\delta_{60\,\mathrm{AU}}$), Figure 5.10 shows the ^{12}CO $J = 6-5$ integrated

intensity cuts along the major axis of the disk for various trial gas distributions. The major parameters that are varied are $\Sigma_{60\,\mathrm{AU,gas}}$, $\delta_{60\,\mathrm{AU}}$ and $\delta_{20\,\mathrm{AU}}$. The integrated intensity cut is chosen along the major axis, because this direction is least affected by foreground absorption (Section 5.3.4). In addition to the integrated intensity cut, the total spectrum is presented. The synthetic spectral image cubes from the models are convolved to the ALMA beam. To verify this approach, the result of the representative model convolved to the ALMA beam is compared to the result of simulated ALMA observations. The ALMA observations have been simulated using the CASA software by converting the model image to u, v-data according to the observed u, v-coverage and then reduced in the same way as the observations. Due to the good u, v-coverage of our observations, the two approaches do not differ measurably in the intensity cut and the total spectrum at velocities ≥ 4 km s^{-1} from the source velocity, which is the focus of this work.

The line center opacity of ^{12}CO is of order 20 in the center of the dust free cavity (40 AU) and of order 100 in the outer disk at 60 AU for the representative model (Table 5.3). It is thus clear that the current observations cannot directly constrain the surface density profile (Bruderer 2013). However, due to temperature changes in the vertical structure and the fact that parts of the lines remain optically thin due to the Keplerian rotation, optically thick lines still show some dependence on the gas surface density profile and in particular on changes like drops inside the dust free cavity. The absolute scaling of the derived surface density profile can be checked with the optically thin emission of C^{17}O. We do not expect that derived surface density profiles are more accurate than a factor of a few. To test our proposed surface density profile with future observations, we will discuss the derived emission of the optically thin isotopologues in Section 5.4.5.

The disk exhibits asymmetries at radii larger than 60 AU (Section 5.3). Most of the emission from these regions of the disk emerge at low velocities in the spectrum (<4 km s^{-1} relative to v_{source}). We ignore these asymmetries here and focus the model-observation comparison to the inner part of the disk and higher velocities.

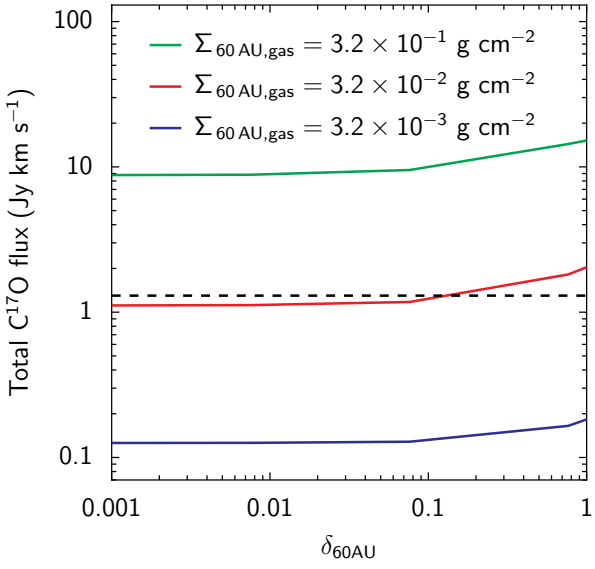


Figure 5.9: *Total flux of C^{17}O for models with $\Sigma_{60\,\mathrm{AU,gas}} = 3.2 \times 10^{-1}, 3.2 \times 10^{-2}$ and 3.2×10^{-3} g cm^{-2} as a function of the gas surface density at 20-60 AU ($\delta_{60\,\mathrm{AU}}$). The dashed vertical line shows the observed total flux. The red line indicates the representative model.*

The outer disk ($\Sigma_{60\mathrm{AU,gas}}$)

Figure 5.10a shows the ^{12}CO integrated intensity cut and total spectrum of the representative model (Figure 5.6 and Table 5.3) and two models with a factor of 10 increased or decreased gas surface density profile in the outer disk (varied $\Sigma_{60\mathrm{AU,gas}}$). The gas mass is likely dominated by the outer disk, and the outer disk surface density profile thus constrains the total gas mass. The representative model with $\Sigma_{60\mathrm{AU,gas}} = 3.2 \times 10^{-2}$ g cm^{-2} (red lines in Figure 5.10) yields an integrated intensity along the major axis between the observed east/west integrated intensity. The total spectrum derived from this model also agrees relatively well to the observed spectrum at high velocities ($\geq$4 km s^{-1} from the source velocity), corresponding to the inner disk. Slower velocity channels, mostly corresponding to the outer disk, show some deviations. The model emission is too strong at 0.5 – 2 km s^{-1}, possibly due to an additional foreground layer and at 5 – 8 km s^{-1} due to azimuthal variations of the outer disk (Section 5.3).

Models with a factor of 10 higher column density overproduce both the integrated intensity cut and the total spectrum by more than a factor of two. The model with a factor of 10 lower column density on the other hand, underproduces the integrated intensity at offsets between 0.5" and 0.8" (60-100 AU). While the total spectrum of this model better reproduces the wings at around 0.5 and 8.5 km s^{-1}, it underproduces the line center.

The C^{17}O total flux yields another, independent constraint on the total mass of the disk and thus the surface density profile of the outer disk. Figure 5.9 compares the modeled C^{17}O total flux of the three models discussed before with the observed 1.3 Jy km s^{-1}. We show the C^{17}O flux for three values of $\Sigma_{60\,\mathrm{AU,gas}}$, varying the amount of gas inside 60 AU ($\delta_{60\,\mathrm{AU}}$). The total gas mass is dominated by the gas mass outside 60 AU for $\delta_{60\,\mathrm{AU}} \lesssim 0.1$ and rises by only ~50 % for $\delta_{60\,\mathrm{AU}} = 0.1 - 1$. It is seen that the representative model reproduces the observed flux to within ~20 %, while the models with increased/reduced surface density over/underproduce the emission. As C^{17}O remains optically thin and thus directly traces the gas mass, its emission scales with the gas mass.

We conclude that the representative model reproduces relatively well the ^{12}CO integrated intensity cut and total spectrum together with the optically thin C^{17}O emission. Some deviations in the ^{12}CO total spectrum are due to azimuthal asymmetries of the disk, not included in our model. The gas mass[2] of the representative model is 1.4×10^{-4} M$_\odot$. This gas mass is low, only ~15 % of the mass of Jupiter. Combined with the dust mass of 1.6×10^{-5} M$_\odot$ (Section 5.4.1), this gives a gas-to-dust mass ratio of about 10. Both gas and dust mass have an uncertainty at a level of a factor of a few.

Inside the gap ($\delta_{60\,\mathrm{AU}}$)

Figure 5.10b shows the model-observation comparison for models with the surface density profile between 20 and 60 AU varied ($\delta_{60\,\mathrm{AU}}$ changed). The representative model is compared to a model with a factor of 10 more/less gas in this region. While the representative model reproduces the integrated intensity cut at offsets <0.5″ well, the models with a factor of 10 higher/lower surface density at 20 – 60 AU over/underproduce the integrated intensity. The integrated intensity cut depends on the surface density inside 60 AU out to a radius of ~90 AU (0.75"), due to the width of the beam. The total spectrum of the model with a factor of 10 higher surface density is too broad in the wings and the spectrum with a factor of 10 lower surface density is too narrow.

[2]This gas mass is much lower than that derived by van der Marel et al. (2013). In that work, we have mistakenly multiplied the number of H_2 molecules derived from the C^{17}O observations with the mass of C^{17}O instead of the H_2 mass.

We conclude that a drop in surface density at 60 AU by about a factor of ∼12 is required to fit the integrated intensity profile and reproduce the line width of the total spectrum.

The inner 20 AU ($\delta_{20\,\mathrm{AU}}$)

The innermost 20 AU have been suggested by van der Marel et al. (2013) to be gas depleted, based on the drop in integrated intensity and the ^{12}CO line wings. They speculated that this drop is related to the presence of an undetected planet or substellar companion. Since the size of this hole is comparable to the beam size (Figures 5.1, 5.2, and 5.4) and a beam centered on the star will receive some of the much stronger emission from outside 20 AU, the current data can only set limits on the gas mass inside 20 AU.

Figure 5.10c shows the representative model with different drops of the gas surface density profile inside 20 AU (varied $\delta_{20\,\mathrm{AU}}$). In absence of any drop of the gas surface density profile at 20 AU, the dip in integrated intensity at the stellar position is not seen. For this amount of gas, the region outside 20 AU is slightly shielded from stellar radiation and the integrated intensity out to an offset of 0.5" decreases. Only models with a drop of surface density $\delta_{20\,\mathrm{AU}} < 2 \times 10^{-2}$ (factor of >50) yield a dip in integrated intensity at the stellar position. A model with a drop $\delta_{20\,\mathrm{AU}} < 9 \times 10^{-3}$ (factor of >110) reproduces the observed dip at the center position. This model and a model with a two orders of magnitude larger drop show very similar integrated intensity cuts and total spectra. Thus, no additional constraints on the gas inside 20 AU can be drawn from the total spectrum.

We conclude that the current data allows us to constrain a drop of a factor of $\gtrsim$110 in gas surface density profile at 20 AU. This corresponds to a factor of $\gtrsim$10 drop in surface density profile at 20 AU compared to the surface density at 20 to 60 AU. Better constraints will require higher angular resolution observations.

5.4.4 How well is the 20 AU radius determined?

How well can the inner radius of the gas disk at 20 AU be determined? To answer this question, we run models with an inner radius of 15, 20, or 25 AU. Models with the surface density profile of the representative and with the surface density profile adjusted such that the emission at the stellar position is approximately reproduced are calculated. The model-observation comparison of these models is shown in Figure 5.11 in the same way as Figure 5.10.

We find that models with an inner cavity of 15 or 25 AU instead of 20 AU are unable to reproduce the observed integrated intensity cuts. Models with the gas surface density profile from the representative model fail to reproduce the integrated intensity at the stellar position, while models with a surface density profile adjusted for the emission at the stellar position over or underproduce the emission at offsets of 0.2" - 0.5". We conclude that the drop of the surface density at 20 AU is constrained to better than ∼5 AU.

5.4.5 Prediction for the CO isotopologue lines

Figure 5.12 presents the integrated intensity cuts of the CO isotopologues ^{12}CO, ^{13}CO, C^{18}O and C^{17}O $J = 3-2$ and $J = 6-5$ transitions convolved to a beam size (FWHM) of $0.25'', 0.1''$ and $0.05''$ for the representative model. The beam sizes have been chosen to represent the current observations, and ALMA in future Cycles. The detection limit of the full ALMA combining all 50 12 m antennas for a 5σ detection with 1 hour on-source observation is 46 mJy km s^{-1} ($J = 6-5$) and 7.7 mJy km s^{-1} ($J = 3-2$). For 18-21 antennas (current

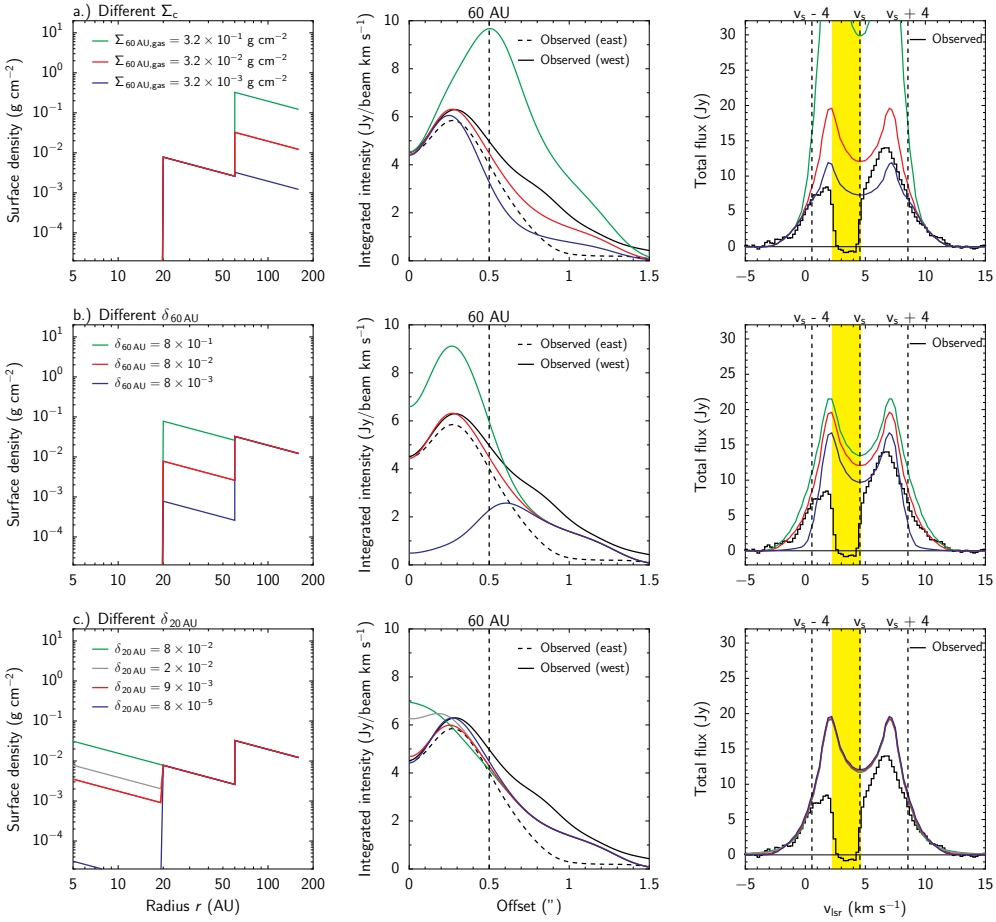


Figure 5.10: *Comparison of modeled and observed ^{12}CO $J = 6-5$ intensity profiles and spectra.* **Left panel:** *Adopted surface density profiles with variations of the representative model. The red line is the representative model.* **Center panel:** *Intensity profile extracted along the major axis of the disk. The dashed vertical line indicates the radius of the dust free cavity.* **Right panel:** *Total spectrum. The yellow region indicates regions affected by the foreground. Vertical dashed lines show the source velocity $v_s = 4.55$ km s^{-1} and velocities $v_s \pm 4$ km s^{-1} representing velocity ranges corresponding to the inner disk (radii $\lesssim 60$ AU)* **a)** *Different surface density profiles in the outer disk (>60 AU).* **b)** *Different surface density profiles inside the dust gap (20 – 60 AU).* **c)** *Different surface density profiles inside 20 AU.*

observations), the detection limit is a factor of 2.5 higher. The limits have been calculated with the ALMA sensitivity calculator[3], using a channel width of 0.2 km s^{-1}, and an intrinsic line width of 1 km s^{-1}. For $J = 6-5$, we have assumed good weather conditions (average precipitable water vapor levels PWV<0.47 mm) and for $J = 3-2$ average weather conditions (PWV<0.91 mm).

The Figure shows that for beam sizes of 0.25″, ^{13}CO and C^{18}O can be easily detected even in this low-mass disk. At the high frequency of the $J = 6-5$ transitions, C^{17}O is only strong enough for detection when integrated over a larger region as done in Section 5.3.3. For lower

[3]https://almascience.nrao.edu/proposing/sensitivity-calculator

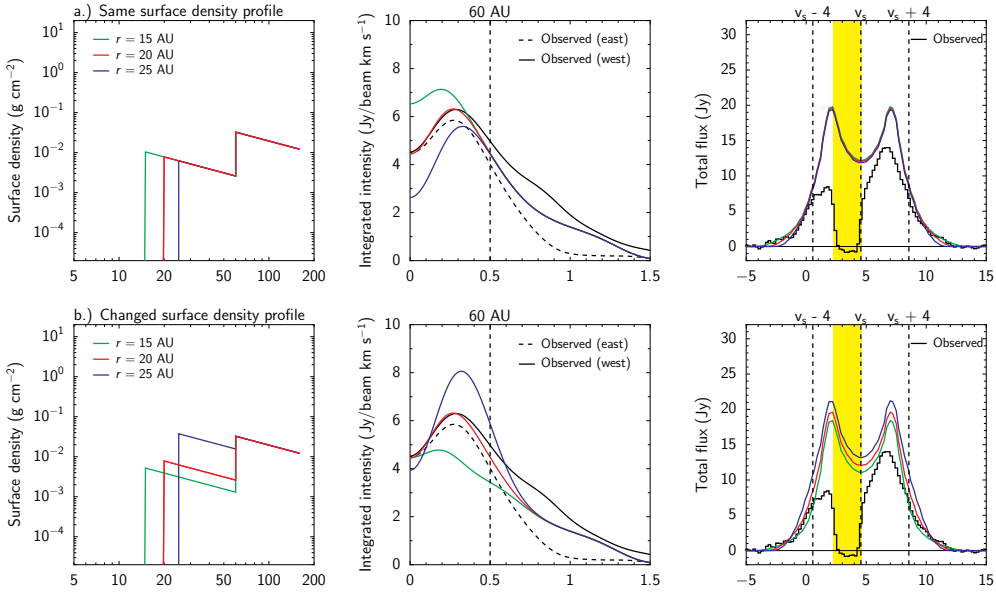


Figure 5.11: *Comparison of modeled and observed ^{12}CO $J = 6-5$ intensity profiles and spectra, showing the effect of changing the inner radius of the gas disk at around 20 AU.* **Left panels:** *Adopted surface density profiles with variations of the representative model. The red line is the representative model.* **Center panel:** *Intensity profile extracted along the major axis of the disk. The dashed vertical line indicates the radius of the dust free cavity.* **Right panel:** *Total spectrum. The yellow region indicates regions affected by the foreground. Vertical dashed lines show the source velocity $v_s = 4.55$ km s^{-1} and velocities $v_s \pm 4$ km s^{-1} representing velocity ranges corresponding to the inner disk (radii $\lesssim 60$ AU).* **a)** *Using the gas surface density profile of the representative model.* **b)** *By varying the surface density such that the emission at the stellar position is approximately reproduced.*

frequency ($J = 3-2$), the $C^{17}O$ is predicted to be detectable, although only at a 5 σ level. For smaller beam sizes than 0.25″, the detection of the isotopologues is challenging, both for $J = 3-2$ and $J = 6-5$. The steep drop in integrated intensity at the stellar position for smaller beams shows that high angular resolution is indeed crucial to provide better constraints on the amount of gas inside 20 AU (Section 5.4.3). In more typical disks with a higher gas mass, the rare isotopologues can be readily detected by ALMA (Bruderer 2013).

5.5 Discussion

5.5.1 The gas mass and surface density profile

The low total gas mass of IRS 48 with $\sim 1.4 \times 10^{-4}$ $M_\odot$ compared to the dust mass of $\sim 1.6 \times 10^{-5}$ $M_\odot$ yields a gas-to-dust ratio of only ~ 10. Since the dust temperature in this disk around an A-type star is too warm for CO freeze-out (Figure 5.8) it is not possible that additional gas is missed due to CO being frozen out. In comparison to HD 142527, another disk around a young Herbig star showing a strongly lopsided continuum emission (Casassus et al. 2013; Fukagawa et al. 2013), the dust mass of IRS 48 is a factor of 2.7 lower, but this disk also shows indications of a gas-to-dust ratio lower than the ISM value of 100 (Fukagawa et al. 2013).

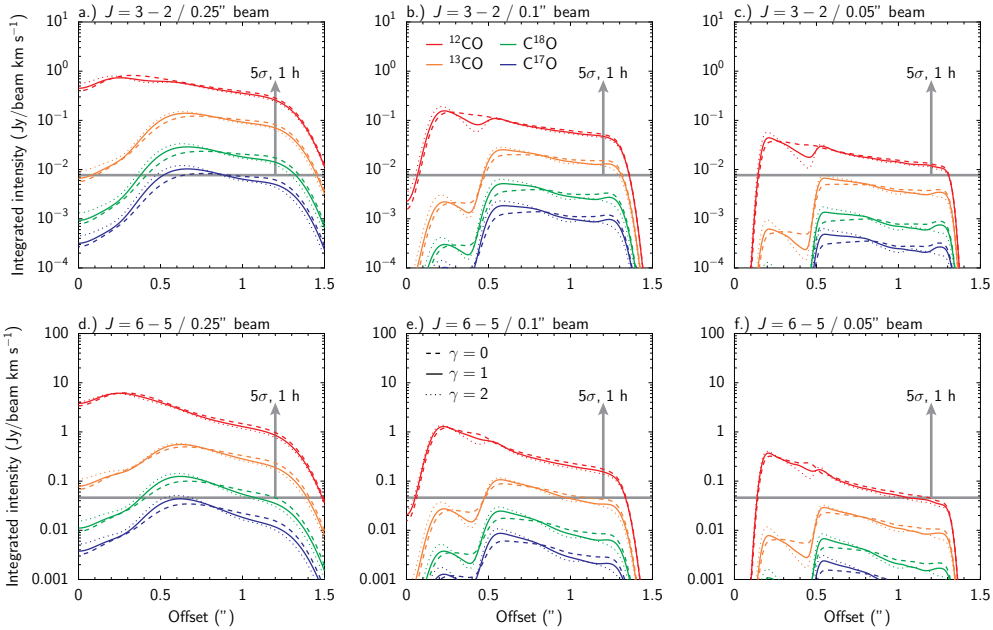


Figure 5.12: *Beam convolved integrated emission of the CO isotopologues for the $J = 3 - 2$ and $J = 6 - 5$ transition shown along the cut through the major axis of the disk. The cuts are given for beam sizes of 0.25", 0.1" and 0.05". The 5σ detection limit within 1 h of the full ALMA using 50 12 m antennas is indicated by the grey horizontal line. Models with a surface density profile slope of $\gamma = 0$ (dashed line), $\gamma = 1$ (solid line), and $\gamma = 2$ (dotted line) are shown.*

What does the low gas-to-dust ratio[4] observed towards IRS 48 imply? Since van der Marel et al. (2013) found evidence for grain growth, a gas-to-dust ratio larger than 100 would be expected if some of the dust has grown beyond the size of a few millimeters. Such larger grains are not traced by the dust continuum observations. The low gas mass derived in this work thus suggests that some of the gas is removed from the disk.

One possible mechanism for gas removal is a wind, as driven by photoevaporation. Photoevaporation has a short processing time-scale and would quickly remove all gas inside the dust cavity (e.g. Clarke et al. 2001). In IRS 48, however, we find a decrease in the gas surface density at 60 AU of only a factor of ∼10, thus making photoevaporation as the only mechanism forming the 60 AU cavity very unlikely, given the short processing time-scale. The drop at 20 AU may not be constrained by our observations and could be deep. However, at least X-ray driven photoevaporation models (Owen et al. 2011; Rosotti et al. 2013) fail to explain hole sizes of 20 AU for an accretion rate of 4×10^{-9} $M_\odot$ yr^{-1} measured towards IRS 48 (Salyk et al. 2013). This accretion rate is also higher than typical EUV photoevaporation rates (Alexander et al. 2006a,b) ruling out EUV driven evaporation. We thus conclude that in IRS 48 photoevaporation is unlikely the reason for the gap formation at 20 and 60 AU.

Another mechanism leading to a lower gas-to-dust ratio is, that gas is bound into one or several giant planets or companions in the dust depleted region inside 60 AU. The dust trap found towards IRS 48, preventing the dust to drift inwards, could filter the gas from the dust

[4]To calculate the gas-to-dust ratio only the observable dust grains with size below a few millimeters are accounted for.

(Zhu et al. 2012). Assuming an initial gas-to-dust ratio of 100, the amount of gas that has been removed corresponds to ~1.5 $M_{Jupiter}$, which can easily be bound into one companion or giant planet. The companion or giant planet is however not limited to this mass if the initial gas-to-dust mass ratio was 100, because some of the dust could currently be bound in grains too large to be observed by continuum emission. It is interesting to note that our proposed surface density profile combined with the calculated temperature structure leads to a positive pressure gradient ($dp/dr > 0$) at 60 AU as required to trap the dust radially. This positive pressure gradient is found independent of the assumed surface density slope γ.

5.5.2 The gas surface density at the dust trap

The current observational data do not allow us to directly determine the surface density at the position of the dust trap (van der Marel et al. 2013), since the ^{12}CO emission is optically thick and the C^{17}O emission too weak for mapping. The difference of the ^{12}CO integrated intensity at the dust trap compared to the same position in the north by a factor of ~3 is quite large (Section 5.3.1). One option to explain this would be a gas temperature difference.

The comparison of a model with gas temperature fixed to the dust temperature to that with calculated gas temperature shows that the ^{12}CO $J = 6-5$ emission in the outer disk (>60 AU) emerges from a layer where gas and dust temperature are coupled ($T_{gas} = T_{dust}$). Thus, in order to decrease the ^{12}CO emission at the dust trap by a factor of 3, the dust temperature needs to be lower by a factor of 3, which in turn implies a factor of about $3^4 = 81$ less (continuum) radiation should be intercept by the dust, possibly due to shielding by an asymmetric inner disk. The UV pumped CO rovibrational lines observed by Brown et al. (2012a) show indeed a strong north/south gradient in intensity, but the VLT-VISIR image by Geers et al. (2007) (Figure 5.7) indicates that stellar light is received by the south part of the disk. It is thus unclear how a factor of 3 lower dust temperature in the south can be explained. Since the interpretation of the dust trap requires an overdensity of a factor of 2 – 3 at the position of the continuum emission, the temperature decrease should actually be even larger. The time-scale to smooth-out dust asymmetries is of the order of Myrs (Birnstiel et al. 2013), and it could also be that the gas asymmetry which created the dust trap has already disappeared. We conclude that unless the layer where gas and dust temperatures decouple is substantially larger than determined by our models, a temperature difference of a factor of 3 is difficult to explain. Other scenarios for the observed asymmetry based on future observations of optically thin line emission need to be explored. Multiple transition observations in order to determine the gas temperature directly will facilitate this exploration.

5.5.3 Consequences of the gas mass for a companion

Assuming that the 20 AU cavity is carved out by a companion or a giant planet, can we derive constraints on the mass of the companion from the proposed gas surface density profile? For a detailed analysis, hydrodynamical models need to be run in which the depth of the gap in the model is compared to that observed, which is beyond the scope of the study. We only note here that a one Jupiter mass planet is already able to carve out a gap with a depth of a factor of 10 to 1000, depending on the viscosity parameter (Pinilla et al. 2012a). For higher masses, the gravitational torque is more important than the viscous torque and the depth of the gap carved out by a 9 $M_{Jupiter}$ mass is about a factor of 1000, independent of viscosity. Relating the drop in surface density to the planet mass thus requires additional constraints on the viscosity, which are observationally difficult to obtain. In order not to stir up the gas too much and allow dust to be azimuthally trapped, van der Marel et al. (2013) propose a low

viscosity parameter $\alpha_t = 10^{-4}$. With such a low α_t, already a giant planet with 1 Jupiter mass could carve out the upper limit on the gap depth at 20 AU in IRS 48.

Hydrodynamical models of planets embedded in disks predict a gap opening as far out as ~2 times the orbital radius of the planet (e.g. Pinilla et al. 2012a). A companion situated at 20 AU is thus unlikely to create the observed drop in surface density of a factor >10 at 60 AU. Possibly, IRS 48 harbors a multiple system as proposed for other transitional disks (Dodson-Robinson & Salyk 2011, Zhu et al. 2011) with a more massive planet inside 20 AU and one or several less massive planets between 20 and 60 AU. More generally, the drops in the gas density structure such as derived here are potentially the best indicators of just formed planets that are too faint to detect directly.

5.6 Conclusions

In this work, we have analyzed high-resolution ALMA submillimeter observations of ^{12}CO and C^{17}O $J = 6-5$ rotational emission from a transition disk using a chemical-physical model. With the model we can set constraints on the surface density profile and the total gas mass of the disk. We can furthermore set constraints on the gas inside a 20 AU cavity and in the 20-60 AU gap, which are thought to be carved out by a companion or one or more giant planets. The main conclusions of our work are:

- The IRS 48 disk has a much lower gas mass than previously derived (~1.4×10^{-4} $M_\odot$). Together with the dust mass of ~1.6×10^{-5} $M_\odot$, the gas mass leads to a gas-to-dust ratio of only 10. Given the uncertainties in determining the gas and dust mass of both a factor of a few, this gas-to-dust ratio is however only marginally below the ISM value of 100. The low gas-to-dust ratio is possibly related to gas filtered from dust at the position of the dust trap, combined with gas inside the dust trap bound into a companion or giant planet.

- Inside a radius of 60 AU, where small dust is thought to be absent, we find that a decrease of the gas surface density profile of a factor of ~12 is required to reproduce observations. Inside a radius of 20 AU, where no CO rotational emission is detected, a drop of at least an additional factor of $\gtrsim$10 is derived, in total a drop of a factor of $\gtrsim$110. To set more stringent constraints, higher resolution observations are required. Observations with beam size of order $0.1''$ are predicted to be sufficient to constrain the drop considerably better. The drops at 20 AU and 60 AU are derived assuming a slope $\gamma = 1$ of the surface density profile ($\Sigma \propto r^{-\gamma}$).

- The inner radius of gas depletion at 20 AU can be constrained to better than ±5 AU.

- Fitting the SED and the 18.7 μm dust continuum image taken by VLT-VISIR requires a small (<1 AU) dusty disk close to the star and a large scale height of the outer disk (scale-height angle $h_{60\,\mathrm{AU}} = 0.14$ radians).

- Despite of the low gas-mass of IRS 48, the full ALMA combining all 50 antennas is predicted to readily detect ^{13}CO $J = 6-5$ and C^{18}O $J = 6-5$. These optically thin isotopologue lines will help to better constrain the gas surface density profile of the disk and to study different scenarios of azimuthal asymmetries.

- The derived gas surface density profile points to the clearing of the cavity by one or several massive planets or companions rather than just photoevaporation or grain-growth.

Acknowledgements. We thank an anonymous referee, Til Birnstiel, Joanna Brown, Cornelis Dullemond, Greg Herczeg, Attila Juhàsz, Paola Pinilla, Markus Schmalzl, and Malcolm Walmsley for useful comments and discussions. S.B. acknowledges a stipend by the Max Planck Society and N.v.d.M. is supported by the Netherlands Research School for Astronomy (NOVA) Band 9 funding. T.v.K thanks Allegro, funded by NWO Physical Sciences ("the Netherlands Organization for Scientific Research (NWO), Physical Sciences"), for financial and technical support. We thank Melissa McClure for providing the Spitzer data in electronic form. This paper makes use of the following ALMA data: ADS/JAO.ALMA no. 2011.0.00635.SSB. ALMA is a partnership of the European Southern Observatory (ESO) (representing its member states), NSF (USA), and National Institutes of Natural Sciences (Japan), together with the National Research Council (Canada) and National Science Council and Academia Sinica Institute of Astronomy and Astrophysics (Taiwan), in cooperation with the Republic of Chile. The Joint ALMA Observatory is operated by the ESO, Associated Universities Inc./ National Radio Astronomy Observatory, and National Astronomical Observatory of Japan. Astrochemistry in Leiden is supported by the Netherlands Research School for Astronomy (NOVA), by a Royal Netherlands Academy of Arts and Sciences (KNAW) professor prize, and by the European Union A-ERC grant 291141 CHEMPLAN.

6

Gas density drops inside dust cavities of transitional disks

van der Marel, N.; van Dishoeck, E. F.; Bruderer, S.; Perez, L. M.; Isella, A. *Gas density drops inside dust cavities of transitional disks around young stars observed with ALMA*. 2015, A&A, 579, 106.

Abstract

Transitional disks with large dust cavities are important laboratories in which to study planet formation and disk evolution. Cold gas may still be present inside these cavities, but quantying this gas is challenging. The gas content is important for constraining the origin of the dust cavity. We use Atacama Large Millimeter/submillimeter Array (ALMA) observations of ^{12}CO 6–5 and 690 GHz (Band 9) continuum of five well-studied transitional disks. In addition, we analyze previously published Band 7 observations of a disk in the ^{12}CO 3–2 line and 345 GHz continuum. The observations are used to set constraints on the gas and dust surface density profiles, in particular, the drop $\delta_{\rm gas}$ of the gas density inside the dust cavity. The physical-chemical modeling code DALI was used to simultaneously analyze the gas and dust images. We modeled SR21, HD135344B, LkCa15, SR24S, and RXJ1615-3255 (Band 9) and J1604-2130 (Band 7). The spectral energy distribution and continuum visibility curve constrain the dust surface density. Then we used the same model to calculate the ^{12}CO emission, which we compared with the observations through spectra and intensity cuts. The amount of gas inside the cavity was quantified by varying the $\delta_{\rm gas}$ parameter. Model fits to the dust and gas indicate that gas is still present inside the dust cavity for all disks, but at a reduced level. The gas surface density drops inside the cavity by at least a factor 10, while the dust density drops by at least a factor 1000. Disk masses are comparable with previous estimates from the literature, cavity radii are found to be smaller than in the data obtained with the 345 GHz SubMillimeter Array. The derived gas surface density profiles suggest that the cavity was cleared by one or more companions in all cases, which trapped the millimeter-sized dust at the edge of the cavity.

6.1 Introduction

Planets are formed in disks of dust and gas that surround young stars (e.g., Williams & Cieza 2011). Of particular interest are the so-called transitional disks with cleared-out cavities in the inner part of the dust disk. These disks are expected to be in the middle of active evolution and possibly planet formation. Transitional disks were originally identified through a dip in the mid-infrared part of the spectral energy distribution (SED), indicating a lack of small micron-sized dust grains close to the star. They were modeled as axisymmetric dust disks with inner cavities (e.g., Strom et al. 1989; Brown et al. 2007; Espaillat et al. 2014), which was subsequently confirmed by millimeter interferometry (e.g., Dutrey et al. 2008; Brown et al. 2009; Andrews et al. 2011; Isella et al. 2012). In recent years it has become clear that the gas and dust do not necessarily follow the same radial distribution in transition disks (e.g., Pontoppidan et al. 2008). High accretion rates ($\sim 10^{-8}$ $M_\odot$ yr^{-1}, e.g., Calvet et al. 2005; Najita et al. 2007) indicate that the dust cavities are not empty, but gas is still flowing through the gap. Near-infrared observations of CO rovibrational lines indicate the presence of warm gas inside the dust cavity (Salyk et al. 2007; Pontoppidan et al. 2008; Salyk et al. 2009; Brittain et al. 2009; Brown et al. 2012a). However, these data do not trace the bulk of the molecular gas. ALMA CO pure rotational line observations directly reveal the presence of gas inside the dust cavity (van der Marel et al. 2013; Bruderer et al. 2014; Pérez et al. 2014; Casassus et al. 2013; Zhang et al. 2014). In addition, the size distribution of the dust is possibly not uniform throughout the disk: micron- and millimeter-sized grains may have different distributions (Garufi et al. 2013; van der Marel et al. 2013) and millimeter- and centimeter-sized grains can show radial variations (Pérez et al. 2012).

Quantifying the density structure of the gas inside the dust hole is essential for distinguishing between the possible clearing mechanisms of the dust in the inner part of disk: photoevaporation (Clarke et al. 2001), grain growth (Dullemond & Dominik 2005), or clearing by (sub)stellar or planetary companions (e.g., Lin & Papaloizou 1979). Instabilities at the edges of dead zones have also been suggested to explain millimeter-dust rings and asymmetries (e.g., Regály et al. 2012). Planet candidates have been found in cavities of the transition disks T Cha (Huélamo et al. 2011), LkCa 15 (Kraus & Ireland 2012), and HD 100546 (Quanz et al. 2015), indicating planet clearing as a possible scenario.

Because detecting planets in disks is challenging, an indicator of the clearing by a (planetary) companion can be inferred from the difference in the structure of the gas compared to the dust in several of the observed disks, as shown by planet-disk interaction models in combination with dust evolution models (e.g., Pinilla et al. 2012a). Companion clearing changes the gas surface density profile from that of a full disk: the density at and around the orbital radius of the planet is decreased, while at the outer edge of this gas gap the density slightly increases. As a result of the induced pressure gradients along the sides of this pressure bump, dust particles will drift toward the edge of the gap, become trapped, and grow efficiently to larger sizes. This results in a dust ring of millimeter-sized dust, or radial dust trap (Pinilla et al. 2012a). The decrease in gas density due to companion clearing depends on the mass of the companion and other parameters such as the viscosity (Zhu et al. 2011; Dodson-Robinson & Salyk 2011; Pinilla et al. 2012a; Mulders et al. 2013; Fung et al. 2014). Other effects that play a role in dynamic clearing are for example migration and planet accretion luminosity (e.g., Kley & Nelson 2012). Therefore, the amount of gas inside a cavity can help to constrain the mass of the companion in the planet disk-clearing and dust-trapping scenario if the viscosity is known. In comparison, the surface density of the millimeter-sized dust drops significantly deeper inside the cavity than the drop in gas surface density, due to the trapping of millimeter-sized dust (Pinilla et al. 2012a). Therefore, the quantification of gas *and* dust inside the cavity

indicates whether the trapping mechanism is due to a planet. Dust trapping at the edges of dead zones will also result in millimeter-sized dust rings, but in that scenario the gas surface density remains the same as for a full disk, apart from a minor density increase (lower than 50%) at the edge (Lyra et al. 2015).

The rovibrational lines used in previous work of transitional disks can indicate the presence of CO inside the dust cavity and the inner radius, but are unsuitable for quantifying the total gas density. The emission is very sensitive to the gas temperature, which is high but uncertain in the models in this regime. The dust opacity of the inner disk, which provides shielding, is likewise uncertain. The pure rotational CO lines provide better constraints on the gas surface density inside the cavity. The brightest molecular lines in the submillimeter regime are the rotational ^{12}CO lines. Before ALMA, interferometric data generally did not have the sensitivity and spatial resolution to detect rotational ^{12}CO emission inside the cavity. However, even if CO line emission is detected, this emission cannot be directly translated into densities, especially inside the dust cavity: the CO abundance is not constant throughout the disk with respect to molecular hydrogen because of the photodissociation by the UV radiation from the star and freeze-out onto dust grains in colder regions close to the midplane (van Zadelhoff et al. 2001; Aikawa et al. 2002). Furthermore, the gas temperature is decoupled from the dust temperature in the surface of the disk, particularly at the cavity wall that is directly heated and inside the dust-depleted cavity (e.g., Kamp & Dullemond 2004; Jonkheid et al. 2004; Gorti & Hollenbach 2008).

To determine the amount of gas that is present inside a dust cavity, the physical and chemical structure of the gas needs to be modeled. For this we make use of the physical-chemical modeling tool DALI (Bruderer et al. 2012; Bruderer 2013), which solves the heating-cooling balance of the gas and chemistry simultaneously to determine the gas temperature, molecular abundances, and molecular excitation for a given density structure. As a result of the disk Keplerian rotation and gas thermal and turbulent motions, the ^{12}CO emission along any line of sight that intercepts the disk is a spectral line comprising an optically thick central part and potentially optically thin wings. With spatially resolved CO observations it is possible to infer emission from different lines of sight, which was not possible with previous single-dish spectral analysis. Bruderer et al. (2014) demonstrated for ^{12}CO 6–5 lines in Oph IRS 48 that the emission in the optically thin wings can be used to constrain the gas density. In this case, the observations are found to be consistent with a physical disk model with two gas density drops inside the millimeter dust cavity. However, Oph IRS 48 has a very low disk mass (constrained by C^{17}O observations), which means that even the ^{12}CO line is close to optically thin. For more massive disks, the bulk of the ^{12}CO emission may remain optically thick even if the gas density inside the dust-depleted cavities drops by one or two orders of magnitude. In that case, the ^{12}CO emission originates from deeper in the disk (closer to the disk midplane) where the gas is colder than in the surface, causing a drop in the optically thick line intensity (Bruderer 2013).

To date, a total of nine transitional disks with large resolved millimeter dust cavities has been observed in ALMA Cycle 0 in dust continuum and ^{12}CO. In this paper, we present observations of the disks SR21, HD135344B, RXJ1615-3255, LkCa15, and SR24S through ^{12}CO 6–5 observations (Pérez et al. 2014) and J1604-2130 through ^{12}CO 3–2 observations (Carpenter et al. 2014; Zhang et al. 2014) . With DALI we determine the density structure of the gas and dust that is consistent with the SED, dust continuum interferometry, and the ^{12}CO observations. If available, information on the hot gas and dust from the literature is included. The goals of this study are to determine the amount of the gas and dust inside the dust hole and the implications for potentially embedded planets, assuming that the millimeter dust rings are indeed dust traps. The derived physical models in this study can be used as a starting

Table 6.1: *Stellar properties*

Target	SpT	L_* ($L_\odot$)	M_* ($M_\odot$)	R_* ($R_\odot$)	$T_{\rm eff}$ (K)	$\dot{M}$ ($M_\odot$ s^{-1})	d (pc)	A_V (mag)	Ref.
SR21	G3	10	1.0	3.2	5830	$< 1 \cdot 10^{-9}$	120	6.3	1,2,3
HD135344B	F4	7.8	1.6	2.2	6590	$6 \cdot 10^{-9}$	140	0.3	4,5,6
LkCa15	K3	1.2	1.0	1.7	4730	$2 \cdot 10^{-9}$	140	1.5	6,7,8
RXJ1615-3255	K5	1.3	1.1	2.0	4400	$4 \cdot 10^{-10}$	185	0.4	5,9
SR24S	K2	2.5	0.7	2.7	4170	$7 \cdot 10^{-8}$	120	7.0	5,10,11
J1604-2130	K2	0.76	1.0	1.4	4550	$1 \cdot 10^{-11}$	145	0.66	12-14

1) Dunkin et al. (1997), 2) Pontoppidan et al. (2008), 3) Grady et al. (2009), 4) Prato et al. (2003), 5) Andrews et al. (2011), 6) Espaillat et al. (2010), 7) Piétu et al. (2007), 8) Ingleby et al. (2009), 9) Wichmann et al. (1997), 10) Natta et al. (2006), 11) Luhman & Rieke (1999), 12) Dahm (2008), 13) Mathews et al. (2012), 14) (Carpenter et al. 2014).

point for future ALMA observations of CO isotopologs, whose emission is optically thin and which therefore directly trace the density structure. Our analysis of the gas density structure is similar to that used for Oph IRS 48 through ^{12}CO 6–5 and C^{17}O 6–5 line observations as presented in Bruderer et al. (2014). The analysis of HD142527, which has been observed in ^{12}CO, ^{13}CO and C^{18}O 6–5, 3–2 and 2–1, is left for future studies. Perez et al. (2015) have modeled the J=2–1 CO isotopologs and determined the gas mass remaining inside the cavity of that disk. Other transition disks that have been observed in ALMA Cycle 0 are HD 100546 (Walsh et al. 2014), TW Hya (Rosenfeld et al. 2014), Sz 91 (Canovas et al. 2015), and MWC 758 (not yet published), but since their dust holes remain unresolved in the current data, they are not considered in this study.

The paper is structured as follows. In Section 6.2.1 we describe the details of the ALMA observations. In Section 6.2.2 we present moment maps of the ^{12}CO observations and the derived stellar position and orientation. The modeling approach and constraints from the literature are presented in Section 6.3. Section 6.4 presents the modeling results. Section 6.5 discusses the implications for embedded planets in the disk.

6.2 Data

The continuum and ^{12}CO line observations were obtained during ALMA Cycle 0 between June 2012 and January 2013, with baselines ranging from 20 to 500 m, probing scales from 0.2 to 4 arcseconds. The sources and their properties are summarized in Table 6.2.

6.2.1 Observational details

Five transitional disks were observed in ALMA program 2011.0.00724.S (PI Pérez), two of these disks were presented in Pérez et al. (2014). The disks were observed in Band 9 (690 GHz, 440 μm), with four adjacent spectral windows of 1875 MHz, each with 3840 channels of 488 kHz (0.2 km s^{-1}) width, for a total continuum bandwidth of 7.5 GHz. One spectral window was centered on the ^{12}CO 6–5 line (691.47308 GHz). The bandpass was calibrated using 3C279, Titan was used as flux calibrator, and the phase and amplitude were calibrated using J1427-4206 (HD135344B), J1625-2527 (SR21, SR24S and RXJ1615-3255) and J0510+180 (LkCa15). Each target was observed for ~25 minutes on source. Given the high signal-to-noise ratio (S/N) of the continuum, amplitude and phase self-calibration were performed on all data and applied afterward to the ^{12}CO data as well.

Table 6.2: *Properties of the ALMA observations*

Target	Position[a] (J2000)	Beam Size (")	Beam PA (°)	rms_L[b,c] (mJy)	$Peak_L$[b] (mJy)	rms_C[c] (mJy)	$Peak_C$ (mJy)	PA (°)	i (°)	v_{src} (km/s)
SR21	16:27:10.27 -24:19:13.0	0.28×0.19	-85	65	1660	1	409	14	15	2.75
HD135344B	15:15:48.43 -37:09:16.4	0.26×0.19	49	114	2010	1.8	318	63	20	7.05
LkCa15	04:39:17.80 +22:21:03.2	0.30×0.23	-33	120	1202	1.8	118	60	55	6.1
RXJ1615-3255	16:15:20.23 -32:55:05.4	0.29×0.20	-74	102	960	1.7	123	153	45	4.6
SR24S	16:26:58.51 -24:45:37.1	0.40×0.20	-75	96	2196	1.9	278	20	45	4.75
J1604-2130[d]	16:04:21.65 -21:30:28.9	0.69×0.44	-78	100	1500	0.20	38	80	10	4.7

Notes. [a] Derived from the CO channel maps. [b] Measured in 0.5 km s^{-1} bins. [c] L=line, C=continuum [d] ^{12}CO 3–2 transition, the other targets are the ^{12}CO 6–5 transition.

Disk J1604-2130 was observed as part of ALMA program 2011.0.00526.S (PI Carpenter) in Band 7 (345 GHz, 880 μm), with one spectral window centered on the ^{12}CO 3–2 line (345.79599 GHz) with 488 kHz (0.42 km s^{-1}) channel width. The data and observational details are presented in Zhang et al. (2014). Because of the longer wavelength, the beam size of these data is considerably larger than that of the Band 9 data.

The data were imaged using CASA v4.2, adopting the Briggs weighting scheme with a robust parameter of 0.5. The resulting rms and beam sizes of the line data are given in Table 6.2. During the cleaning process of the SR24S data, it became clear that there is extended emission that could not be recovered by the shortest baselines of these ALMA observations (50 kλ, or 4" scales).

6.2.2 Continuum and line maps

Figure 6.1 shows the ALMA continuum image, zero-moment ^{12}CO map, and ^{12}CO spectrum of each of our targets. The spectrum was extracted from the region of the zero-moment map size. The contours indicate the 3σ detection limit in each image. The continuum images reveal ring-like structures for all targets except RXJ1615-3255, even though its SED and the 345 GHz visibility curve show signs of a dust cavity (Andrews et al. 2011). The rings clearly show azimuthal asymmetries, which have been confirmed to be real intensity asymmetries for SR21 and HD135344B (Pérez et al. 2014). For SR24S and LkCa15 the asymmetries are most likely caused by the geometry of the disk ($i \sim 45°$) and the dust continuum becoming optically thick at this wavelength (0.45 mm). The S/N on the continuum varies between ~65 and 400, which is much higher than previous SubMillimeter Array (SMA) observations.

The zero-moment ^{12}CO maps and intensity cuts (Figure 6.2 reveal gas inside the dust hole for all targets, demonstrating different distributions of gas and dust. This does not mean that there can be no decrease in the gas density compared to a full disk density profile, because the ^{12}CO emission is expected to be optically thick. The maps of HD135344B and J1604-2130 show a decrement of emission around the stellar position, directly indicating a strong decrease of gas density. The size of this gas hole is much smaller than the dust hole and similar to the beam size. For LkCa15 there appears to be a slight offset between the continuum and integrated CO emission peaks; the maps are currently aligned to the same central position. This may be related to the proposed eccentric inner disk (Thalmann et al. 2014), which casts a more

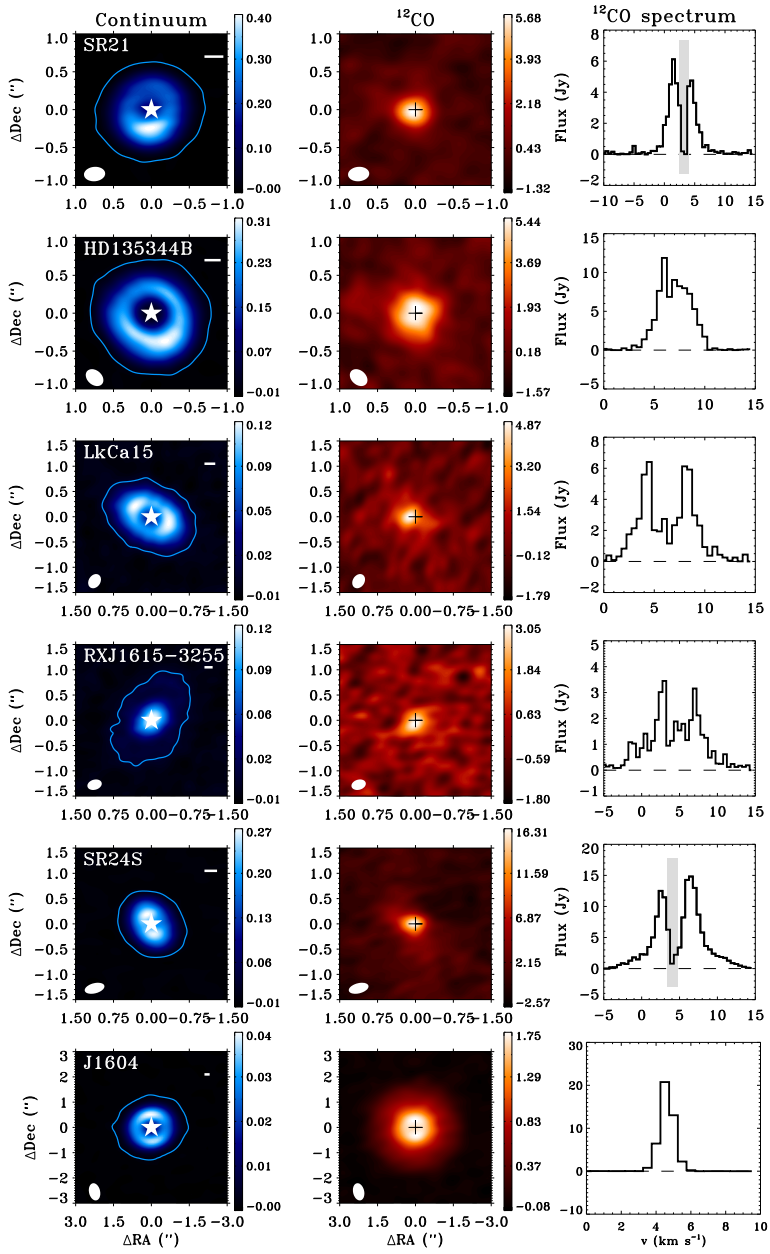


Figure 6.1: *ALMA observations of the continuum and ^{12}CO line. The first five disks show the 690 GHz (440 µm) continuum and the ^{12}CO J=6–5 line, the sixth is the 345 GHz (880 µm) continuum and ^{12}CO J=3–2 line.* **Left:** *Continuum image. The stellar position is indicated by a white star, the white bar in the upper right corner indicates the 30 AU scale, and the yellow contour gives the 3σ detection limit. The colorbar units are given in Jy beam^{-1}.* **Center:** *zero-moment ^{12}CO map. The colorbar units are given in Jy beam^{-1} km s^{-1} .* **Right:** *^{12}CO spectrum integrated over the entire disk. The dashed line indicates the zero flux level, and the gray areas indicate the parts of the spectrum affected by foreground absorption (seen in SR21 and SR24S). The beam is indicated in each map by a white ellipse in the lower left corner.*

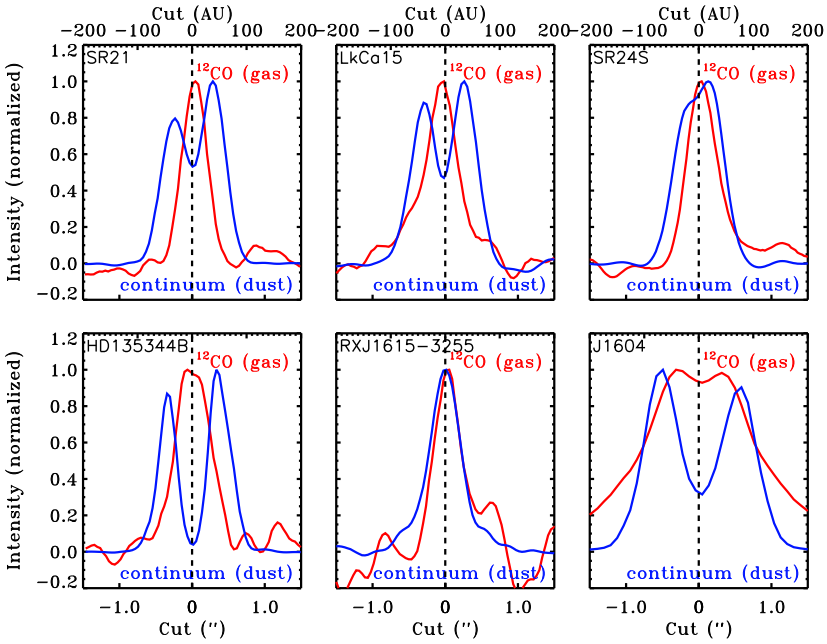


Figure 6.2: *Normalized intensity cuts through the major axis of each disk of the ^{12}CO emission (red) and the dust continuum emission (blue). The cuts clearly reveal gas being present inside the dust cavities.*

pronounced shadow on one side of the disk. However, considering the limited significance of this shift, modeling this asymmetry is beyond the scope of this paper.

All ^{12}CO spectra are consistent with a rotating disk at an inclination >15°, revealing a double-peaked velocity profile, except for J1604-2130, which is known to be viewed almost face-on (Mathews et al. 2012; Zhang et al. 2014). The spectra of SR21 and SR24S are probably affected by foreground absorption, which is commonly observed in the Ophiuchus star-forming region (e.g. van Kempen et al. 2009), although no single-dish spectra of these targets are available to confirm this. The SR21 spectrum is somewhat asymmetric: the red side is narrower than the blue side. Furthermore, the data of SR24S are affected by extended emission outside the field of view of the ALMA observations. This may be related to the suggested circumbinary disk around SR24N, which is located 5" north, and SR24S (Mayama et al. 2010), but this cannot be confirmed with the available data. The apparent double peak in the spectrum is caused by foreground absorption: the bulk of this emission does not originate from the disk. Therefore, we did not aim to model the gas surface density of this target and only modeled the dust continuum structure.

The ^{12}CO channel maps (binned to 1 km s^{-1}) and first moment maps are presented in the Appendix. We derive the stellar position, inclination, position angle, and source velocity from the channel maps and first-moment map and overlay the corresponding Keplerian velocity pattern in white contours. The derived parameters are consistent within 5° with values from the literature for resolved gas and dust, where available (e.g., Pontoppidan et al. 2008; Andrews et al. 2011). For the stellar mass, we used values from the literature (see Table 6.1). The derived parameters are given in Table 6.2. The peak S/N of the channel maps is at least

10.

Table 6.3: *Velocity range within the cavity radius*

Target	Velocity (km s^{-1})
SR21	<1.25 and >4.0
HD135344B	<5.0 and >9.0
LkCa15	<2.2 and >10
SR24S	<1.25 and >8.25
RXJ1615-3255	<-0.3 and >9.5
J1604-2130	<4.1 and >5.3

The channel maps confirm the presence of gas inside the dust cavities. The velocity range that falls within the derived dust cavity radius $r_{\rm cav}$ is given in Table 6.3. The velocity is calculated using $v_{\rm obs} = \sqrt{\frac{GM_*}{r_{\rm cav}}} \sin i$ with G the gravitational constant. The channel maps also reveal that the detected CO emission is more extended in the outer disk than the dust continuum for all sources except SR21, although the S/N and image quality are low in the outer parts of the disks. The emission is probably not affected by spatial filtering, as shown in the visibilities (Figure 6.5): the emission is well covered down to ~40kλ, corresponding to 5" (>600 AU) diameter scales. Whether or not the difference in extent is significant needs to be quantified with a physical model, because the dust emission may simply be too weak in the outer disk to be detected, while ^{12}CO remains detectable because it is optically thick. The redshifted side of both SR21 and HD135344B is somewhat weaker than the blueshifted side, as also seen in the spectrum (Figure 6.1). The location of the decrease is cospatial with the peak of the asymmetry in the continuum map. This is possibly related to a higher continuum optical depth or lower temperature at the location of the asymmetry, as was also seen for H_2CO emission of Oph IRS 48 (van der Marel et al. 2014).

6.3 Method

6.3.1 Modeling

Our aim is to constrain a physical disk model that describes both the dust and gas structure of each disk. The main goal is to determine the drop in gas surface density $\delta_{\rm gas}$ inside the dust hole, within the constraints of a model that fits the gas and dust in the outer disk (Figure 6.3). Therefore the other disk parameters need to be constrained first, as they have a significant influence on the strength of the CO emission inside the cavity: the disk mass relates to the optical depth of the ^{12}CO lines; the vertical structure affects the temperature by shadowing and the amount of exposed disk surface atmosphere by stellar light; the amount of dust inside the cavity, including the inner disk, shields the CO from photodissociation but also provides cooling; and the location of the cavity wall determines the temperature of the wall, where the bulk of the ^{12}CO emission is expected to originate. To this end, information was combined from the SED, the ALMA continuum and integrated CO visibilities, and the CO disk-integrated spectrum and zero-moment map.

Although the model is not expected to be unique, it sets a structure for the disk that can be tested with future ALMA observations of CO isotopologs. The main goal of this study is to compare the strongest possible decrease of the gas surface density with the minimum required

decrease of the dust density inside the cavity. If the drop in gas density is less deep than for the millimeter-sized dust, this is direct evidence for the trapping scenario.

The axisymmetric physical-chemical model DALI was used for the analysis (Bruderer 2013, details next section), thus any azimuthal asymmetries were ignored. The most prominent asymmetries are seen in the millimeter-sized dust continuum in SR21 and HD135344B (Pérez et al. 2014), but the influence of the millimeter dust on the gas temperature and UV shielding is negligible, therefore axisymmetry can be safely assumed. The small dust grains are the main heating agents of the gas. In the visibilities we therefore used the amplitude ($\sqrt{Real^2 + Imag^2}$), because the asymmetries and thus the variations in the imaginary part are small. The visibilities constrain the radial structure of the emission. Because of the limited u, v-coverage in these Cycle 0 data, the visibilities provide better constraints on the structure than the images alone, especially on the cavity radius through the location of the first null.

6.3.2 DALI

The determination of the gas disk from the ^{12}CO emission requires a thermo-chemical disk model, in which the heating–cooling balance of the gas and chemistry are solved simultaneously to determine the gas temperature and molecular abundances at each position in the disk. Moreover, even though the densities in disks are high, the excitation of the rotational levels may not be in local thermodynamic equilibrium (LTE), and the gas and dust temperature are decoupled, especially inside and at the cavity edge. The DALI model (Bruderer et al. 2012; Bruderer 2013) uses a combination of a stellar radiation field with a disk density distribution as input. DALI solves for the dust temperatures through continuum radiative transfer from UV to millimeter wavelengths and calculates the chemical abundances, the molecular excitation, and the thermal balance of the gas. It was developed for the analysis of gas emission structures in protoplanetary disks including transitional disks with varying gas-to-dust ratios (GDR) (Bruderer 2013).

DALI uses a reaction network described in detail in Bruderer et al. (2012) and Bruderer (2013). It is based on a subset of the UMIST 2006 gas-phase network (Woodall et al. 2007). About 110 species and 1500 reactions are included. In addition to the gas-phase reactions, some basic grain-surface reactions (freeze-out, thermal and nonthermal sublimation and hydrogenation such as g:O $\rightarrow$ g:OH $\rightarrow$ g:H_2O and H_2/CH^+ formation on PAHs (Jonkheid et al. 2006) are included. The g:X notation refers to atoms and molecules on the grain surface. The photodissociation rates are obtained from the wavelength-dependent cross-sections by van Dishoeck et al. (2006). The adopted cosmic-ray ionization rate is $\zeta_{H_2} = 5 \times 10^{-17}$ s^{-1}. X-ray ionization (X-ray luminosity of 10^{30} erg s^{-1}) and the effect of vibrationally exited H_2 are also included in the network. Elemental abundances are taken from Jonkheid et al. (2006).

6.3.3 Approach

Physical model

As a starting point for our models we adopted the physical structure suggested by Andrews et al. (2011), as implemented by Bruderer (2013) and applied for a similar analysis of Oph IRS 48 (Bruderer et al. 2014). The gas surface density was assumed to be an exponential power-law following the time-dependent viscosity disk model $\nu \sim r^\gamma$ (Lynden-Bell & Pringle 1974; Hartmann et al. 1998)

$$\Sigma(r) = \Sigma_c \left(\frac{r}{r_c}\right)^{-\gamma} \exp\left(-\left(\frac{r}{r_c}\right)^{2-\gamma}\right) \tag{6.1}$$

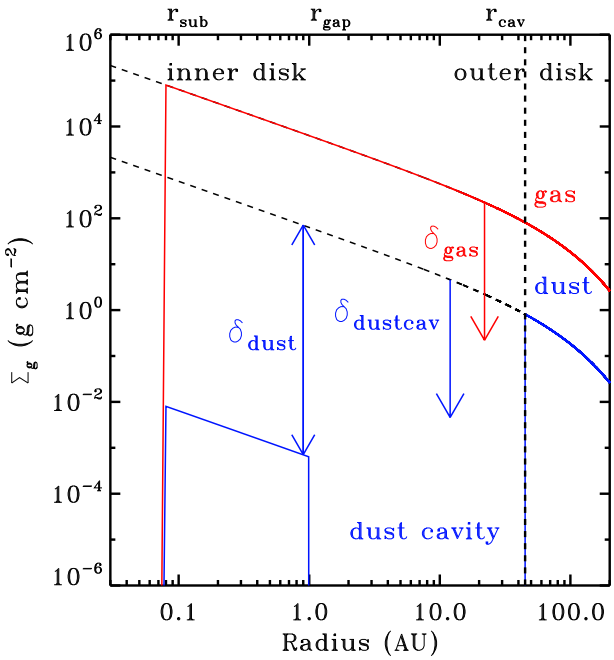


Figure 6.3: *Generic surface density profile for the gas and dust.*

and is defined by surface density Σ_c at critical radius r_c. The power-law index γ was taken as 1, in line with the results for normal disks with continuous dust distributions and other transition disk studies (Andrews et al. 2011). The previous gas study of ^{12}CO observations in IRS 48 (Bruderer et al. 2014) demonstrated that the slope of the surface density profile could not be determined with their data; the data in this new study have an even lower S/N, therefore we did not vary γ . The outer radius is set to $r_{\rm out}$. The dust density was taken to be $\Sigma(r)$/GDR, with the GDR set to 100 initially. The inner dust disk was defined by the $\Sigma(r)$ profile, starting from the sublimation radius $r_{\rm sub} = 0.07(L_*/L_\odot)^{1/2}$ (assuming $T_{\rm sub}$=1500 K) out to $r_{\rm gap}$=1 AU, scaled down by a factor $\delta_{\rm dust}$ to fit the near-infrared part of the SED. The size of the inner disk is arbitrary as it does not have a significant effect on the near infrared excess. Between $r_{\rm gap}$ and $r_{\rm cav}$, the cavity radius, the dust density was scaled down by a factor $\delta_{\rm dustcav}$ (the drop in dust density inside the cavity), while the gas density $\Sigma(r)$ was scaled down by a factor $\delta_{\rm gas}$. Figure 6.3 shows the generic density structure, and Table 6.4 explains each parameter.

For the stellar photosphere we generated a blackbody with the luminosity and temperature as in Table 6.1. Additional UV excess from accretion was added through a $T_{\rm acc}$=10 000 K blackbody for the $L_{\rm acc}$ corresponding to the measured accretion rate (Table 6.1), using

$$L_{\rm acc}(\nu) = \pi B_\nu(T_{\rm acc},\nu)\frac{GM_*}{R_*}\dot{M}\frac{1}{\sigma T_{\rm acc}^4} \tag{6.2}$$

with $B_\nu(T_{\rm acc},\nu)$ the Planck blackbody function, G the gravitational constant, M_* and R_* the mass and radius of the star, $\dot{M}$ the mass accretion rate, and σ the Stefan-Boltzmann constant. For SR21, no accretion luminosity was added since only an upper limit for the accretion is measured. Note that observed values of $\dot{M}$ are uncertain up to an order of magnitude and are

Table 6.4: *Parameter-fitting procedure*

Category	Parameter	Value	Description
Surface density profile ($\Sigma(r)$)	r_c	*free*	Critical radius
	Σ_c	*free*	Gas density at r_c
	γ	1	Surface density gradient
	GDR	100	Gas-to-dust ratio
Radial structure	$r_{\rm sub}$	*fixed by formula*	Sublimation radius
	$r_{\rm gap}$	*free*	Size of the inner disk
	$r_{\rm cav}$	*free*	Cavity radius
	$r_{\rm out}$	*free*	Outer radius
Scaling $\Sigma(r)$	$\delta_{\rm dust}$	*free*	Dust density drop in the inner disk ($r_{\rm sub}$–$r_{\rm gap}$)
	$\delta_{\rm dustcav}$	*free*	Dust density drop inside the cavity ($r_{\rm gap}$–$r_{\rm cav}$)
	$\delta_{\rm gas}$	*free*	Gas density drop inside the cavity ($r_{\rm sub}$–$r_{\rm cav}$)
Vertical structure ($h(r)$)	h_c	*free*	Scale height angle at r_c
	ψ	*free*	Flaring angle
Dust properties	sg-pop	0.005–1 μm	Small dust grain population
	lg-pop	0.005 μm–1 mm	Large dust grain population
	$f_{\rm ls}$	*free*	Fraction of large grains
	χ	0.2	Scale height of the large grain fraction
	PAH	0.1%	PAH fraction w.r.t. ISM abundance
Ionization	$\zeta_{\rm H_2}$	$5{\times}10^{-17}$ s^{-1}	Cosmic-ray ionization rate
	X-ray	10^{30} erg s^{-1}	X-ray ionization rate

often variable with time (e.g., Salyk et al. 2013). The interstellar radiation field incident on the disk surface was also included, but it does not affect the results presented here.

The vertical structure follows a Gaussian distribution, defined by a scale height angle $h = h_c \left(\frac{r}{r_c}\right)^{\psi}$. A disk in hydrostatic equilibrium will have ψ=0.25, while a flat (h/r = constant) disk will have $\psi = 0$. The near- and far-infrared excess in the SED relate directly to the resulting scale height $h(r)$ at $r_{\rm sub}$ and $r_{\rm cav}$, respectively. Our vertical structure is a simplification and does not account for hydrostatic equilibrium of gas or dust temperature. One of the main effects of the hydrostatic equilibrium is a puffed-up inner rim. Previous studies (e.g., Andrews et al. 2011) often used a parametrized puffed-up inner rim to fit the near- and far-infrared excess by adding a narrow scale height peak, but during our fitting procedure it became clear that a parametrized optically thick inner disk rim blocks a large amount of the UV irradiation and lowers the gas temperature significantly, as was also demonstrated in Woitke et al. (2009).

For the dust opacities we used the same approach as Andrews et al. (2011): a small (0.005–1 μm) and large (0.005 μm – 1 mm) population of dust with a mass fraction $f_{\rm ls}$ in large grains. Settling was parametrized by defining the scale-height of the large grains as χh, that is, h is reduced by a factor χ (see Andrews et al. (2011) for definitions). We initially fixed $f_{\rm ls}$ and χ to 0.85 and 0.2, respectively, as adopted by Andrews et al. (2011). We included PAHs since many of our observed sources show PAH features (Brown et al. 2007; Geers et al. 2006), but at a low abundance of 0.1% of the ISM abundance. The turbulent width was set to 0.2 km s^{-1}. Stellar parameters taken from the literature are given in Table 6.1.

Model-fitting approach

In the fitting procedure, we used an approach of manual fitting by eye and varied the parameters in a logical order so that they converged to a model that fits the data, similar to

the approach in Bruderer et al. (2014). We did not use a χ^2 or Markov chain Monte Carlo (MCMC) method because the computational time of the models is too long and the number of parameters too large. Although this approach reduces computational time, it means that it is not possible to derive uncertainties of model parameters, verify the uniqueness of the fit, and estimate the correlation between parameters. The fitting parameters are defined in Table 6.4.

1. Fit Σ_c and $\delta_{\rm dust}$ roughly through the SED and continuum image, using the $r_{\rm cav}$ value from Andrews et al. (2011).
2. Adjust $r_{\rm sub}$, $r_{\rm gap}$ and $\delta_{\rm dust}$ if necessary for the NIR excess.
3. Vary the scale-height angle to fit the NIR and/or FIR excess in the SED by changing h_c and ψ.
4. Vary $r_{\rm cav}$ and r_c to match the null and slope of the submillimeter-dust visibility curve.
5. If the MIR/FIR excess is too high, adjust the size distribution by increasing $f_{\rm ls}$ and χ.
6. Find the highest possible value for $\delta_{\rm dustcav}$ (drop of dust density inside the cavity) that is still consistent with the dust continuum.
7. Check the fit to the CO intensity map, spectrum, and visibilities assuming the GDR to be 100 in the outer disk. If necessary, truncate the outer radius to fit the spectrum.
8. Explore small variations in the vertical parameters to change the temperature structure; this is required to fit the optically thick ^{12}CO emission.
9. Finally, keep all other parameters constant while varying $\delta_{\rm gas}$ to find the lowest possible value for $\delta_{\rm gas}$ that is still consistent with the CO data.

We stress that this approach does not result in a unique model because of the degeneracies in parameter choices and because ^{12}CO is optically thick. However, this approach seemed reasonable considering the different data sets taken into account, of which ALMA is the crucial one. Carmona et al. (2014) also demonstrated a modeling procedure that combines different datasets. The submillimeter continuum sets firm constraints on the total flux, the cavity size (the null in the visibility) and the dust extent (through r_c) of the disk, as also shown in Andrews et al. (2011). The mid-infrared part of the SED and the ^{12}CO are both sensitive to the combination of temperature and density structure of the disk, not only to the density, as both of these emission regimes are mostly optically thick. The temperature is controlled by the adopted vertical structure in the disk, as this determines the direct irradiation by the star, especially at the cavity wall. Therefore, several iterations were required to find a compromise for a decent fit of both the SED and ^{12}CO.

CO emission inside the cavity

As the CO emission inside the cavity only partly depends on density, the derived $\delta_{\rm gas}$ parameter is merely a constraint within the derived physical model. As discussed above, there are several effects that influence the strength of the emission: most important are gas temperature and CO abundance, which are very sensitive to the small dust grains inside the cavity. Different effects can play a role, as discussed extensively in Bruderer (2013).

- Although the bulk of the ^{12}CO emission is optically thick, the drop in gas surface density can still be constrained to within an order of magnitude with spatially resolved

Table 6.5: *Results of the fitting procedure for the gas density profile of each transition disk.*

	Parameter	SR21	HD135344B	LkCa15	RXJ1615-3255	SR24S	J1604-2130
Surface density	r_c (AU)	15	25	85	115	15	60
	Σ_c (g cm^{-2})	400	200	34	60	1200	12
	$M_{\rm dust}$ ($10^{-3} M_\odot$)	0.12	0.17	0.95	3.5	0.35	0.095
	$M_{\rm gas}$ ($10^{-3} M_\odot$)	12	24	103	470	-	20
Radial structure	$r_{\rm cav}$ (AU)	25	40	45	20	25	70
	$\delta_{\rm dustcav}$	10^{-3}	$< 10^{-4}$	$< 10^{-4}$	$< 10^{-5}$	$< 10^{-4}$	$< 10^{-6}$
	$\delta_{\rm gas}$	10^{-2}	10^{-1}	10^{-1}	$> 10^{-4}$	-	10^{-5}[a]
	$r_{\rm out}$	100	150	400	200	-	400
Inner disk	$r_{\rm sub}$ (AU)	0.18	0.18	0.08	0.08	0.14	0.04
	$r_{\rm gap}$	1	0.25	1	1	1	0.06
	$\delta_{\rm dust}$ (AU)	10^{-6}	10^{-2}	10^{-5}	10^{-6}	10^{-4}	10^{-1}
Vertical structure	h_c (rad)	0.07	0.15	0.06	0.04	0.12	0.065
	ψ (AU)	0.15	0.05	0.04	0.2	0.01	0.68
	$f_{\rm ls}$	0.85	0.95	0.98	0.85	0.98	0.98

Notes. [(a)] This value refers to the drop inside the inner cavity of 30 AU ($\delta_{\rm gas2}$ in the text).

observations. Optically thick emission will slightly drop with decreasing $\delta_{\rm gas}$ because the $\tau = 1$ surface moves deeper into the disk, so the emission traces colder regions in the disk, as demonstrated in Section 5.2 and Figures 9-10 in Bruderer (2013).

- An inner disk will cast a shadow on the gas inside the cavity, depending on the amount of dust and scale height. This will lower the gas temperature inside the cavity. On the other hand, the inner disk shields the stellar UV radiation that would photodissociate CO, so the CO abundance is increased. The structure of the inner disk is only poorly constrained from the available data, while it may have significant effects on the heating of the outer disk.
- The presence of small dust grains and PAHs inside the cavity shields stellar UV radiation and decreases the photodissociation, thus increasing the CO abundance. The dust contributes to the heating and cooling of the gas, depending on the density. For high gas density, the gas temperature decreases when dust is added as a result of cooling by gas-grain collisions. For low gas density, the gas temperature decouples and becomes higher than the dust temperature as a result of photoelectric heating on grains and PAHs.
- The increase of the gas temperature (increase of small dust grains) or an increase of the UV radiation (decrease of small dust grains) will also lead to an increase of vibrationally pumped H_2, again increasing the formation of CO.
- The presence of small dust grains and PAHs increases the formation of CH^+ on the grain surfaces, which leads to increased formation of CO.

The consequences for the CO emission of adding small dust, either inside the entire cavity or just in the inner disk, strongly depends on the details of the structure of the disk. This is the reason why the SED and submillimeter visibilities are also included in the modeling procedure, and why a full physical-chemical model is required to analyze the CO emission.

6.4 Results

Our best-fitting results for the dust and gas density structure are presented in Figures 6.4 to 6.6 and Table 6.5. In Figure 6.4 the output of the physical model is compared to the SED, the 690

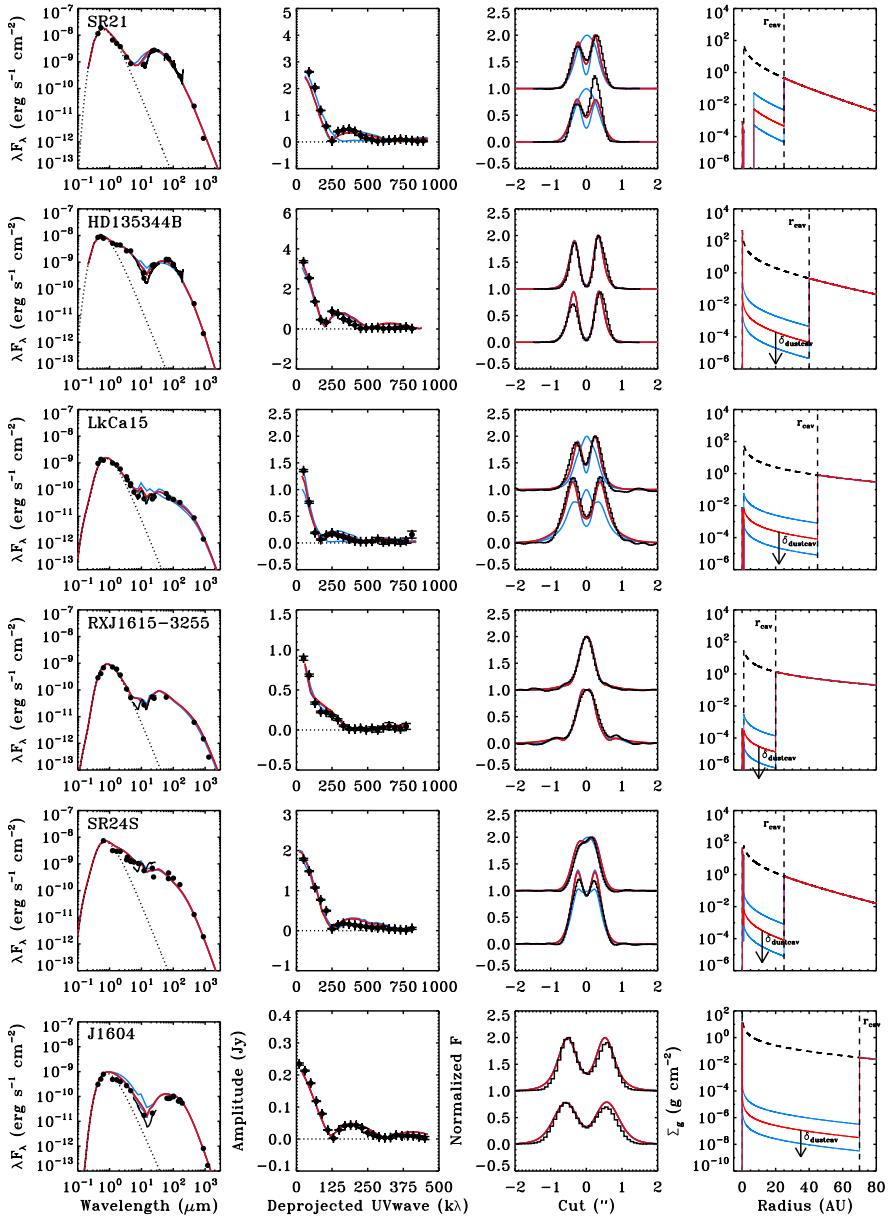


Figure 6.4: *Modeling results and observations of the dust surface density, comparing* $\delta_{\rm dustcav}$ *ranging between* 10^{-2} *and* 10^{-8} *as indicated in the right panel. The observations are plotted in black.* **Left:** *Spectral energy distribution.* **Middle left:** *Amplitude of the 690 GHz continuum visibility for the deprojected baselines. The null line is indicated with a dashed line.* **Middle right:** *Normalized intensity cuts through the major (bottom) and minor (top) axis of the 690 GHz continuum image. The model images are convolved with the same beam as the ALMA observations.* **Right:** *Dust surface density profile. Indicated are the* $\delta_{\rm dust}$*, the drop in density to fit the inner disk through the near-infrared emission, and* $\delta_{\rm dustcav}$*, the minimum drop in dust density inside the cavity to fit the observations. In SR21 (top panel) the region inside 7 AU is assumed to be empty because of additional constraints (see main text). In all other disks* $\delta_{\rm dustcav}$ *is found to be at most* 10^{-4}*. All other disk parameters are as listed in Table 6.5.*

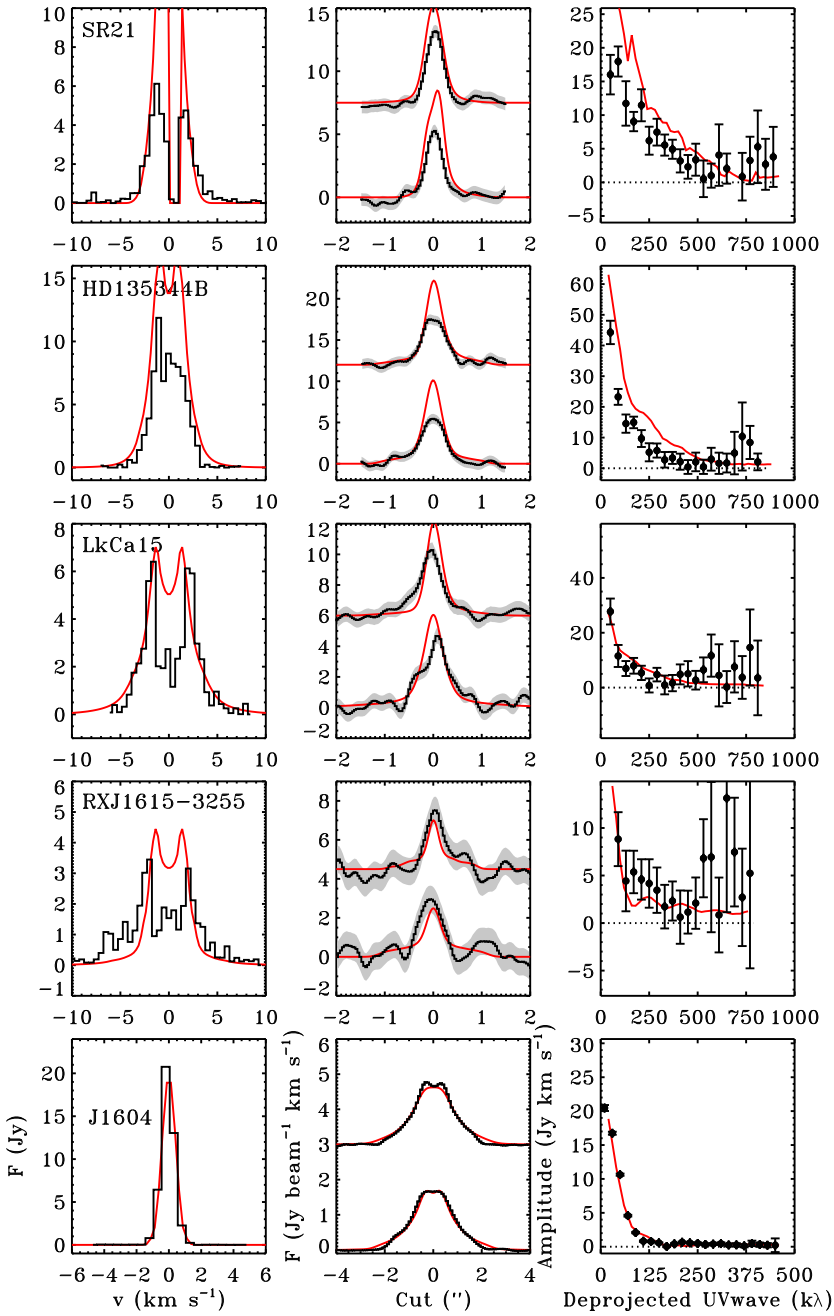


Figure 6.5: *Modeling results and observations of the ^{12}CO emission for the best-fitting physical model derived from the dust (see Figure 6.4 and Table 6.5), with $\delta_{\rm gas}$=1 (no drop in gas surface density inside the cavity). The observations are plotted in black, the models in red.* **Left:** *^{12}CO spectrum integrated over the entire disk.* **Center:** *Intensity cuts through the major (bottom) and minor (top) axis of the ^{12}CO zero moment map. The noise level is indicated by the gray zone. The model images are convolved with the same beam as the ALMA observations.* **Right:** *Amplitude of the integrated ^{12}CO visibility for the deprojected baselines. The null line is indicated with a dashed line, and error bars indicate the noise.*

GHz continuum visibility curve, and the normalized major/minor axis cuts of the 690 GHz continuum image (left panel of Figure 6.1). Data points of the SED were dereddened using the extinction law by Weingartner & Draine (2001) with R_V=5.5. The SED constrains the vertical structure of the disk, while the visibility curve determines the cavity size and extent through the location of the null. The image cuts show the direct comparison of the image with model. Within each figure, the $\delta_{\rm dustcav}$ value (drop of dust density inside the cavity) is varied with values between 10^{-2} and 10^{-6}, to constrain the minimum drop in dust density inside the cavity. In the rightmost panel we present the density structure of the model.

Reasonable fits are found for the continuum visibilities and SED within the constraints of our physical model for all targets. The inferred disk masses are similar to previous findings within a factor of a few, for instance, to those of Andrews et al. (2011). The models with $\delta_{\rm dustcav}$=10^{-2} overproduce the emission inside the cavity in all cases, as seen both in the mid-infrared part of the SED and in the dust continuum image. Therefore, $\delta_{\rm dustcav}$ is constrained to be at most a factor of 10^{-4}, and even as low as 10^{-6} for J1604-2130. In the modeling of the gas, we set $\delta_{\rm dustcav}$ to zero, except for SR21, where $\delta_{\rm dustcav}$ is constrained by the visibilities. For the gas modeling of HD135344B and J1604-2130, we included some additional dust between $r_{\rm cav}$ and 30 AU as shown in the dust density profile in Figure 6.6.

To analyze the gas density, we compared the result of the adopted disk model to the ^{12}CO spectrum, the intensity cuts through the zero moment map, and the ^{12}CO visibility curve in Figure 6.5. SR24S was not included in this part of the analysis because the CO emission is too heavily confused by large-scale emission (Figure 6.9). The models were calculated assuming $\delta_{\rm gas}$=1, that is, no drop in the gas surface density inside the dust cavity, except for J1604-2130, which shows a resolved drop in the CO emission inside 30 AU, which is adopted already. Because the CO visibilities do not show a clear null and the disks are not fully symmetric in the gas, the visibility curve was not used to fit our data exactly: it is merely included here to show that the emission from the moment map is well retrieved from the visibilities.

The models reproduce the CO emission well in the outer part of the disk ($r > r_{\rm cav}$). There was no need to change the GDR of 100 in any of the cases in the outer disk. This conclusion needs to be confirmed by optically thin CO isotopolog observations. The images and visibilities show that the outer extent of the dust and CO emission can indeed be fit with the same physical model, although observations with a better S/N are required to confirm this.

For SR21, HD135344B, and LkCa15, the initial model overproduces the central part of the intensity cut by a factor 1.5–2, suggesting a decrease of gas surface density inside the dust cavity. In Figure 6.6 we present the same physical model with $\delta_{\rm gas}$ varying from 10^0 to 10^{-4} in steps of 10 to compare with the observations. The emission drops by less than a factor of 2 in each of these steps, which is due to the optical depth of the ^{12}CO line, but within the noise level of the moment map this is sufficient to constrain $\delta_{\rm gas}$ to within an order of magnitude because of the different gas temperatures at the $\tau = 1$ surface in the disk. This result is different from Oph IRS 48, where the ^{12}CO line wings were found to be optically thin (Bruderer et al. 2014). Only the emission in J1604-2130 inside 30 AU radius becomes optically thin. The range of $\delta_{\rm gas}$ is indicated in the right panel of Figure 6.6 and in Table 6.5.

In the following section we discuss the properties of each disk in more detail.

6.4.1 Results of individual targets

SR21

It is possible to fit the SED and amplitudes of the continuum visibilities simultaneously at least up to baselines of 600 kλ. The small inconsistency at longer baselines is possibly related

to the dust asymmetry (Pérez et al. 2014), which is not taken into account. To fit the SED, we used for this disk an alternative dust opacity table for the small grains, without small silicates, because the normal dust table results in a strong silicate feature that is not seen in the data. We find a cavity size of at most 25 AU, which is significantly lower than the value of 36 AU previously found in the SMA data at 345 GHz (Brown et al. 2009; Andrews et al. 2011). It remains unclear whether this is due to differences in the modeling approach or a physical effect, since the 345 GHz emission traces somewhat larger dust grains (see also Section 5.2). Similar to Andrews et al. (2011), we find that this disk has a remarkably small radius: r_c is only 15 AU, resulting in no detectable emission outside a radius of 75 AU.

Both hot CO line emission (Pontoppidan et al. 2008) and mid-infrared interferometry (Benisty, private comm.) suggest a hot ring at 7 AU and no material inside. Scattered light also shows that there is small dust down to <14 AU (Follette et al. 2013). Therefore, we assume that there is no gas between the star and 7 AU for SR21 (but still an inner dust disk due to the NIR excess), and dust with only a small grain population between 7 AU and $r_{\rm cav}$. The dust between 7 AU and the dust hole cavity of 25 AU is partly constrained by the visibility curve: without the additional dust, the second null is much further out, although this may also be due to the asymmetry. In constraining $\delta_{\rm dustcav}$, this drop is assumed to start from 7 AU rather than from $r_{\rm gap}$ (taken as 1 AU).

The central ^{12}CO emission in the intensity cut is overproduced by about a factor of 2 in the initial model, especially inside the cavity region (Figure 6.5). Only a deep drop in $\delta_{\rm gas}$ of 2 orders of magnitude can match the peak of the zero-moment map, although the intensity cut is somewhat wider than the data.

HD135344B

The continuum visibility is reasonably well fit with a model with a cavity of 40 AU, slightly smaller than the 45 AU cavity found in previous work with 345 GHz SMA data (Brown et al. 2009; Andrews et al. 2011; Carmona et al. 2014). An increase of the large-grain fraction and large-grain scale height ($\chi = 0.8$) is needed to fit the peak of the far-infrared part of the SED.

We find a smaller critical radius of only 25 AU and thus smaller extent of the disk than was reported by Andrews et al. (2011) (who found r_c=55 AU), but the ALMA data quality is much better than the quality of the SMA data. Another main difference in the modeling procedure is the different vertical structure of this disk in our parametrization (no puffed-up inner rims), although this is not expected to change the emission in the outer disk. Scattered-light images show that there is small dust inside the millimeter-dust cavity down to 30 AU for HD135344B (millimeter-dust cavity is ∼46 AU) (Garufi et al. 2013). Therefore we assume a finite drop in dust density between $r_{\rm cav}$ and 30 AU. The scattered-light images, SED, and visibilities do not constrain the amount of dust: we chose a drop of 10^{-3}. Garufi et al. (2013) and Muto et al. (2012) show signatures of spiral arms in the scattered-light images. The ALMA data resolution is too low to detect these arms if they were visible at millimeter wavelengths.

The initial model for this disk overproduces the CO emission inside the cavity. A $\delta_{\rm gas}$ of 10^{-1} – 10^{-2} is sufficient to fit the peak in the moment map. A decrease in gas density inside the cavity was previously inferred from SMA CO line observations (Lyo et al. 2011). Carmona et al. (2014) required a surface density that increases with radius inside the cavity to fit the rovibrational CO lines in this disk. Fitting these lines is beyond the scope of this paper, but the drop in surface density may be similar to this increasing density profile, as discussed in Section 5.1. Motivated by the dust structure, we also tried to fit a gas model with a cavity size of 30 AU instead of 40 AU. There is no significant difference in the outcome for a gas cavity radius of 30 AU or 40 AU, however. As Figure 6.7a shows, $\delta_{\rm gas} = 10^{-1} - 10^{-2}$ also fits best for a gap of 30 AU.

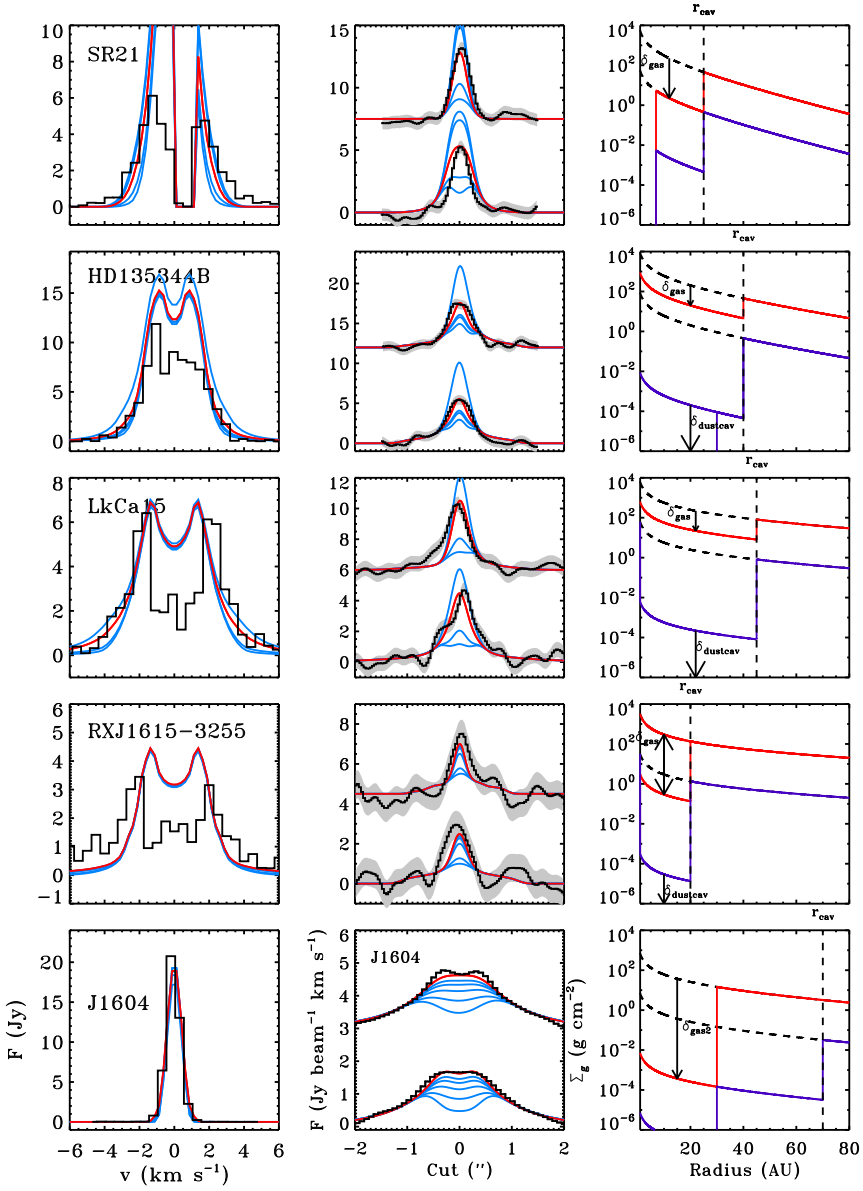


Figure 6.6: *Modeling results and observations of the ^{12}CO emission for the best-fitting physical model for gas and dust (Figure 6.5) comparing δ_{gas} (gas density drop inside the dust cavity). δ_{gas} is varied as 10^0, 10^{-1}, ... , 10^{-4} with the best fit in red and the other models in blue, while the observational data are plotted in black.* **Left:** *The ^{12}CO spectrum integrated over the disk area.* **Middle:** *The intensity cuts through the major (bottom) and minor (top) axis of the ^{12}CO zero-moment map for different δ_{gas}. The noise level is indicated by the gray area. The model images are convolved with the same beam as the ALMA observations.* **Right:** *The best-fitting result for possible values of δ_{gas} and $\delta_{dustcav}$ in red and blue.*

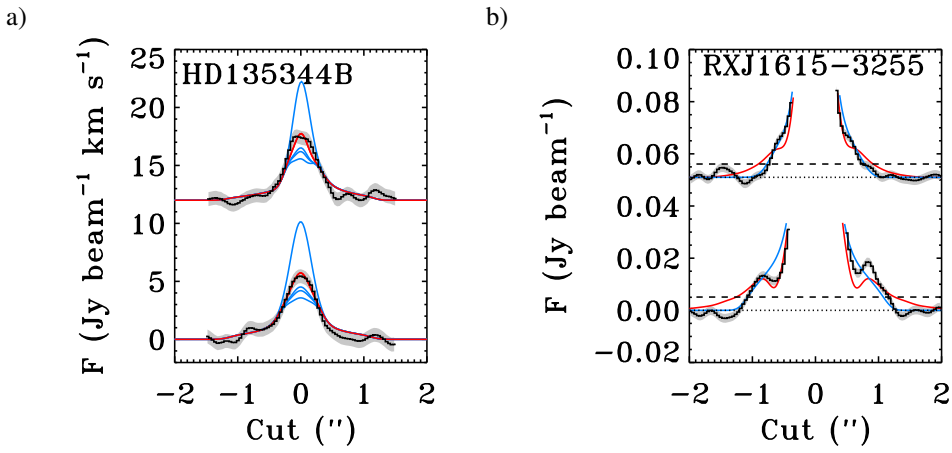


Figure 6.7: a) *Modeling results and observations of the ^{12}CO emission for the best-fitting physical model for HD135344B for a cavity of 30 AU instead of 40 AU for gas and dust (Figure 6.5) for different values of $\delta_{\rm gas}$ (gas density drop inside the dust cavity). $\delta_{\rm gas}$ is varied as 10^0, 10^{-1}, ... , 10^{-4} with the best fit in red and the other models in blue. The observations are plotted in black. The panel shows the intensity cuts through the major (bottom) and minor (top) axis of the ^{12}CO zero-moment map.* **b)** *Modeling results and observations of the 690 GHz continuum of RXJ1615-3255. The panel shows the intensity cuts through the major (bottom) and minor (top) axis of the continuum image, zoomed in on the lowest flux levels ($< 20\sigma$). The observations are plotted in black with the 1σ errors in gray. In red and blue we present the models with and without a dust gap between 110 and 130 AU. The dotted and dashed lines indicate the zero flux and 3σ limits, respectively.*

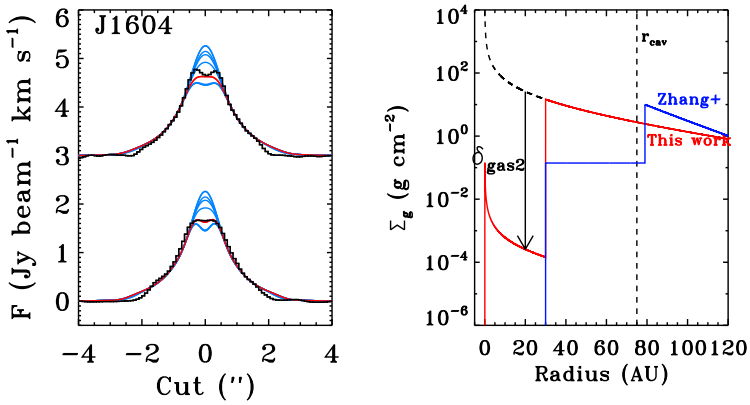


Figure 6.8: Left: *Modeling results and observations of the ^{12}CO emission for the best-fitting physical gas model for J1604-2130 for the inner 30 AU cavity comparing $\delta_{\rm gas2}$ (gas density drop inside the 30 AU dust cavity). $\delta_{\rm gas2}$ is varied as 10^0, 10^{-1}, ... , 10^{-6} with the best fit in red and the other models in blue ($\delta_{\rm gas}$ is taken as 1). The observations are plotted in black. The panel shows the intensity cuts through the major (bottom) and minor (top) axis of the ^{12}CO zero-moment map.* **Right:** *Comparison between the density profile derived in this study and the profile used in Zhang et al. (2014).*

LkCa15

LkCa15 is a well-studied transition disk with a large cavity of 50 AU (Isella et al. 2012). We modeled LkCa15 with a rather flat but massive disk structure. Our derived disk dust mass is three times higher than typically found in the literature, and the 690 GHz continuum is indeed optically thick, which explains the apparent asymmetry in the continuum image: the northwest side of the disk is brighter than the southeast side because of the geometry.

Just like HD135344B, the initial model for this disk overproduces the CO emission inside the cavity, indicating a $\delta_{\rm gas}$ of at least 10^{-1}.

RXJ1615-3255

RXJ1615-3255 does not reveal a cavity in the continuum image, and the visibilities only show a hint of a null at the longer baselines (>500 kλ). Our best-fitting model has a cavity of 20 AU, somewhat smaller than the best-fit cavity in Andrews et al. (2011) of 30 AU. A model without cavity cannot fit the SED, which clearly indicates a deficit of dust close to the star. This indicates that the Band 9 continuum might be optically thick. An interesting aspect of this target is the outer part of the disk: a narrow radial dip is seen in the image at 0.6" from the center (corresponding to 110 AU at the distance of this disk). Figure 6.7b shows a zoomed-in image of the intensity cut from Figure 6.4. This hints at the presence of a dust gap in the outer part of the disk between 110 and 130 AU, or an additional outer ring of dust, as seen in recent ALMA data of HD100546 (Walsh et al. 2014).

The model with $\delta_{\rm gas}$=1 does not reproduce the high velocity emission seen in the CO spectrum, but the S/N is low, which means that the significance of this remains debatable. The intensity cuts show that the gas density inside the dust hole can be up to four orders of magnitude lower before the CO becomes optically thin.

SR24S

SR24S is an inclined disk with a barely resolved cavity of about 30 AU. The long-wavelength part of the Spitzer IRS spectrum and the MIPS-24 flux are known to be confused by emission from its nearby companion SR24N (see, e.g., Andrews et al. 2011), thus these points were only used as upper limits in our fit. The visibility curve becomes inconsistent with our model for baselines >350 kλ, hinting at substructure inside the cavity. As we do not have any additional information on dust inside the cavity of this disk, we did not explore this further.

J1604

J1604-2130 is a transition disk at 345 GHz that was frequently studied with both SMA (Mathews et al. 2012) and ALMA (Zhang et al. 2014). Mathews and Zhang and collaborators both provided physical models for the dust and the gas. Zhang et al. (2014) used the same ALMA dataset as discussed here, but did not use a full physical-chemical model for the gas analysis. In neither of the two studies the near infrared excess was taken into account. The problem is the apparent variability: whereas the Spitzer IRAC photometry (taken in 2006 and used by Mathews) shows no near-infrared excess, the Spitzer IRS and WISE photometry (taken in 2007 and 2012, respectively) do reveal the excess. Zhang et al. noted this discrepancy and stated that the near-infrared excess can be fit with an optically thick inner disk ring, but did not include this in their model. Since the inner disk has a strong influence on the CO emission inside the cavity (and on the shadowing of the dust cavity wall), we chose to include the more recent photometry with near-infrared excess in our SED and fit the models accordingly.

Mathews et al. (2012) introduced a two-drop dust density model to fit their SMA data, which was also adopted by Zhang et al. (2014) in the analysis of the ALMA data: one drop

at 75 and one at 20 AU. We found that such a two-step decrease is indeed required to fit the continuum visibilities and adopted the same structure, although we set the inner drop radius at 30 AU to be consistent with the gas cavity. On the other hand, we required a much larger critical radius of 60 AU instead of the 10-20 AU used by Mathews and Zhang. This is most likely the result of shadowing by an inner disk. Our disk dust mass of 0.1 $M_{\rm Jup}$ is similar to their estimates.

In the gas a clear signature for a drop at 30 AU is seen in the CO moment map, which was modeled by Zhang et al. (2014) in a parametrized gas model of a power-law temperature profile with an empty gap. Their result is consistent with that of our full physical-chemical model, and the derived surface density profile is similar (right panel of Figure 6.8). We can constrain the inner density drop to $\delta_{\rm gas2} = 10^{-5}$ (see left panel of Figure 6.8), although this depends on the inner cavity size: a smaller cavity size would require an even deeper drop, a larger size a less deep drop. On the other hand, $\delta_{\rm gas}$ (the drop inside the dust cavity radius) is 1, there is no visible drop in density between 30 and 70 AU.

6.5 Discussion

6.5.1 Implications of gas density drop

The key parameter in our analysis is $\delta_{\rm gas}$, the drop in gas density inside the dust hole, in comparison with $\delta_{\rm dustcav}$. For each target, the minimum required drop in dust density $\delta_{\rm dustcav}$ is significantly lower than the possible values of $\delta_{\rm gas}$. Figure 6.6 and Table 6.5 show the range of possible values for these parameters for each target.

The significantly larger drop in dust density compared with the gas is consistent with the dust-trapping scenario by a companion, with gas present inside the millimeter-sized dust cavity (Pinilla et al. 2012a). For the sources studied here, photoevaporation by itself is unlikely based on just the large cavity sizes and high accretion rates (Owen et al. 2011; Rosotti et al. 2013), and our results further strengthen this hypothesis. Especially SR21, HD135344B, and LkCa15 require a minimum drop of a factor 10-100 within the gap in the gas surface density and are thus promising candidates for disks with embedded planets. The drop is deep enough to rule out the dead-zone scenario, which has a drop that is much smaller than an order of magnitude (Lyra et al. 2015). On the other hand, one has to be careful to avoid an overinterpretation at this point: the CO emission inside the gap is sensitive to the amount of small dust inside the cavity due to its shielding effect, which can also explain the apparent drop in CO emission. We have explored this within the constraints of our physical model, but any addition of dust or PAHs inside the cavity that is sufficient to lower the CO emission at the same time increases the mid-infared continuum emission in the SED to levels that are inconsistent with the data. The combination of SED modeling and spatially resolved ^{12}CO emission thus provides unique constraints on the temperature and small dust grain composition. On the other hand, the vertical structure also influences the temperature structure and thus the ^{12}CO emission and mid-infrared continuum emission, and this degeneracy remains uncertain.

The depth of the gas density drops at the cavity radius is still modest, only a factor $\delta_{\rm gas} \sim 10^{-1} - 10^{-2}$. Comparison with the planet-disk interaction models of Jupiter-mass planets in Figure 1 in Pinilla et al. (2012a) indicates that any embedded planets responsible for this drop are unlikely to be more massive than 1-2 Jupiter masses, and even then only with high viscosity ($\alpha \sim 10^{-2}$). A high viscosity is inconsistent with the presence of long-lived vortices (e.g., Ataiee et al. 2013). Pérez et al. (2014) interpreted the asymmetries of SR21 and HD135344B as possible vortices by comparing their analytic solution for the asymmetric dust structures

with the vortex prescription of Lyra & Lin (2013). The lack of a deep gap in the CO argues against this interpretation. Pinilla et al. (2015a) also concluded that for SR 21 the vortex scenario is unlikely by analyzing the observed dust distribution at different wavelengths with hydrodynamic and dust evolution models. However, a smaller gas cavity size with a deeper density drop would also fit our observations and be consistent with low viscosities. More high spatial resolution observations of CO isotopologs are needed to clearly distinguish cavity size and gas density drop.

The planet-disk interaction models predict rounded-off gradients rather than steep vertical drops such as parametrized in our model. A rounded-off dust wall was indeed inferred from mid-infrared interferometry data of HD 100546 (Mulders et al. 2013) by fitting the visibility curve, but the S/N of our data is insufficient to test this. One important conclusion of Pinilla et al. (2012a) is that the gas cavity radius (location of the planet) is expected to be up to a factor of 2 smaller than the dust cavity radius (location of the radial pressure bump where the dust is trapped). This was indeed observed for J1604-2130 (Zhang et al. 2014, this study), Oph IRS 48 (Bruderer et al. 2014), and HD 142527 (Perez et al. 2015). As stated above, our estimates of the drop in gas density inside the cavity would probably increase if we were to assume a smaller gas cavity size, but the spatial resolution of our data is insufficient to constrain this. For HD135344B we show the outcome for a gas cavity of 30 instead of 40 AU (Figure 6.7a), but for this radius the $\delta_{\rm gas}$ is still limited to $10^{-1} - 10^{-2}$. For J1604-2130, we find clear evidence for an inner drop at 30 AU and no additional drop between 30 and 70 AU of 10^{-1}, as found for Oph IRS 48 (Bruderer et al. 2014). A structure with a double drop or smaller gas cavity size hints at the possibility that there is more than one companion, or alternatively a shallow increasing slope such as seen in Pinilla et al. (2012a, 2015a). This possibility cannot be excluded for any of the other sources in this study with the available observations. Carmona et al. (2014) suggested a gas surface profile that increases with radius inside the cavity to match the gas and dust density distribution of HD135344B, although this is only constrained by observations for the inner few AU. Modeling the shape of the gap is beyond the scope of this paper. Spatially resolved observations of CO isotopologs will provide better constraints on the density profile.

6.5.2 Cavity size and dust distribution

Another interesting aspect of our results is that all disks have significantly smaller cavity sizes (by 5-10 AU) in the 690 GHz continuum data than those derived by Andrews et al. (2011) based on the 345 GHz continuum observations taken with the SMA. The cavity size as derived with the ALMA continuum visibilities (location of the null) is constrained to better than ±5 AU. The S/N of the SMA data is much lower, so the cavity size is less precisely constrained, but the systematic trend is significant. For comparison, we list the location of the first null for both the 690 GHz and 345 GHz continuum of our adopted model in Table 6.6 and compare them with the null in Andrews et al. (2011).

Note that the null as derived from the models can shift slightly for the two frequencies as a result of the difference in dust opacity at the observed wavelengths. The null in the observed 345 GHz continuum is significantly smaller for SR21, HD135344B, and RXJ1615-3255 than that at 690 GHz, indicating a larger cavity size at this longer wavelength. This indicates a radial variation of the dust size distribution, as the continuum emission is sensitive to larger grains at longer wavelengths. A more concentrated dust ring (i.e., a narrower ring and thus a larger dust cavity size) is consistent with the dust-trapping scenario, because larger dust grains are further decoupled from the gas and thus more affected by radial drift and trapping (Brauer et al. 2008). Higher S/N ALMA Band 7 observations are required to confirm this.

Table 6.6: *Location of the null in the visibilities of models and SMA observations at various frequencies (Andrews et al. 2011).*

Target	Model-690 null (kλ)	Model-345 null (kλ)	Observed-345 null (kλ)
SR21	252	247	200-220
HD135344B	196	204	160–180
LkCa15	171	155	140-160
RXJ1615-3255	484	349	250–300
SR24S	255	260	240–260

6.6 Conclusions

We have analyzed high spatial resolution ALMA submillimeter observations of ^{12}CO line emission from six transitional disks using a physical-chemical model. By comparing the SED, the 690 GHz continuum visibilities and the ^{12}CO emission simultaneously, we derived a physical model of the gas and dust. With the model we set constraints on the surface density profile of the dust and gas and specifically, the amount of dust and gas in the cavity.

1. All disks show clear evidence for gas inside the dust cavity.
2. The gas and dust observations can be fit with a surface density profile with a steep density drop at the cavity radius, taking a gas-to-dust ratio of 100 in the outer disk.
3. The combination of SED and spatially resolved ^{12}CO intensity fitting sets constraints on the vertical and thus on the temperature structure of each disk.
4. All disks except SR24S have a potential drop of 1 or 2 orders of magnitude in the gas surface density inside the mm-sized dust cavity, while the minimum required drop in dust surface density inside the cavity is at least 3 orders of magnitude.
5. J1604-2130 has a deep resolved gas cavity that is smaller than the dust cavity. For the other disks it is possible that the gas cavity radius is smaller than the dust cavity radius, in which case the density drop will be deeper, but this cannot be constrained with the available data.
6. The derived density profiles suggest the clearing of the cavity by one or more companions, as a result of which, the millimeter dust is trapped at the edge of the cavity.
7. Our model for J1604-2130 is mostly consistent with the proposed physical structure by Zhang et al. (2014), derived using a parametrized temperature model.
8. The continuum of RXJ1615-3255 shows an additional dust ring around 120 AU.
9. The derived cavity sizes of the millimeter dust (and location of the null in the visibilities) are consistently smaller for the 690 GHz/0.44 mm continuum than for the 345 GHz/0.88 mm continuum. This is consistent with the dust-trapping scenario, because trapping is more efficient for larger dust grains probed at longer wavelengths.

The derived physical model can be used as a start for the analysis of CO isotopolog observations, placing better constraints on the gas density inside and outside the cavity. We have recently obtained CO isotopolog ALMA observations for two disks of the sample in this study (van der Marel et al. 2015b).

6.A Channel maps

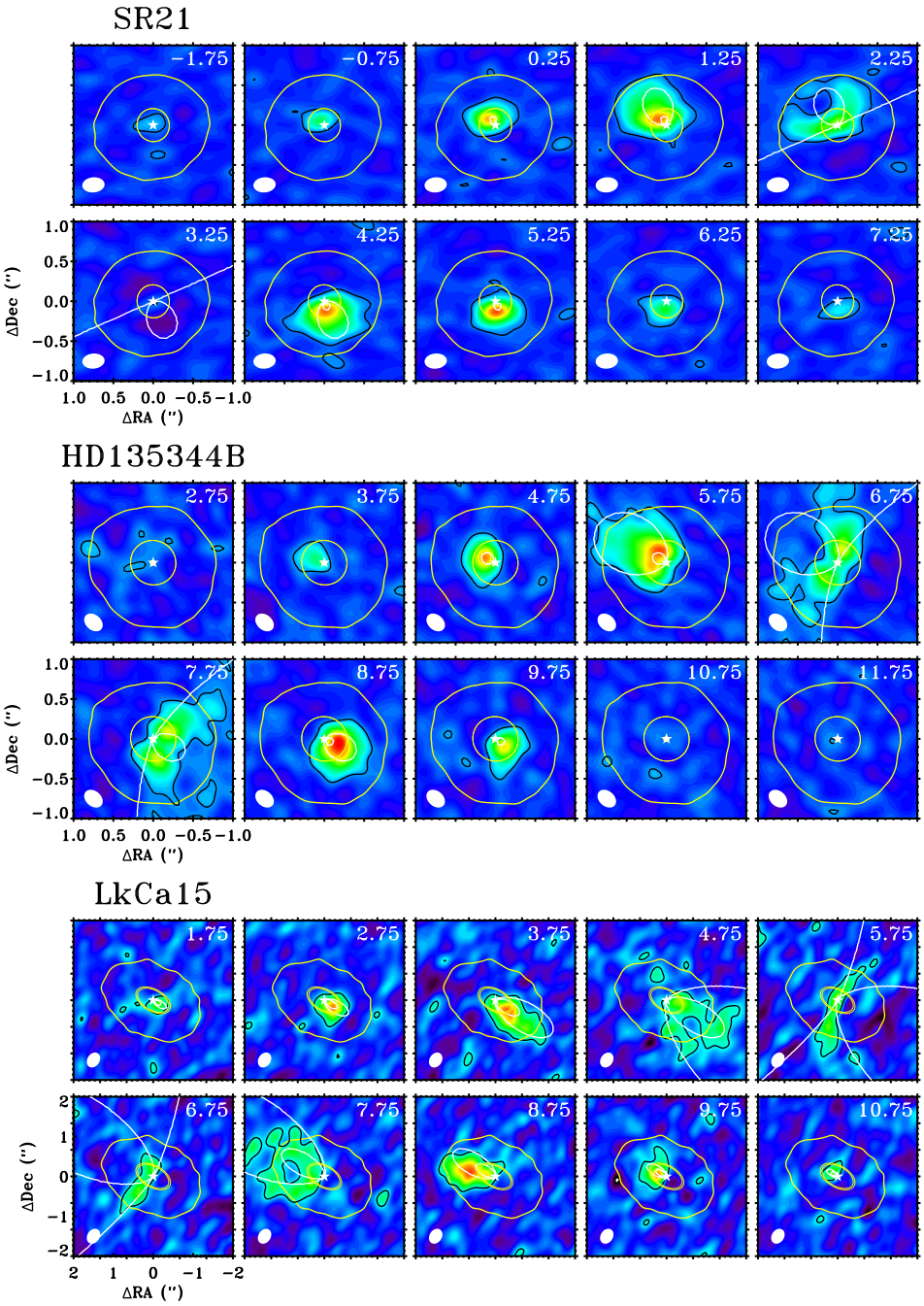


Figure 6.9: ^{12}*CO channel maps for each observed target. Overlaid in white contours are the Keplerian velocity profiles for the derived inclination and given stellar mass. The yellow contours indicate the dust hole radius and the 5σ outer radius of the dust continuum.*

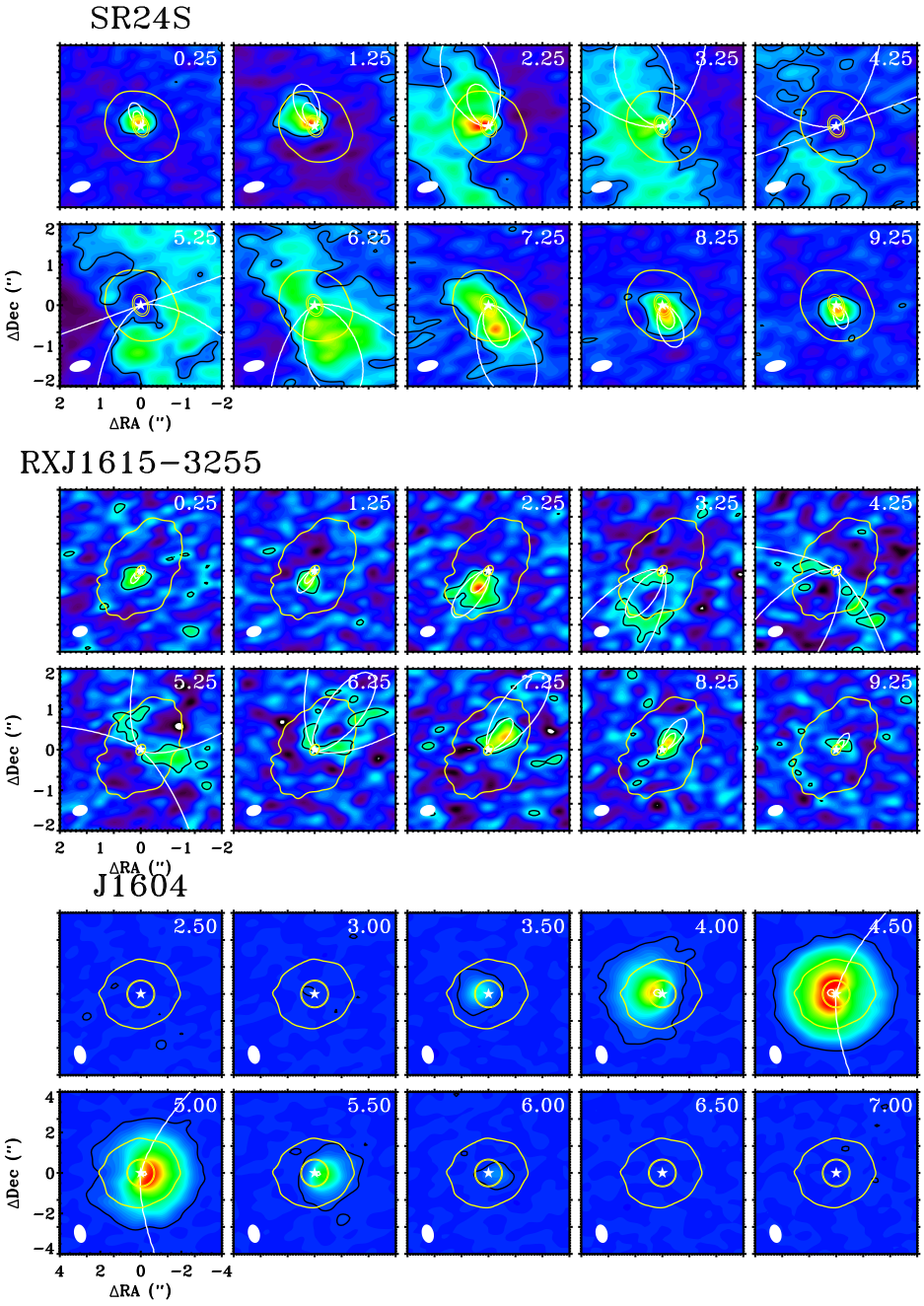


Figure 6.9: ^{12}*CO channel maps for each observed target (continued)*

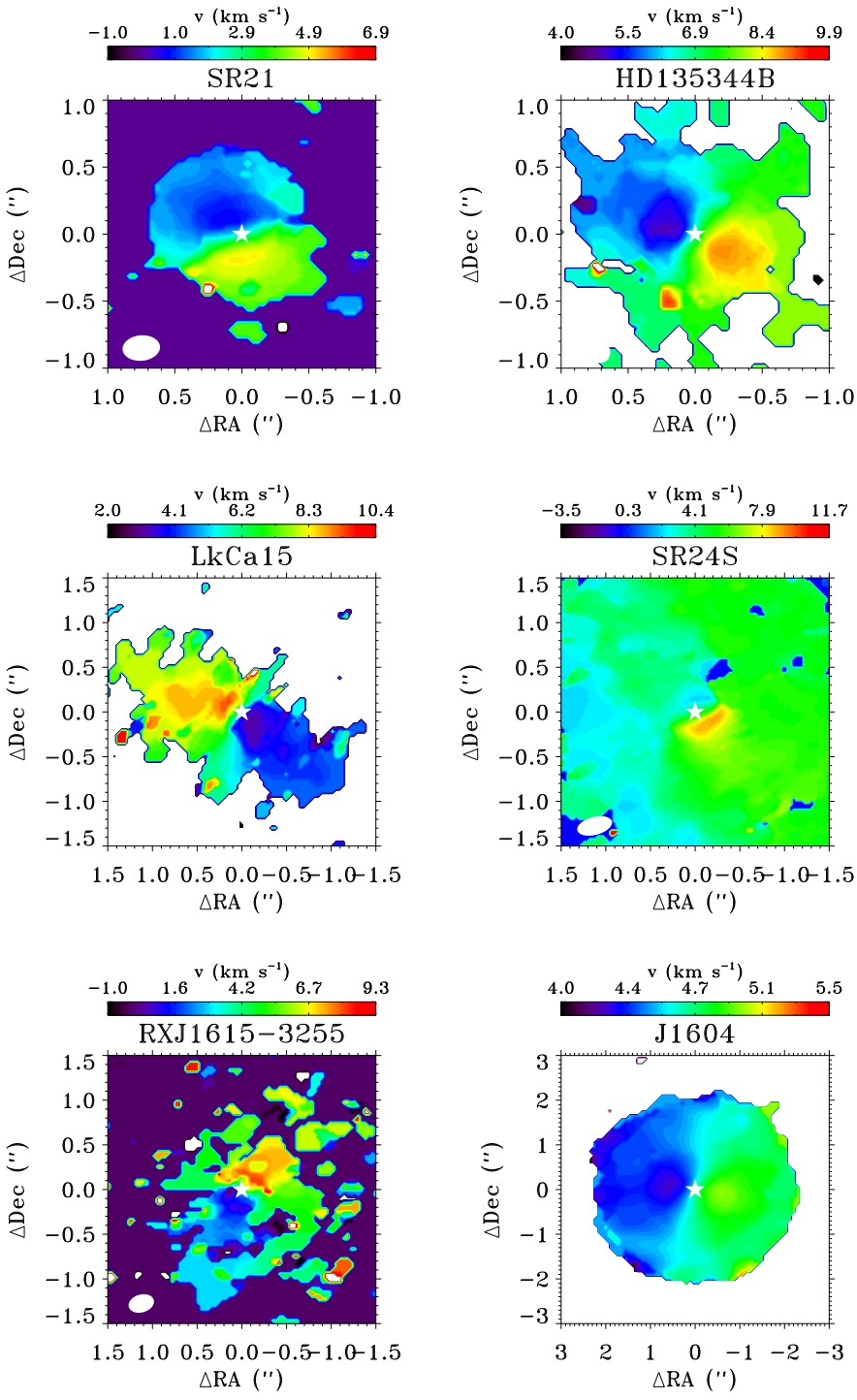


Figure 6.10: ^{12}*CO velocity maps for each observed target.*

Acknowledgements. The authors would like to thank P. Pinilla, A. Juhasz, and C. Walsh for useful discussions and the referee for the constructive comments. N.M. is supported by the Netherlands Research School for Astronomy (NOVA), S.B. acknowledges a stipend by the Max Planck Society. Astrochemistry in Leiden is supported by the Netherlands Research School for Astronomy (NOVA), by a Royal Netherlands Academy of Arts and Sciences (KNAW) professor prize, and by the European Union A-ERC grant 291141 CHEMPLAN. This paper makes use of the following ALMA data: ADS/JAO.ALMA/2011.0.00724.S and 2011.0.00526.S. ALMA is a partnership of ESO (representing its member states), NSF (USA) and NINS (Japan), together with NRC (Canada) and NSC and ASIAA (Taiwan), in cooperation with the Republic of Chile. The Joint ALMA Observatory is operated by ESO, AUI/NRAO and NAOJ.

7

Resolved gas cavities in transitional disks inferred from CO isotopologues

van der Marel, N.; van Dishoeck, E.F.; Bruderer, S.; Andrews, S.M.; Pontoppidan, K.M.; Herczeg, G.J.; van Kempen, T.; Miotello., A. *Resolved gas cavities in transitional disks inferred from CO isotopologues with ALMA.* subm. to A&A.

Abstract

Transitional disks around young stars with large dust cavities are promising candidates to look for recently formed, embedded planets. Planet-disk interaction models predict that young planets clear a gap in the gas while trapping dust at larger radii. Previous observations have revealed that gas is still present inside these cavities, but the spatial distribution of this gas remains uncertain. We present high spatial resolution observations with the Atacama Large Millimeter/submillimeter Array (ALMA) of ^{13}CO and C^{18}O 3–2 or 6–5 lines of four well-studied transitional disks around pre-main sequence stars with large dust cavities. The line and continuum observations are used to set constraints on the the gas surface density, specifically cavity size and density drop inside the cavity. The physical-chemical model DALI is used to analyze the gas images of SR21, HD135344B (also known as SAO 206462), DoAr44 and IRS 48. The main parameters of interest are the size, depth and shape of the gas cavity in each of the disks. CO isotope-selective photodissociation is included to properly constrain the surface density in the outer disk from C^{18}O emission. The gas cavities are up to 3 times smaller than those of the dust in all four disks. Model fits indicate that the surface density inside the gas cavities decreases by a factor of 100 to 10000 compared with the surface density profile derived from the outer disk. The data can be fit by either introducing one or two drops in the gas surface density or a surface density profile increasing with radius inside the cavity. A comparison with an analytical model of gap depths by planet-disk interaction shows that the disk viscosities are likely low, between between 10^{-3} and 10^{-4} for reasonable estimates of planet masses up to 10 Jupiter masses. The resolved measurements of the gas and dust in transition disk cavities support the predictions of models that describe how planet-disk interactions sculpt gas disk structures and influence the evolution of dust grains. These observed structures suggest the presence of giant planetary companions in transition disk cavities, although at smaller orbital radii than is typically indicated from the dust cavity radii alone.

7.1 Introduction

Protoplanetary disks around young stars are the birth cradles of planets (e.g. Williams & Cieza 2011). Disks with inner dust cavities, also called transition disks, are good candidates to search for young planets that have recently been formed and cleared out their orbit. Dust cavities have been inferred from modeling of Spectral Energy Distributions (SEDs) (Espaillat et al. 2014, and references therein) and millimeter interferometry (e.g. Brown et al. 2009; Andrews et al. 2011). Planet candidates have been found in cavities of several transition disks (Kraus & Ireland 2012; Quanz et al. 2013, 2015). However, planet-disk interaction models indicate that dust cavities are only an indirect consequence of planet clearing: a planet will lower the gas surface density along its orbit, creating a gas gap with a pressure bump at its outer edge where the millimeter-sized dust gets trapped (e.g. Zhu et al. 2011; Dodson-Robinson & Salyk 2011; Pinilla et al. 2012a). The result is a millimeter-dust ring (or in particular cases an azimuthal asymmetry, due to a Rossby-wave instability of the pressure bump, van der Marel et al. 2013; Fukagawa et al. 2013; Casassus et al. 2013) and a gas cavity that can be up to two times smaller than the radius of the dust ring. Other mechanisms that could cause a dust cavity or dust ring are photoevaporation (Clarke et al. 2001) and instabilities at the edges of dead zones (e.g. Regály et al. 2012). Measuring the gas density inside the cavity is essential to distinguish between these mechanisms: photoevaporation clears the dust and gas from the inside out; dead zones do not change the gas density inside the cavity; planetary clearing creates a gas cavity. Furthermore, the decrease of gas surface density inside the gas cavity radius depends on the mass of the companion and the disk viscosity. More generally, the fundamental property of a disk is its gas surface density profile, rather than that of the dust, which does not necessarily follow the gas.

The presence of gas inside the dust cavities was discovered through accretion (e.g. Valenti et al. 1993; Najita et al. 2007) and H_2 emission (Bergin et al. 2003; Ingleby et al. 2009). Other first indicators of warm molecular gas inside the cavities were near infrared observations of CO rovibrational lines, in several cases revealing a gas cavity that was indeed smaller than the dust cavity (Pontoppidan et al. 2008; Brittain et al. 2009; Salyk et al. 2009; Brown et al. 2012a). Due to a combination of high critical densities and non-LTE excitation, rovibrational CO data can be difficult to interpret and derived gas masses are highly model-dependent.

For a proper derivation of the molecular gas densities, CO pure rotational line observations are required. Spatially resolved ALMA observations of ^{12}CO emission confirm the presence of gas inside the dust cavity (van der Marel et al. 2013; Casassus et al. 2013; Pérez et al. 2014; Zhang et al. 2014; Canovas et al. 2015). Using a disk model based on the dust structure derived from the SED and millimeter imaging, the ^{12}CO data suggest a gas density decrease of 1 or 2 orders of magnitude inside the dust cavity compared to the density profile of the outer disk (van der Marel et al. 2015c). On the other hand, the dust density decreased by at least 3 orders of magnitude inside the cavity. In cases of IRS 48 and J1604-2130, the gas cavities are sufficiently empty so that ^{12}CO becomes optically thin inside the dust cavity, and it was found that the gas cavity radius is indeed smaller than the dust cavity (Bruderer et al. 2014; Zhang et al. 2014; van der Marel et al. 2015c), consistent with the planet-disk interaction predictions. The same result was found for HD 142527 using CO isotopologue observations (Perez et al. 2015).

Since detection of planets in disks is challenging, quantifying the gas density structure of the disk inside the cavity can provide important clues on the properties of embedded unseen planets. The depth and shape of the gap depend primarily on the planet mass and the disk viscosity (Zhu et al. 2011; Pinilla et al. 2012a; Fung et al. 2014). These models show that a planet does not create a steep gas gap, but a gradual decrease over several AUs. While spatially

resolved ^{12}CO can provide some information on the gas density profile, as demonstrated in Bruderer et al. (2014) and van der Marel et al. (2015c), the emission remains optically thick throughout most of the disk and is thus not a very good absolute density tracer. Spatially resolved CO isotopologue observations are required to constrain the outer disk mass and the gas cavity radius, as well as the depth and potentially the shape of the gas surface density profile.

Before ALMA, interferometric data did not have the sensitivity and spatial resolution to detect rotational CO emission inside the cavity. Moreover, converting CO emission into density is not trivial: the CO abundance with respect to H_2 is not constant throughout the disk due to photodissociation by the stellar UV radiation and freeze out onto dust grains in the cold regions in the midplane and outer disk (van Zadelhoff et al. 2001; Aikawa et al. 2002). CO photodissociation is subject to self-shielding. As CO isotopologues have lower abundances, they are not self-shielded until deeper into the disk. Therefore, models that do not include isotope-selective photodissociation predict higher CO abundances than when this effect is included, as recently demonstrated by Miotello et al. (2014). Also, the gas temperature is decoupled from the dust temperature in the upper layers in the disk and at the directly heated cavity wall (e.g. Kamp & Dullemond 2004; Jonkheid et al. 2004; Gorti & Hollenbach 2008). For a proper interpretation of CO emission, the physical and chemical structure of gas and dust needs to be modeled. We make use of physical-chemical modeling with DALI (Bruderer et al. 2012; Bruderer 2013), which simultaneously solves the heating-cooling balance of the gas and chemistry to determine the gas temperature, molecular abundances and molecular excitation for a given density structure.

Table 7.1: *Stellar properties*

Target	SpT	L_* ($L_\odot$)	M_* ($M_\odot$)	R_* ($R_\odot$)	$T_{\rm eff}$ (K)	$\dot{M}$ ($M_\odot$ yr^{-1})	d (pc)	A_V (mag)	Ref.
HD135344B	F4	7.8	1.6	2.2	6590	$6 \cdot 10^{-9}$	140	0.3	1,2,3
SR21	G3	10	1.0	3.2	5830	$< 1 \cdot 10^{-9}$	120	6.3	4,5,6
DoAr44	K3	1.4	1.3	1.75	4730	$9 \cdot 10^{-9}$	120	2.2	5,6
IRS48	A0	14.3	2.0	1.3	10000	$4 \cdot 10^{-9}$	120	11.5	7,8

1) Prato et al. (2003), 2) Andrews et al. (2011), 3) Espaillat et al. (2010), 4) Dunkin et al. (1997), 5) Pontoppidan et al. (2008), 6) Grady et al. (2009), 7) Brown et al. (2012a), 8) Salyk et al. (2013)

Table 7.2: *Properties of the ALMA observations*

Target	Position[a] (J2000)	Beam Size (")	Beam PA (°)	rms$_{^{13}\rm CO}$[b] (mJy)	rms$_{\rm C^{18}O}$[b] (mJy)	rms$_{\rm C}$ (mJy)	PA (°)	i^a (°)	$v_{\rm LSR}$ (km/s)
HD135344B	15:15:48.42 -37:09:16.4	0.26×0.21	46	9.8	14	0.26	63	16	7.25
SR21	16:27:10.27 -24:19:13.0	0.25×0.19	-65	6.4	8.9	0.12	14	16	3.0
DoAr44	16:31:33.46 -24:27:37.5	0.25×0.19	-65	6.8	8.9	0.14	30	20	4.35
IRS48	16:27:37.18 -24:30:35.4	0.19×0.15	87	23	25	0.59	100	50	4.55

Notes. [(a)] Derived from the ^{13}CO channel maps. [(b)] Measured in 0.5 km s^{-1} bins

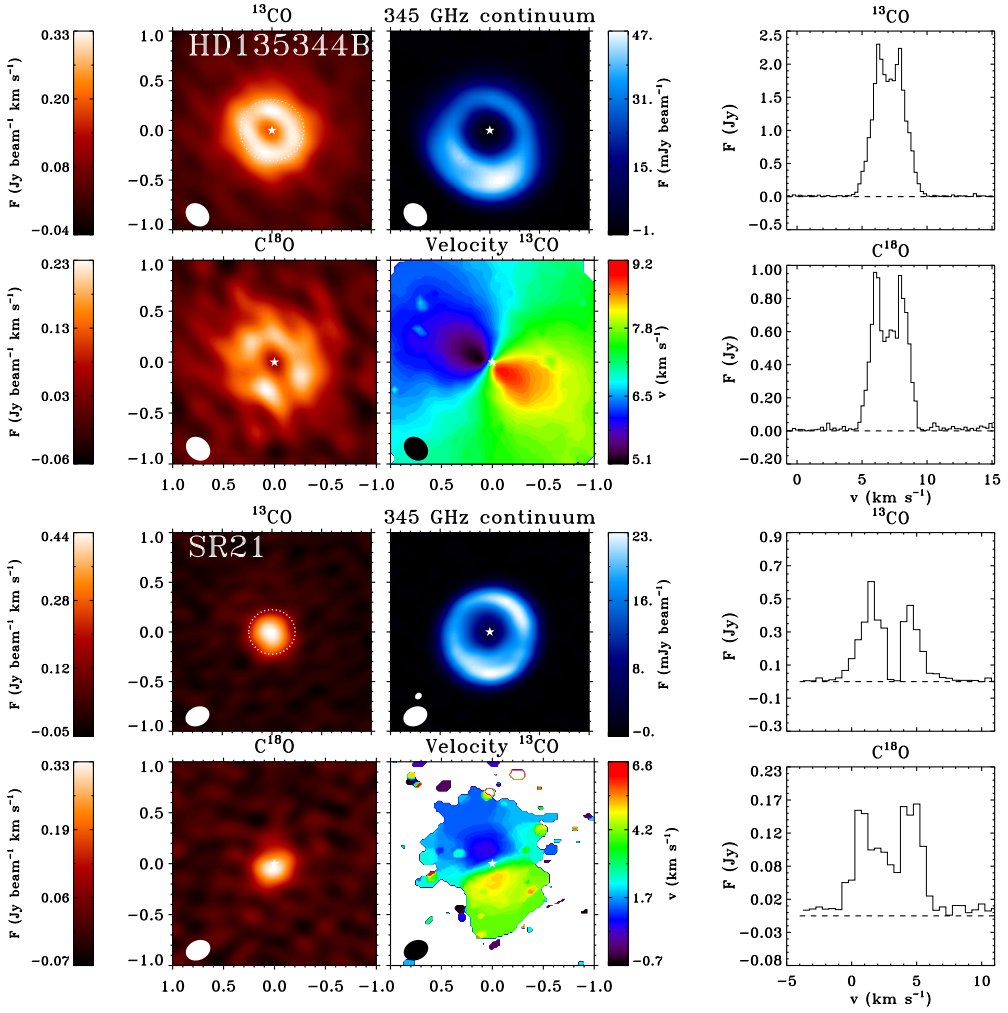


Figure 7.1: *ALMA observations of the continuum, ^{13}CO and $C^{18}O$ 3-2 lines of the first two targets.* **Top left:** *zero-moment ^{13}CO map.* **Top middle:** *Continuum map;* **Top right:** *^{13}CO spectrum integrated over the entire disk;* **Bottom left:** *zero-moment $C^{18}O$ map;* **Bottom middle:** *first moment ^{13}CO map (velocity map);* **Bottom right:** *$C^{18}O$ spectrum integrated over the entire disk. The beam is indicated in each map by a white ellipse in the lower left corner. The dotted white ellipse indicates the dust cavity radius.*

To date, only one transitional disk has been observed and analyzed in rotational CO isotopologue transitions (Perez et al. 2015). In this paper, we present ALMA Cycle 1 and 2 observations of CO isotopologues ^{13}CO and C^{18}O at $\sim 0.2 - 0.25''$ resolution of 4 additional well-studied transitional disks: SR 21, HD135344B, DoAr44 and IRS 48. For IRS 48, the 6–5 transitions are observed, for the other disks the lower 3–2 transitions. Apart from DoAr44, these disks were previously analyzed with DALI using ^{12}CO ALMA observations (Bruderer et al. 2014; van der Marel et al. 2015c). The derived models will be used as a starting point for analysis of the isotopologues. With DALI we determine a gas density structure that is consistent with the CO observations, SED and continuum dust interferometry. Information on the hot gas and dust from the literature is included. The goals of this study are to determine the

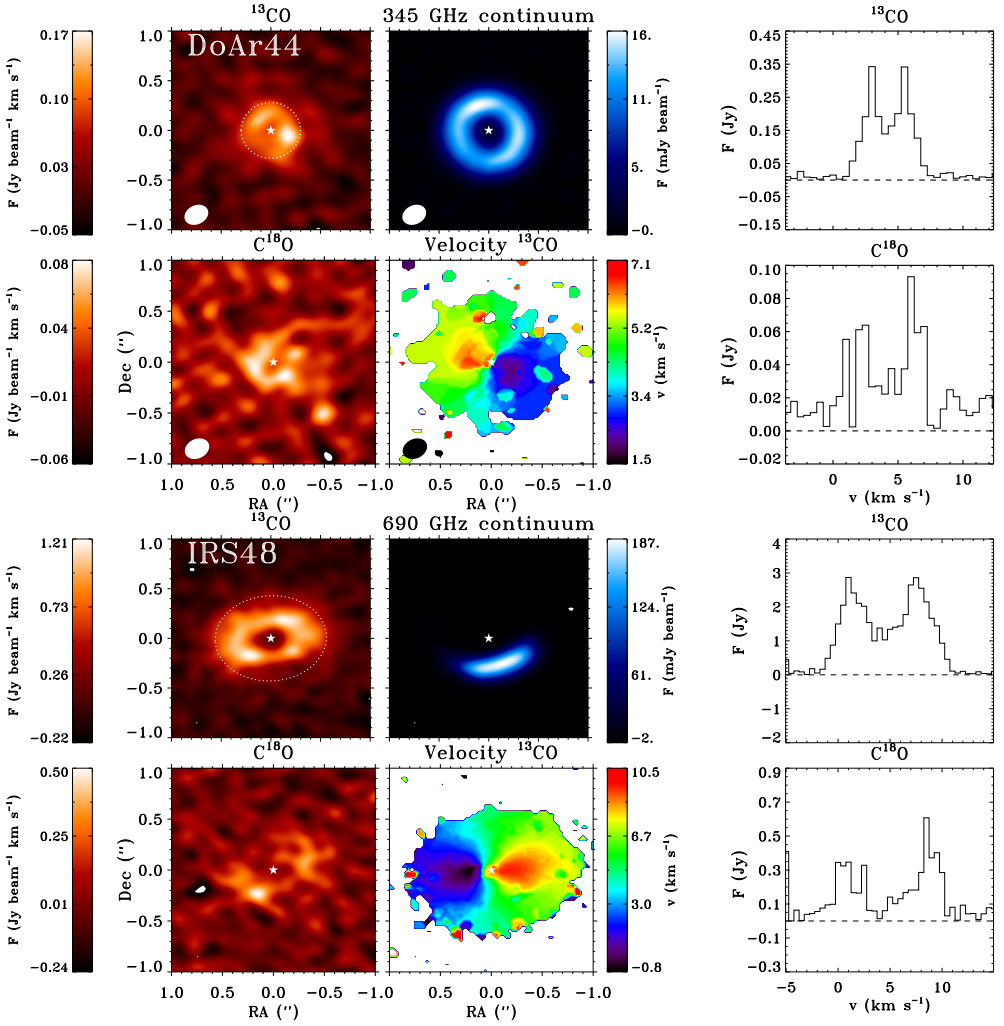


Figure 7.2: *ALMA observations of the continuum, the ^{13}CO and $C^{18}O$ 6-5 lines of the third and fourth target.* **Top left:** *zero-moment ^{13}CO map.* **Top middle:** *Continuum map;* **Top right:** *^{13}CO spectrum integrated over the entire disk;* **Bottom left:** *zero-moment $C^{18}O$ map;* **Bottom middle:** *first moment ^{13}CO map (velocity map);* **Bottom right:** *$C^{18}O$ spectrum integrated over the entire disk. The beam is indicated in each map by a white ellipse in the lower left corner. The dotted white ellipse indicates the dust cavity radius.*

gas surface density profile, specificially the size, depth and shape of the gas density structure inside the dust cavity in order to constrain the properties of the embedded planets.

The paper is structured as follows. In Section 7.2.1 we describe the details of the ALMA observations. In Section 7.2.2 we present moment maps of the ^{13}CO and ^{18}CO observations. The modeling approach is presented in Section 7.3. Section 7.4 presents the modeling results. Section 7.5 discusses the implications for embedded planets in the disk.

7.2 Data

The observations were obtained during ALMA Cycle 1 and 2 in June and July 2014, with baselines ranging from 20 to 1100 m, probing scales from 0.15 to 8 arcseconds. The sources and their properties are summarized in Table 7.2.

7.2.1 Observational details

The disks SR 21, HD 135344B and DoAr 44 were observed in ALMA Cycle 1 program 2012.1.00158.S (PI van Dishoeck) in Band 7 (~335 GHz or 896 μm) in the C32-5 configuration. The observations were taken in four spectral windows of 3840 channels: three windows have a bandwidth of 469 MHz (channel width 122 kHz, equivalent to 0.1 km s^{-1}), centered on the ^{13}CO 3–2, C^{18}O 3–2 and CN 3–2 transitions with rest frequencies of 330.58796, 329.33056 and 340.24778 GHz, respectively. The fourth spectral window was centered on 342.15000 GHz with a bandwidth of 1875 MHz (channel width 488 kHz, equivalent to 0.5 km s^{-1}) aimed at higher continuum sensitivity. The total continuum bandwidth was ~3.2 GHz. For HD135344B, the flux was calibrated using Ceres, and J1427-4206 was used for calibration of both bandpass and gain. SR 21 and DoAr 44 were observed in one scheduling block, with Titan as flux calibrator, J1517-2422 as bandpass calibrator and J1625-2527 as gain calibrator. In both objects, the flux calibrator (Ceres resp. Titan) is highly resolved on long baselines. The gain calibration on the flux calibrator was thus performed using a subset of the antennas. The total on-source integration time was 30 minutes each for SR 21 and DoAr 44, and 54 minutes for HD 135344B.

IRS 48 was observed in ALMA Cycle 2 program 2013.1.00100.S (PI van der Marel) in Band 9 (~680 GHz or 440 μm) in the C34-3 configuration. The observations were taken in four spectral windows of 1920 channels: three windows with a bandwidth of 937.5 MHz (channel width 488 kHz or 0.3 km s^{-1}), centered on the ^{13}CO 6–5, C^{18}O 6–5 and H_2CO 9–8 transitions with rest frequencies of 661.067276, 658.553278 and 674.80978 GHz, respectively. The fourth spectral window was centered on 672 GHz with a bandwidth of 1875 MHz (channel width 977 kHz or 0.5 km s^{-1}) aimed at higher continuum sensitivity. The total continuum bandwidth was ~4.7 GHz. The flux was calibrated using J1517-243, the bandpass with J1427-4206 and the gain with J1626-2951. J1700-2610 was set as secondary gain calibrator, but not used in the final calibration. The total on-source integration time was 52 minutes.

The data were calibrated and imaged in CASA version 4.2.1. Given the high signal-to-noise ratio of these observations amplitude and phase self-calibration was performed after standard phase referencing. The data were cleaned using Briggs weighting with a robust of 0.5, resulting in a beam size of $\sim 0.25'' \times 0.20''$ (Cycle 1 data) and $\sim 0.19'' \times 0.15''$ (Cycle 2 data). Table 7.2 lists the observational properties of the continuum and spectral line maps of the imaging results.

7.2.2 Continuum and line maps

Figures 7.1 and 7.2 show the zero-moment ^{13}CO and C^{18}O maps and spectra, the velocity map (first moment) of the ^{13}CO and the continuum. The spectrum was extracted from the region of the zero-moment map size. Channel maps of the ^{13}CO emission are given in the Appendix. Three of the four sources, HD135344B, DoAr44 and IRS48, show a clear hole in the ^{13}CO and C^{18}O images (Figure 7.1 and 7.2), that was not seen in ^{12}CO (van der Marel et al. 2015c). IRS48 shows a full gas ring in ^{13}CO, which does not suffer from foreground absorption found

in the ^{12}CO (Bruderer et al. 2014). On the other hand, the foreground absorption absorption seen in the ^{12}CO emission of SR 21 (van der Marel et al. 2015c) also affects the ^{13}CO spectra.

All CO data reveal rotating gas disks with inclination >15°, with a double-peaked velocity profile. The gas rings for HD135344B, DoAr44 and IRS 48 are in all cases smaller than the continuum cavities, as shown directly in the ^{13}CO panels in Figure 7.1 and 7.2 and in the radial cuts in Figure 7.3. The emission inside the gas cavities is at least a factor of 2 lower than in the surrounding rings. In contrast, SR 21 does not appear to have a cavity in the gas at this spatial resolution. The peak S/N in the integrated maps is 12-30 for the ^{13}CO and 5-20 for C^{18}O.

The ^{13}CO channel maps and velocity maps are used to derive the stellar position, the position angle, inclination and source velocity, which are within errors consistent with the values derived from the ^{12}CO data (van der Marel et al. 2015c). The derived parameters are given in Table 7.2.

The continuum images show ring-like structures for SR21, HD135344B and DoAr44, and a highly asymmetric structure for IRS 48, as seen in previous Cycle 0 data (van der Marel et al. 2013). The S/N on the continuum ranges between 130 and 500 for the different disks. The Band 7 continuum data of SR21 and HD135344B show minor azimuthal asymmetries with a contrast of less than a factor 2, similar to the Band 9 continuum (Pérez et al. 2014; van der Marel et al. 2015c), although the asymmetry in SR21 appears to be less pronounced in Band 7 than in Band 9. The Band 9 and Band 7 continuum images are compared and analyzed in Pinilla et al. (2015b). The continuum emission in IRS 48 is discussed in van der Marel et al. (2015a). The DoAr44 continuum emission is azimuthally symmetric.

7.3 Modeling

7.3.1 Physical model

As a starting point for our models we adopt the physical structure suggested by Andrews et al. (2011), as implemented by Bruderer (2013) and fully described in van der Marel et al. (2015c). The surface density $\Sigma(r)$ is assumed to be a radial power-law with an exponential cut-off following the time-dependent viscosity disk model $\nu \sim r^{\gamma}$ with $\gamma = 1$ (Lynden-Bell & Pringle 1974; Hartmann et al. 1998)

$$\Sigma(r) = \Sigma_c \left(\frac{r}{r_c}\right)^{-\gamma} \exp\left(-\left(\frac{r}{r_c}\right)^{2-\gamma}\right) \tag{7.1}$$

The gas and dust follow the same density profile, but the gas-to-dust ratio is varied throughout the disk, as shown in Figure 7.4. Inside the cavity, the dust density is zero, apart from the inner disk, which is set by $\delta_{\rm dust}$. The gas density inside the cavity is varied with drops $\delta_{\rm gas}$. In the outer disk, the gas-to-dust ratio is set by a constant number. The vertical structure is defined by the scale height h_c and the flaring angle ψ, following $h(r) = h_c(r/r_c)^{\psi}$. The fraction of large grains $f_{\rm ls}$ and the scale height of the large grains χ are used to describe the settling. More details on the star, the adopted stellar UV radiation, the dust composition and vertical structure are described in van der Marel et al. (2015c).

7.3.2 Model fitting approach

The best fit models from van der Marel et al. (2015c) are used as initial model for the vertical structure and dust density structure for SR21 and HD135344B, based on a combination of

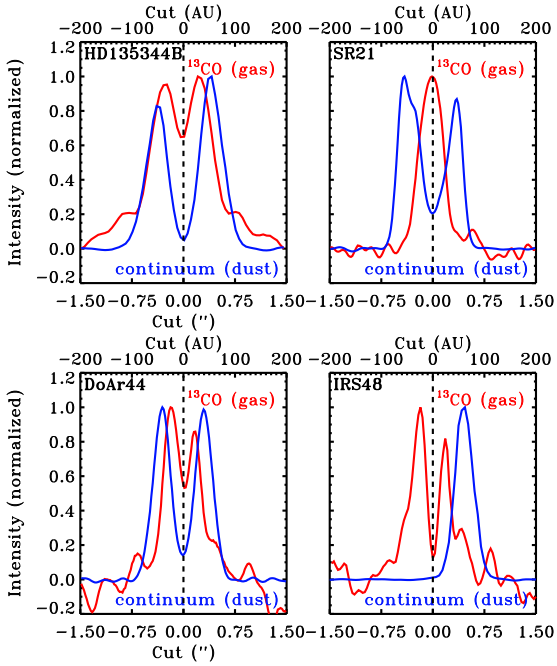


Figure 7.3: *Normalized intensity cuts through the major axis of each disk of the ^{13}CO 3-2 emission (red) and the dust continuum emission (blue). In case of IRS48, the deprojected intensity cut of the minor axis is taken, to cover the (asymmetric) continuum profile. The cuts clearly reveal that the gas cavity radii are smaller than the dust cavity radii.*

SED, dust 690 GHz continuum visibility and ^{12}CO 6–5 modeling. The dust density inside the cavity (between $r_{\rm gap}$ and $r_{\rm cavdust}$) is set to be entirely empty of dust grains. SR21 is an exception: a small amount of dust is included between 7 and 25 AU, following van der Marel et al. (2015c). The dust structure of DoAr44 was analyzed in a similar way in Appendix 7.A through SED and dust 345 GHz continuum visiblity modeling. For IRS48, we use the model derived by Bruderer et al. (2014), although we choose to use an exponential power-law density profile instead of a normal power-law, to be consistent with the other three disks in this study.

The outer disk CO emission and submillimeter continuum flux are fit simultaneously by varying Σ_c and the gas-to-dust-ratio GDR. The outer radius $r_{\rm out}$ is set by fitting the CO spectrum (the maxima in the spectra or double peaks, arising from the Keplerian motion) and provides outer boundaries for computing the gas masses. Using this surface density profile, the emission inside the cavity is constrained by the δ parameters (Figure 7.4). The near infrared excess determines the dust density in the inner disk through $\delta_{\rm dust}$. The gas cavity radius $r_{\rm cavgas}$ and drop $\delta_{\rm gas2}$ are fit to the CO emission. In some cases, an additional drop in gas surface density is required between $r_{\rm cavgas}$ and the dust cavity radius $r_{\rm cavdust}$. This drop is indicated by $\delta_{\rm gas}$.

The main parameters that are varied are the gas cavity radius $r_{\rm cavgas}$ and the drop in gas density $\delta_{\rm gas2}$ between $r_{\rm sub}$ and $r_{\rm cavgas}$. The CO isotopologues provide better constraints on the density than the ^{12}CO because they are less optically thick (^{13}CO) or even optically thin (C^{18}O). The effects of isotope-selective photodissociation are properly considered in the modeling and discussed in Section 7.4.3.

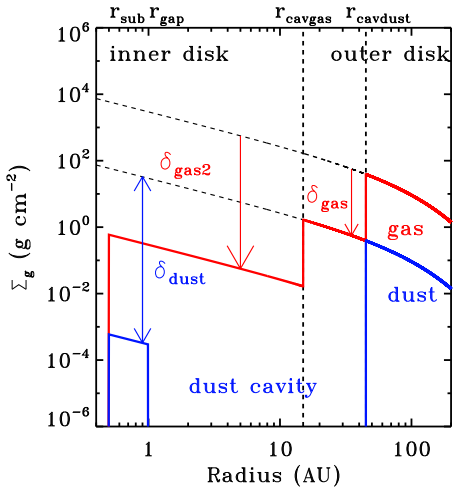


Figure 7.4: *Generic surface density profile for the gas and dust.*

7.4 Results

Data and models are compared through the spectra and the zero moment maps (intensity maps) of both ^{13}CO and C^{18}O. For each target we show the direct comparison of the images of the intensity map of the best fit model, and the constraint on both $r_{\rm cavgas}$ and $\delta_{\rm gas2}$ through spectra and intensity cuts through the major and minor axis of the zero-moment map.

In three of the four targets an inner gas cavity (smaller than the dust cavity) was required to fit the data. In SR21 the 7 AU cavity previously derived from rovibrational emission was adopted, but no gas cavity is resolved at the spatial resolution of $\sim$ 0.2" in our observations. The depth is constrained to within an order of magnitude and the cavity size to within $\pm$5 AU, mainly through the comparison of the spatially resolved emission, but further confirmed by the line wings in the spectra. In the intensity cuts in Figure 7.5 the $\delta_{\rm gas2}$ parameter is varied. The comparison shows that the uncertainty on the density drop is less than an order of magnitude. In Appendix 7.C we show the intensity cuts for larger and smaller gas cavity radii, respectively. These plots show that the uncertainty on the gas cavity radius is typicall $\lesssim$5 AU. Furthermore, in both SR21 and DoAr44 an additional drop $\delta_{\rm gas}$ between $r_{\rm cavgas}$ and $r_{\rm cavdust}$ is required to fit the data.

The models of the ^{12}CO fits of van der Marel et al. (2015c) fit remarkably well the isotopologue data in the outer disk. Only minor corrections in surface density and gas-to-dust-ratio were required to fit the new data. However, inside the cavity the previously derived results for the gas surface density were found to be inconsistent. A modest drop in the gas density inside the dust cavity radius $r_{\rm cav}$ was sufficient to explain the ^{12}CO data but no gas cavity was seen. Since the gas cavity becomes visible in the isotopologue data and turns out to be smaller than the dust cavity radius, the gas cavity radius $r_{\rm cavgas}$ could be fit independently of the depth.

7.4.1 Results of individual targets

HD135344B

HD135344B shows a clear gas cavity, both in ^{13}CO and C^{18}O images, which is significantly smaller than the dust cavity (see top two panels of Figure 7.1). The modeling constrains the gas

Table 7.3: *Results for the gas density profile of each transition disk.*

	Parameter	HD135344B	SR21	DoAr44	IRS48
Surface	r_c (AU)	25	15	25	60
density	Σ_c (g cm^{-2})	120	400	60	0.5
	GDR	80	100	100	12
	$M_{\rm dust}^{(a)}$ ($10^{-3} M_\odot$)	0.13	0.075	0.05	0.015
	$M_{\rm gas}^{(a)}$ ($10^{-3} M_\odot$)	15	7.7	2.5	0.55
Radial	$r_{\rm cavgas}$ (AU)	30	7	16	25
structure	$\delta_{\rm gas2}$	$2{\cdot}10^{-4}$	10^{-20} (b)	$\leq 10^{-4}$	$\leq 10^{-3}$
	$r_{\rm cavdust}$ (AU)	40	25	32	60
	$\delta_{\rm gas}$	1	$5 \cdot 10^{-2}$	10^{-2}	1
	$r_{\rm out}$ (AU)	125	60	60	90
Inner	$r_{\rm sub}$ (AU)	0.18	0.18	0.08	0.4
disk	$r_{\rm gap}$ (AU)	0.25	1.0	1.0	1.0
	$\delta_{\rm dust}$ (AU)	$2{\cdot}10^{-4}$	$1{\cdot}10^{-6}$	$1{\cdot}10^{-2}$	$1{\cdot}10^{-3}$
Vertical	h_c (rad)	0.15	0.07	0.1	0.14
structure	ψ	0.05	0.15	0.1	0.22
	$f_{\rm ls}$	0.95	0.85	0.85	0.85
	χ	0.8	0.2	0.2	0.2

Notes. a) The masses are only constrained within $r_{\rm out}$ for the detected surface brightness. b) The drop inside 7 AU could not be constrained by the ALMA data, we adopt the value from CO rovibrational spectroastrometry by Pontoppidan et al. (2008).

cavity radius to 30 AU (dust cavity radius is 40 AU) and the drop is $2 \cdot 10^{-4}$ (top right panels in Figure 7.5). Previously, the model based on the ^{12}CO data required $\delta_{\rm gas}$ of 10^{-1} – 10^{-2} for a cavity radius of 40 AU. A 30 AU gas cavity was also derived in van der Marel et al. (2015c) considering the inner radius of the small dust grains derived from the scattered light emission (Garufi et al. 2013), but a $\delta_{\rm gas}$ value as low as $\sim 10^{-4}$ underproduces the ^{12}CO emission inside the cavity. As the ^{12}CO is optically thick and mainly traces the temperature at the $\tau = 1$ surface, this new result suggests that the temperature structure is somewhat higher than in our model, perhaps due to some residual dust in the cavity or the vertical structure (Bruderer 2013).

The residual of the ^{13}CO emission (image panels in Figure 7.5) shows that the model overpredicts the emission in the outer disk (>0.5"). On the other hand, the C^{18}O residual has an underprediction of the emission in the outer disk. The residuals are spatially insignificant, but integrated over the whole disk they are likely related to real structure. Because the ^{13}CO emission is optically thick and therefore more sensitive to the temperature (and thus vertical) structure, this can be related to the same change in density structure. The radius of $\sim$ 100 AU coincides with that of one of the spiral arms observed in scattered light observations, which have been suggested to be launched by a planet in the outer disk (Muto et al. 2012). If there is indeed a planet at this large orbit, it is expected to clear a gap in the gas, which could possibly explain the structure in the outer disk. As the focus of this study is only on the emission inside the dust cavity, this is not investigated further.

SR21

Unlike the other disks, the CO emission in SR21 does not appear to have a cavity. Rovi-

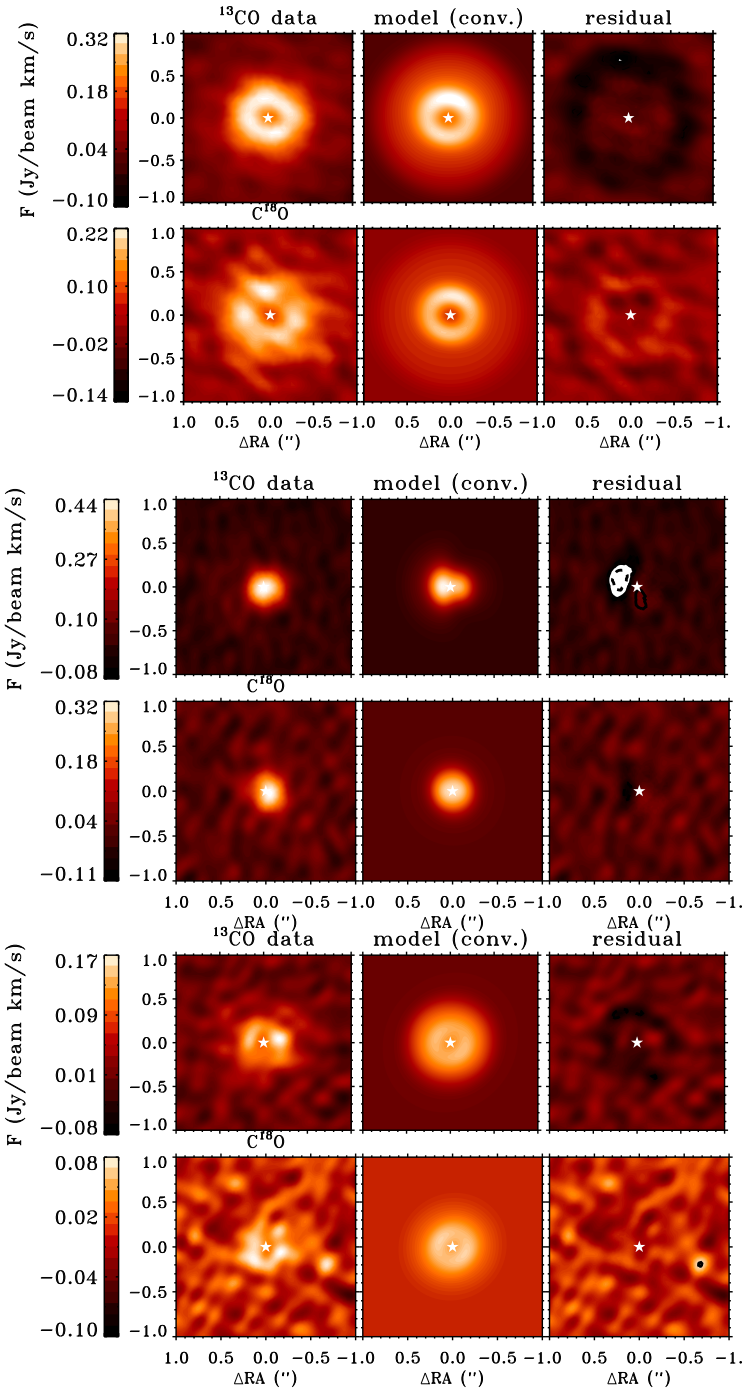


Figure 7.5: *Modeling results and observations of the ^{13}CO and $C^{18}O$ emission for the best fitting models in derotated images and spectra. These panels show the direct image comparison of the zero-moment map: derotated observations, model, convolved model and residual. In the residual map the overlaid contours indicate the 3σ levels, where dashed lines are negative.*

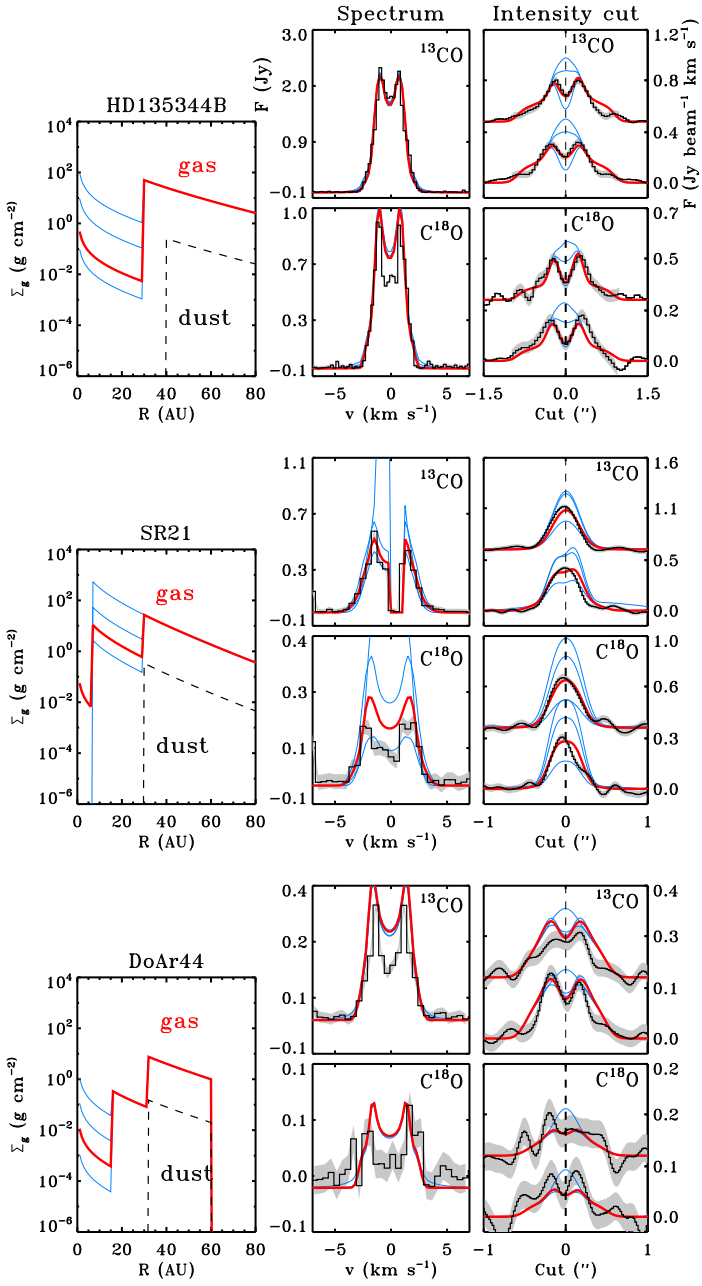


Figure 7.5: *Modeling results and observations of the ^{13}CO and $C^{18}O$ emission for the best fitting models in derotated images and spectra. The left panels show the gas density profiles with different δ_{gas2} drops in solid lines and the dust density profile in dashed lines. The right panels show the resulting intensity cuts for major and minor axis for both ^{13}CO and $C^{18}O$. The best-fitting model is indicated in red, other δ_{gas2} values in blue. The drop in density can be constrained to within an order of magnitude.*

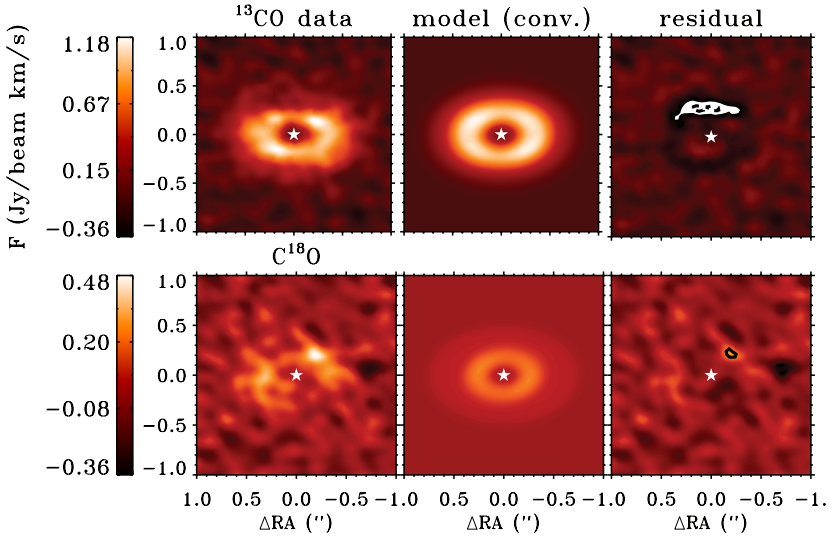


Figure 7.5: *Continued.*

brational CO emission suggests a gas cavity of 7 AU radius (Pontoppidan et al. 2008), which remains unresolved at the ALMA spatial resolution (14 AU diameter~0.12”). The physical model includes this 7 AU cavity. The ^{12}CO emission already indicated a drop in density between 7 AU and the dust cavity radius of 25 AU. The intensity cuts of the CO isotopologues also suggest a drop in density considering the strength of the emission (right panels in Figure 7.5). According to the model fitting, this drop is about two orders of magnitudes.

DoAr44

DoAr44 is the only disk in this study with a symmetric dust ring. The dust cavity radius was found to be 32 AU (see Section 7.A), using the same modeling approach as in van der Marel et al. (2015c). The cavity size and disk mass are similar to previous studies of SMA 345 GHz continuum data (Andrews et al. 2011). The drop in dust density inside the cavity ($\delta_{\rm dustcav}$) is at least a factor 1000. The CO isotopologue intensity maps have low signal to noise compared to the other disks, likely due to the lower disk mass, but still show a gas cavity that is only half the size of the dust cavity: 16 AU. The $\delta_{\rm gas2}$ inside 16 AU is at most 10^{-4}. An additional drop in gas density between 16 and 32 AU of 10^{-2} is required to fit the emission.

IRS48

The CO isotopologue emission in IRS48 confirms the presence of a gas cavity with a considerably smaller radius than that of the peak of the dust asymmetry (60 AU), as found by Bruderer et al. (2014), consistent with the 30 AU gas ring found in rovibration CO emission (Brown et al. 2012a). In order to be consistent with the models of the other disks, we assume a radial power-law with exponential cut-off rather than a simple power-law as done by Bruderer et al. (2014), but a similar vertical structure, density structure and mass are found as in their study. Because DALI considers only axisymmetric models, the millimeter continuum asymmetry is not fit: the total submillimeter flux, the VISIR 18μm image and the SED are again used to constrain the dust density and dust cavity radius. The gas cavity radius is found to be 25 rather than 20 AU found by Bruderer et al. (2014), and no additional drop in density

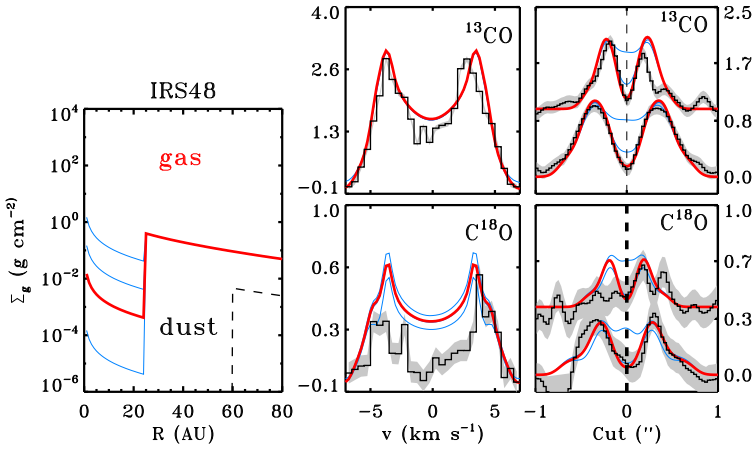


Figure 7.5: *Continued.*

is required to fit the emission (right panels in Figure 7.5).

^{13}CO shows a full ring of emission. However, the emission is weaker at the location of the dust trap, as seen in the residual image (image panels in Figure 7.5). The ^{13}CO emission is barely optically thick at the dust trap radius of 60 AU (the $\tau = 1$ surface is at the midplane) and the drop in emission is likely due to continuum optical depth or a drop in temperature due to the local increase of dust density. The S/N of the C^{18}O emission is too low to show the gas ring or this local drop in emission, but the data have been used to set constraints on the gas density.

7.4.2 A gradual drop

The structure with two gas density drops inside the cavity found in DoAr44 and SR21 (and previously IRS 48, Bruderer et al. 2014) has been interpreted as implication of multiple planets at different orbits. An alternative explanation is a gradual drop or increasing surface density profile inside the cavity. In order to investigate this, we have run additional models where the exponential power-law $\Sigma(r)$ is replaced by an increasing exponential law between $r_{\rm cavdust}$ and $r_{\rm cavgas}$, motivated by planet-disk interaction models, following:

$$\Sigma(r) = \Sigma(r_{\rm cav}) \cdot e^{(r-r_{\rm cav2})/w} \tag{7.2}$$

where the width w is given by

$$w = \frac{r_{\rm cav} - r_{\rm cav2}}{\ln(\Sigma(r_{\rm cav})/\delta_{\rm gas2}\Sigma(r_{\rm cav2})} \tag{7.3}$$

The width is just chosen to connect $\Sigma(r)$ at $r_{\rm cavdust}$ and $r_{\rm cavgas}$, fitting $\delta_{\rm gas2}$, and no new parameters are introduced. This 'straight connection' is further motivated by the shape of the gaps in Figure 7 in de Juan Ovelar et al. (2013) of planet-disk interaction models. Using the above relation and the derived cavity radii, the drop in density is derived again for the best fitting model (see Figure 7.6). The best fitting values are within a factor of 2 of the $\delta_{\rm gas2}$ values in the vertical drop model (Tabel 7.3): we find $2{\cdot}10^{-4}$, 10^{-3}, $2{\cdot}10^{-4}$ and $5{\cdot}10^{-2}$ for HD135344B, SR21, DoAr44 and IRS48 respectively, although IRS48 is a poor fit compared

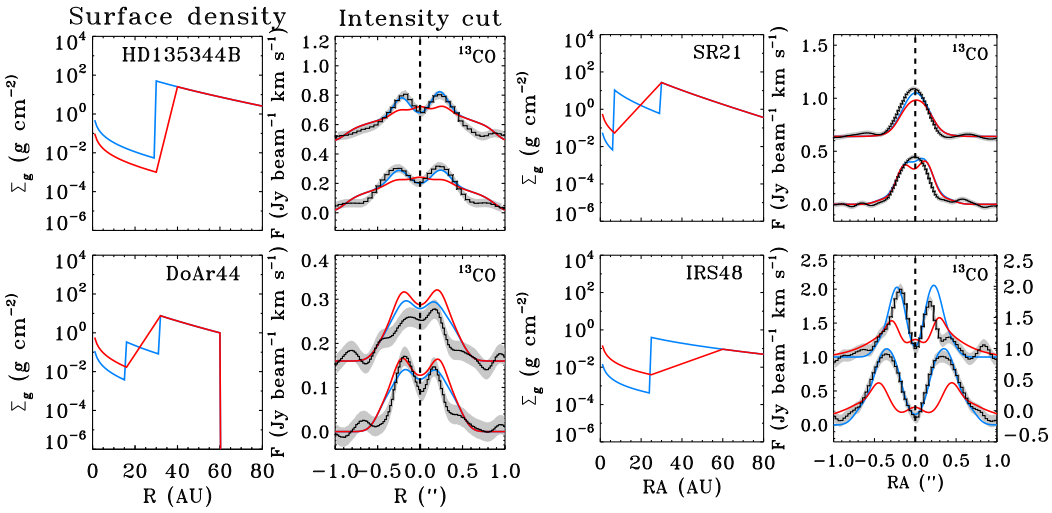


Figure 7.6: *Comparison of the intensity cuts between the best fit models (blue) and a gradual model (red) as defined in Equation 7.2. The right panel gives the density profile. All disks except IRS48 can be fit equally well with this gradual increase profile.*

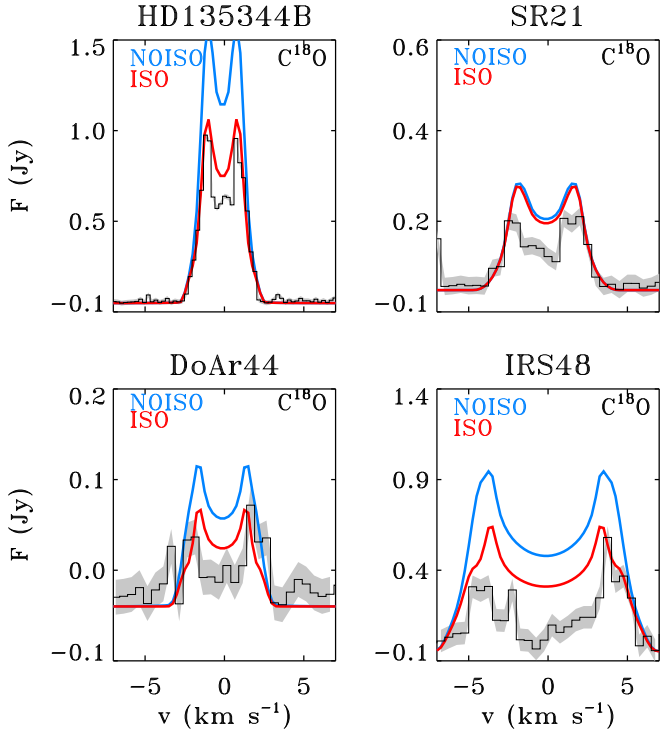


Figure 7.7: *Comparison of the spectra of the C^{18}O emission with (red, ISO) and without (blue, NOISO) implementing isotope-selective photodissociation. For HD135344B, DoAr44 and IRS48 there is a difference up to a factor of 2, while no difference is seen for SR21.*

to the double drop model. However, the outer radius of the slope ($r_{\rm cav}$) of 60 AU has been constrained from the SED and VISIR image rather than from the millimeter continuum as in the other disks, due to the asymmetric structure, making this approach rather uncertain.

7.4.3 Isotopologue selective photodissociation

The main process regulating the survival of CO in disks, photodissociation, does not equally affect different CO isotopologues (van Dishoeck & Black 1988). ^{12}CO becomes optically thick at low column densities and shield itself throughout the disk from the photodissociating flux. On the other hand, less abundant isotopologues, like C^{18}O, are not self-shielded until much deeper into the disk and continue being photodissociated. This results in regions where C^{18}O is less abundant than predicted by a constant [^{16}O/^{18}O] ratio found in the ISM. Accordingly, this leads to reduced C^{18}O line intensities. The importance of isotope selective effects varies depending disk parameters, dust properties and the stellar FUV field (Miotello et al. 2014).

For this reason, isotope-selective photodissociation has been implemented in the modeling of all disks in our sample. Isotope-selective effects are substantial only for C^{18}O line emission and in the outer disk regions, where the bulk of the gas phase CO is located (Figure 7.7). The effect on the outer disk emission is not detectable for SR21. On the other hand, IRS48 has an even lower disk mass but shows a significant difference. This may be related to the low gas-to-dust ratio in this disk. This shows how isotope-selective photodissociation depends on the combination of disk and stellar parameters and not only on the total disk gas mass.

Interestingly, isotope-selective photodissociation does not significantly affect the CO isotopologues emission from inside the cavity, likely because of the higher temperatures in that region. However, this is only true for conditions in these four disks. Possible effects in more extreme scenarios can not be excluded.

7.5 Discussion

The main outcome of Figure 7.3 and the modeling is that all four transition disks have gas inside the cavity, with a gas cavity that is smaller than the dust cavity (for SR21 adopted from Pontoppidan et al. (2008)). The CO isotopologues confirm the main result from the ^{12}CO data: gas is present inside the dust cavities and has a smaller decrease in density than the millimeter-dust. With the new optically thin isotopologue data, the density profiles are now much better constrained than based on just ^{12}CO data (van der Marel et al. 2015c).

Two other transition disks have been sufficiently spatially resolved in CO and continuum to also confirm a gas cavity smaller than the dust cavity: HD142527 (Fukagawa et al. 2013; Perez et al. 2015) and J1604-2130 (Zhang et al. 2014; van der Marel et al. 2015c). To date, no counterexample has been found for which the gas follows the same distribution as the dust. This hints at the exciting possibility that the origin of transition disks indeed lies in embedded planets that have cleared their orbit in the gas and trapped the millimeter-dust at the edge.

An upper limit on any embedded companions has been derived for HD135344B using direct imaging in Vicente et al. (2011): less than 1 brown dwarf mass at >37 AU radius. For SR21, companions with $q > 0.01$ or $> 10 M_{\rm Jup}$ are ruled out for 11-21 AU orbital radius according to near-infrared aperture masking interferometry (Andrews et al. 2011). For the other two disks no limits on companions are known. Unfortunately the derived limits are outside the orbital range suggested by our gas cavity radii, assuming the companion orbital radius is close to the gas cavity radius.

The difference between gas cavity radius and dust cavity radius can be compared with modeling results of planet-disk interaction by de Juan Ovelar et al. (2013). They show a relation between the observed dust cavity wall in the near infrared (SPHERE-ZIMPOL predictions), tracing the small dust grains, and the millimeter-dust cavity wall as observed by ALMA. Simulations were run for different planet masses at different radii (Figure 8 and Equation 1 in the mentioned paper). The simulations were performed assuming a viscosity of $\alpha \sim 10^{-3}$ for a disk of 0.05 $M_\odot$. The ratio between the two radii $f(M_p)$ is found to follow

$$f(M_p) = c \cdot \left(\frac{M_p}{M_{\rm Jup}}\right)^{\gamma} \tag{7.4}$$

with $c \sim 0.85$, and $\gamma \sim [-0.22, -0.18, -0.16]$ for planet orbital radius = [20, 40, 60] AU, respectively. Assuming that the small dust grains follow the gas, this relation can be applied directly to our cavity radii. The gas/dust cavity radii ratios for our targets are 0.75, 0.28, 0.5 and 0.42 for HD135344B, SR21, DoAr44 and IRS48, respectively, with gas cavity radii of 30, 7, 16 and 25 AU. Using the $\gamma = -0.22$ relation (closest to our gas cavity radii), planet masses are predicted to be 2, 11 and 25 $M_{\rm Jup}$ for HD135344B, DoAr44 and IRS48. For SR21, we extrapolate γ for the 7 AU gas cavity radius to be -0.26, resulting in a planet mass of 71 Jupiter masses. The derived masses remain uncertain due to the fixed viscosity in the models: a lower viscosity would result in lower masses.

Another way to compare the observations with planet-disk interactions models is using the $\delta_{\rm gas2}$ drop value. The outcome of the gradual drop model is particularly interesting as it is a better resemblance to the shape of the gap carved by a planet as seen in planet-disk interaction simulations (Crida et al. 2006; Zhu et al. 2011; de Juan Ovelar et al. 2013; Fung et al. 2014). Fung et al. have derived an analytical prescription based on the outcome of numerical simulations of the depth of the gap, which can set constraints on the mass of the planet in combination with the viscosity in their Equation 14:

$$\Sigma_{\rm gap}/\Sigma_0 = 4.7 \times 10^{-3} \left(\frac{q}{5 \times 10^{-3}}\right)^{-1} \left(\frac{\alpha}{10^{-2}}\right)^{1.26} \left(\frac{h/r}{0.05}\right)^{6.12} \tag{7.5}$$

with q the mass ratio between planet and star, α the viscosity parameter, h/r the scale height and $\Sigma_{\rm gap}/\Sigma_0$ the drop in density, or $\delta_{\rm gas2}$. The equation is only valid for $q = 10^{-4} - 10^{-2}$. A similar relation was recently derived by Kanagawa et al. (2015). The derived parameters can thus provide an estimate for the planet mass, assuming a certain viscosity value. The relation has a very strong dependence on h/r, due to the strong dependencies of the torque on the disk angular frequency. Note that the disks of these simulations are isothermal to make h/r constant as a function of radius. Since the gas temperature has in reality a strong vertical gradient due to the UV heating, especially at the cavity wall, this makes Equation 5 uncertain. On the other hand, these processes are happening close to the midplane and the isothermal approximation is not entirely incorrect. In applying the relation to our findings, h/r is only marginally constrained by our models due to the degeneracies in SED modeling. As $h/r = c_s/v_k$, with the sound speed $c_s \propto \sqrt{T}$ and v_k the Keplerian velocity, it can be computed also directly from the derived midplane temperatures. We find h/r in our models using the midplane temperature at the gas cavity radius of 0.077, 0.063, 0.048 and 0.11 for HD135344B, SR21, DoAr44 and IRS48, respectively, which is generally not too far off from the h/r derived from our radiative transfer modeling. Using these values for h/r in combination with the $\delta_{\rm gas2}$ values derived for the gradual drop models for our disks, planet masses can be derived for α between 10^{-2} and 10^{-4}.

For $\alpha = 10^{-2}$, the q-values are > 0.01 (except for DoAr44), which is outside the range

for which the analytical relation was derived. Higher q-values, implying substellar mass companions, would result in eccentric gaps and/or entire disruption of the disk, which is why the relation is no longer valid. For reasonable planet masses (up to 10 Jupiter masses) that are consistent with the upper limits for companions mentioned above, this implies low viscosity values between $\alpha \sim 10^{-3}$ and 10^{-4}, much lower than found in the TW Hya and HD163296 disks based on turbulent broadening (Hughes et al. 2011).

The estimates derived here remain highly uncertain, due to the uncertainties in our modeling and the assumptions in the numerical models: the relation was empirically derived based on the outcome of numerical simulations with several important limitations: the vertical structure is isothermal, accretion onto the planet is ignored and the dust and gas are coupled, which is not true for a realistic physical disk. However, the $\delta_{\rm gas}$ or $\Sigma_{\rm gap}/\Sigma_0$, has been measured for the first time with an accuracy of better than an order of magnitude with these new observations. This parameter is inversely linear with q or planet mass and sets a constraint on the properties of these potential embedded planets.

7.6 Conclusions

In this work, we have analyzed high spatial resolution ALMA submillimeter observations of ^{13}CO and C^{18}O line emission from 4 transition disks using full physical-chemical modeling. Using a previously derived surface density model of the dust, based on the SED and millimeter continuum visibilities, a physical model of the gas and dust was derived for each of the disks. The structure and amount of gas inside the cavity is the main point of interest as it gives direct information about potential embedded planets.

1. All four disks show a gas cavity that is up to two times smaller in radius than the dust cavity. Two other examples are known from the literature.

2. All disks can be fit to a gas density model with one or two drops in the gas density inside the cavity.

3. The gas density drop inside the cavity is at least a factor of 1000 compared to the gas surface density profile of the outer disk.

4. An alternative model with an gradual increase of surface density with radius inside the cavity fits the data equally well for three of the four disks.

5. The derived values of the gas mass from the CO isotopologues are within a factor of a few compared to previously derived values from spatially resolved ^{12}CO observations, submillimeter continuum and a gas to dust ratio of 100. The isotopologues are however crucial for the gas density profile inside the cavity.

6. The depth of the gas density drop indicates that the viscosities in these disks are low for reasonable companion masses.

7.A Dust model DoAr44

Unlike the other disks, the dust surface density profile of DoAr44 was not yet constrained by ALMA data from previous papers. Using the same approach as in (van der Marel et al. 2015c), a model was found by fitting the SED, the 345 GHz continuum visibility curve and the 345 GHz continuum intensity cuts. The cavity size is 32 AU, similar to the previous result by Andrews et al. (2011). The depth of the dust density inside the cavity was constrained by varying the $\delta_{\rm dustcav}$ between $r_{\rm gap}$ and $r_{\rm cavdust}$. It was found that the dust density drops by at least a factor 10^3, similar to the other disks.

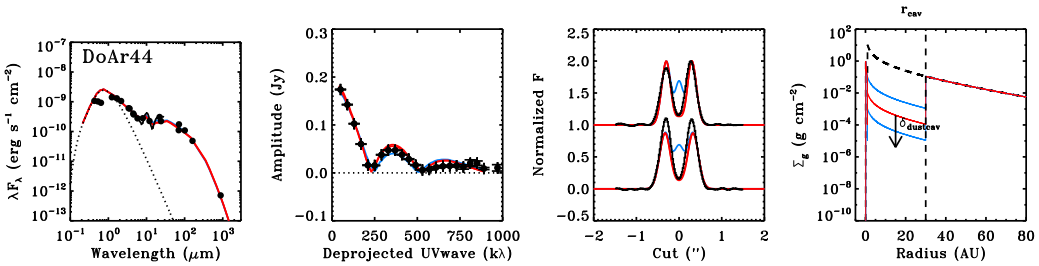


Figure 7.8: *Modeling results and observations of DoAr44 of the dust surface density, comparing* δdustcav *ranging between* 10^{-2} *and* 10^{-4} *as indicated in the right panel. The observations are plotted in black.* **Left:** *Spectral Energy Distribution;* **middle left:** *Amplitude of the 345 GHz continuum visibility for the deprojected baselines. The null line is indicated with a dashed line;* **middle right:** *Normalized intensity cuts through the major (bottom) and minor (top) axis of the 345 GHz continuum image. The model images are convolved with the same beam as the ALMA observations;* **right:** *The dust surface density profile. Indicated are the* $\delta_{\rm dust}$ *, the drop in density to fit the inner disk through the near infrared emission, and* $\delta_{\rm dustcav}$ *, the minimum drop in dust density inside the cavity to fit the observations.*

7.B Channel maps

In this section we present the ^{13}CO channel maps for each observed target.

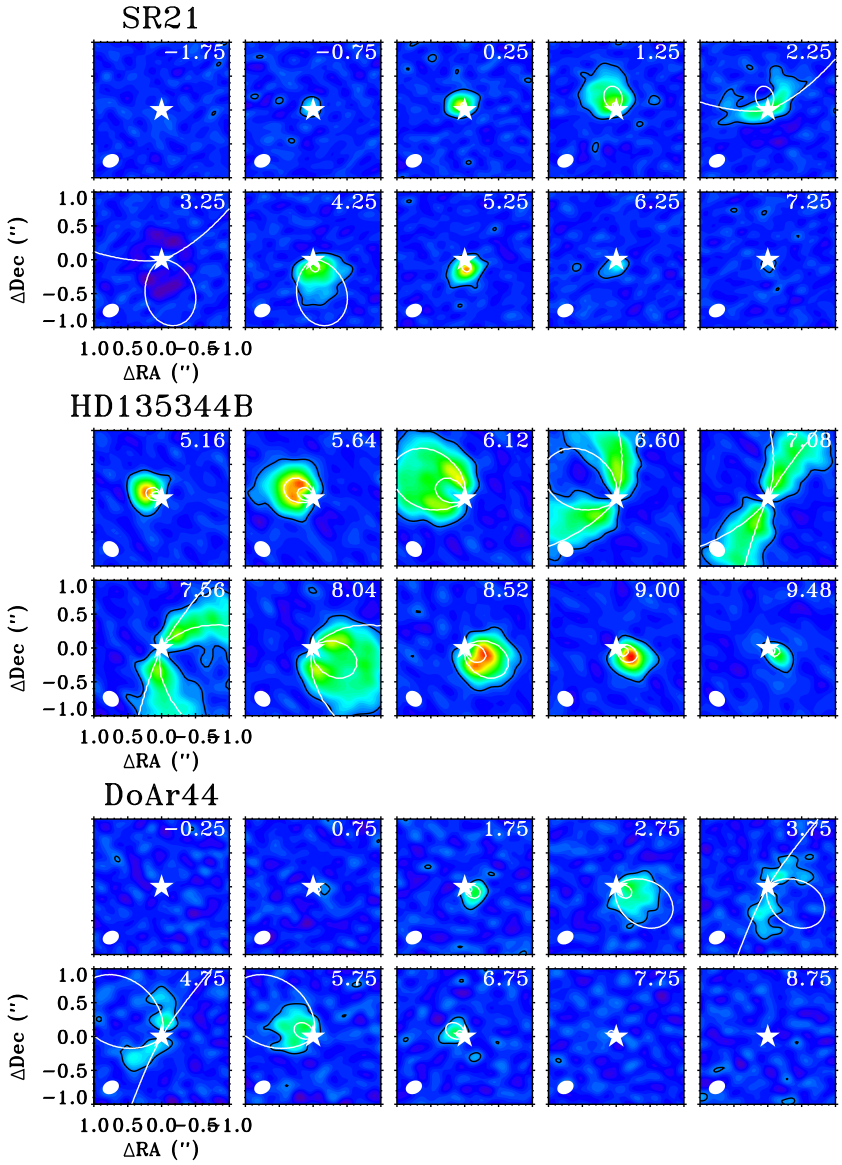


Figure 7.9: *^{13}CO channel maps for each observed target. Overlaid in white contours are the Keplerian velocity profiles for the derived inclination and given stellar mass.*

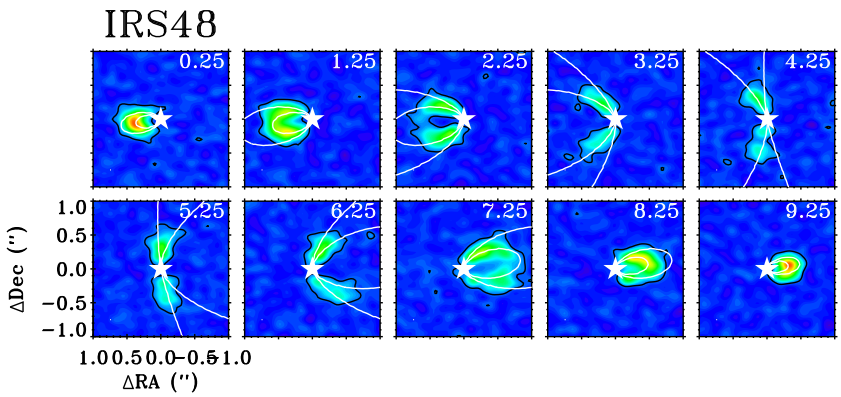


Figure 7.9: *Continued.*

7.C Additional models

Figure 7.10 shows the modeling results for ^{13}CO for the baseline model (Table 7.3) for different gas cavity sizes. The plots demonstrate that the gas cavity radius is determined to within 5 AU uncertainty.

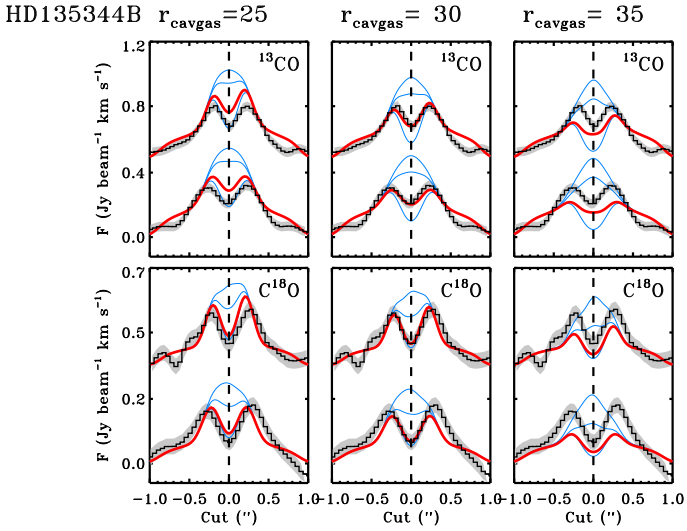


Figure 7.10: *Modeling results for different cavity sizes. The plots show the ^{13}CO intensity cuts of the data (black) and the models (colors) for different density drops $\delta_{\rm gas2}$. The central panel uses the gas cavity size $r_{\rm cavgas}$ of the final model (see Table 7.3), the left panel the results for a 5 AU smaller gas cavity and the right panel the results for a 5 AU larger cavity. For SR21 the 7 AU radius remains unresolved in the ALMA data so the radius is not explored. The plots reveal that the gas cavity radius is determined to within 5 AU uncertainty.*

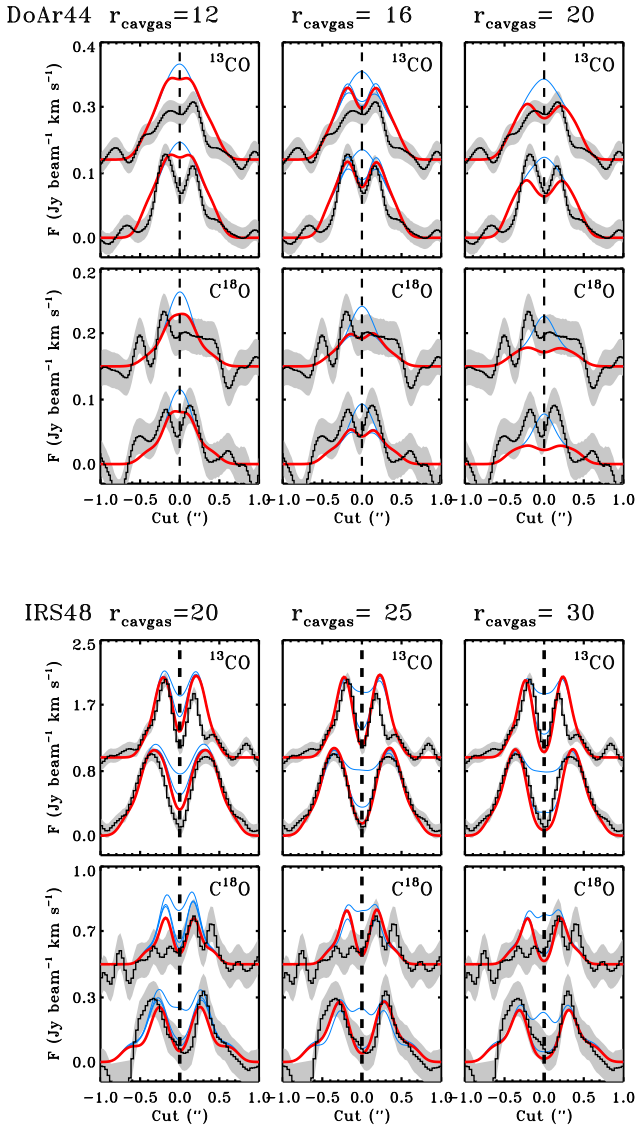


Figure 7.10: *Continued.*

Acknowledgements. The authors would like to thank P. Pinilla for useful discussions. Astrochemistry in Leiden is supported by the Netherlands Research School for Astronomy (NOVA), by a Royal Netherlands Academy of Arts and Sciences (KNAW) professor prize, and by the European Union A-ERC grant 291141 CHEMPLAN. This paper makes use of the following ALMA data:
ADS/JAO.ALMA/2012.1.00158.S. ALMA is a partnership of ESO (representing its member states), NSF (USA) and NINS (Japan), together with NRC (Canada) and NSC and ASIAA (Taiwan), in cooperation with the Republic of Chile. The Joint ALMA Observatory is operated by ESO, AUI/NRAO and NAOJ.

8

Warm formaldehyde in Oph IRS 48

van der Marel, N.; van Dishoeck, E. F.; Bruderer, S.; van Kempen, T. A. *Warm formaldehyde in the Ophiuchus IRS 48 transitional disk.* 2014, A&A, 563, 113V

Abstract

Simple molecules such as H_2CO and CH_3OH in protoplanetary disks are the starting point for the production of more complex organic molecules. So far, the observed chemical complexity in disks has been limited because of freeze-out of molecules onto grains in the bulk of the cold outer disk. Complex molecules can be studied more directly in transitional disks with large inner holes because these have a higher potential of detection through the UV heating of the outer disk and the directly exposed midplane at the wall.We used Atacama Large Millimeter/submillimeter Array (ALMA) Band 9 (~680 GHz) line data of the transitional disk Oph IRS 48, which was previously shown to have a large dust trap, to search for complex molecules in regions where planetesimals are forming.We report the detection of the H_2CO 9(1,8)–8(1,7) line at 674 GHz, which is spatially resolved as a semi-ring at $\sim$ 60 AU radius centered south from the star. The inferred H_2CO abundance is $\sim 10^{-8}$, derived by combining a physical disk model of the source with a non-LTE excitation calculation. Upper limits for CH_3OH lines in the same disk give an abundance ratio H_2CO/CH_3OH >0.3, which indicates that both ice formation and gas-phase routes play a role in the H_2CO production. Upper limits on the abundances of $H^{13}CO^+$, CN and several other molecules in the disk were also derived and found to be consistent with full chemical models.The detection of the H_2CO line demonstrates the start of complex organic molecules in a planet-forming disk. Future ALMA observations are expected to reduce the abundance detection limits of other molecules by 1–2 orders of magnitude and test chemical models of organic molecules in (transitional) disks.

8.1 Introduction

Planets are formed in disks of dust and gas that surround young stars. Although the chemical nature of the gas is simple, with only small molecules such as H_2, CO, HCO^+, or H_2CO detected so far, the study of molecules in protoplanetary disks has resulted in a much better understanding of the origin of planetary systems (e.g. Williams & Cieza 2011; Henning & Semenov 2013). Molecular line emission serves as a probe of disk properties, such as density, temperature, and ionization. Furthermore, simple species are the start of the growth of more complex organic and possibly prebiotic molecules (Ehrenfreund & Charnley 2000; Mumma & Charnley 2011). Molecules in disks are incorporated into icy planetesimals that eventually grow to comets and asteroids that may have delivered water and organic material to Earth. Therefore, a better understanding of the chemical composition of protoplanetary disks where these icy bodies are formed provides insight into the building blocks of comets and Earth-like planets elsewhere in the Universe.

Protoplanetary disks have sizes of up to a few 100 AU, which makes them similar to or larger than our own solar system (~50 AU radius). However, at the distance of the nearest star-forming regions these disks subtend less than a few arcsec on the sky, so that telescopes with high angular resolution and high sensitivity are needed to study their chemical composition. Most of the disks observed so far show no high chemical complexity (e.g. Dutrey et al. 1997; Thi et al. 2004; Kastner et al. 2008; Öberg et al. 2010). In the surface layers of the disk, molecules are destroyed by photodissociation by ultraviolet (UV) radiation from the central protostar. In the outer disk and close to the disk midplane, temperatures quickly drop to 100 K and lower, where all detectable molecules, including CO, freeze out onto dust grains at temperatures determined by their binding energies (Bergin et al. 2007). The chemical composition thus remains hidden in ices. Only a very small part of the ice molecules is brought back into the gas phase by nonthermal processes such as photodesorption.

Transition disks have a hole in their dust distribution and thus form a special class of protoplanetary disks (Williams & Cieza 2011). The hole allows a view into the usually hidden midplane composition because the ices at the edge of this hole are directly UV irradiated by the star, which results in increased photodesorption and thermal heating of the ices (Cleeves et al. 2011). The hole is also an indicator that the disk may be at the stage of forming planets. So far, the chemical composition of the outer regions of transitional disks appears to be similar to that of full disks, with detections of simple molecules including H_2CO (Thi et al. 2004; Öberg et al. 2010, 2011). However, these data were taken with a typical resolution of >2".

The study of the chemistry in protoplanetary disks has recently gained much more perspective due to the impending completion of the Atacama Large Millimeter/submillimeter Array (ALMA). ALMA allows us to study astrochemistry within protoplanetary disks at an unprecedented level of complexity and at very small scales. It has the sensitivity to detect not only the dust, but also the gas inside dust gaps in transitional disks (van der Marel et al. 2013; Casassus et al. 2013; Fukagawa et al. 2013; Bruderer et al. 2014).

The disk around Oph IRS 48 forms a unique laboratory for testing basic chemical processes in planet-forming zones. IRS 48 is a massive young star ($M_* = 2M_\odot$, T_* ~10 000 K) in the Ophiuchus molecular cloud (distance 120 pc) with a transition disk with a large inner dust hole, as revealed by mid-infrared imaging, which traces the hot small dust grains (Geers et al. 2007). The submillimeter continuum data (685 GHz or 0.43 mm) from thermal emission from cold dust obtained with ALMA show that the millimeter-sized dust is concentrated on one side of the disk, in contrast to the gas and small dust grains. Gas was detected inside the dust gap down to 20 AU radius with ALMA data (Bruderer et al. 2014), and strong PAH emission is also observed from within the cavity (Geers et al. 2007). The continuum asymmetry

has been modeled as a major dust trap (van der Marel et al. 2013), triggered by the presence of a substellar companion at ∼20 AU. The dust trap provides a region where dust grains concentrate and grow rapidly to pebbles and then planetesimal sizes, producing eventually what may be the analog of our Kuiper Belt.

Bruderer et al. (2014) presented and modeled the ALMA CO and continuum data, together with complementary data at other wavelengths, to derive a three-dimensional axisymmetric physical model of the IRS 48 disk. One important conclusion is that the dust in the disk is warm, even out to large radii, because the UV radiation can pass nearly unhindered through the central hole. This implies that the dust temperature is higher than 20 K throughout the disk so that CO does not freeze out close to the midplane of the disk (Collings et al. 2004; Bisschop et al. 2006). The lack of a freeze-out zone of CO is important, since much of the chemical complexity in a protoplanetary disks is thought to start with the hydrogenation of the CO ice (Herbst & van Dishoeck 2009). In the absence of CO ice, gas-phase chemistry is the current main contributor to complex molecule formation. Alternatively, the disk may have been colder in the past before the hole was created, with the ices produced at that time now evaporating. One of the simplest complex organic molecules, H_2CO, can form both through hydrogenation of CO-ice (Tielens & Hagen 1982; Hidaka et al. 2004; Fuchs et al. 2009; Cuppen et al. 2009) and through gas-phase reactions. H_2CO has been detected in several astrophysical environments, such as the warm inner envelopes of low- and high-mass protostars and protoplanetary disks including transitional disks (Dutrey et al. 1997; Ceccarelli et al. 2000; Aikawa et al. 2003; Thi et al. 2004; Bisschop et al. 2007; Öberg et al. 2010, 2011; Qi et al. 2013a). In contrast with H_2CO, CH_3OH can only be formed through ice chemistry (Geppert et al. 2006; Garrod et al. 2006), which means that the H_2CO/CH_3OH ratio gives information on the H_2CO formation mechanism. Furthermore, H_2CO is a very interesting molecule for comparing the chemical composition of disks, comets, and our solar system, because H_2CO- and CN-bearing molecules such as HCN and CN are precursors of amino acids. Synthesis of amino acids occurs in large asteroids in the presence of liquid water, for instance, through the Strecker synthesis route (Ehrenfreund & Charnley 2000).

In this work we present the detection of the H_2CO 9(1,8)–8(1,7) line in IRS 48 down to scales of ∼30 AU, a high-excitation line originating from a level at 174 K above ground. We model its abundance and discuss the implications of the origin of this molecule in combination with the nondetection of other molecular lines. We were only able to detect this line thanks to the tremendous increase in sensitivity at these high frequencies (∼ 670 GHz) using ALMA.

8.2 Observations

Oph IRS 48 (α_{2000} =16^{h}27^{m}37^s.18, δ_{2000} =-24°30′35.3″) was observed using the Atacama Large Millimeter/submillimeter Array (ALMA) in Band 9 in the extended configuration in Early Science Cycle 0. The observations were taken in three observation execution blocks of 1.7 hours each in June and July 2012. During these executions, 18 to 21 antennas with baselines of up to 390 meters were used. The spectral setup contained four spectral windows, centered on 674.00 , 678.84, 691.47, and 693.88 GHz. The target lines of this setup were the ^{12}CO J=6–5, C^{17}O J=6–5, CN N=$6_{11/2}$–$5_{11/2}$, and H^{13}CO$^+$ J=8–7 transitions and the 690 GHz continuum. Each spectral window consists of 3840 channels, a channel separation of 488 kHz, and thus a bandwidth of 1875 MHz, which allows for serendipitous detection of other lines. The resulting velocity resolution is 0.21 km s^{-1} (for a reference of 690 GHz). Table 8.1 summarizes the observed lines and frequencies. For CH_3OH, another transition was covered in our spectral setup at 678 GHz (4(2,3)–3(1,2)) but with the same Einstein coefficient and E_U

as the 674 GHz transition. For CN, the $6_{11/2}$–$5_{11/2}$ component covered in our observations has a rather low Einstein A coefficient (averaged over the unresolved hyperfine components). The CN lines at 680 GHz with Einstein A values stronger by two orders of magnitude were just outside the correlator setting, which was optimized for ^{12}CO and C^{17}O 6–5.

We reduced and calibrated the data using the Common Astronomy Software Application (CASA) v3.4. The bandpass was calibrated using quasar 3c279, and fluxes were calibrated against Titan. For Titan, the flux was calibrated with a model that was fit to the shortest one-third of the baselines, since Titan was resolved out at longer baselines and the fit to the model would not be improved. The absolute flux calibration uncertainty in ALMA Band 9 is ∼20%.

The resulting images have a synthesized beam of 0.32" × 0.21" or 38×25 AU ($1.87{\cdot}10^{-12}$ sr) and a position angle of 96° after applying natural weighting and cleaning. After extracting the continuum data and the line data of ^{12}CO J=6–5 and C^{17}O J=6–5, we performed a search for lines of other simple and complex molecules within our spectral setup, but apart from H_2CO, no other convincing features were found. A rectangular cleaning mask centered on the detected emission peaks was used during the cleaning process of the ^{12}CO line and was adapted to the detected emission of each channel. The final channel-dependent mask was then applied to the frequencies of the targeted weaker lines, given in Table 8.1. The final rms level was 20-30 mJy beam^{-1} per 1 km s^{-1} channel, depending on the exact frequency.

For more details on the data reduction see van der Marel et al. (2013).

Table 8.1: *Molecular lines in addition to CO observed toward IRS48 (parameters taken from the Cologne Database for Molecular Spectroscopy (Müller et al. 2001, 2005))*

Molecule	Transition	Rest frequency (GHz)	E_u (K)	$^{10}\log(A_{u\ell})$
H_2CO	9(1,8)–8(1,7)	674.80978	174	-2.04
CH_3OH	4(2,2)–3(1,3)	678.78546	61	-2.87
$H^{13}CO^+$	8–7	693.87633	150	-1.56
CN	$6_{11/2}$–$5_{11/2}$	678.84488	114	-5.35
$^{34}SO_2$	13(5,9)–12(4,8)	691.99178	143	-2.67
C^{34}S	14–13	674.47362	180	-2.27
HNCO	9(1,9)–10(0,10)	678.23827	91	-2.80
c-C_3H_2	10(10,1)–9(9,0)	693.68725	182	-1.77
N_2D^+	9–8	693.80616	167	-1.42
D_2O	4(2,2)–4(1,3)	692.24358	236	-1.80

8.3 Results

The H_2CO 9(1,8)–8(1,7) line was detected at 3–8σ levels in the channels between $v_{\rm LSR}$ = -0.5 and +9.5 km s^{-1} (the source velocity is 4.55 km s^{-1}, van der Marel et al. 2013). The integrated flux between -0.5 and +9.5 km s^{-1} shows a flattened structure centered just south of the star (Figure 8.1). The stellar position was determined from the fastest velocity channels where the ^{12}CO emission from the same data set was detected. The emission is extended across the spatial region, corresponding to a rectangle [-1.0" to +1.0", -0.3" to +0.2"] having an area of $2.1{\cdot}10^{-11}$ sr. Across this area, the integrated flux is found to be ∼3.1 ± 0.6 Jy km s^{-1} (see Figure 8.1 and 8.2). The emission is, where detected, cospatial with the ^{12}CO 6–5 emission at the same velocity channels, although the northern half of the emission is missing

(see Figure 8.3). Gas orbiting a star in principle follows Kepler's laws, with the velocity v depending on the orbital radius r according to $v = \sqrt{GM/r}$, with G the gravitational constant and M the stellar mass. The CO 6–5 emission is found to follow Keplerian motion in an axisymmetric disk (Bruderer et al. 2014). The emission in the high-velocity channels is significantly stronger than the velocities closer to the source velocity, which can be partly explained by limb brightening due to the 50° inclination of the disk. Some H_2CO and CO emission is found in various channels in the southeast corner (at velocities of +1–2 km s^{-1}) and not follow the Keplerian motion pattern (Bruderer et al. 2014), but because of the low S/N it is not possible to distinguish whether this emission is real or a cleaning artifact for the case of H_2CO.

A striking aspect of these images is that H_2CO is only detected south of the star, as is also found for the submillimeter continuum, which shows a north-south asymmetry of the disk with a contrast factor of >100. The north-south contrast of H_2CO can only be constrained to be a factor >2 because of the low S/N of this detection. Moreover, the H_2CO does not follow the submillimeter continuum exactly: at the continuum peak no H_2CO emission is detected at all. The velocity channels in ^{12}CO between 2.5 and 4.5 km s^{-1} suffer from absorption by foreground clouds, but the H_2CO abundance and excitation in these clouds is too low to absorb the H_2CO disk emission in this highly excited line. Thus, the absence of H_2CO at the peak millimeter continuum is significant.

The other targeted molecules remain undetected, but the non-detection provides 3σ upper limits that can be used in the models. For the 25 mJy beam^{-1} km s^{-1} rms level, we estimated the upper limit on the total flux of CH_3OH as follows: for the H_2CO detected emission, the total surface area dΩ with emission > 3σ is $\sim 1.3 \cdot 10^{-11}$ sr or ~7 beams, and the detectable emission lies between -0.5 and +9.5 km s^{-1} (11 channels). The 3σ upper limit on the total flux is thus

$$F_{\rm upp} = \sqrt{d\Omega/\Omega_{\rm beam}} \cdot 3\sigma_{\rm rms} \cdot 1.2\sqrt{11 \cdot 1} = 0.79 \text{ Jy km s}^{-1}, \quad (8.1)$$

where the factor 1.2 is introduced to compensate for small-scale noise variations and calibration uncertainties at this high frequency of the observations. Note that this is a conservative limit because the H_2CO emission is most likely narrower in the radial direction than the spatial resolution. For the CN, $H^{13}CO^+$ and other molecules in Table 8.1 we expect the emission to be cospatial with the CO emission, which covers $\sim 4.8 \cdot 10^{-11}$ sr or ~ 26 beams and integrated between -3 and +12 km s^{-1}. The upper limit is thus

$$F_{\rm upp} = \sqrt{d\Omega/\Omega_{\rm beam}} \cdot 3\sigma_{\rm rms} \cdot 1.2\sqrt{15 \cdot 1} = 1.8 \text{ Jy km s}^{-1}. \quad (8.2)$$

8.4 Model

8.4.1 Physical structure

Analysis of the abundance and spatial distribution of the H_2CO in the disk requires a physical model of the temperature and gas density as a function of radius and height in the disk. We used the best-fitting model of the gas structure from Bruderer et al. (2014) based on the ^{12}CO and $C^{17}O$ 6–5 lines from the same ALMA data set and the dust continuum. The proper interpretation of the gas disk seen in ^{12}CO 6–5 emission requires a thermo-chemical disk model, in which the heating–cooling balance of the gas and chemistry are solved simultaneously to determine the gas temperature and molecular abundances at each position in the disk. Moreover, even though the densities in disks are high, the excitation of the rotational levels may

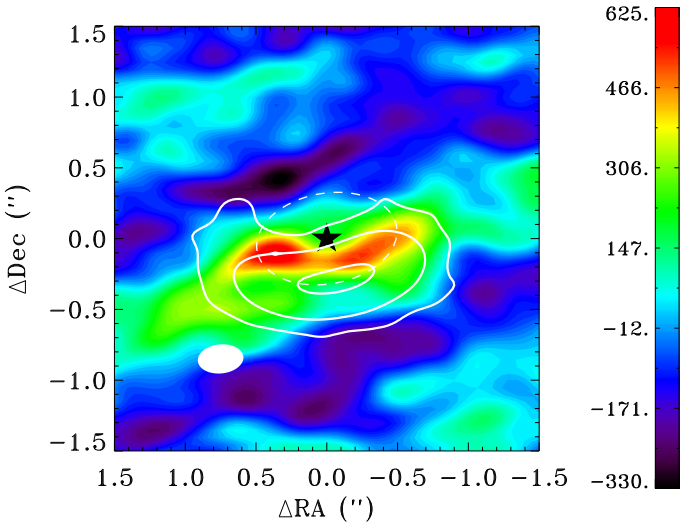


Figure 8.1: *Integrated intensity map of the H_2CO 9(1,8)–8(1,7) emission. The color bar gives the flux scale in mJy beam^{-1} km s^{-1}. The white contours indicate the 690 GHz continuum at 3, 30, and 300 σ from the thermal emission of the millimeter-sized dust grains. The position of the star IRS 48 is indicated by the star and the 60 AU radius (the dust trap radius) by a white dashed ellipse.*

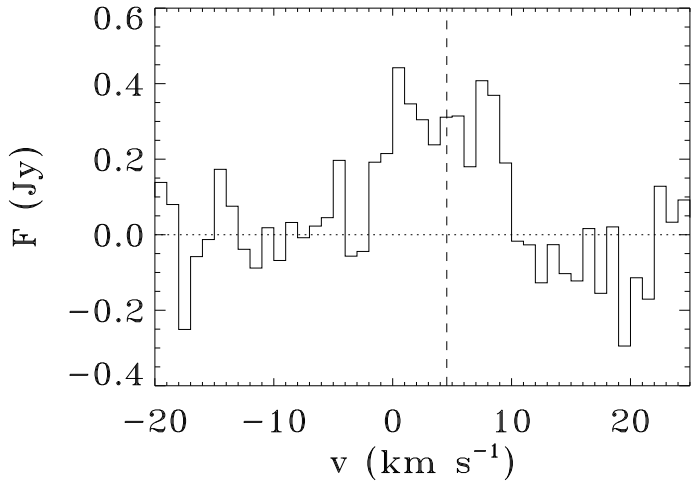


Figure 8.2: *Spectrum of H_2CO 9(1,8)-8(1,7) toward IRS 48 spatially integrated over the rectangle [-1.0" to +1.0", -0.3" to +0.2"]. The dotted line indicates the zero-emission line and the dashed line the source velocity of 4.55 km s^{-1}.*

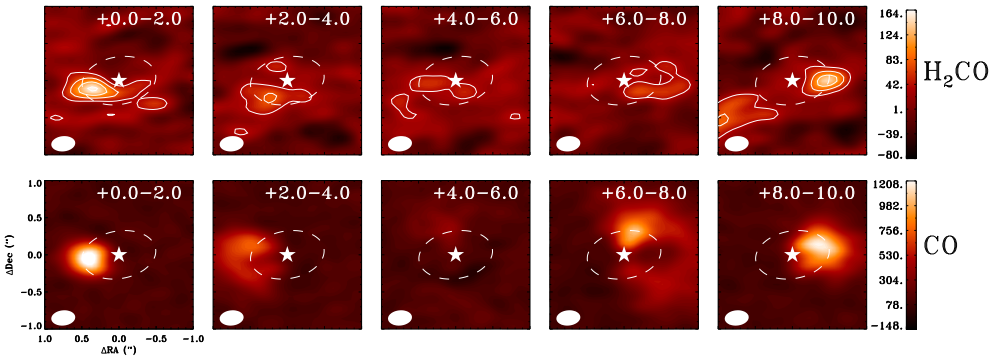


Figure 8.3: *Comparison of channel maps H_2CO 9(1,8)–8(1,7) (top row) with ^{12}CO 6–5 (bottom row), data taken from Bruderer et al. (2014). The color bar indicates the fluxes in mJy beam^{-1}. The number in the upper right corner of each map is the velocity range of that map. In the H_2CO maps, the white contours indicate the 20%, 40%, 60%, 80%, and 100% of the peak intensity of all channels (the peak intensity is 195 mJy beam^{-1}). The dashed ellipse indicates the 60 AU radius ring. The CO +4–6 km s^{-1} channels are affected by foreground absorption.*

not be in thermodynamic equilibrium, and there are steep temperature gradients in both radial and vertical directions in the disk. The DALI model (Bruderer et al. 2012; Bruderer 2013) uses a combination of a stellar photosphere with a disk density distribution as input. For IRS 48, the stellar photosphere is represented by a blackbody of 10 000 K. It solves for the dust temperatures through continuum radiative transfer from UV to millimeter wavelengths and calculates the chemical abundances, the molecular excitation, and the thermal balance of the gas. It was developed for the analysis of the gas emission structures such as are found for transitional disks (Bruderer 2013).

DALI uses a reaction network described in detail in Bruderer et al. (2012) and Bruderer (2013). It is based on a subset of the UMIST 2006 gas-phase network (Woodall et al. 2007). About 110 species and 1500 reactions are included. In addition to the gas-phase reactions, some basic grain-surface reactions (freeze-out, thermal and nonthermal evaporation and hydrogenation like g:O $\rightarrow$ g:OH $\rightarrow$ g:H_2O and H_2/CH^+ formation on PAHs) are included. The g:X notation refers to atoms and molecules on the grain surface. The photodissociation rates are obtained from the wavelength-dependent cross-sections by van Dishoeck et al. (2006). The adopted cosmic-ray ionization rate is $\zeta = 5 \times 10^{-17}$ s^{-1}. X-ray ionization and the effect of vibrationally exited H_2 are also included in the network. The model chemistry output will be used to compare with the HCO^+ and CN data. However, since no extensive grain-surface chemistry is included, it is not suitable to model the H_2CO and CH_3OH chemistry.

The surface density profile for the best-fitting model for IRS 48 (Bruderer et al. 2014) including the gap is shown in Figure 8.4. It is found that the gas disk around IRS 48 has a very low mass ($1.4{\cdot}10^{-4}$ $M_\odot$ = 0.15 M_{Jup}) compared with the mean disk mass of ~5 M_{Jup} for normal disks (Williams & Cieza 2011; Andrews et al. 2013). Furthermore, the disk has a large scale-height, allowing a large portion of the inner walls to be irradiated by the star. The radial gas structure has two density drops: a drop δ_{20} of $< 10^{-2}$ in the inner 20 AU (probably caused by a planetary or substellar companion) and an additional drop δ_{60} of 10^{-1} at 60 AU radius.

The resulting densities, temperatures and CO abundances of the model are given in Figure 8.5. The gas density is 10^{5-6} molecules cm^{-3} in the upper layers of the disk, increasing to 10^8 cm^{-3} close to the midplane near 60 AU. The gas temperature is typically a few 100 K, except

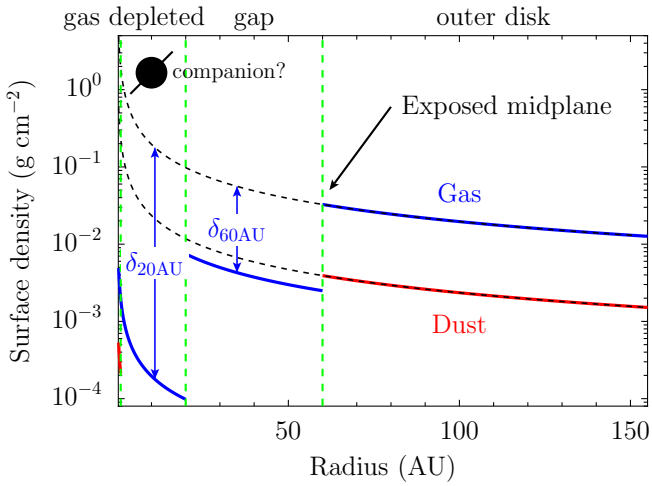


Figure 8.4: *Adopted radial density structure of the IRS 48 disk, taken from Bruderer (2013). The blue lines indicate the gas surface density, the red lines the dust surface density. The dotted black lines show the undisturbed surface density profiles if it continued from outside inwards without depletion. The green dashed lines indicate the radii at which the depletions start.*

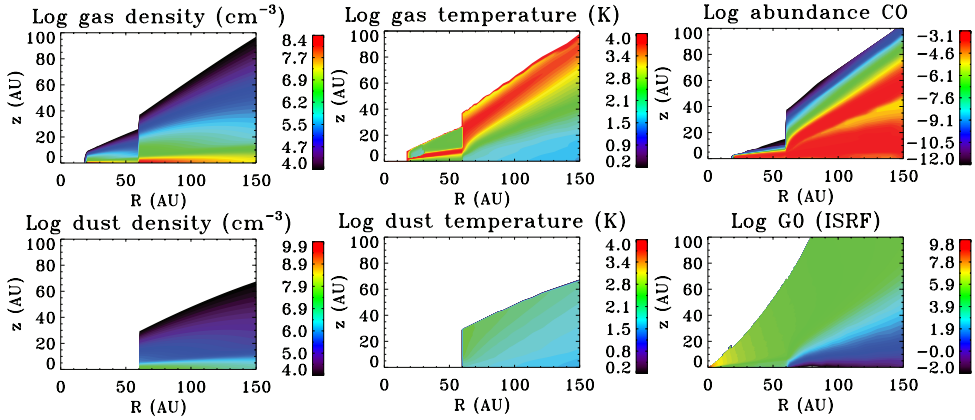


Figure 8.5: *Physical-chemical model of IRS 48 from Bruderer et al. (2014). The panels show gas density (cm^{-3}), gas temperature (K), CO abundance with respect to H_2, dust density (cm^{-3}), dust temperature (K), and UV field in G_0 (G_0 = 1 refers to the standard interstellar radiation field). The given numbers are in ^{10}log scale.*

in the upper layers where the temperature reaches several thousand K. The UV radiation field is enhanced by factors of up to 10^8 in the disk, indicated by G_0 (panel 6 in Figure 8.5). $G_0 = 1$ refers to the interstellar radiation field defined as in Draine (1978), $\sim 2.7 \times 10^{-3}$ erg s^{-1} cm^{-2} with photon-energies in the far UV range between 6 eV and 13.6 eV. The CO abundance is $\sim 10^{-4}$ compared with H_2 throughout the bulk of the outer disk and is not frozen out.

The H_2CO emission was modeled using the LIne Modeling Engine (LIME), a non-LTE excitation spectral line radiation transfer code (Brinch & Hogerheijde 2010). The physical structure described above is used as input. The first step in the analysis is to empirically

constrain the H_2CO abundance by using three different trial abundance profiles guided by astrochemical considerations. The inferred abundances were then *a posteriori* compared with those found in the full chemical models. In Model 1, the abundance was assumed to be constant throughout the disk, testing abundances between 10^{-5} and 10^{-11} with respect to H_2. In Model 2, the abundance was taken to follow the CO abundance calculated by the DALI model, taking a fractional abundance ranging between 10^{-3} and 10^{-8} with respect to CO. Model 3 was inspired by Cleeves et al. (2011) by setting the H_2CO to zero except for a ring between 60 and 70 AU. This model assumes that the UV irradiated inner rim has an increased chemical complexity that can be observed directly, as material from the midplane has been liberated from the ices. The abundance profile is additionally constrained by the photodissociation and freeze out. H_2CO can only exist below the photodissociation height, which was taken as the height (z direction) where a hydrogen column density of $N(H_2) = 4 \cdot 10^{20}$ cm^{-2} is reached. At this column, the CO photodissociation rate drops significantly due to shielding by dust as well as self-shielding and mutual shielding by H_2 for low gas-to-dust ratios (Visser et al. 2009). Therefore, at each radius this value was calculated and the abundance was set to zero above it. For radii <60 AU, H_2CO is photodissociated almost entirely down to the midplane because of the lower total column density. Furthermore, H_2CO is expected to be frozen out on the grains at temperatures <60 K since it has a higher binding energy (Ioppolo et al. 2011) than CO, therefore the abundance in regions below this temperature were also set to zero. All three abundance profiles are shown in Figure 8.6.

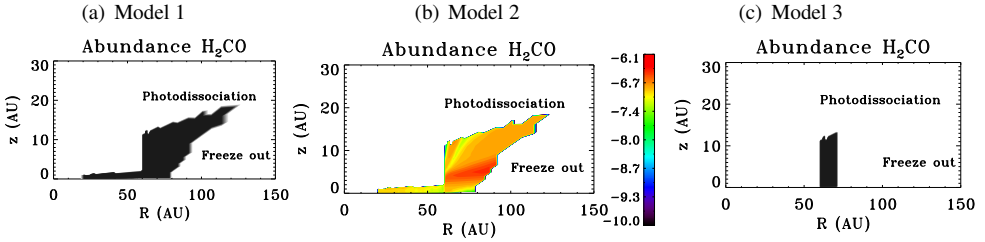


Figure 8.6: *Trial abundance models 1, 2 and 3 for H_2CO. The H_2CO abundance is limited by photodissociation in the upper layer and freeze out below 60 K. Model 1 assumes a constant abundance, Model 2 assumes a fractional abundance with respect to CO, Model 3 assumes a constant abundance in between 60 and 70 AU radius and zero abundance at other radii.*

The LIME grid was built using linear sampling, with the highest grid density starting at 60 AU, using 30 000 grid points and 12 000 surface grid points, using an outer radius of 200 AU. The image cubes were calculated for 60 velocity channels of width 0.5 km s^{-1} spectral resolution, in 5"×5" maps with 0.025" pixels. Collisional rate coefficients were taken from the Leiden Atomic and Molecular Database (LAMDA) (Schöier et al. 2005) with references to the original collisional rate coefficients as follows: H_2CO (Troscompt et al. 2009), CH_3OH (Rabli & Flower 2010), $H^{13}CO^+$ (Flower 1999), and CN (Lique et al. 2010). For the other molecules the emission was only calculated in LTE, using the parameters from CDMS (Müller et al. 2001, 2005).

For CH_3OH, $H^{13}CO^+$, CN and the other molecules we ran models to constrain the upper limits. For CH_3OH, the same abundance profiles as for H_2CO were taken because CH_3OH is expected to be cospatial with H_2CO when they are both formed through solid-state chemistry. For the $H^{13}CO^+$ abundance the initial CO abundance was taken and multiplied with factors 10^{-5}–10^{-11}, as the HCO^+ is known to form via CO through the H_3^+ + CO proton donation reaction and is indeed observed to be strongly correlated with CO (Jørgensen et al. 2004). For

the other molecules the same approach for the abundance as for $H^{13}CO^+$ was used.

8.4.2 Results

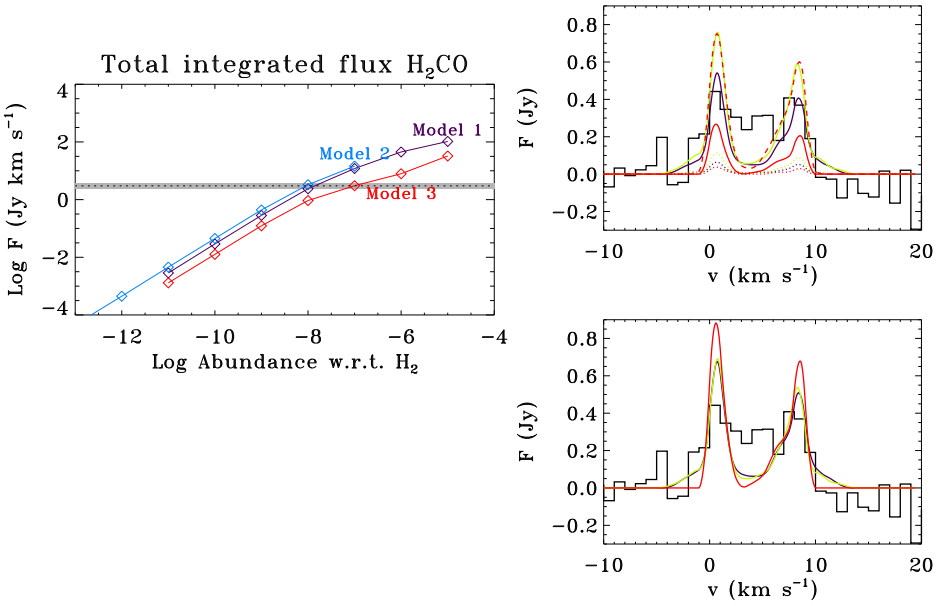


Figure 8.7: *Results of H_2CO abundance models:* **Left:** *Total flux integrated over the emission rectangle of the observations for different abundances for Model 1 (purple), Model 2 (blue), and Model 3 (red). The fractional abundances with respect to CO for Model 2 have been multiplied with 10^{-4} for easier comparison as the CO/H_2 abundance is typically 10^{-4}. The dotted line indicates the measured observed flux, and the gray bar indicates the error on this value based on the flux calibration uncertainty.* **Right:** *Spectra integrated over the emission rectangle of the observations for different abundances for Model 1 (purple), Model 2 (green), and Model 3 (red) for abundances 10^{-7} (dashed), 10^{-8} (solid), and 10^{-9} (dotted). The black spectrum represents the observational data. Abundances for Model 2 are multiplied with 10^{-4} to translate the abundance w.r.t. CO to H_2. The top figure shows the original models. The bottom figure shows the model spectra scaled to match the total flux of the observations.*

The model results for H_2CO are presented in Figure 8.7. Integrated fluxes were computed by summing the model fluxes over the same rectangular region as the H_2CO observations, after subtracting the continuum. Figure 8.7 presents the model fluxes as a function of H_2CO abundance for the three trial abundance structures. Model 1 with constant H_2CO abundance $\sim 10^{-8\pm0.15}$ with respect to H_2 or Model 2 with abundance $\sim 10^{-4}$ with respect to CO reproduce the total observed flux well within the error bar. There is little difference between Model 1 and Model 2 except for a factor of 10^4 that has been taken into account in Figure 8.7. This is expected because most of the CO abundance in the defined region is 10^{-4} with respect to H_2. Model 3 requires an abundance of 10^{-8} higher by a factor 3 in the 60–70 AU ring to give the same integrated flux. Note that the LIME model fluxes obtained with non-LTE calculations are only about 25% lower than the LIME models in LTE due to the high densities in the disk.

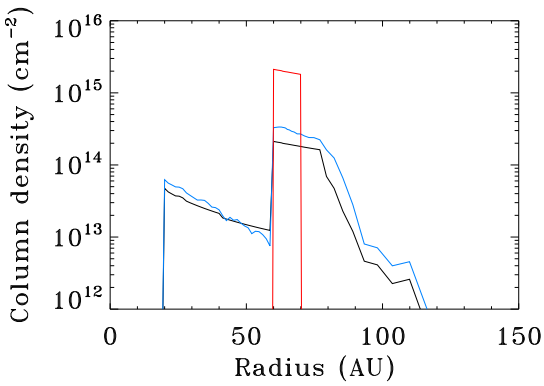


Figure 8.8: *Column density profiles of H_2CO for the best abundance fits for models 1 (black), 2 (blue), and 3 (red). Abundances are 10^{-8} for Model 1, 10^{-4} w.r.t. CO for Model 2 and 10^{-7} for Model 3.*

The spectra (Figure 8.7) confirm that the best match for the flux for Model 1 is for an abundance of $\sim 10^{-8}$, although the peaks at the highest velocities are up to twice as high as the data. The slight asymmetry in these model spectra is caused by the spatial integration over a rectangle, whereas the disk has a position angle of 100°. The line wings in models 1 and 2 originate from the emission from radii <60 AU, which is missing in Model 3, but the S/N of the data is too low to detect the difference. In the bottom panel of Figure 8.7 the spectra have been scaled so that the total flux exactly matches that from the observations.The current models underproduce the emission close to the central velocity ratios, suggesting that the abundance may be even more enhanced in the central southern part of the disk at these velocities and is not constant along the azimuthal direction of the semi-ring. It is also possible that there is enhanced H_2CO at larger radii than assumed here when the freeze-out zone is taken out, although this does not add a significant amount of emission at the central velocities. Calculation of an abundance model where the freeze-out zone is removed shows that this indeed increases the emission at central velocities, but the S/N of the data is insufficient to confirm or exclude emission at larger radii. Overall, it is concluded that the abundance is $\sim 10^{-8}$ compared with H_2 within factors of a few.

The final comparison between models and data is made by comparing images. To produce images from the model output cubes the images were convolved with the ALMA beam of the observations (0.31"×0.21", PA 96°). Similar as in Bruderer et al. (2014), the result of the model images convolved to the ALMA beam was compared with the result of simulated ALMA observations. An alternative method is to convert the model images to u, v-data according to the observed u, v-spacing using the CASA software and reduce them in the same way as the observations. Because of the good u, v-coverage of our observations, the two approaches do not differ measurably within the uncertainty errors. Figures 8.9 and 8.10 indicate that the three models have a similar ring-like structure as the observations, apart from the emission in the north that is lacking in the data. The differences between the models are best seen in the velocity channel maps: models 1 and 2 still show some emission within the ring at 30–60 AU, which is higher for Model 1 than for Model 2 because the CO abundance is somewhat lower between 40 and 60 AU. Model 3 does not show any emission within the ring by design.

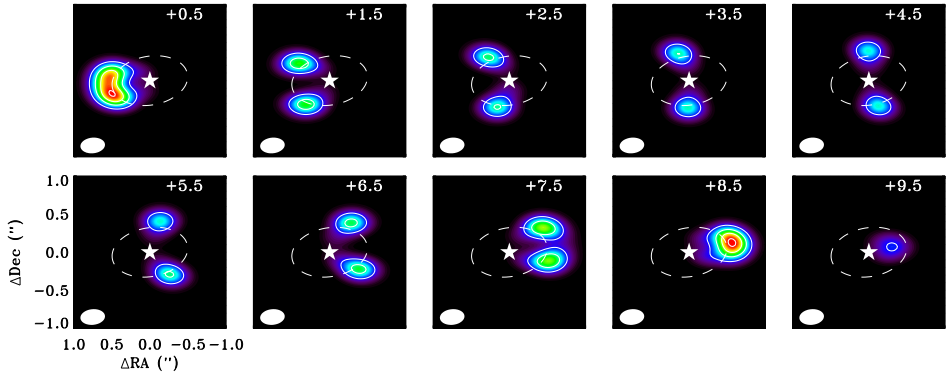


Figure 8.9: *Results of H_2CO abundance modeling: channelmap convolved with the ALMA beam of the observations for Model 1 at 10^{-8} abundance. The color bar gives the flux scale in mJy beam^{-1}. The 60 AU radius is indicated with a dashed ellipse and the stellar position with a star. The white contours indicate the 20%, 40%, 60%, 80% and 100% of the peak (peak is 212 mJy beam^{-1}).*

A possible explanation for the missing H_2CO emission at the peak of the dust continuum is that the dust is not entirely optically thin. The optical depth τ_d was calculated as $\tau_d \sim 0.43$ (van der Marel et al. 2013) averaged over the continuum region. If we assume all the H_2CO emission I_{line} to originate from behind the dust, the resulting intensity is

$$I_\nu = B_\nu(T_{dust}) \cdot (1 - e^{-\tau_d}) + e^{-\tau_d} I_{line}. \tag{8.3}$$

The first term is the measured dust intensity, which is subtracted from the H_2CO data. The second term indicates a reduction of the line intensity by continuum extinction. This extinction was calculated by multiplying the model output with the exponent of a 2D τ_d profile, where τ_d is following the continuum emission profile of the observed dust trap area. The maximum τ_d was taken as 0.86, recovering the averaged opacity over this area. This correction represents an upper limit of the continuum extinction effect. The result is shown in the bottom panels of Figure 8.10. The continuum extinction decreases the H_2CO emission in the south by more than a factor 2, while some emission between the star and the dust continuum remains (for models 1 and 2). Although the strength of this emission compared with the peaks at the edges is still lower than in the observations, the model image is now more consistent with the observations. The total integrated flux is only 10% lower because the rectangle used for the spatial integration did not cover most of the dust continuum. Both the S/N of the line data and the unknown mixing of the gas and dust prevent a more detailed analysis of this problem, but it is clear that the continuum extinction cannot be neglected. The observations show a decrease of a factor 4 between the east and west limbs compared with the emission at the location of the dust peak (see Figure 8.1), which requires a τ_d of at least 1.4. Submillimeter imaging at longer wavelengths is required to measure the dust optical depth more accurately.

Overall, the conclusion is that the current data can constrain the H_2CO abundance in the warm gas where H_2CO is thought to reside to $\sim 10^{-8}$, but the current S/N is too low to distinguish the different assumptions on the radial distribution of H_2CO. However, the three models make different predictions for the distribution, which we expect to see more clearly in future higher S/N ALMA data.

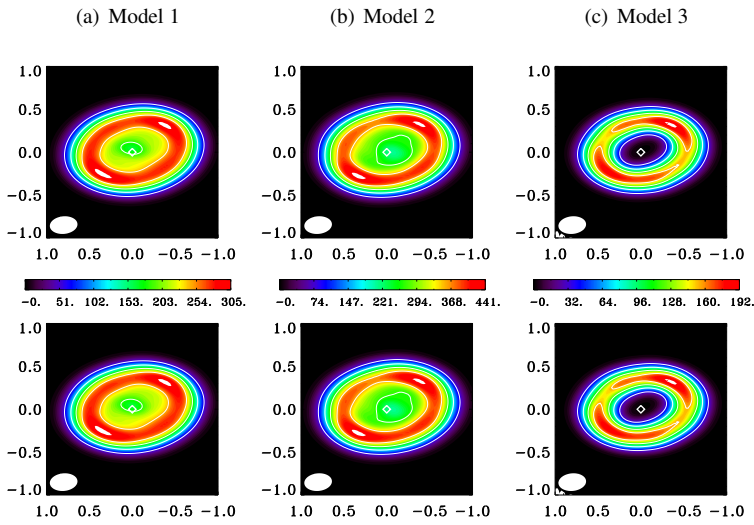


Figure 8.10: *Results of H_2CO abundance models: Integrated intensity maps convolved with the ALMA beam for Model 1 at 10^{-8} abundance (left), Model 2 at 10^{-4} fractional abundance of CO (center) and Model 3 at 10^{-8} abundance (right). The color bar gives the flux scale in mJy beam^{-1}. The white contours indicate the 20%, 40%, 60%, 80% and 100% of the peak. The top panel gives the result for the non-altered model image, the bottom panel gives the result with a correction for the continuum extinction.*

The total model fluxes for the CH_3OH, $H^{13}CO^+$ and CN are compared with the derived upper limits in Figure 8.11, where all abundances have been multiplied with 10^{-4} to translate the abundance w.r.t. CO to H_2. The other targeted molecules with upper limits were compared in the same way (plots not displayed here). For the CH_3OH lines, the upper limit on the integrated flux is consistent with an abundance limit in Model 1 of $< 3 \cdot 10^{-8}$, thus $H_2CO/CH_3OH > 0.3$. For $H^{13}CO^+$, the upper limit sets the abundance at $< 10^{-6}$ with respect to CO. This indicates an HCO^+/CO abundance ratio of $< 10^{-4}$, or an absolute abundance HCO^+/H_2 of $< 10^{-8}$. The CN emission is poorly constrained: the upper limit sets the CN/CO abundance at $< 5 \cdot 10^{-4}$ or $CN/H_2 < 5 \cdot 10^{-8}$. The reason is the low Einstein A coefficient of this particular transition, which is almost three orders of magnitude lower than that of the other transitions in this study.

All derived absolute abundance limits are given in Table 8.2. For $^{34}SO_2$ and $C^{34}S$ we found absolute abundances of $< 10^{-8}$ and $< 10^{-9}$ respectively, corresponding to abundances of $< 2 \cdot 10^{-7}$ and $< 2 \cdot 10^{-8}$ for the main isotopes, assuming an elemental abundance ratio of sulfur of $^{32}S/^{34}S$ of 24 (Wilson & Rood 1994). For the deuterated molecules N_2D^+ and D_2O the isotope ratio D/H in these molecules is not known, therefore no upper limits on N_2H^+ or H_2O can be obtained.

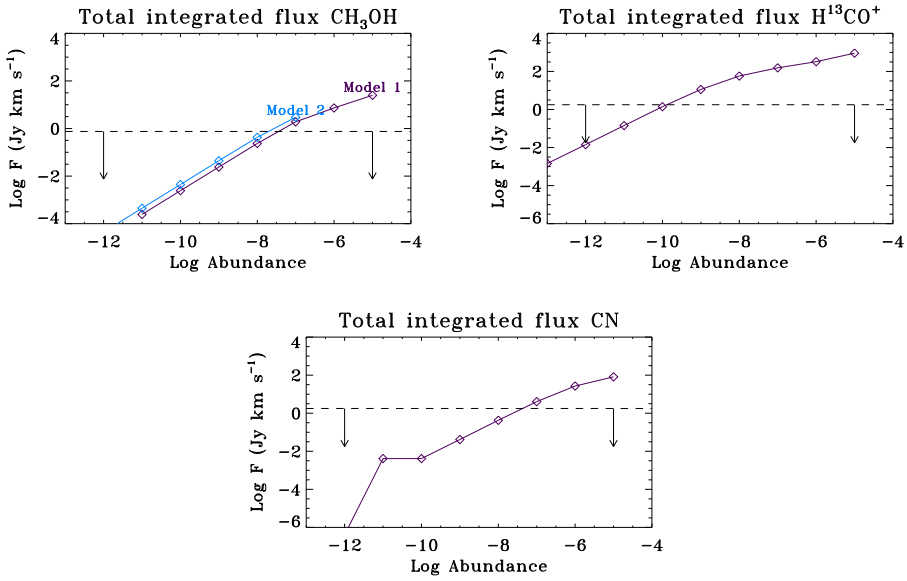


Figure 8.11: *Model results for the integrated fluxes found for CH_3OH, $H^{13}CO^+$ and CN in the empirical models. The dashed line indicates the upper limit of the integrated intensity, assuming the molecule is cospatial with the H_2CO (CH_3OH) or CO ($H^{13}CO^+$ and CN). Abundances were calculated with respect to the CO abundance, but in these plots are multiplied with 10^{-4} to translate the abundance w.r.t. CO to H_2.*

Table 8.2: *Derived abundance limits w.r.t. H_2.*

Molecule	Abundance
H_2CO	$1 \cdot 10^{-8}$
CH_3OH	$< 3 \cdot 10^{-8}$
$H^{13}CO^+$	$< 1 \cdot 10^{-10}$
CN	$< 5 \cdot 10^{-8}$
$^{34}SO_2$	$< 1 \cdot 10^{-8}$
$C^{34}S$	$< 1 \cdot 10^{-9}$
HNCO	$< 3 \cdot 10^{-9}$
c-C_3H_2	$< 3 \cdot 10^{-9}$
N_2D^+	$< 1 \cdot 10^{-10}$
D_2O	$< 1 \cdot 10^{-9}$

8.5 Discussion

8.5.1 Origin of the H_2CO emission

H_2CO can be formed efficiently in the ice phase by hydrogenation of solid CO, as shown in laboratory experiments, which can be followed by the formation of CH_3OH (Hiraoka et al.

2002; Watanabe & Kouchi 2002; Watanabe et al. 2004; Hidaka et al. 2004; Fuchs et al. 2009):

$$CO \rightarrow HCO \rightarrow H_2CO \rightarrow H_2COH \rightarrow CH_3OH. \quad (8.4)$$

Because CO ice is highly abundant in the cold dusty regions in clouds and disks, this formation route is commonly assumed as the origin of gas-phase H_2CO, following thermal or nonthermal desorption. In that case, CH_3OH is expected to have a similar or higher abundance than H_2CO because they are formed along the same sequence (Tielens & Hagen 1982; van der Tak et al. 2000; Cuppen et al. 2009). If all ices are thermally desorbed, gas-phase abundances can be as high as $\sim 10^{-6} - 10^{-5}$.

There is no known efficient gas-phase chemistry for the formation of CH_3OH (Geppert et al. 2006; Garrod et al. 2006), whereas H_2CO can also be formed rather efficiently in the gas phase. At low temperatures, the reaction

$$CH_3 + O \rightarrow H_2CO + H \quad (8.5)$$

dominates its formation, whereas it is mainly destroyed through reactions with ions such as $HCO^+$and H_3O^+. These reactions lead to H_3CO^+, which cycles back to H_2CO through dissociative recombination

$$H_3CO^+ + e^- \rightarrow H_2CO + H. \quad (8.6)$$

However, since the branching ratio to H_2CO is only 0.3, the ion reactions lead to a net destruction of H_2CO. Typical dark-cloud gas-phase model abundances are a few$\times 10^{-8}$ relative to H_2 (McElroy et al. 2013). At low dust temperatures (< 60 K), H_2CO can freeze out after formation.

At higher temperatures in the presence of abundant H_2O ($T > 100$ K), formaldehyde can also form through gas-phase reactions such as $CH_2^+ + H_2O \rightarrow H_3CO^+ + H$ followed by dissociative recombination. Above a few 100 K, formaldehyde is destroyed efficiently through $H + H_2CO + 1380\ K \rightarrow HCO + H_2$.

H_2CO has been detected in warm protostellar cores together with CH_3OH. Typical H_2CO abundances in the warm gas are $3\sim 10^{-7}$ with respect to hydrogen, whereas CH_3OH has an abundance higher by a factor of 5 ($H_2CO/CH_3OH \approx 0.2$) (Bisschop et al. 2007), suggesting a main formation route through solid-state chemistry followed by sublimation. Recent observations of these molecules in the Horsehead PDR and core show a higher abundance ratio H_2CO/CH_3OH of 1–2, which cannot be produced by pure gas-phase chemistry (Guzmán et al. 2013). H_2CO has been detected in several protoplanetary disks (Dutrey et al. 1997; Aikawa et al. 2003; Thi et al. 2004; Öberg et al. 2010, 2011; Qi et al. 2013a), which has usually been interpreted through the solid state chemical path, even though gas-phase CH_3OH has not been detected in any of these disks due to sensitivity limitations. For high enough sensitivity the combination of H_2CO and CH_3OH observations would clearly distinguish between the ice-phase and gas-phase chemistry. For the disk around HD163296, the rotational temperature of H_2CO was measured to be <30 K by fitting the emission of several transitions, and its abundance was found to be enhanced outside the CO 'snowline' at 20 K, suggesting a solid-state route (Qi et al. 2013a).

The measured H_2CO/CH_3OH ratio limit for Oph IRS 48 of >0.3 is similar to the limit found for LkCa 15 (Thi et al. 2004) and only slightly higher than that found in warm protostars. This low limit therefore does not exclude the solid-state chemistry formation route but is also consistent with a gas-phase chemistry contribution to H_2CO. However, the H_2CO abundance of 10^{-8} is much higher than the detections and upper limits of the disk-averaged abundances in Thi et al. (2004), which are typically $< 10^{-11}$. Most of this difference stems from the fact that

the disks in Thi et al. (2004) are two orders of magnitude more massive and also colder, with a large portion of the CO and related molecules frozen out. This cold zone is lacking in the IRS 48 disk, and our analysis has already removed the zones in which H_2CO is photodissociated or frozen out. Nevertheless, as shown below, the H_2CO emission is unusually strong in IRS 48 for its disk mass, hinting at an increased richness of chemistry in transitional disks due to the directly irradiated inner rim at the edge of the gas gap, as predicted (Cleeves et al. 2011).

Another interesting aspect of the H_2CO emission is the azimuthal asymmetry in IRS 48, which happens to be similar although not exactly cospatial to the dust continuum asymmetry. The dust asymmetry was modeled (van der Marel et al. 2013) as a dust trap caused by a vortex in the gas distribution with an overdensity of a factor 3, and it is possible that the increased emission of H_2CO at this location is in fact tracing this overdensity in the gas. The image quality and S/N of the observations is insufficient to confirm this claim, however, and no overdensity was observed in the ^{12}CO 6–5 emission (Bruderer et al. 2014). Moreover, the H_2CO emission does not peak exactly at the peak of the dust continuum emission: in fact, the H_2CO emission is decreased at the continuum peak, as discussed in Section 8.4.2 (see Figure 8.1). It is possible that this decrease is caused by the high optical depth of the millimeter dust, which absorbs the line emission of the optically thin gas all the way from the midplane (see Figure 8.10 and Eq. 3). This cannot be confirmed because of the unknown vertical mixing of the gas and dust. Finally, a nondetection of an overdensity in the gas is consistent with the dust-trapping scenario: a vortex in the gas may already have disappeared while the created dust asymmetry remains because the time scale of smoothing out a dust asymmetry is on the order of several Myr (Birnstiel et al. 2013).

Another possibility for the increased H_2CO emission in the south is a local decrease in the temperature compared with the north. In that case H_2CO is destroyed efficiently in the north through the H + H_2CO + 1380 K $\rightarrow$ HCO + H_2 reaction, but not in the south. This possibility is consistent with the reduced CO emission in the south in both the rovibrational lines (Brown et al. 2012a) and the ^{12}CO 6–5 lines (Bruderer et al. 2014), where Bruderer et al. (2014) suggested the temperature decrease to be of a factor 3. This temperature decrease might be caused by UV shielding in the inner disk. Note that the millimeter dust that is concentrated in the south does not provide sufficient cooling to change the gas temperature significantly through gas-grain collisions: the small dust grains have most the surface and gas-grain temperature exchange. If the temperature drops locally to between 20 and 30 K, the H_2CO might even be an ice-phase product, but this is very unlikely. A final possibility is that the increase of H_2CO is caused by the increased dust density and dust collisions in this region. If the grain-grain collisions are at high enough speed (which depends on the turbulence in the disk), the ice molecules may become separated from the grains. However, the dust grains have reached temperatures above the sublimation temperature of 60 K long before reaching the dust trap, therefore this is not very likely within reasonable time scales.

8.5.2 Comparison with chemical models

The column density of H_2CO for the best-fitting model with abundance 10^{-8} is $\sim 10^{14}$ cm^{-2} for radii>60 AU (Figure 8.8), which is within an order of magnitude of the predictions of chemical models (Semenov & Wiebe 2011; Walsh et al. 2012, 2013) for protoplanetary disks. For the $10^{-7.5}$ abundance upper limit for CH_3OH we found a column density limit of $\sim 2 - 4 \cdot 10^{14}$ cm^{-2} for radii>60 AU, which is well above the numbers derived in chemical models (Walsh et al. 2012; Vasyunin et al. 2011), which are typically 10^{10} cm^{-2}.

The DALI-model (Bruderer et al. 2014) produces predictions for HCO^+ and CN: the HCO^+ abundance peaks at $5{\cdot}10^{-9}$, but only in a very thin upper layer of the disk where the

CO + H_2 reaction operates. The disk-averaged abundance is much lower. The predicted integrated model intensity for $H^{13}CO^+$ is 0.02 Jy km s^{-1}, far below our detection limit of 1.8 Jy km s^{-1}. The peak abundance for CN is $3{\cdot}10^{-7}$ with an integrated intensity of 1.1 Jy km s^{-1}, which is close to our upper limit. The other CN 6–5 lines at 680 GHz (outside the range of the spectral window of our observations) have an Einstein coefficient that is 2 orders of magnitude higher and should be readily detectable with an integrated flux of 15 Jy km s^{-1}.

8.5.3 Comparison of upper limits with other observations

The HCO^+/CO ratio of $< 10^{-4}$ (or $HCO^+/H_2 < 10^{-8}$) for IRS 48 is consistent with values found in disks, protostellar regions and dark clouds. The ratio is often found to be $\geq 10^{-5}$, where the lower limit is due to the unknown optical depth of the observed HCO^+ line (Thi et al. 2004). Our $H^{13}CO^+$ line does not suffer from this problem, but our inferred HCO^+ abundance is not more stringent because of the very low gas mass of IRS 48. For similar abundances, all measured fluxes would be a factor of 10–100 lower than for other full disks.

HCO^+ is produced by the gas-phase reaction $H_3^+ + CO \rightarrow HCO^+ + H_2$, which relates the abundance directly to ionization, because the parent molecule H_3^+ is formed efficiently through cosmic-ray ionization. Our abundance cannot set a strong limit on the ionization fraction in the disk. The ionization fraction in disks is important because the magneto-rotational instability (MRI), believed to drive viscous accretion, requires ionization to couple the magnetic field to the gas (Gammie 1996). Insufficient ionization may suppress the MRI and create a so-called dead zone that can create dust traps at its edge where the dust grains will gather (Regály et al. 2012). However, the ionization needs to be lower than about 10^{-12} to induce a dead zone (Ilgner & Nelson 2006). On the other hand, recent models suggest that cosmic rays may be excluded altogether from disks around slightly lower-mass stars (Cleeves et al. 2013). A detection of HCO^+ at the level suggested by our models would provide direct proof of the presence of cosmic rays that ionize H_2 at a rate of $\sim 5 \times 10^{-17}$ s^{-1}.

The CN upper limit is difficult to compare with literature values because our upper limit is very high due to the low Einstein A coefficient. Literature values give derived abundances (Thi et al. 2004) of $\sim 10^{-10}$, three orders of magnitude lower than our upper limit, which is again caused by the low gas mass of our disk. As noted above, the full chemical model by Bruderer (2013) suggests abundances very close to our inferred upper limits. The CN/HCN ratio is a related tracer for photodissociation in the upper layers and at the rim of the outer disk: a high ratio indicates a strong UV field, since CN is produced by radical reactions with atomic C and N (in the upper layers) and by photodissociation of HCN, whereas CN cannot easily be photodissociated itself (Bergin et al. 2003; van Dishoeck et al. 2006). The CN/HCN ratio is generally found to be higher in disks around the hotter Herbig stars. HCN observations are required to measure this ratio for IRS 48.

Several of the other targeted molecules have been detected towards cores and protostars, such as $^{34}SO_2$ (Persson et al. 2012), N_2D^+ (Emprechtinger et al. 2009) and HNCO (Bisschop et al. 2007). N_2D^+ can be used as a deuteration tracer in combination with N_2H^+, and therefore a tracer of temperature evolution, but this line was not within our spectral setup. The H_2CO/HNCO abundance limit of >0.3 as derived for IRS 48 is rather conservative compared with values in cores of ∼10 (Bisschop et al. 2007), but the N-bearing molecules are weak in IRS 48. The c-C_3H_2 molecule was recently detected for the first time in the HD163296 disk (Qi et al. 2013b), and their derived column density of $\sim 10^{12}$ cm^{-2} is well below our observed limit for IRS 48 of 10^{13} cm^{-2}.

8.5.4 Predictions of line strengths of other transitions

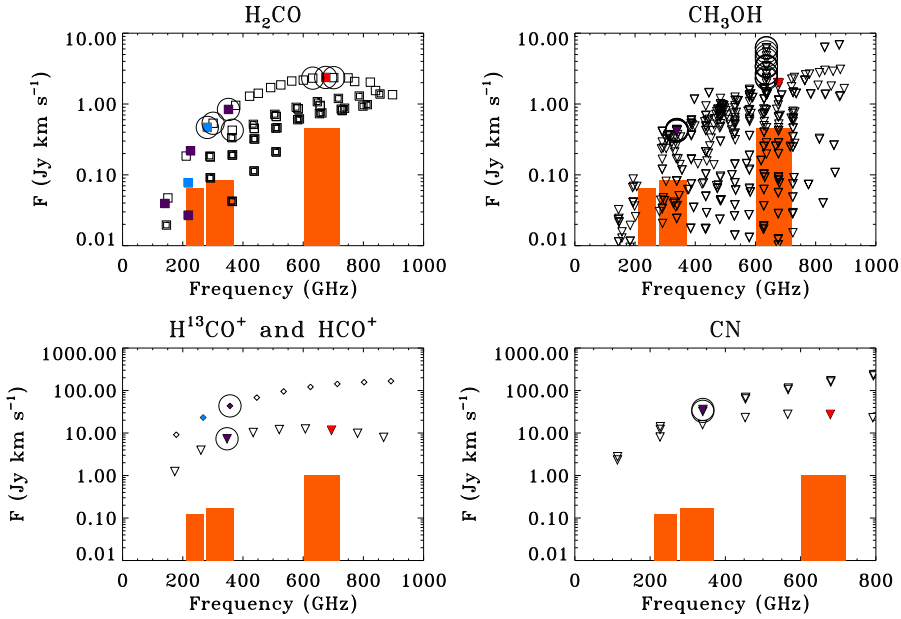


Figure 8.12: *Model predictions for the integrated fluxes for H_2CO (both ortho and para lines, assuming an ortho/para ratio of 3), and upper limits for A-CH_3OH, $H^{13}CO^+$, HCO^+ (triangles and diamonds, respectively), and CN based on our best-fit models for detections and upper limits. The boxes show the 3σ upper limit of the ALMA sensitivity for Band 6 (230 GHz), Band 7 (345 GHz), and Band 9 (690 GHz), integrated over the line profile for one hour integration in the full array. The targeted lines in observations are indicated in red (this study), blue (Öberg et al. 2010,2011), and purple (Thi et al. 2004). The lines that have the best potential for observation compared with the ALMA sensitivity are encircled.*

Most observations of molecules in disks present only intensities, but do not derive abundances, since a physical disk model is generally not available. To compare our observations with these data, we calculated the expected disk-integrated fluxes for other transitions, using our physical model and derived abundances or upper limits. These results are presented in Figure 8.12. The ALMA sensitivity limits for Band 6, Band 7, and Band 9 (230, 345 and 690 GHz) for the ALMA full array of 54 antennas for 1 hour integration are included to investigate which lines provide the best constraints for future observations.

Figure 8.12 shows the potential for future observations of IRS 48, indicating that with full ALMA much better upper limits or detections can be reached for all of these species in just one hour of integration by choosing the correct lines. The H_2CO flux can be measured with much better S/N and there is a wide range of abundances that can be tested. Lines in Band 7 (345 GHz) generally have the highest potential.

For H_2CO, lines that have been targeted most often are the para H_2CO 3(0,3)-2(0,2) and 3(2,2)-2(2,1) transitions at 218.22 and 218.47 GHz, as well as the ortho-H_2CO 4(1,4)-3(1,3) line at 281.53 GHz (Öberg et al. 2010, 2011). Comparing the observed fluxes with our predictions for these lines ($\sim$ 0.3 Jy km s^{-1}) shows that the H_2CO emission of IRS 48 is quite similar to that found in other disks. This is remarkable because of the low disk mass of IRS

48.

CH_3OH has not been detected in other disks to date. Upper limits derived for a few disks (Thi et al. 2004) give abundances $< 10^{-10}$, below our limits for IRS 48. The fact that our observed H_2CO fluxes are similar to those of other disks in spite of the low disk mass bodes well for future studies. Targeted ALMA observations of the strongest lines will allow much better sensitivity and are expected to easily reduce the abundance limits by 1–2 orders of magnitude. Together with searches for other complex organic molecules made preferentially in the ice, this will allow direct tests of the mechanism of sublimation of mid-plane ices in transitional disks proposed by Cleeves et al. (2011).

8.6 Conclusions

We observed the Oph IRS 48 protoplanetary disk with ALMA Early Science at the highest frequencies, around 690 GHz, allowing the detection of warm H_2CO and upper limits on the abundances of several other molecules including CH_3OH, $H^{13}CO^+$, and CN lines at unprecedented angular resolution.

1. We detected and spatially resolved the warm H_2CO 9(1,8)-8(1,7) line, which reveals a semi-ring of emission at ~60 AU radius centered south from the star. No emission is detected in the north. This demonstrates that H_2CO, an ingredient for building more complex organic molecules, is present in a location of the disk where planetesimals and comets are currently being formed.

2. The H_2CO emission was modeled using a physical disk model based on the dust continuum and CO emission (Bruderer et al. 2014), using three different trial abundance profiles. None of the profiles were able to match the observed data exactly, but the absolute flux indicates an abundance with respect to H_2 of $\sim 10^{-8}$.

3. The combination of the H_2CO abundance in combination with upper limits for the CH_3OH emission indicates a H_2CO/CH_3OH ratio >0.3. This limit together with the overall abundance suggests that both solid-state and gas-phase processes occur in the disk.

4. Although the H_2CO emission is located only on the southern side of the disk, just like the millimeter dust continuum, the offset with the continuum peak and the low S/N do not allow a firm claim on a relation with the dust-trapping mechanism.

5. The upper limit for $H^{13}CO^+$ indicates an HCO^+ abundance of $< 10^{-8}$, consistent with our model. The upper limit for CN of $10^{-7.3}$ relative to H_2 is directly at the level of that predicted by our model. Upper limits on the abundances of the other targeted molecules are consistent with earlier observations.

6. Future ALMA observations of intrinsically stronger lines will allow abundances to be measured that are one or more orders of magnitude below the upper limits derived here. This will allow full tests of the chemistry of simple and more complex molecules in transitional disks.

Acknowledgements. The authors would like to thank C. Walsh for useful discussions and M. Schmalzl for help with the observational setup. N.M. is supported by the Netherlands Research School for Astronomy (NOVA), T.v.K. by the Dutch ALMA Regional Center Allegro financed by Netherlands Organization for Scientific Research (NWO) and S.B. acknowledges a stipend by the Max Planck Society. Astrochemistry in Leiden is supported by the Netherlands Research School for Astronomy (NOVA), by a Royal Netherlands Academy of Arts and Sciences (KNAW) professor prize, and by the European Union A-ERC grant 291141 CHEMPLAN. This paper makes use of the following ALMA data: ADS/JAO.ALMA#2011.0.00635.S. ALMA is a partnership of ESO (representing its member states), NSF (USA) and NINS (Japan), together with NRC (Canada) and NSC and ASIAA (Taiwan), in cooperation with the Republic of Chile. The Joint ALMA Observatory is operated by ESO, AUI/NRAO and NAOJ.

9

The (w)hole survey: transition disk candidates from the Spitzer catalogs

van der Marel, N.; Verhaar, B.W.; Terwisga, S., Merín, B.; Herczeg, G.J.; Ligterink, N.F.W.; van Dishoeck, E.F. *The (w)hole survey: an unbiased sample study of transition disk candidates from the Spitzer catalogs.* in prep.

Abstract

Understanding disk evolution and dissipation is essential for studies of planet formation. Transition disks, i.e., disks with large dust cavities, are promising candidates of active evolution. About two dozen SED-selected candidates have been confirmed to have dust cavities through millimeter interferometric imaging, but this sample is biased towards the brightest disks. We aim to find a large unbiased sample of transition disk candidates in nearby star-forming regions for studying their global properties as well as their origin. The *Spitzer* surveys of nearby low-mass star forming regions have resulted in more than 4000 Young Stellar Objects (YSOs). Using color criteria we have selected a sample of ~150 candidates, and an additional 40 candidates and known transition disks from the literature. The *Spitzer* data were complemented by new observations at longer wavelengths, including new JCMT and APEX submillimeter photometry, and *WISE* and *Herschel*-PACS mid and far-infrared photometry. Furthermore, optical and near infrared spectroscopy was obtained and stellar types were derived for 85% of the sample, including the information from the literature. The SEDs were fit to a grid of RADMC-3D disk models with a limited number of parameters: disk mass, inner disk mass, scale height and flaring, and disk cavity radius, where the latter is the main parameter of interest. A large fraction of the targets turn out to have dust cavities based on the SED. The derived cavity sizes are consistent with imaging/modeling results in the literature, where available. Trends are found with $L_{\rm disk}/L_*$ and stellar mass and a possible connection with exoplanet orbital radii. A comparison with a previous study where color observables are used (Cieza et al. 2010) reveals large overlap between their category of planet-forming disks and our transition disks with cavities. The color criteria are a proper tool to select transition disk candidates. In this work we present a large number of transition disks that are suitable for follow-up observations with ALMA.

9.1 Introduction

A central question in planet formation is how the optically thick protoplanetary disks around classical T Tauri stars evolve into the optically thin debris disks around older systems (Williams & Cieza 2011). An important part of the evolution occurs in the transitional phase between these two regimes. Transitional disks, disks with inner dust cavities, are considered to form the evolutionary link, although it remains uncertain whether all disks go through this phase at some point during their lifetime (e.g. Cieza et al. 2007; Currie & Kenyon 2009). The transition disk fraction is thought to be 5%-25% depending on the definition, implying that the evolutionary path through a transition disk is either rapid or uncommon. Transitional disk candidates are traditionally identified through a deficit of infrared flux in the mid-IR spectral energy distribution (SED) (e.g. Strom et al. 1989; Calvet et al. 2002; Espaillat et al. 2014, for review). The deficit arises from the absence of hot small dust particles close to the star, which can be caused by either grain growth, photoevaporative clearing or interaction with a stellar companion or recently formed planet, all processes closely linked to disk evolution. Thanks to *Spitzer* mid-infrared spectroscopy surveys, a large number of transitional disks has been discovered through the dip in their SED (e.g. Brown et al. 2007; Najita et al. 2007; Kim et al. 2009; Merín et al. 2010). Submillimeter observations of about two dozen of the brightest disks have directly resolved large holes with pioneering interferometers, confirming their transition disk status (e.g. Piétu et al. 2005; Brown et al. 2008, 2009; Isella et al. 2010a,b; Andrews et al. 2011). The hole sizes generally match well with estimates from SED modeling, suggesting that the current interpretation and modeling of SEDs can correctly infer this parameter provided that the mid-infrared part of the SED is well covered observationally. The Atacama Large Millimeter/submillimeter Array (ALMA) has produced even sharper dust images of a small sample of transition disks with evidence for dust trapping (van der Marel et al. 2013; Casassus et al. 2013; Pérez et al. 2014; Zhang et al. 2014). ALMA has also revealed the gas distribution through CO observations, showing that substantial amounts of gas are present inside the dust cavities (Bruderer et al. 2014; van der Marel et al. 2015c; Perez et al. 2015; van der Marel et al. 2015b). However, ALMA has so far focused on the most well-studied and brightest transition disks. For a better understanding of the role of transition disks in the disk evolution and planet formation process, a large unbiased sample of transition disks with large holes is required to study the general picture.

One of the most exciting explanations for transition disks is the presence of a young planet that has cleared out its orbit (Lin & Papaloizou 1979). This scenario has been confirmed through the tentative detection of planets embedded in transition disks through direct imaging for a handful of disks (Huélamo et al. 2011; Kraus & Ireland 2012; Quanz et al. 2013; Reggiani et al. 2014; Quanz 2015). As it remains unclear how and at what stage planets are formed in a disk, finding them at the earliest stage and study of their environment can provide important clues on the planet formation process.

Transition disk candidates have been identified through a range of different criteria (Brown et al. 2007; Muzerolle et al. 2010; Oliveira et al. 2010; Merín et al. 2010; Cieza et al. 2010, 2012b; Romero et al. 2012), usually involving the Spitzer colors in the (mid) infrared. The availability of *Spitzer* IRS spectra between 5-35 μm was crucial for classification and determination of the hole size in these studies especially in covering the 8-20 micron region where the SEDs reach their minimum but which is not well covered by the 8 and 24 micron photometry points. In recent years, far infrared *Herschel* PACS and SPIRE photometry has been used to identify and characterize (transition) disks (e.g Ribas et al. 2013; Bustamante et al. 2015; Rebollido et al. 2015). Other studies identified candidates by comparing the infrared part of their SEDs with the 'median' T Tauri disk SED (e.g. Harvey et al. 2007; Merín et al. 2008).

These studies define a separate class of transition disks as 'anemic' disks: disks with homologous depletion of dust due to grain growth or settling at all radii, exhibiting a low infrared excess at all wavelengths. Furthermore, some studies distinguish between pre-transitional and transitional disks: disks with a gap (inner disk present inside the cavity) and disks with a hole (Espaillat et al. 2007) although there is no obvious evolutionary connection. A 'cold disk' (Brown et al. 2007) refers to a transition disk with a strong deficit in the mid infrared, implying a cavity with a steep inner wall. Note that a few transition disks have been found in millimeter imaging without evidence for mid infrared dip in their SED, e.g. MWC 758 (Isella et al. 2010b)

Selection of candidates is sometimes followed up by radiative transfer modeling of the radial disk structure, to constrain the dust cavity size and disk mass (Kim et al. 2009; Merín et al. 2010) to determine the origin of the cavity besides clearing by a companion. Increased grain growth in the inner part of disk would result in the appearance of a dust deficit in the SED (Dullemond & Dominik 2005), although this would not be visible in millimeter imaging (Birnstiel et al. 2010). Furthermore, multiplicity studies can define the origin of the cavity as circumbinary disk whereas measuring the accretion through optical Hα can determine photoevaporative clearing (Najita et al. 2007; Espaillat et al. 2007; Cieza et al. 2010). Theoretical work has also shown that photoevaporative clearing cannot explain the largest observed cavities and a combination of processes may be responsible (Owen & Clarke 2012; Rosotti et al. 2013).

Overall, the definition of a transition disk candidate remains loose and has been used in various contexts in different studies. Due to lack of a large sample of transition disks, general properties remain uncertain and it is still unclear whether the origin for all transition disk cavities is the same, or whether disks follow different evolutionary paths (Cieza et al. 2007). Also, the distribution of cavity radii is not known, while this could constrain the birth sites of giant planets before migration. The analysis of a large unbiased sample of transition disks and candidates will provide firm constraints on their general properties. *Spitzer* surveys in all nearby (<500 pc) star-forming regions (Cores to Disks (c2d), Gould-Belt (GB) and Taurus) have provided identification and SEDs of several thousands of Young Stellar Objects (YSOs) (e.g. Evans et al. 2009; Rebull et al. 2010; Dunham et al. 2015, and references therein), out of which many transition disk candidates. In addition, in recent years the AllWISE catalog with mid infrared targets has become available (Wright et al. 2010), and the *Herschel* telescope (Pilbratt et al. 2010) has observed large parts of nearby star forming regions in the far infrared. Due to the availability of *Spitzer* data combined with WISE and *Herschel* data, the timing is perfect for a large transition disk SED survey.

In this work, we analyze transition disk candidates selected from the *Spitzer* catalogs using robust color criteria developed by Merín et al. (2010). These criteria were developed after deep analysis of the SEDs including IRS spectra. Our sample is complemented by additional candidates and known transition disks from the literature. The SEDs are complemented with optical, new archival far infrared *Herschel*, *Spitzer* IRS spectra (where available) and new submillimeter observations and modeled using the dust radiative transfer code RADMC-3D with a generic disk structure with a cavity. The main parameter of interest is the cavity size $r_{\rm cav}$. In Section 9.2 we discuss the selection criteria of the sample and the additional observations, Section 9.3 presents the results of the observations, Section 9.4 discusses the modeling procedure and limitations and the resulting disk parameters and in Section 9.5 we discuss the robustness of the sample and comparison with previous studies. One of the aims of this study is to define an unbiased sample of transition disks with dust cavities that are large enough to be imaged in the future by ALMA ($\geq$10 AU or $\sim$0.03", for the largest distances). The resolved images of gas and dust will provide more clues on the origin of the dust cavities and the place

of transition disks in disk evolution.

9.2 Observations

9.2.1 Target selection

The c2d, GB and Taurus *Spitzer* Legacy programs completed full infrared surveys using the Infrared Array Camera (IRAC; 3.6-8.0 μm) and Multiband Imaging Photometer (MIPS; 24-160 μm) in the nearby star-forming regions ($\leq$450 pc), resulting in more than 4000 identified YSOs (see Table 9.1 for an overview of papers presenting the data). Several bright YSOs from the c2d survey were targeted for additional observation with the *Spitzer* InfraRed Spectrograph (IRS; 5-35 μm). Merín et al. (2010, hereafter M10) analyzed 35 possible transition disk candidates for which IRS spectra were available in detail through SED modeling, and defined two sets of color criteria:

$$\begin{aligned} [\mathrm{A}] : 0.0 < [3.6] - [8.0] < 1.1; \\ 3.2 < [8.0] - [24.0] < 5.3; \end{aligned} \tag{9.1}$$

$$\begin{aligned} [\mathrm{B}] : 1.1 < [3.6] - [8.0] < 1.8; \\ 3.2 < [8.0] - [24.0] < 5.3; \end{aligned} \tag{9.2}$$

where the bracketed numbers refer to the magnitudes at the *Spitzer* wavelengths. The Region A criteria select 'clean' inner holes (disks for which there is no substantial excess in any IRAC band and there is a clear signature of an inner dust hole) and the Region B criteria select disks with a clear signature of an inner dust hole, but some excess in the IRAC bands, possibly resulting from an inner disk. The latter criterion includes several of the confirmed imaged transition disks (Brown et al. 2009; Andrews et al. 2009), but may also include some disks without holes (M10).

M10 finds one transition disk with a particularly large hole (Sz 84, object 17), which falls outside of the color criteria mentioned above. Inspection of its SED reveals a steep slope between the 24 μm and 70 μm flux. Therefore we set an additional color criterium:

$$\begin{aligned} [\mathrm{L}] : 0.0 < [3.6] - [8.0] < 1.1; \\ 10.0 > [24.0] - [70.0] > 3.8; \end{aligned} \tag{9.3}$$

In this case the MIPS-2 flux at 70 μm has to be detected rather than an upper limit. Due to the large beam size of *Spitzer* at 70 μm (18", see Table 9.3), this flux can be confused with nearby sources. The long wavelength flux thus has to be taken with extra care for the Region L criteria. The Region L targets are not mutually exclusive with the Region A criteria: some targets follow in both.

The color criteria were applied to the three main *Spitzer* catalogs, resulting in 153 candidates. In addition to the catalogs, we searched the literature for additional transition disk candidates, by using the color criteria on *Spitzer* targets that were not included in the catalogs (row 'Other' in Table 9.2), finding an additional 12 disks. Targets in Orion, Cepheus (Kirk et al. 2009) and IC 5146 (Harvey et al. 2008) are not included due to their large distances (450, 500 and 950 pc respectively). Finally, we added 7 confirmed transition disks known from resolved millimeter imaging and 21 targets that were marked as transition disk candidate by various authors, but were not yet included by the color criteria. The number of targets from various selections are listed in Table 9.2 with corresponding references. All targets in

the sample are listed in Table 9.12. Several of the color-selected targets have been identified as transition disk candidates or confirmed by millimeter imaging, as indicated in the last column of Table 9.12.

The distance to Serpens has been uncertain for a long time, with values between 250 and 400 pc (discussion in e.g. Oliveira et al. 2009). However, VLBA observations have demonstrated a distance of 415 pc for the Main Cloud (Dzib et al. 2010), which has been used in more recent work (Erickson et al. 2015; Ortiz-León et al. 2015), and has also been used in this study.

Table 9.1: *Overview Spitzer papers of YSOs in star forming regions*

Cores to Disks (c2d)		d (pc)	Paper
Ophiuchus (MIPS)	Padgett et al. (2008)	120	VII
Serpens	Harvey et al. (2007)	250-400[a]	IX
Cham II	Alcalá et al. (2008)	180	X
Lupus I,III,IV	Merín et al. (2008)	150-200	XI
Perseus	Young et al. (2015)	250	XII
WTTS (c2d)	Padgett et al. (2006); Cieza et al. (2007)	-	
Disks with holes (c2d)	Merín et al. (2010)	-	
	Gould Belt (GB)		
IC5146	Harvey et al. (2008)	950	I
Cepheus	Kirk et al. (2009)	300	II
CrA	Peterson et al. (2011)	150	III
Lupus V & VI (full)	Spezzi et al. (2011)	150	IV
Ophiuchus North	Hatchell et al. (2012)	120	V
Auriga	Broekhoven-Fiene et al. (2014)	450	VI
	Others		
η Cham (IRAC)	Megeath et al. (2005)	97	
η Cham (MIPS)	Sicilia-Aguilar et al. (2009)	97	
Cham I	Luhman et al. (2008)	160	
Taurus	Rebull et al. (2010); Luhman et al. (2010)	140	
λ Orionis	Hernández et al. (2010)	450	
Orion	Megeath et al. (2012)	450	
	Wahhaj et al. (2010)		
FEPS	Carpenter et al. (2008)	-	

Notes. [(a)] The distance to Serpens has been uncertain for a long time, but with recent VLBA observations it has been set to 415 pc (Dzib et al. 2011), which has been used in this study.

9.2.2 Additional photometry

For each target, an SED was constructed using the *Spitzer* IRAC and MIPS photometry, complemented with optical B, V and R data from the NOMAD catalog (Zacharias et al. 2005) and near infrared J, H and K photometry from 2MASS (Cutri et al. 2003). Reduced *Spitzer* IRS low-res spectra of 5-35 μm were taken from the Cornell Atlas of Spitzer/IRS Sources (CASSIS) (Lebouteiller et al. 2011) when available. For ID63 (DoAr28), the IRS spectrum in CASSIS included extended emission, a properly reduced spectrum was kindly provided by Melissa McClure (McClure et al. 2010). Unfortunately IRS spectra are not available for the entire sample, while colors only provide limited constraints on the derived cavity size. Bright isolated targets could be complemented with *IRAS* photometry, especially when *Spitzer* data

Table 9.2: *Target selection in each catalog*

Catalog/Criterion	[A]	[B]	[L]
c2d (Evans et al. 2009)	30	34	9
GB (Dunham et al. 2015)	25	15	31
Taurus (Rebull et al. 2010)	7	12	6
Other samples[a]	7	4	1
Additional targets[b]	7 imaging 21 SED		

Notes. [(a)] Targets were selected using our color criteria in the following papers, for targets not included in the c2d/GB/Taurus catalogs: Padgett et al. (2006); Silverstone et al. (2006); Carpenter et al. (2008); Luhman et al. (2008); Kim et al. (2009); Sicilia-Aguilar et al. (2009); Cieza et al. (2010); Luhman et al. (2010) [(b)] Some targets were added from the literature that did not follow the color criteria. Imaging targets were taken from Piétu et al. (2006); Ohashi (2008); Brown et al. (2009); Isella et al. (2010a); Andrews et al. (2010, 2011); Rosenfeld et al. (2013); van der Marel et al. (2013). The other targets were identified as transition disk candidate by Megeath et al. (2005); Hernández et al. (2007); Merín et al. (2008); Monnier et al. (2008); Hughes et al. (2008); Sicilia-Aguilar et al. (2008); Ireland & Kraus (2008); Kim et al. (2009); McClure et al. (2010); Najita et al. (2010); Espaillat et al. (2011); Furlan et al. (2011)

were saturated. The *Wide-field Infrared Survey Explorer (WISE)* performed an all sky survey in four wavelength bands: 3.4, 4.6, 12.0 and 22 μm leading to the AllWISE Source catalog (Wright et al. 2010). The coordinates of the targets in our sample were matched with the WISE targets (within 2") and the fluxes were added to the SEDs. Although 3 of the 4 bands overlap with *Spitzer*, the 12 μm flux provides an important data point in between IRAC and MIPS wavelengths when no IRS spectra are available. Furthermore, the diffraction limited beam size of the *WISE* satellite is twice as large as the *Spitzer* beam (see Table 9.3). The comparison between the *WISE* 22 μm flux with the MIPS-1 24 μm flux gives an independent check of confusion at longer wavelengths: if the 22 μm flux is much larger, there is likely a nearby source that will confuse 70 μm MIPS-2 flux as well. Although the *Spitzer* c2d and GB catalogs provide a quality flag on the MIPS-2 flux (MP2_Q_det_c) for possible confusion, this independent alternative check showed more directly which targets were confused at longer wavelengths. A difference between the 22 and 24 μm flux could also originate from infrared variability, for example due to a scale height changes in the inner disk (e.g. Flaherty & Muzerolle 2010; Espaillat et al. 2011). However, such variability is typically on the order of 20-40%. Therefore, we only consider confusion if the difference in flux is more than 50%. The fluxes of different telescopes are taken with years in between, so without infrared monitoring there is no possibility to quantify this effect for the targets in our sample, but the effect on our SED modeling is expected to be minor. The following targets were removed from the sample due to possible confusion and their SEDs were not further analyzed: IDs 30, 32, 82, 85, 86, 88, 90, 92, 93, 95, 97, 98, 116, 123, 126, 202, 346 and 347.

At longer wavelengths, the SEDs were complemented with (sub)millimeter data from the literature where available (see refs in Table 9.14). A subsample of the remaining targets were observed with the James Clerk Maxwell Telescope (JCMT) [1] and the Atacama Pathfinder

[1]The James Clerk Maxwell Telescope has historically been operated by the Joint Astronomy Centre on behalf of the Science and Technology Facilities Council of the United Kingdom, the National Research Council of Canada and the Netherlands Organisation for Scientific Research. Additional funds for the construction of SCUBA-2 were provided by the Canada Foundation for Innovation.

Table 9.3: *Beam sizes and apertures for photometry*

Telescope	Instrument	Wavelength range (μm)	Beam size/ Aperture(")
Spitzer	IRAC	3.6,4.5,5.8,8.0	1.7–1.9
	MIPS	24.0,70.0	6.0,18
WISE		3.4,4.6,12,22	6.1,6.4,6.5,12
Herschel	PACS	70,100,160	5.5,6.5,11
APEX	SABOCA	350	7.8
	LABOCA	870	19
JCMT	SCUBA-2	850	15

Experiment (APEX) [2]. Targets were selected on their expected submillimeter brightness considering their 70 μm flux. The details of these observations are discussed in Section 9.2.3.

The SEDs were further complemented with far infrared fluxes from the *Herschel* Space Observatory (Pilbratt et al. 2010). The data reduction is discussed in Section 9.2.4.

9.2.3 Submillimeter observations

Observations of 32 of our targets were taken with the SABOCA and/or LABOCA instruments at the APEX telescope at the Chajnantor plateau in Chile. Observations were taken in service mode in 2012 and 2013 in ESO programs 089.C-0940, 090.C-0820 and 091.C-0822 and Max Planck programs M0010_88 and M0003_90. SABOCA is a 39-channel bolometer array operating at 350 μm (Siringo et al. 2010), LABOCA is a 295-channel bolometer array at 870 μm (Siringo et al. 2009). Imaging was performed in wobbler on-off mode. For a few sources, imaging was also performed in mapping mode (map size 1.5') to check the pointing and to check for extended emission. One source (MP Mus, ID 20) was observed with the new ArTeMiS camera in mapping during its commissioning phase, operating at 350 μm (Revéret et al. 2014). Integration times were 5-40 minutes on source. The data were reduced using the CRUSH software (Kovács 2008) and (for the wobbler observations) verified using the BoA software (Schuller 2012). The results from both reduction techniques were found to agree within error bars and the CRUSH results are reported in Table 9.8. Flux calibration uncertainties (not included in Table 9.8) are typically 10% for LABOCA and 25-30% for SABOCA.

Observations of 41 of our targets were taken with the SCUBA-2 instrument at the JCMT telescope at Mauna Kea, Hawaii. Observations were taken in service mode in 2012 and 2013 in programs M12AN07, M12BN13 and M13AN01. SCUBA-2 is a 10,000 pixel bolometer camera operating simultaneously at 450 and 850 μm (Holland et al. 2013). Imaging was performed in the smallest possible map size (Daisy 3' pattern). Observations were taken in grade 3-5 weather, which is generally insufficient for observing at 450 μm, so only the 850 μm data are considered. Integration times were 5-50 minutes on source. The data were reduced using the default online pipeline. The resulting FITS images were inspected by eye for extended emission and fluxes and noise levels were derived. The noise levels were estimated by measuring the standard deviation in the map, after subtraction of point sources. The results are reported in Table 9.7. The flux calibration uncertainty (not included in Table 9.7) is typically 10% for SCUBA-2.

[2]This publication is based on data acquired with the Atacama Pathfinder Experiment (APEX). APEX is a collaboration between the Max-Planck-Institut fur Radioastronomie, the European Southern Observatory, and the Onsala Space Observatory.

9.2.4 Herschel observations

We have searched the *Herschel* Science Archive for observations with the PACS broadband photometer (Poglitsch et al. 2010) at the coordinates of all targets in the sample. In photometry mode, PACS observes simultaneously at either 70 (PACS blue) and 160 μm (PACS red) or 100 (PACS green) and 160 μm. Therefore, targets are recovered in either two or three of these wavelength bands. Only data products of reduction level higher than 2.0 were used, using the high pass filter.

Photometry of the PACS data was performed using the *annularSkyAperturePhotometry*-task in the Herschel Interactive Processing Environment (HIPE), version 12.1.0. This task derives background-corrected fluxes from point sources by comparing the flux inside a region centered on the point source and an annulus around it. We used the values for the aperture and annulus radii as used by Ribas et al. (2013). The background was estimated using the DAOPhot algorithm. Errors were estimated manually at several positions near the source position, to avoid including nearby extended emission originating from clouds. The presence of nearby clouds is indicated in Table 9.13. The flux calibration uncertainty (not included in Table 9.13) is typically 5% for PACS photometry.

9.2.5 Spectroscopy

Stellar properties such as the spectral type must be determined to correct for the extinction and deredden the SED flux points. The stellar luminosity is required to understand and interpret the SEDs properly. For about half of the targets in the sample, spectral types are available from the literature. The targets without known spectral type were observed with optical or near-infrared spectroscopy (the latter for targets that are optically faint due to high extinction).

Optical

Optical spectra were taken for 90 targets, including reobservation of 24 targets for which the literature spectral type was still uncertain (see Table 9.4). These observations were taken during 5 nights in visitor mode in August 2012 at the 4.2m William Herschel Telescope (WHT) at La Palma, using the Intermediate dispersion Spectrograph and Imaging System (ISIS) spectrograph. We used the double arm to obtain spectra between 3200–10000 Å with resolving power of $\sim$ 1000, using the R316R and R600B gratings. R magnitudes ranged between 9 and 19 mags, requiring integration times between 1 and 60 minutes. The slit width was set each night depending on the seeing.

The images were reduced and spectra extracted using standard methods with custom codes in IDL. All spectra were flux-calibrated using spectrophotometric standards (Oke 1990) and corrected for a telluric extinction, calculated independently each night. The spectra span from 3200–10000 Å with resolution of $\sim$ 1000.

Spectral types were determined by comparing spectra to template spectra of young stars, following Herczeg & Hillenbrand (2014). Veiling estimates were included in the spectral fits. The Hα line equivalent width was calculated by fitting a Gaussian profile to the line.

Near-infrared spectroscopy

28 optically faint targets were observed during 6 nights in visitor mode in August 2013 at the 4.2 William Herschel Telescope using the Long-slit Intermediate Resolution Infrared Spectrograph (LIRIS) instrument. We used the hr_k grism to obtain K-band spectra with a resolving power of R=3000 between 2 and 2.4 μm. K-band magnitudes ranged between 9 and 14 mags,

Table 9.4: *Optical/near infrared spectroscopy observations*

Date	Telescope	Instrument	Coverage	Resolving power
August 2012	WHT	ISIS	3500-9000 Å	R=1000
August 2013	WHT	LIRIS	2-2.4 μm	R=3000
June - August 2014	VLT	X-shooter	0.3-3.7 μm	R=8000

requiring integration times between 10 and 60 minutes. Telluric standards were observed once per hour. The LIRIS data are not yet reduced and therefore not included in this Chapter.

20 optically faint targets were observed in service mode in Summer 2014 at the Very Large Telescope using the X-shooter instrument as part of program 093.C-0757. X-shooter covers the entire optical and near infrared wavelength range between 0.3 and 3.7 μm with a resolving power of R=8000. The X-shooter data are not yet reduced and therefore not included in this Chapter.

9.3 Results

Table 9.5: *Comparison PACS photometry with previous estimates*

ID	$F_{70\mu m}$ (Jy)		$F_{100\mu m}$ (Jy)		$F_{160\mu m}$ (Jy)		Ref
	This study	Previous	This study	Previous	This study	Previous	
4	< 0.1	< 0.08	< 0.07	< 0.14	< 0.41	< 1.10	1
5	0.18 ± 0.05	0.15 ± 0.02	0.17 ± 0.03	0.17 ± 0.04	< 0.33	< 1.07	1
6	3.11 ± 0.31	3.08 ± 0.46	2.90 ± 0.29	2.82 ± 0.42	2.15 ± 0.25	2.32 ± 0.35	1
7	0.21 ± 0.04	< 0.28	0.21 ± 0.03	0.21 ± 0.01	< 0.31	< 0.32	2
9	< 0.65	0.60 ± 0.09	< 0.71	0.77 ± 0.12	< 1.06	0.98 ± 0.15	1
11	3.86 ± 0.39	3.88 ± 0.58	3.80 ± 0.38	3.63 ± 0.54	3.65 ± 0.37	3.86 ± 0.58	1
12	0.44 ± 0.05	0.38 ± 0.06	0.40 ± 0.05	0.36 ± 0.06	< 0.39	0.20 ± 0.03	1
13	< 0.11	< 0.04	0.14 ± 0.03	< 0.07	< 0.55	< 0.85	1
14	0.69 ± 0.08	0.68 ± 0.10	0.55 ± 0.06	0.57 ± 0.09	0.41 ± 0.07	< 0.30 ± 0.05	1
15	1.58 ± 0.16	1.61 ± 0.24	2.31 ± 0.23	2.19 ± 0.33	2.80 ± 0.28	2.74 ± 0.41	1
16	26.06 ± 2.92	25.91 ± 3.88	36.06 ± 3.9	32.32 ± 4.85	38.45 ± 6.0	27.3 ± 4.10	1
17	0.21 ± 0.05	< 0.25	0.25 ± 0.03	0.23 ± 0.01	0.30 ± 0.09	0.28 ± 0.05	2
24	0.17 ± 0.04	0.07 ± 0.02	0.11 ± 0.03	0.10 ± 0.02	< 0.09	< 0.13	3
25	< 0.34	0.11 ± 0.03	< 0.32	0.16 ± 0.04	< 0.38	< 0.23	3
26	< 0.26	0.10 ± 0.02	< 0.12	0.18 ± 0.04	< 0.02	< 0.19	3
27	0.61 ± 0.07	0.51 ± 0.13	0.80 ± 0.08	0.68 ± 0.17	0.96 ± 0.17	0.72 ± 0.18	3
179	1.23 ± 0.13	1.04 ± 0.26	1.41 ± 0.14	1.26 ± 0.31	1.69 ± 0.19	1.57 ± 0.39	3
185	0.21 ± 0.06	0.17 ± 0.04	0.24 ± 0.05	0.23 ± 0.06	< 0.91	0.29 ± 0.07	3
200	0.48 ± 0.06	0.36 ± 0.09	0.37 ± 0.05	0.37 ± 0.09	0.47 ± 0.15	0.26 ± 0.07	3

Refs. 1) Ribas et al. (2013), 2) Olofsson et al. (2013), 3) Bustamante et al. (2015)

9.3.1 Stellar parameters

Spectral types as derived from our observations and taken from the literature are given in Table 9.6. The observations of previously characterized stars resulted generally in the same spectral

types as derived before. Some of the WHT-ISIS targets did not show any lines and no spectral type could be determined: ID 32, 47, 101, 112, 114, 124, 125, 131, 164, 202 and 204, these SEDs were fit assuming a K7 star. ID 68, 80, 84, 104, 110, 119, 122 and 129 turned out to be giants, these SEDs were not further analyzed. For a handful of targets, the spectral type could not be determined to subtype accuracy. This paper presents new spectral types for 85 targets. For our final sample, spectral types are known for ~85% of our targets.

Spectral types are converted to the effective temperature $T_{\rm eff}$ using the scales in Kenyon & Hartmann (1995). The extinction A_V and stellar luminosity L_* (or stellar radius R_*, as $L_* = 4\pi R_*^2 \sigma T^4$) are fit simultaneously to the SEDs, assuming the distances listed at the bottom of Table 9.12. Kurucz models of stellar photospheres (Castelli & Kurucz 2004) are used as templates for the broadband emission. The 2MASS J-band and optical V and R band fluxes are taken as reference to constrain the fit, assuming no excess in these bands. When both V and R were missing, the extinction was estimated adopting $A_J = 1.53 \times E(J-K)$, where $E(J-K)$ is the observed color excess with respected to the expected photospheric color (Kenyon & Hartmann 1995), depending on its spectral type. The extinction law is parametrized as a function of wavelength assuming R_V=5.5 (Indebetouw et al. 2005) and scaled to the visual extinction A_V. The resulting values are listed in Table 9.6. Stellar masses are derived by interpolation of evolutionary models of Baraffe et al. (1998) in the position of the target on the HR diagram. For targets that could not be fit by the Baraffe models (which only include stars up to 1 $M_\odot$), masses were derived using the evolutionary models by Siess et al. (2000). Since uncertainties in stellar age are large, they are not tabulated here. We note that for the Serpens targets an alternative distance of 250 pc as used in previous work would often result in very high age estimates (>10 Myr), confirming that the 415 pc used here is likely more accurate (also demonstrated in Oliveira et al. 2009, 2013). For 10 targets no stellar mass could be derived, suggesting that their derived stellar properties are uncertain. Most of these are targets without known spectral type or late M stars.

The presence or absence of accretion can be assessed from the strength and shape of emission of the Hα and other optical lines (e.g. White & Basri 2003; Natta et al. 2006). Although a proper treatment of the accretion requires simultaneous fitting of extinction, luminosity and accretion through broadband spectroscopy (e.g. with X-shooter, Manara et al. 2014), as accretion also results in broadband UV/blue excess, the analysis in this study is limited to a simple designation of accretion by the width of the Hα line and we do not aim to quantify the accretion in terms of $M_\odot$ yr^{-1} due to the large uncertainties when deriving accretion from the line width only. Both the equivalent width EW[Hα] and the Hα 10% width have been used to distinguish between accretors and non-accretors, where the EW[Hα] cut-off depends on the spectral type (White & Basri 2003). Typically, a star is classified as an accretor if the Hα 10% width is >300 km s^{-1} (Natta et al. 2004), or if EW[Hα] > 3Å for an early-K star, > 10Å for a late-K star and > 20Å for an M star. Since other studies often only list the EW[Hα] values, our accretion designation is largely based on that. In recent years, several YSOs have been analyzed with broadband high resolution spectroscopy, including some of the targets in our sample (e.g. Alcalá et al. 2014; Manara et al. 2014). This accretion information is preferred above the derivation from the equivalent width as this method is more reliable, and those targets have been marked explicitly in Table 9.6. Accretion properties are known for 84% of our sample: about 64% of these targets are accreting, the remaining targets show little or no signs of accretion

Table 9.6: *Stellar parameters*

ID	SpT	T_{eff} (K)	A_V (mag)	L_* ($L_\odot$)	M_* ($M_\odot$)	EW[Hα] (Å)	FW10%[Hα][a] (km s^{-1})	Accretion[d] (Y/N)	Ref
1	K0	5250	2.0	1.34	1.1	-	400	Y	1,2
2	K5	4350	0.4	0.73	1.2	4.4	330	Y	3
3	M4	3370	2.4	0.14	0.3	35	330	Y	3
4	M3.5	3370	4.9	0.26	0.4	-	-	U	4
5	M4	3370	3.0	0.17	0.3	[b]	-	N	5
6	K2	4780	1.3	1.88	1.5	[b]	-	Y	6
7	M3.25	3470	5.7	0.16	0.4	200	-	Y	7
9	K0	5250	0.0	2.47	1.4	[b]	-	N	5
10	G5	5770	3.0	15.19	2.3	-	-	U	4
11	K2	4780	0.7	1.36	1.4	[b]	-	Y	6
12	K7	4060	3.4	0.41	1.0	[b]	-	Y	6
13	M0	3850	4.3	0.57	1.0	1	249	N	8
14	M0.5	3720	0.3	0.34	0.8	[b]	-	Y	6
15	K0	5250	2.4	4.99	2.0	[b]	-	Y	5
16	K5	4350	3.4	4.41	0.9	65	-	Y	9,4
17	M6	3050	6.9	0.17	0.1	43.6	-	Y	10
18	M2.5	3470	2.3	0.33	0.5	[b]	-	Y	6
20	K1	5080	0.9	1.35	1.2	-47	-	Y	11
21	F6	6360	1.4	23.58	2.3	[c]	-	Y	12
22	M3.5	3370	4.1	0.20	0.3	-0.4	-	N	13
23	M1.5	3580	0.1	0.38	0.6	-	375	Y	14
24	M4.5	3240	2.6	0.22	0.3	12.9	-	N	13
25	M4	3370	3.7	0.47	0.5	-	426	Y	14
26	M5	3240	1.0	0.19	0.3	-	201	Y	14
27	M0.5	3720	0.8	0.29	0.7	-	374	Y	14
28	M6	3050	0.0	0.22	0.1	-	189	Y	14
29	M5	3240	2.7	0.32	0.3	[b]	-	Y	6
30	K5	4350	0.8	0.05	1.0	0.1	-	N	13
31	M5.5	3050	4.9	1.51	-	-	-	U	13
32	-	4060	14.0	0.79	1.0	0.3	-	N	13
33	F4	6590	0.8	11.48	1.8	[c]	-	Y	12
34	M2	3580	5.7	0.12	0.5	-14.5	-	N	15
35	M1	3720	1.3	0.21	0.7	10.3	227	N	16
36	M6	3050	8.4	0.49	0.1	174.5	-	Y	13
38	K7	4060	0.0	1.08	1.2	[b]	-	Y	6
39	K5	4350	0.5	0.73	1.2	26.7	-	Y	13
40	K7	4060	4.6	0.88	1.2	-	470	Y	13,17
41	M2	3580	2.9	0.12	0.5	-	567	Y	17
43	M3	3470	4.2	0.38	0.5	88.7	-	Y	13
44	M2	3580	3.9	0.38	0.6	-	365	Y	17

Refs. 1) Alcala et al. (1995), 2) Schisano et al. (2009), 3) Lawson et al. (2004), 4) Luhman (2007), 5) Manara et al. (2015), 6) Manara et al. (2014), 7) Luhman & Muench (2008), 8) Spezzi et al. (2008), 9) Luhman (2004), 10) Comerón et al. (2004), 11) Silverstone et al. (2006), 12) Garcia Lopez et al. (2006), 13) This work, 14) Alcalá et al. (2014), 15) Sicilia-Aguilar et al. (2008), 16) Wahhaj et al. (2010), 17) Cieza et al. (2010), 18) Natta et al. (2006), 19) Brown et al. (2012a), 20) Wilking et al. (2005), 21) Oliveira et al. (2009), 22) White & Ghez (2001), 23) Rebull et al. (2010), 24) Salyk et al. (2013), 25) Nguyen et al. (2012), 26) Furlan et al. (2006), 27) Calvet et al. (2004), 28) Furlan et al. (2011), 29) Mooley et al. (2013), 30) Merín et al. (2010), 31) Cieza et al. (2007), 32) Cieza et al. (2012b), 33) Romero et al. (2012), 34) Rigliaco et al. (2015), 35) Kraus & Hillenbrand (2009), 36) Herczeg & Hillenbrand (2014), 37) Carpenter et al. (2008)

Notes. [a] We have reversed the signs of the width of the Hα line taken from Rebull et al. (2010) and Winston et al. (2009), as they list a negative value for emission and positive for absorption. [b] The accretion properties have been derived using a full X-shooter spectrum rather than only fitting the Hα line. [c] The accretion properties have been derived using other lines (e.g. Brγ). [d] 'Y' means accreting, 'N' means non-accreting', 'U' means unknown.

Table 9.6: *Stellar parameters*

ID	SpT	T_{eff} (K)	A_V (mag)	L_* ($L_\odot$)	M_* ($M_\odot$)	EW[Hα] (Å)	FW10%[Hα][a] (km s^{-1})	Accretion (Y/N)	Ref
45	K2	4780	5.8	2.07	1.5	[c]	-	Y	18
46	M0	3850	3.3	0.44	0.9	-	301	Y	13,17
47	-	4060	15.0	0.41	1.0	-0.6	-	N	13
48	M5.5	3050	5.8	0.38	0.1	[b]	-	Y	6
49	K5	4350	1.9	2.53	0.9	-	450	Y	13,17
50	M2	3580	2.9	0.38	0.6	[b]	-	Y	6
51	A0	9520	10.6	14.50	1.9	[c]	-	Y	19
52	K3	4730	2.9	1.46	1.4	[b]	-	Y	6
53	M4	3370	6.7	0.12	0.3	60.2	-	Y	13
54	G3	5830	5.5	6.50	1.7	[b]	-	Y	6
55	G	5830	6.0	1.76	1.2	8.4	-	Y	13
56	-	4060	11.2	0.04	-	-	-	U	
58	K8	3960	3.3	0.43	1.0	28.4	-	Y	13,20
59	M4	3370	5.2	0.20	0.3	-	159	N	13,17
60	M0	3850	3.7	0.28	0.9	[b]	-	Y	6
61	M2.5	3470	1.5	0.19	0.4	7.4	-	N	13
62	K5	4350	1.8	0.83	1.3	-	493	Y	13,17
63	K5	4350	2.6	0.73	1.2	44.5	-	Y	13
64	K5	4350	0.0	0.55	1.1	5.3	-	Y	13
65	F3	6740	0.8	10.71	1.7	-4.3	-	N	13
66	M5	3240	6.6	3.45	-	32	-	Y	13
67	-	4060	6.7	3.92	0.6	-	-	U	
68	M-GIANT	-	-	-	-	-	-	N	13
69	B9	10500	4.4	39.52	2.4	-9.8	-	N	13
70	G5	5770	5.2	3.23	1.4	5.8	-	Y	13
71	FG	6030	7.4	3.05	1.3	1.2	-	N	13
73	-	4060	14.4	7.14	0.7	-	-	U	
74	-	4060	10.6	1.53	1.2	-	-	U	
75	-	4060	13.2	3.92	0.6	-	-	U	
76	A0	9520	3.4	29.59	2.2	-9.2	-	N	13
77	F5	6440	4.5	4.48	1.4	-3.2	-	N	13
78	M5.5	3050	7.0	1.25	-	21.6	-	Y	13
79	A0	9520	1.8	23.97	2.2	-10.3	-	N	13
80	M-GIANT	-	-	-	-	-	-	N	13
81	FG	6030	10.8	4.30	1.4	-15.8	-	N	13
82	-	4060	9.3	0.02	1.0	-	-	U	
83	M4.5	3240	6.0	0.22	0.3	68.5	-	Y	13
84	M-GIANT	-	-	-	-	-	-	N	13
85	-	4060	14.0	0.12	1.0	-	-	U	
86	-	4060	14.9	0.12	1.0	-	-	U	
88	-	4060	11.0	2.83	1.0	-	-	U	
89	A6	8350	5.7	25.22	2.0	-5.7	-	N	13
90	-	4060	10.6	0.20	1.0	-	-	U	
91	-	4060	12.0	0.30	0.9	-	-	U	
92	-	4060	14.9	0.12	1.0	-	-	U	
93	A0	9520	12.4	32.63	1.0	-	-	N	13
94	-	4060	14.9	2.83	0.6	-	-	U	
95	-	4060	8.7	0.71	1.0	-	-	U	
96	-	4060	7.0	1.92	1.3	-	-	U	
97	-	4060	9.3	0.06	1.0	-	-	U	
98	-	4060	11.4	0.12	1.0	-	-	U	
99	A2	8970	2.7	16.85	1.9	-9.6	-	N	13
100	A7	7850	8.8	13.68	1.8	-6.6	-	N	13
101	-	4060	7.2	0.79	1.1	0.3	-	N	13
102	-	4060	19.8	0.35	1.0	-	-	U	
103	-	4060	15.0	0.88	1.2	-	-	U	
104	M-GIANT	-	-	-	-	-	-	N	13
105	FG	6030	8.7	3.86	1.4	1.7	-	N	13

Table 9.6: *Stellar parameters*

ID	SpT	T_{eff} (K)	A_V (mag)	L_* ($L_\odot$)	M_* ($M_\odot$)	EW[Hα] (Å)	FW10%[Hα][a] (km s^{-1})	Accretion (Y/N)	Ref
106	A7	7850	1.9	46.82	2.5	-6.6	-	N	13
107	M3	3470	3.4	0.38	0.5	4.8	-	N	13
108	-	4060	7.0	8.52	-	-	-	U	
110	M-GIANT	-	-	-	-	-	-	N	13
111	K2	4780	3.8	4.23	1.6	13.4	-	Y	13,21
112	-	4060	4.0	1.53	1.2	17.5	-	Y	13
113	FG	6030	5.2	0.19	-	-1.3	-	N	13
114	-	4060	7.1	8.52	-	-5.1	-	N	13
115	K7	4060	7.5	1.53	1.2	131.3	-	Y	13,21
116	FG	6030	6.6	2.68	1.0	-1.5	-	N	13
117	GK	5250	4.7	0.99	1.0	-5.3	-	N	13
118	M1	3720	1.0	0.21	0.7	9.3	-	N	13
119	M-GIANT	-	-	-	-	-	-	N	13
120	M2	3580	2.9	0.15	0.5	[b]	-	N	6
121	-	4060	3.8	0.12	1.0	-	-	U	
122	M-GIANT	-	-	-	-	-	-	N	13
123	B8	11900	4.0	52.20	1.0	-9.1	-	N	13
124	-	4060	11.0	0.63	1.1	-	-	U	
125	F4	6590	8.9	5.50	1.4	42.7	-	Y	13
126	M2	3580	1.0	0.21	1.0	88.6	-	Y	13,21
127	M1	3720	2.8	0.76	0.8	[b]	-	Y	6
128	K7	4060	3.8	1.41	1.2	10.9	273	Y	21
129	M-GIANT	-	-	-	-	-	-	N	13
130	K7	4060	4.3	0.20	0.8	38.0	-	Y	13
131	-	4060	5.1	0.63	1.1	9.8	-	Y	13
132	A2	8970	5.6	39.42	2.2	9.9	-	Y	13,21
133	K5	4350	0.7	1.04	1.4	7.4	-	Y	13,21
134	M2	3580	0.7	0.38	0.6	1.4	-	N	13
135	M1	3720	0.7	0.25	0.7	[b]	-	Y	6
136	K2	4780	0.8	1.88	1.5	9.5	-	Y	22
137	M2.5	3470	2.0	0.03	0.4	28.0	-	Y	13,23
138	M3	3470	5.6	0.29	0.5	4.2	-	N	13,23
139	K5	4350	5.1	0.08	-	18.2	-	Y	13,23
140	F2	6890	1.5	3.98	1.4	-5.5	-	N	23
142	A8	7580	0.7	34.37	2.3	[c]	-	Y	24
144	K1	5080	3.0	0.15	-	-1.1	-	N	13,23
145	M1	3720	0.5	0.44	0.8	-	348	Y	23,25
146	K3	4730	2.6	3.54	1.5	-1.1	-	N	23
147	M6	3050	3.0	0.02	0.1	17.3	-	N	23
148	M0	3850	0.6	0.51	0.9	11	-	Y	22
149	B8	11900	9.5	131.67	3.1	-	-	U	26
150	M4.5	3240	1.7	0.32	0.3	-	210	N	23
151	A0	9520	0.9	16.65	1.9	10	-	Y	23
152	K7	4060	1.1	0.79	1.1	-	180	N	23
153	G1	5945	2.8	17.11	2.3	[c]	-	Y	27
154	M0	3850	17.0	1.05	1.0	-	-	U	23
155	M1.25	3720	2.8	0.34	0.8	2.3	-	N	28
156	G5	5770	2.4	0.04	-	-2.4	-	N	13
157	M5	3240	3.7	0.44	0.2	21.8	-	Y	13
158	K0	5250	1.0	1.75	1.2	-1.2	110	N	16
159	A0	9520	1.6	112.53	3.1	[c]	-	Y	29,24
160	K4	4560	5.7	0.19	0.8	205	-	Y	13
161	K4	4560	5.7	0.19	0.8	17.6	-	Y	13,30
162	M0	3850	2.5	0.20	0.8	4.8	-	N	30
163	K6	4205	3.3	0.34	1.0	104.7	-	Y	13
164	-	4060	7.0	0.30	0.9	64.7	-	Y	13
165	K7	4060	7.1	0.35	1.0	4.3	-	N	30
166	FG	6030	5.4	3.86	1.4	-1.2	-	N	13

Table 9.6: *Stellar parameters*

ID	SpT	T_{eff} (K)	A_V (mag)	L_* ($L_\odot$)	M_* ($M_\odot$)	EW[Hα] (Å)	FW10%[Hα][a] (km s^{-1})	Accretion (Y/N)	Ref
167	K	4730	9.3	0.37	0.8	-2.9	-	N	13
168	M3	3470	3.1	0.16	0.4	130	504	Y	30
169	M4	3370	7.9	0.14	0.3	-5.7	-	N	13,30
171	M1	3720	2.6	0.69	0.8	11.5	-	N	31
172	M0.75	3720	0.7	0.17	0.7	-	280	N	32
173	G3	5830	3.0	12.75	2.2	[b]	-	Y	6
174	M0	3850	2.1	0.33	0.9	-	370	Y	13,32
175	M0	3850	3.2	0.16	0.8	-	350	Y	13,32
176	M4	3370	4.1	0.02	0.3	10.3	-	N	13
177	K7	4060	2.7	0.09	0.6	-	310	Y	32
178	-	4060	8.8	0.09	1.0	-	-	U	
179	K0	5250	1.3	1.34	1.1	-	532	Y	33
180	M0.75	3720	1.9	0.39	0.8	-	440	Y	33
181	K0	5250	4.8	2.22	1.3	-	360	Y	32
182	M2	3580	1.1	0.09	0.5	-	130	N	32
183	M2	3580	2.1	0.25	0.6	-	140	N	32
184	B9	10500	2.8	79.81	2.7	-	-	N	32
185	M5	3240	0.0	0.22	0.3	[b]	-	Y	14
186	M1	3720	0.0	0.25	0.7	82.6	416	Y	16
187	M0.5	3720	1.5	0.29	0.7	29.3	-	Y	23,34
188	M0	3850	1.0	0.33	0.9	99	-	Y	23
189	K5	4350	20.4	0.32	0.9	-	-	U	23
190	M2.25	3580	1.5	0.04	0.5	-	-	U	23
191	M6	3050	4.1	0.49	0.1	-	-	U	23
192	K6	4205	2.5	0.55	1.1	22	-	Y	23,35
193	M4.5	3240	4.3	0.29	0.3	114.6	-	Y	13
194	M5	3240	4.0	0.57	0.2	997.2	-	Y	23
195	M3.5	3370	8.6	0.26	0.4	-	-	U	23
196	M3.5	3370	3.7	1.34	0.3	-	-	N	36
197	K7	4060	2.5	1.65	1.2	-	458	Y	23,25
198	M1	3720	0.9	0.83	0.8	-	453	Y	25
200	M0	3850	0.5	0.57	1.0	24.2	-	Y	13
201	M3	3470	1.7	0.52	0.5	51.3	-	Y	13
202	-	4060	7.1	0.25	1.0	150.2	-	Y	13
203	-	4060	5.4	3.17	0.6	-	-	U	
204	-	4060	16.1	0.63	1.0	-	-	U	
301	M0.5	3720	0.7	0.50	0.8	0.2	311	N	30
303	-	4060	12.8	0.04	-	-	0	U	
307	-	4060	0.0	2.20	1.3	-	0	U	
309	K6	4205	1.3	0.34	1.0	[b]	-	Y	6
310	-	4060	0.5	0.02	-	-	0	U	
314	-	4060	4.6	0.25	0.9	-	0	U	
316	-	4060	16.1	0.63	1.0	-	0	U	
317	-	4060	2.2	2.35	1.0	-	0	U	
318	K1	5080	5.5	8.66	2.4	1.5	450	N	30
319	K7	4060	1.9	2.06	1.3	29.2	-	Y	13
321	F6	6360	4.4	9.96	1.7	-2.3	-	N	13,21
322	-	4060	2.3	0.71	1.1	-	0	U	
325	K3	4730	1.2	1.01	1.2	[b]	-	Y	6
326	M1	3720	0.1	0.29	0.7	-	185	N	23,25
329	K5	4350	0.3	0.83	1.3	[b]	-	Y	6
333	-	4060	0.0	2.35	1.3	-	0	U	
334	-	4060	2.7	0.01	-	-	0	U	
335	K6	4205	4.0	1.02	1.3	71.4	-	Y	13,30
348	G7	5630	0.6	3.27	1.4	-	-	U	37
349	K2	4780	0.7	0.92	1.2	[b]	-	Y	6
350	K2	4780	0.7	0.68	1.0	[b]	-	Y	6

9.3.2 Photometry

Herschel PACS surveys cover 92% of our targets. The derived fluxes and upper limits are listed in Table 9.13. For 152 targets at least one of the three wavelengths result in a detection. For 18 targets the emission is confused by cloud emission at all three wavelengths, for 27 only at 100 and 160 μm and for 62 targets only at 160 μm. For 25 of the targets without cloud confusion no flux is detected at any of the wavelengths.

The PACS 70 μm fluxes and upper limits are consistent with the MIPS-2 fluxes and upper limits. The PACS sensitivity is sometimes shallower than the MIPS-2, resulting in a higher upper limit. For some targets, a more thorough data reduction of the PACS data was performed in other work (Ribas et al. 2013; Olofsson et al. 2013; Bustamante et al. 2015). In Table 9.5 the derived fluxes and upper limits are compared. Our values are similar within errors with previous estimates, confirming the validity of our data reduction.

The submillimeter photometry resulted in a total of 34 detections and 39 upper limits, listed in Table 9.7 and 9.8. In addition, we have taken (sub)millimeter photometry from the literature (see Table 9.14). With 57 (sub)mm detections and 47 upper limits, about 50% of the targets in our sample have constraints at longer wavelengths.

Table 9.7: *JCMT photometry at 850 μm for our sample*

ID	Flux$_{850\mu m}$ (mJy)	ID	Flux$_{850\mu m}$ (mJy)
22	< 31	124	< 19
23	153	127	< 29
26	< 30	137	63 ± 18
29	31 ± 7	154	< 56
32	< 47	155	55 ± 18
36	73 ± 18	156	< 31 [a]
44	38 ± 11	161	< 115
47	< 50	163	< 117 [a]
56	< 59	166	167 ± 14
60	< 24	171	17 ± 6
63	95 ± 16	174	< 27
70	32 ± 11	178	222 ± 16
82	< 57	187	126 ± 18
86	< 107 [a]	189	93 ± 16
88	< 137 [a]	192	< 29
89	< 35	193	32 ± 9
92	< 79	196	69 ± 19
100	< 37	202	< 56
107	< 17 [a]	333	< 56
113	< 18		
120	< 21		

Notes. [(a)] The flux is contaminated by extended emission near the source position.

9.3.3 Disk parameters

Millimeter fluxes can be used to obtain a rough estimate of the disk mass assuming optically thin dust emission and a gas-to-dust ratio of 100. Disk masses $M_{\rm disk,mm}$ in our sample are

Table 9.8: *APEX photometry at 350 and 870 μm for our sample.*

ID	$F_{350\mu m}$ (Jy)	$F_{870\mu m}$ (mJy)	ID	$F_{350\mu m}$ (Jy)	$F_{870\mu m}$ (mJy)
1	2.4 ± 0.2	210 ± 20	40	< 0.7	< 20
2	-	< 40	43	-	< 18
6	0.69 ± 0.18		46	0.8 ± 0.2	164 ± 14
9	-	< 15	55	< 0.9	92 ± 6
10	-	< 20	58	-	< 18
11	2.4 ± 0.5		62	< 0.6	62 ± 9
14	-	24 ± 6	95	-	49 ± 11
15	4 ± 0.2	420 ± 50	98	-	63 ± 8
16	9.8 ± 2.4		99	-	360 ± 30 [a]
18	-	20 ± 6	132	-	109 ± 11 [a]
20	-	390 ± 10	200	-	< 40
22	< 0.3		203	-	55 ± 10 [a]
25	-	< 30	303	-	136 7
27	0.19 ± 0.04		307	-	123 ± 14
35	-	28 ± 4 [a]	316	-	98 ± 13
36	0.22 ± 0.06 [a]	< 30	321	-	< 20

Notes. [(a)] The flux is contaminated by extended emission near the source position.

calculated following the relations presented in Cieza et al. (2008) with standard assumptions and parameters:

$$M_{\rm disk} = 0.17 \left(F_{1.3mm}({\rm mJy}) \times \frac{d^2}{140{\rm pc}} \right) M_{\rm Jup} \tag{9.4}$$

$$M_{\rm disk} = 0.08 \left(F_{0.85mm}({\rm mJy}) \times \frac{d^2}{140{\rm pc}} \right) M_{\rm Jup} \tag{9.5}$$

with F_λ the flux at wavelength λ and d the distance to the star. Using this relation, disk masses of our sample range between <0.4 and 168 $M_{\rm Jup}$, and an average disk mass of 14 Jupiter masses, similar to large millimeter studies of disks (e.g. Andrews & Williams 2007a). However, these disk masses remain highly uncertain as the vertical structure, cavities and the stellar radiation field are not taken into account and the dust opacities and gas-to-dust ratio are uncertain.

Furthermore, we derive $L_{\rm disk}$ for each target by integrating over all data points after subtraction of the fitted stellar photosphere. The ratio $L_{\rm disk}/L_*$ is a measure of disk processing, as it traces the total amount of dust that is reprocessing stellar light. As disks become more tenuous, settle and eventually disappear, $L_{\rm disk}$ is expected to decline. The majority of the disks have $0.001 < L_{\rm disk}/L_* < 0.4$, as expected for flared disks. Disks with $L_{\rm disk}/L_* < 10^{-3}$ are generally considered as debris disks (e.g. Wahhaj et al. 2010). On the other hand, targets with $L_{\rm disk}/L_* >> 1$ are either embedded Class I objects or edge-on disks which are more difficult to analyze (Merín et al. 2010). ID178 has $L_{\rm disk}/L_* \sim 17$ and is thus removed from the analyzed sample.

Both $L_{\rm disk}/L_*$ and $M_{\rm disk,mm}$ are listed in Table 9.9. The final sample consists of 184 targets for which the SEDs will be analyzed.

9.4 Modeling

In order to determine the presence of a dust cavity and measure its size, the SEDs are modeled using the dust radiative transfer code RADMC-3D [3] (Dullemond & Dominik 2004). This code performs a Monte Carlo continuum radiative transfer calculation based on the input dust density profile and stellar photosphere, followed by raytracing of the SED. The model has a large number of input parameters and we have fixed as many as possible that are not important for our science goals. The model assumes a passive disk which reprocesses the stellar radiation field.

The modeling procedure consists of two steps: first using a rough grid with a broad range of parameters, followed by a finer grid for the specific stellar type. The modeling was performed blindly, without taking any results from previous SED modeling or imaging studies, for an uniform approach for each disk in this sample. In Section 9.5 the derived parameters are compared with previously found results.

9.4.1 Approach

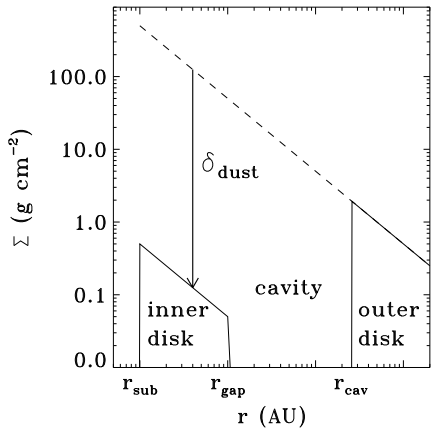


Figure 9.1: *Gas surface density profile used for the modeling, assuming a gas-to-dust ratio of 100.*

The disks are modeled using a large grid of models, computed by RADMC-3D. The model assumes an axisymmetric gas surface density profile, following a radial power-law

$$\Sigma_g(r) = \Sigma_c \left(\frac{r}{r_c}\right)^{-1} \tag{9.6}$$

with r_c the characteristic radius and a gas-to-dust ratio of 100. The outer radius is set to 200 AU and the inner radius to the sublimation radius $r_{\rm sub}$ with $r_{\rm sub} = 0.07(L_*/L_\odot)^{1/2}$, assuming a sublimation temperature of 1500 K (Dullemond et al. 2001). The dust density inside the cavity is parametrized by setting the density equal to zero between $r_{\rm gap}$ and $r_{\rm cav}$. The inner disk (between $r_{\rm sub}$ and $r_{\rm gap}$) is set by varying $\delta_{\rm dust}$ to fit the near infrared excess (see Figure

[3] http://www.ita.uni-heidelberg.de/~dullemond/software/radmc-3d/

9.1). The $r_{\rm gap}$ is fixed to 1 AU as it can not be constrained well by the SED. A full disk without a cavity is simulated by setting $r_{\rm cav} = r_{\rm gap}$.

The stellar photosphere in the model is described by its temperature and stellar luminosity, which has been fit independently together with the extinction. The disk is assumed to be flared, so that the vertical structure of the disk is described by

$$h(r) = h_c \left(\frac{r}{r_c}\right)^{\psi} \tag{9.7}$$

with h_c the scale height at r_c and ψ the flaring angle, which are both varied to fit the near and mid infrared part of the SED. As the scale height is degenerate with the cavity radius, the flaring angle is taken as a conservative value of either 1/7 or 2/7, following Chiang & Goldreich (1997). The derived cavity radius is thus likely a lower limit if the disk is flatter. With the inclusion of the *Herschel* fluxes, the scale height is better constrained than in previous SED modeling studies. Dust composition and settling is prescribed following Andrews et al. (2011), with a large and small dust grain population where the large grains have a lower scale height than the small grains. The inclination of the disks is taken as a constant of 30° and was not varied in the modeling, as only very high inclination angles (edge-on disks) result in a significant difference in the near infrared emission (and in addition, obscuration of the star). With our color criteria, edge-on disks are not expected to be included (Merín et al. 2010) and also the computation of the stellar masses from the stellar luminosities implies that most of the targets are not edge-on (although higher inclinations than 30° are still possible).

The five free parameters are thus $r_{\rm cav}$, $\delta_{\rm dust}$, Σ_c or disk mass, h_c and ψ, where $r_{\rm cav}$ is the main parameter of interest. The fitting was performed in two steps. First, a large grid of models with a broad range of disk parameters and a limited number of stellar parameters was fit to each SED. Second, each SED was fine-tuned individually, using the exact stellar photosphere and starting from the best fit from the broad grid. The disk grids per object have a large range of cavity radii (our main parameter of interest), in combination with a small range of scale heights and disk masses. In the fitting procedure, a χ^2 minimization was performed between the dereddened SED data points and the model SEDs. In the grid fitting, the data points were weighted by their excess above the stellar photosphere at each wavelength: fluxes at longer wavelengths got a larger weight than those in the optical and near infrared since the stellar photosphere is largely known from the extinction fitting. Uncertainties on the cavity radii are given in Table 9.9, based on fits with up to 10% variation in χ^2.

9.4.2 Results

Each SED can be fit to a disk model with or without a cavity. Table 9.9 presents the results of the fitting procedure. Figure 9.2 presents the distribution of hole sizes and disk masses (assuming a gas-to-dust ratio of 100) of the full sample, showing a broad distribution of both parameters. The disk masses obtained from the fit generally agree within a factor of 2-3 with the mass estimate from the millimeter flux. During the fit procedure it became clear that certain disks have really large cavities (>150 AU) but very low scale heights, which can not be well reproduced by our flared models. These disks are likely debris disks, as also suggested by their low $L_{\rm disk}/L_*$ values.

Table 9.9: *Results of disk fitting procedure and classification*

ID	r_{cav} (AU)	Σ_c (g cm^{-2})	$M_{disk,fit}$[a] (M_{Jup})	δ_{dust}	h_c	ψ	$M_{disk,mm}$[a] (M_{Jup})	L_{disk}/L_*	Classification[b]
1	140^{+10}_{-10}	7.0e-02	7.8	1.0e-02	0.10	1/7	3.7	0.467	ML
2	6^{+4}_{-4}	3.0e-03	1.1	1.0e-02	0.01	1/7	< 1.5	0.067	LS
3	10^{+2}_{-2}	3.0e-04	0.1	1.0e-04	0.01	1/7	-	0.038	LL
4	45^{+15}_{-5}	3.0e-04	0.1	1.0e-06	0.01	2/7	-	0.178	LL
5	30^{+50}_{-18}	3.0e-03	0.9	1.0e-01	0.05	2/7	-	0.195	LL
6	60^{+10}_{-10}	8.0e-02	20.9	1.0e-06	0.05	1/7	20.6	0.105	ML
7	8^{+2}_{-2}	3.0e-03	1.1	1.0e-02	0.15	1/7	-	0.685	LS
9	120^{+20}_{-10}	3.0e-04	0.0	1.0e-03	0.01	1/7	< 1.6	0.008	DD
10	190_{-10}	3.0e-04	0.0	1.0e-02	0.01	1/7	< 2.1	0.001	DD
11	30^{+10}_{-10}	5.0e-02	15.8	1.0e-04	0.05	2/7	32.8	0.329	ML
12	15^{+5}_{-5}	3.0e-03	1.0	1.0e-03	0.05	1/7	< 22.2	0.183	LL
13	190_{-10}	1.0e-02	0.2	1.0e-04	0.01	1/7	-	0.007	DD
14	10^{+4}_{-4}	3.0e-02	10.6	1.0e-04	0.05	1/7	2.5	0.201	ML
15	1^{+1}	1.5e-01	55.6	1.0e+00	0.03	1/7	43.9	0.083	MS
16	50^{+30}_{-49}	3.8e-01	106.1	1.0e-01	0.20	1/7	-	0.934	ML
17	15^{+15}_{-5}	3.0e-03	1.0	1.0e-06	0.05	2/7	-	0.172	LL
18	30^{+5}_{-5}	3.0e-03	0.9	1.0e-06	0.05	1/7	2.1	0.139	LL
20	1^{+3}	1.0e-01	37.1	1.0e+00	0.04	1/7	15.9	0.170	MS
21	110^{+10}_{-20}	6.0e-01	100.6	1.0e-01	0.10	1/7	216.0	0.366	ML
22	50^{+40}_{-10}	5.0e-03	1.4	1.0e-06	0.05	1/7	-	0.465	LL
23	60^{+10}_{-10}	1.0e-01	26.1	1.0e-06	0.05	2/7	25.0	0.152	ML
24	16^{+2}_{-4}	3.0e-03	1.0	1.0e-06	0.02	1/7	< 3.8	0.151	LL
25	4^{+4}_{-2}	3.0e-03	1.1	1.0e-04	0.01	1/7	-	0.100	LS
26	2^{+2}	3.0e-04	0.1	1.0e-02	0.05	1/7	< 5.0	0.307	LS
27	120^{+30}_{-20}	2.3e-02	3.4	1.0e-06	0.05	1/7	5.7	0.170	LL
28	2^{+2}	3.0e-04	0.1	1.0e-02	0.10	1/7	< 3.4	0.434	LS
29	70^{+40}_{-10}	6.0e-02	14.5	1.0e-08	0.02	1/7	2.8	0.136	ML
31	170^{+10}_{-20}	3.0e-04	0.0	1.0e-02	0.01	1/7	-	0.193	DD
33	80^{+10}_{-10}	1.5e-01	33.5	1.0e-01	0.05	1/7	49.6	0.233	ML
34	10^{+4}_{-4}	3.0e-04	0.1	1.0e-02	0.20	1/7	-	0.250	LL
35	2^{+2}	9.0e-02	33.2	1.0e-02	0.02	1/7	< 2.8	0.104	MS
36	1	1.5e-02	5.6	1.0e+00	0.05	1/7	6.7	0.337	NH
38	10^{+10}_{-2}	4.5e-01	159.2	1.0e-06	0.03	1/7	60.1	0.094	ML
39	16^{+4}_{-6}	1.0e-01	34.3	1.0e-04	0.03	1/7	16.8	0.117	ML
40	1	3.0e-03	1.1	1.0e+00	0.10	1/7	< 1.3	0.434	NH
41	1	3.0e-04	0.1	1.0e+00	0.05	1/7	< 1.3	0.107	NH
43	45^{+5}_{-20}	1.0e-03	0.3	1.0e-01	0.15	2/7	< 1.1	0.257	LL
44	4^{+2}_{-2}	7.0e-03	2.6	1.0e-04	0.05	1/7	2.4	0.146	LS
45	50^{+40}_{-20}	6.0e-02	16.8	1.0e-01	0.20	1/7	35.1	0.764	ML
46	20^{+10}_{-5}	3.0e-02	10.1	1.0e-06	0.05	1/7	10.5	0.114	ML
47*	1^{+1}	3.0e-03	1.1	1.0e+00	0.05	1/7	-	0.270	LS
48	8^{+6}_{-7}	3.0e-02	10.7	1.0e-02	0.05	1/7	-	0.350	MS
49	20^{+30}_{-10}	3.0e-03	1.0	1.0e-01	0.01	1/7	< 0.8	0.048	LL
50	2^{+2}	1.0e-03	0.4	1.0e-04	0.01	1/7	< 0.7	0.110	LS
51	120^{+10}_{-100}	2.0e-02	3.0	1.0e-04	0.10	1/7	11.5	0.310	LL

Notes. (*) Fit results are uncertain due to unknown spectral type. (a) Disk masses refer to the full disk mass, computed assuming a gas-to-dust ratio of 100. (b) NH = disks without holes, ML = massive disks with large holes, MS = massive disks with small holes, LL = low-mass disks with large holes, LS = low-mass disks with small holes, DD = low-mass disks with very low scale heights. See also definition in the text.

Table 9.9: *Results of disk fitting procedure and classification*

ID	r_{cav}	Σ_c	$M_{disk,fit}$ [a]	δ_{dust}	h_c	ψ	$M_{disk,mm}$ [a]	L_{disk}/L_*	Classification[b]
52	80^{+10}_{-20}	2.5e-02	5.6	1.0e-02	0.10	1/7	13.4	0.345	ML
53	1	3.0e-02	11.1	1.0e+00	0.01	1/7	-	0.054	NH
54	60^{+20}_{-15}	3.0e-02	7.8	1.0e-01	0.10	2/7	34.3	0.356	ML
55*	1	2.1e-02	7.8	1.0e+00	0.03	1/7	5.9	0.227	NH
56*	4^{+6}_{-2}	1.0e-02	3.6	1.0e-06	0.20	1/7	-	0.842	LS
58	1	8.0e-04	0.3	1.0e+00	0.15	1/7	< 1.1	0.418	NH
59	2^{+2}	3.0e-04	0.1	1.0e-04	0.01	1/7	-	0.115	LS
60	2^{+2}	3.0e-03	1.1	1.0e-06	0.01	2/7	< 1.5	0.062	LS
61	5^{+85}_{-3}	3.0e-04	0.1	1.0e-02	0.05	1/7	-	0.192	LS
62	1	1.2e-02	4.4	1.0e+00	0.05	1/7	4.0	0.238	NH
63	20^{+5}_{-5}	3.5e-02	11.7	1.0e-06	0.03	1/7	6.1	0.087	ML
64	70^{+20}_{-30}	5.0e-02	12.1	1.0e-04	0.08	1/7	20.4	0.359	ML
65	190_{-10}	3.0e-04	0.0	1.0e-06	0.01	1/7	-	0.001	DD
66	30^{+10}_{-26}	3.0e-03	0.9	1.0e-03	0.05	1/7	-	0.276	LL
67*	110^{+10}_{-10}	3.0e-04	0.1	1.0e-06	0.01	1/7	-	0.004	DD
69	190_{-10}	3.0e-04	0.0	1.0e-06	0.01	1/7	-	0.001	DD
70	80^{+30}_{-10}	6.0e-02	13.4	1.0e-04	0.03	1/7	8.3	0.077	ML
71*	180^{+10}_{-20}	3.0e-04	0.0	1.0e-04	0.01	1/7	-	0.003	DD
73*	190_{-10}	3.0e-02	0.6	1.0e-04	0.01	1/7	-	0.011	DD
74*	140^{+10}_{-100}	3.0e-02	3.4	1.0e-04	0.01	1/7	-	0.025	DD
75*	190_{-20}	3.0e-02	0.6	1.0e-04	0.01	1/7	-	0.013	DD
76	190_{-10}	3.0e-04	0.0	1.0e-06	0.01	1/7	-	0.002	DD
77	190_{-10}	3.0e-04	0.0	1.0e-06	0.01	1/7	-	0.002	DD
79	190_{-10}	3.0e-04	0.0	1.0e-06	0.01	1/7	-	0.000	DD
81*	70^{+30}_{-10}	3.0e-03	0.7	1.0e-02	0.05	1/7	-	0.129	LL
83	2^{+16}	3.0e-03	1.1	1.0e-04	0.01	2/7	-	0.053	LS
89	110^{+40}_{-10}	3.0e-05	0.0	1.0e-06	0.10	1/7	< 9.0	0.004	LL
91*	30^{+50}_{-25}	3.0e-02	9.5	1.0e-02	0.10	1/7	-	0.272	ML
94*	190_{-150}	3.0e-04	0.0	1.0e-04	0.10	1/7	-	0.010	LL
96*	60^{+50}_{-30}	3.0e-04	0.1	1.0e-04	0.05	1/7	-	0.039	LL
99	190_{-10}	6.0e+00	111.7	1.0e-10	0.01	2/7	91.8	0.025	ML
100	190_{-10}	6.0e-01	11.2	1.0e-06	0.01	1/7	< 9.4	0.016	ML
101*	5^{+85}_{-2}	1.0e-01	36.3	1.0e-06	0.01	1/7	-	0.045	MS
102*	45^{+115}_{-40}	3.0e-02	8.7	1.0e-01	0.20	1/7	-	0.702	ML
103*	40^{+5}_{-5}	3.0e-02	8.9	1.0e-01	0.10	1/7	-	0.338	ML
105*	190_{-10}	3.0e-04	0.0	1.0e-04	0.01	1/7	-	0.002	DD
106	190_{-10}	3.0e-04	0.0	1.0e-04	0.01	1/7	-	0.001	DD
107	70^{+40}_{-20}	3.0e-04	0.1	1.0e-06	0.10	1/7	< 4.4	0.047	LL
108*	180^{+10}_{-40}	3.0e-04	0.0	1.0e-02	0.05	1/7	-	0.011	LL
111	1	3.0e-01	111.2	1.0e+00	0.05	1/7	-	0.207	NH
112*	1	3.0e-03	1.1	1.0e+00	0.10	1/7	-	0.304	NH
113*	60^{+20}_{-20}	3.0e-03	0.8	1.0e-06	0.05	2/7	-	0.167	LL
114*	180^{+10}_{-130}	3.0e-03	0.1	1.0e-06	0.01	1/7	-	0.010	DD
115	5^{+35}_{-4}	5.0e-03	1.8	1.0e-01	0.20	1/7	< 12.4	0.889	LS
117*	60^{+40}_{-10}	3.0e-04	0.1	1.0e-06	0.01	1/7	-	0.019	LL
118	2^{+2}	3.0e-04	0.1	1.0e-02	0.15	1/7	-	0.397	LS
120	10^{+5}_{-8}	3.0e-03	1.1	1.0e-06	0.05	1/7	< 5.4	0.170	LL
124*	10^{+10}_{-5}	3.0e-03	1.1	1.0e-04	0.05	1/7	-	0.118	LL
125	50^{+10}_{-49}	3.0e-02	8.4	1.0e-01	0.20	1/7	-	0.927	ML
127	80^{+20}_{-10}	4.5e-02	10.1	1.0e-05	0.03	2/7	< 7.5	0.086	ML
128	25^{+45}_{-24}	3.0e-03	1.0	1.0e-02	0.05	1/7	-	0.086	LL

Table 9.9: *Results of disk fitting procedure and classification*

ID	$r_{\rm cav}$	Σ_c	$M_{\rm disk,fit}$ [a]	$\delta_{\rm dust}$	h_c	ψ	$M_{\rm disk,mm}$ [a]	$L_{\rm disk}/L_*$	Classification[b]
130	30^{+40}_{-25}	3.0e-04	0.1	1.0e-06	0.10	1/7	-	0.077	LL
131*	10^{+10}_{-5}	1.0e-02	3.5	1.0e-03	0.05	1/7	1.2	0.257	LL
132	180^{+10}_{-176}	5.0e-01	18.6	1.0e-04	0.05	1/7	27.8	0.146	ML
133	1	3.0e-02	11.1	1.0e+00	0.15	1/7	-	0.582	NH
134	190_{-10}	3.0e-04	0.0	1.0e-04	0.01	1/7	-	0.006	DD
135	4^{+2}_{-2}	9.0e-02	32.8	1.0e-06	0.05	1/7	16.8	0.121	MS
136	50^{+40}_{-10}	2.5e-02	7.0	1.0e-04	0.05	1/7	12.0	0.206	ML
137	4^{+2}_{-2}	4.0e-02	14.6	1.0e-01	0.20	2/7	5.1	1.236	MS
138	180^{+10}_{-20}	3.0e-03	0.1	1.0e-06	0.01	1/7	-	0.100	DD
139	2^{+2}	3.0e-03	1.1	1.0e-03	0.10	1/7	-	0.603	LS
140	190_{-10}	3.0e-04	0.0	1.0e-05	0.01	1/7	< 2.2	0.001	DD
142	25^{+15}_{-5}	3.0e-02	9.8	1.0e-01	0.05	1/7	29.4	0.203	ML
144	110^{+40}_{-10}	3.0e-03	0.5	1.0e-06	0.01	1/7	-	0.037	DD
145	1^{+1}	1.5e-02	5.6	1.0e+00	0.10	1/7	3.9	0.328	MS
146	190_{-10}	3.0e-04	0.0	1.0e-04	0.01	1/7	-	0.001	DD
147	6^{+9}_{-2}	3.0e-02	10.8	1.0e-01	0.05	2/7	-	0.426	MS
148	100^{+10}_{-30}	1.2e-02	2.2	1.0e-01	0.10	1/7	2.7	0.235	LL
149	10^{+8}_{-8}	3.0e-02	10.6	1.0e-06	0.03	1/7	51.0	0.153	ML
150	15^{+5}_{-5}	3.0e-04	0.1	1.0e-06	0.10	2/7	< 0.6	0.291	LL
151	190_{-10}	1.0e-04	0.0	1.0e-06	0.05	1/7	-	0.001	LL
152	150^{+20}_{-20}	3.0e-04	0.0	1.0e-04	0.01	1/7	< 0.7	0.003	DD
153	2^{+2}	3.0e-02	11.1	1.0e-02	0.10	1/7	44.8	0.385	MS
154	6^{+2}_{-2}	6.0e-02	21.7	1.0e-04	0.02	1/7	-	0.082	MS
155	50^{+10}_{-5}	1.2e-02	3.4	1.0e-06	0.05	1/7	4.4	0.141	LL
156	10^{+60}_{-5}	1.0e-02	3.5	1.0e-06	0.01	2/7	< 2.5	0.033	LL
157	1^{+4}	3.0e-03	1.1	1.0e+00	0.05	1/7	-	0.325	LS
158	190_{-10}	3.0e-04	0.0	1.0e-06	0.01	1/7	-	0.001	DD
159	1^{+5}	2.2e-02	8.2	1.0e+00	0.05	1/7	28.7	0.152	MS
160	1	1.0e-01	37.1	1.0e+00	0.20	1/7	-	1.191	NH
161	2^{+4}	8.0e-03	2.9	1.0e-03	0.20	1/7	< 29.4	0.785	LS
162	2^{+2}	1.5e-02	5.5	1.0e-06	0.05	2/7	3.4	0.321	MS
163	1^{+1}	3.0e-02	11.1	1.0e+00	0.20	1/7	< 29.9	0.978	MS
164*	1^{+3}	1.0e-03	0.4	1.0e+00	0.20	1/7	-	0.505	LS
165	8^{+4}_{-4}	1.0e-03	0.4	1.0e-04	0.02	1/7	< 0.8	0.052	LS
166*	140^{+20}_{-10}	1.5e-01	16.8	1.0e-01	0.15	1/7	42.5	0.424	ML
167*	8^{+42}_{-4}	3.0e-02	10.7	1.0e-04	0.05	1/7	-	0.238	MS
168	5^{+20}_{-3}	3.0e-03	1.1	1.0e-04	0.05	1/7	< 0.8	0.177	LL
169	2^{+2}	3.0e-04	0.1	1.0e-04	0.02	1/7	-	0.194	LS
171	1	1.2e-02	4.4	1.0e+00	0.10	1/7	4.4	0.343	NH
172	2^{+1}	3.2e-02	11.8	1.0e-06	0.10	1/7	7.9	0.384	MS
173	120^{+10}_{-20}	3.0e-01	44.7	1.0e-04	0.05	1/7	53.6	0.331	ML
174	18^{+10}_{-6}	9.0e-02	30.5	1.0e-06	0.05	1/7	< 22.2	0.257	ML
175	4^{+8}_{-2}	1.5e-03	0.5	1.0e-04	0.15	2/7	0.8	0.542	LS
176	2^{+2}	3.0e-03	1.1	1.0e-06	0.05	2/7	-	0.195	LS
177	25^{+10}_{-10}	6.0e-03	2.0	1.0e-06	0.01	1/7	< 0.4	0.019	LL
179	1^{+59}	2.0e-02	7.4	1.0e+00	0.05	1/7	9.2	0.141	MS
180	14^{+4}_{-4}	3.0e-04	0.1	1.0e-06	0.05	1/7	< 1.8	0.071	LL
181	6^{+12}_{-5}	3.0e-03	1.1	1.0e+00	0.01	1/7	< 0.6	0.067	LS
182	2^{+23}	1.0e-02	3.7	1.0e-04	0.01	1/7	-	0.044	LS
183	4^{+1}_{-2}	3.0e-03	1.1	1.0e-06	0.05	1/7	< 0.8	0.119	LS
184	160^{+20}_{-10}	1.0e-04	0.0	1.0e-04	0.01	1/7	< 1.5	0.003	DD

Table 9.9: *Results of disk fitting procedure and classification*

ID	r_{cav}	Σ_c	$M_{disk,fit}$[a]	δ_{dust}	h_c	ψ	$M_{disk,mm}$[a]	L_{disk}/L_*	Classification[b]
185	1	1.0e-02	3.7	1.0e+00	0.12	1/7	< 9.4	0.582	NH
186	1	3.0e-04	0.1	1.0e+00	0.10	2/7	-	0.274	NH
187	4^{+2}_{-2}	2.7e-02	9.9	1.0e-01	0.20	1/7	10.0	1.076	MS
188	1	5.0e-03	1.9	1.0e+00	0.15	1/7	2.6	0.452	NH
189	40^{+80}_{-30}	3.0e-02	8.9	1.0e-01	0.07	1/7	-	0.302	ML
190	2^{+2}	1.5e-02	5.5	1.0e-04	0.05	1/7	1.4	0.147	MS
191	2^{+2}	1.0e-03	0.4	1.0e-02	0.05	1/7	-	0.449	LS
192	25^{+10}_{-10}	3.0e-03	1.0	1.0e-02	0.20	1/7	< 2.3	0.617	LL
193	10^{+10}_{-8}	8.0e-03	2.8	1.0e-04	0.05	1/7	2.6	0.125	LL
194	10^{+2}_{-5}	7.0e-02	24.8	1.0e-05	0.02	1/7	2.3	0.157	ML
195	2^{+2}	3.0e-04	0.1	1.0e-02	0.05	1/7	-	0.264	LS
196	2^{+2}	1.1e-02	4.1	1.0e-04	0.05	1/7	5.5	0.219	LS
197	1	3.0e-02	11.1	1.0e+00	0.03	1/7	10.4	0.114	NH
198	90^{+50}_{-10}	2.0e-02	4.1	1.0e-02	0.15	1/7	7.2	0.314	LL
200	1	2.0e-02	7.4	1.0e+00	0.10	1/7	< 6.5	0.397	NH
201	1^{+3}	7.0e-02	25.9	1.0e+00	0.05	1/7	-	0.340	MS
203*	2^{+98}	4.0e-02	14.7	1.0e-01	0.10	2/7	-	0.900	MS
301	2^{+2}	3.0e-02	11.1	1.0e-02	0.05	1/7	-	0.242	MS
303*	4^{+6}_{-2}	7.0e-02	25.5	1.0e-04	0.20	2/7	-	2.820	MS
307*	160^{+10}_{-20}	4.5e-02	3.4	1.0e-06	0.05	2/7	-	0.107	LL
309	10^{+2}_{-2}	3.0e-02	10.6	1.0e-04	0.02	1/7	-	0.066	ML
310*	20^{+60}_{-14}	6.0e-01	201.1	1.0e-02	0.20	2/7	-	1.477	ML
314*	20^{+10}_{-10}	1.0e-02	3.4	1.0e-06	0.05	1/7	-	0.146	LL
318	70^{+30}_{-10}	3.0e-04	0.1	1.0e-02	0.05	2/7	-	0.048	LL
319	1^{+17}	3.0e-03	1.1	1.0e+00	0.05	1/7	-	0.116	LS
321	190_{-10}	3.0e-03	0.1	1.0e-05	0.01	1/7	< 5.1	0.018	DD
322*	70^{+10}_{-10}	3.0e-01	72.6	1.0e-08	0.05	1/7	-	0.225	ML
325	80^{+40}_{-35}	1.3e-01	29.0	1.0e-01	0.05	1/7	32.8	0.159	ML
326	6^{+2}_{-2}	3.0e-02	10.8	1.0e-06	0.10	1/7	-	0.460	MS
329	30^{+10}_{-5}	1.6e-01	50.6	1.0e-04	0.05	2/7	51.2	0.211	ML
333*	50^{+30}_{-10}	1.0e-02	2.8	1.0e-05	0.10	1/7	-	0.533	LL
334*	8^{+112}_{-7}	3.0e-01	107.3	1.0e-01	0.20	2/7	-	1.528	MS
335	2^{+8}_{-1}	3.0e-01	110.6	1.0e-01	0.05	2/7	-	0.280	MS
348	20^{+10}_{-8}	3.0e-03	1.0	1.0e-01	0.10	1/7	-	0.328	LL
349	160^{+10}_{-10}	3.0e-01	22.3	1.0e-04	0.05	1/7	8.9	0.201	ML
350	10^{+2}_{-2}	6.0e-02	21.2	1.0e-06	0.03	1/7	-	0.228	ML

Figures 9.12 to 9.16 present the SEDs with the best fitting models overlaid. The SEDs are grouped into 5 different classifications:

- NH: Disks without holes (r_{cav}=1 AU)
- ML: Massive disks with large holes (r_{cav} >10 AU, $M_{disk} > 5M_{Jup}$)
- MS: Massive disks with small holes (r_{cav} <10 AU, $M_{disk} > 5M_{Jup}$)
- DD: Low-mass disks with large holes and very low scale heights (r_{cav} >100 AU, $M_{disk} < 5M_{Jup}$, $h_c \sim 0.01$)

- LL: Low-mass disks with large holes
  ($r_{\rm cav}$ >10 AU, $M_{\rm disk} < 5 M_{\rm Jup}$, $h_c > 0.01$)
- LS: Low-mass disks with small holes
  ($r_{\rm cav}$ <10 AU, $M_{\rm disk} < 5 M_{\rm Jup}$)

For the disks classified as NH (no hole), we have excluded the targets that could be fit with a cavity >1 AU within the 10% χ^2 limit. A large fraction of the disks (~23%) falls in the ML category of large holes in massive disks. It turns out that several of these disks are indeed the famous, bright disks with large inner holes known from imaging surveys (Andrews et al. 2011; Williams & Cieza 2011), confirming the strength of our SED modeling, even if rather simple. The new targets in the ML, MS and some in the LL groups are promising disks for follow up observations with ALMA. Excluding the DD and NH disks, a total of 133 targets (72% of our analyzed sample) can be labeled as disks with cavities, transition disks. More than half of these (~ 70 targets) are new transition disks; about 40 had been imaged or modeled before and another 20 had been recognized as a possible transition disk. Of the new transition disks, two thirds have a known spectral type.

9.5 Discussion

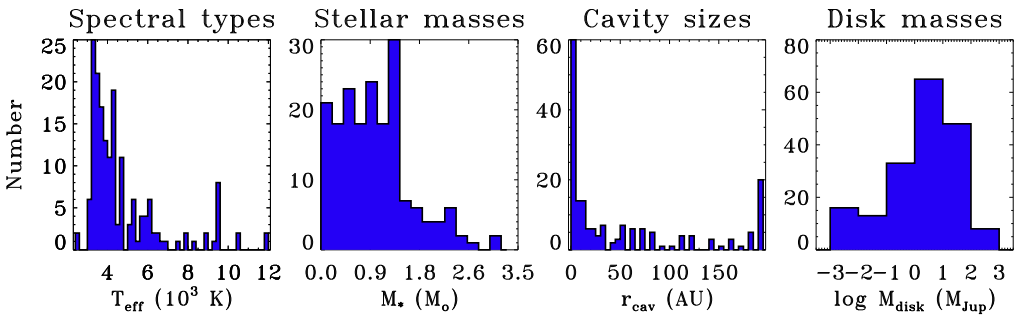


Figure 9.2: *Distribution of spectral types, stellar masses, cavity sizes and disk masses in this study. The disk mass is calculated assuming a gas-to-dust ratio of 100.*

The SED modeling has confirmed the presence of cavities in a large unbiased sample of transition disks. At least 72% of the sample could be modeled as a disk with a cavity, including about 110 new transition disks that had not been identified as transition disk before.

9.5.1 Comparison of cavity radii with literature values

In order to quantify the quality of our fitting, the fit results for the cavity size are compared with values from the literature from both SED modeling and resolved millimeter imaging in Table 9.10 for the targets where this information is available. The values generally agree well within a factor of two with previously derived parameters. Especially the similarity to the imaging results is encouraging: this implies that a large number of our new targets are suitable for resolved imaging. Exceptions for the imaging targets are T Cha, RY Tau and AB Aur. For T Chathe overestimate of the cavity size could be caused by the assumed low inclination: imaging has shown that the inclination is in reality ~ 67° so close to edge-on (Huélamo et al.

Table 9.10: *Comparison cavity radii with literature values.*

ID	Name	r_{cav}^{here}	r_{cav}^{lit}	Type[a]	Ref	ID	Name	r_{cav}^{here}	r_{cav}^{lit}	Type[a]	Ref
1	TCha	140^{+10}_{-10}	19	I	1	51	IRS48	120^{+10}_{-100}	60	I	13
3	RECX5	10^{+2}_{-2}	33	M	2	52	DoAr44	80^{+10}_{-20}	30	I	10
4	CHXR22E	45^{+15}_{-5}	7	M	3	54	SR21	60^{+20}_{-15}	36	I	8
6	CSCha	60^{+10}_{-10}	38	M	4	60	oph62	2^{+2}	3	M	6
9	T54	120^{+20}_{-10}	37	M	3	64	J160421	70^{+20}_{-30}	80	I	14
10	T21	190_{-10}	146	M	3	120	J182911	10^{+5}_{-8}	8	M	6
11	SZCha	30^{+10}_{-10}	29	M	3	127	Serp127	80^{+20}_{-10}	25	M	6
12	T35	15^{+5}_{-5}	15	M	3	128	J182935	25^{+45}_{-23}	7	M	6
14	T56	10^{+4}_{-4}	18	M	3	135	DMTau	4^{+2}_{-2}	18	I	10
15	CRCha	1^{+1}	10	M	4	136	UXTauA	50^{+40}_{-10}	25	I	10
18	T25	30^{+5}_{-5}	8	M	3	142	MWC758	25^{+15}_{-5}	73	I	10
21	HD142527	110^{+10}_{-20}	100	I	5	148	IPTau	100^{+10}_{-30}	2	M	4
24	Lup60	16^{+2}_{-4}	3	M	6	153	RYTau	2^{+2}	$26^{(b)}$	I	15
27	Sz91	120^{+30}_{-20}	97	I	7	159	ABAur	1^{+4}	115	I	16
29	Sz84	70^{+40}_{-10}	55	M	6	161	ASR118	2^{+4}	1	M	6
33	HD135344	80^{+10}_{-10}	46	I	8	165	J034227	8^{+4}_{-4}	5	M	6
35	Sz76	2^{+2}	1	M	9	168	J034434	5^{+20}_{-3}	3	M	6
38	RXJ1615	10^{+10}_{-2}	30	I	10	169	IC348LRL190	2^{+2}	5	M	6
39	V4046Sgr	16^{+4}_{-6}	29	I	11	173	LkH-alpha330	120^{+10}_{-20}	68	I	10
45	SR24S	50^{+40}_{-20}	30	I	10	309	TWHya	10^{+2}_{-2}	4	M	17
46	RXJ1633	20^{+10}_{-5}	27	I	12	325	LkCa15	80^{+40}_{-35}	50	I	10
48	WSB60	8^{+6}_{-6}	15	I	10	326	CoKu-Tau-4	6^{+2}_{-2}	10	M	18
50	J162245	2^{+2}	1	M	6	329	GMAur	30^{+10}_{-5}	20	I	10

Refs. 1) Huélamo et al. (2015), 2) Bouwman et al. (2010), 3) Kim et al. (2009), 4) Espaillat et al. (2011), 5) Fukagawa et al. (2013), 6) Merín et al. (2010), 7) Canovas et al. (2015), 8) Brown et al. (2009), 9) Padgett et al. (2006), 10) Andrews et al. (2011), 11) Rosenfeld et al. (2013), 12) Cieza et al. (2012a), 13) van der Marel et al. (2013), 14) Mathews et al. (2012), 15) Isella et al. (2010a), 16) Piétu et al. (2005), 17) Andrews et al. (2012), 18) D'Alessio et al. (2005)

Notes. [a] M = derived from SED modeling, I = derived from millimeter imaging. [b] This value is not a real cavity size, but a transition radius: the disk was fit with a surface density profile that radially increases and decreases, peaking at 26 AU.

2015), affecting the near infrared emission from the inner disk. Also their flaring angle is lower than ours. For RY Tau, the cavity radius found by imaging is not defined in the same way as here: it is the peak of the surface density, assuming a surface density that first increases and then decreases with radius (Isella et al. 2010a). Therefore, the values can not be compared directly. For AB Aur, only a very small hole of at most 2 AU can be fit with our models, while millimeter imaging has revealed a large cavity of 115 AU at 1.4mm, with a complex, possibly spiral-arm structure (Piétu et al. 2005; Tang et al. 2012). It remains unclear what the reason is for this discrepancy between the SED and the millimeter image. For the comparison with SED modeling there are large discrepancies for CHXR22E, T54, CR Chaand IP Tau. These targets were not modeled with a full radiative transfer code but a parametrized temperature profile and optically thin dust emission inside the cavity rather than an inner disk (Kim et al. 2009; Espaillat et al. 2011), so the results can not be compared directly.

9.5.2 Binaries

Some transition disks can be explained as circumbinary disks due to the dynamical interaction between the disk and a stellar companion. The cavity size is expected to be ~2 times as large as the binary separation (Artymowicz & Lubow 1996). The fraction of the transition disks in

our sample for which binarity has been studied is limited, but for those targets where spatially resolved information is available from the literature (either detections or upper limits), the properties are listed in Table 9.11, together with the cavity sizes found in this study.

Table 9.11: *Multiplicity properties*

ID	Separation (arcsec)	Separation (AU)	r_{cav} (AU)	Ref	ID	Separation (arcsec)	Separation (AU)	r_{cav} (AU)	Ref
1	0.062	6.7	140^{+10}_{-10}	1	60	<0.1	<12	2^{+2}	9
4	<0.1	<16	45^{+15}_{-5}	2	62	<0.1	<12	1	9
5	<0.1	<16	30^{+50}_{-18}	2	63	<0.13	<16	20^{+5}_{-5}	10
6	-	4	60^{+10}_{-10}	3	64	<0.01/>0.3	<1.5/>50	70^{+20}_{-30}	11
7	<0.75	<120	8^{+2}_{-2}	4	134	<0.13	<18	190_{-10}	12
9	0.25	40	120^{+20}_{-10}	2	135	>0.03	>4	4^{+2}_{-2}	13
10	0.14	22	190_{-10}	2	136	>0.03	>4	50^{+40}_{-10}	13
11	<0.07/5.122	<11/800	30^{+10}_{-10}	2	140	<0.1	<14	190_{-10}	14
12	<0.07	<11	15^{+5}_{-5}	2	149	0.06/4.1	8/560	10^{+8}_{-8}	15
14	<0.07	<11	10^{+4}_{-4}	2	150	<0.1	<14	15^{+5}_{-5}	14
15	<0.08	<13	1^{+1}	2	152	<0.1	<14	150^{+20}_{-20}	14
16	<0.12	<19	50^{+30}_{-49}	2	153	>0.03	>4	2^{+2}	13
17	<0.75	<120	15^{+15}_{-5}	4	162	<0.1	<25	2^{+2}	14
18	<0.08	<13	30^{+5}_{-5}	2	172	<0.1	<25	2^{+1}	14
21	0.088	13	110^{+10}_{-20}	5	174	<0.1	<45	18^{+10}_{-6}	14
23	<0.7	<140	60^{+10}_{-10}	6	175	0.83	116	4^{+8}_{-2}	14
24	<0.1	<20	16^{+2}_{-4}	7	177	1.2	168	25^{+10}_{-10}	14
25	<0.8	<160	4^{+4}_{-2}	6	179	<0.1	<15	1^{+59}	7
27	<0.1	<20	120^{+30}_{-20}	7	180	0.5	72	14^{+4}_{-4}	7
28	<0.1	<20	2^{+2}	7	181	<0.1	<25	6^{+12}_{-5}	14
33	<0.1	<14	80^{+10}_{-10}	8	182	<0.1	<25	2^{+23}	14
40	<0.1	<12	1	9	183	<0.1	<25	4^{+1}_{-2}	14
41	<0.1	<12	1	9	184	<0.1	<25	160^{+20}_{-10}	14
43	<0.13	<16	45^{+5}_{-20}	10	191	0.22	30	2^{+2}	16
44	<0.1	<12	4^{+2}_{-2}	9	200	<0.06	<12	1	6
46	<0.1	<12	20^{+10}_{-5}	9	309	<0.1	<5	10^{+2}_{-2}	8
47	<0.13	<16	1^{+1}	10	318	-	1.5	70^{+30}_{-10}	17
48	<0.1	<12	8^{+6}_{-7}	8	319	0.638	80	1^{+17}	10
49	0.33	41	20^{+30}_{-10}	9	325	>0.03	>4	80^{+40}_{-35}	13
50	0.54	68	2^{+2}	9	326	0.053	8	6^{+2}_{-2}	18
58	<0.13	<16	1	10	329	>0.03	>4	30^{+10}_{-5}	13
59	<0.1	<12	2^{+2}	9					

Refs. 1) Huélamo et al. (2011), 2) Lafrenière et al. (2008), 3) Guenther et al. (2007), 4) Comerón (2012), 5) Biller et al. (2012), 6) Ghez et al. (1997), 7) Romero et al. (2012), 8) Vicente et al. (2011), 9) Cieza et al. (2010), 10) Ratzka et al. (2005), 11) Kraus et al. (2008), 12) Kohler & Leinert (1998), 13) Pott et al. (2010), 14) Cieza et al. (2012b), 15) Leinert et al. (1997), 16) Biller et al. (2011), 17) Loinard et al. (2008), 18) Ireland & Kraus (2008)

Although for a handful of targets the cavity can indeed be explained by a binary companion, for the bulk of the disks the limits are not sufficient to exclude circumbinary disks. Previous binary studies of transition disks already revealed that most of the sharp cavities are not due to binary systems (Pott et al. 2010; Vicente et al. 2011).

9.5.3 Accretion

By combining the outcome of the SED modeling with our information on accretion, the possibility of photoevaporation as origin of the cavities can be checked. According to photoevaporation models (e.g. Alexander et al. 2006a), UV photons from the star heat and ionize the

gas in the disk; beyond a critical radius, the thermal velocity of the ionized gas exceeds its escape velocity and the material is dissipated as a wind. During the lifetime of the disk, the accretion rate is expected to gradually decrease: when the rate drops below the photoevaporation rate, the outer disk can no longer resupply the inner disk with material and an inner hole is formed. This process is called photoevaporative clearing, and transition disks created by this mechanism are expected to have no or very low accretion. Clearing of a gap by a planet and photoevaporation could also happen simultaneously (e.g. Rosotti et al. 2013), making the distinction not purely measurable by accretion alone. Figure 9.3 shows the number of objects in each class that are accreting/non-accreting. The accretors are dominated by disks without holes and massive disks with large holes, which are likely transition disks with a cavity due to clearing by a companion. The non-accretors are dominated by the low-scale height low-mass disks (DD), confirming that they are likely debris disks. The non-accreting low-mass disks are possibly disks where the hole is caused by photoevaporative clearing, but as there are several low-mass accreting disks as well there is no general trend for the low-mass disks. The non-accreting disk without a hole (ID171) is an outlier, but the equivalent width of this target is on the edge of accreting/non-accreting, probably due to the ubiquitous variable accretion (Mendigutía et al. 2012), and should thus have been classified as an accretor.

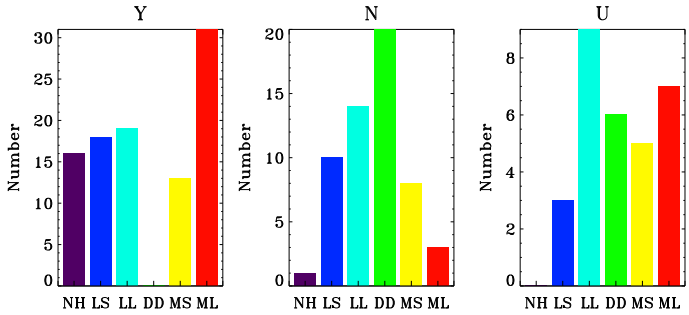


Figure 9.3: *Comparison of accretion properties from Table 9.6 with disk hole parameters: Y means accreting, N means non-accreting, U means unknown.*

9.5.4 Evaluation of color criteria

Considering the high success rate of new transition disks found in the sample in this study, it is now possible to re-evaluate the criteria used to select the targets. Figure 9.4 presents the the resulting classifications from our SED modeling for each of the four color selection criteria.

From Figure 9.4 it is clear that the disks without holes are most dominant in the B criteria, but overall at a low fraction. The L criteria are particularly biased towards the low scale height disks and low-mass disks with large holes. Massive disks with large holes are found in all colors. Evaluating the M10 criteria directly in the color-color plot, the DD disks fall outside the A and B range. A small amount of disks with holes falls outside the range of the A, B criteria (these are targets from the literature), generally with a shallower 8-24 μm slope.

9.5.5 Comparison with Cieza survey

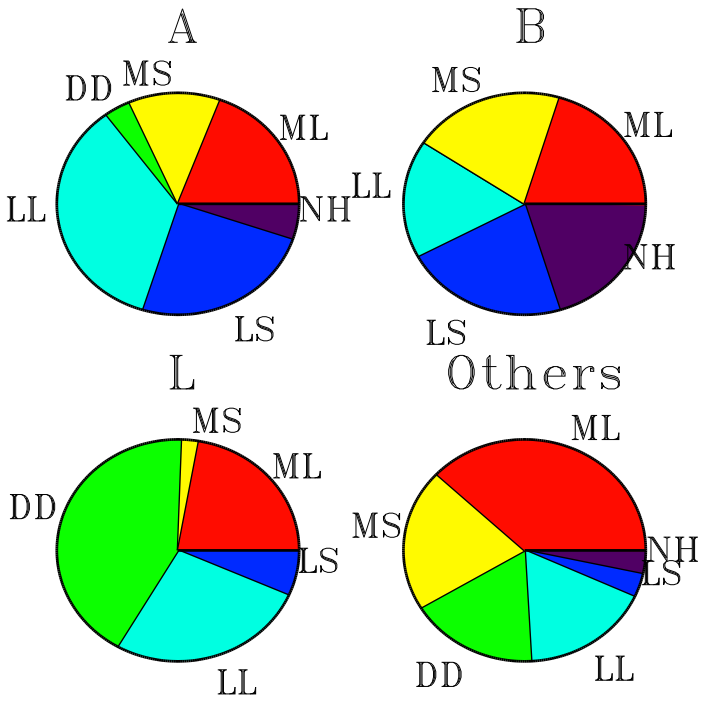


Figure 9.4: *Evaluation of the color criteria (Region A, B and L colors) vs the outcome of the SED modeling.*

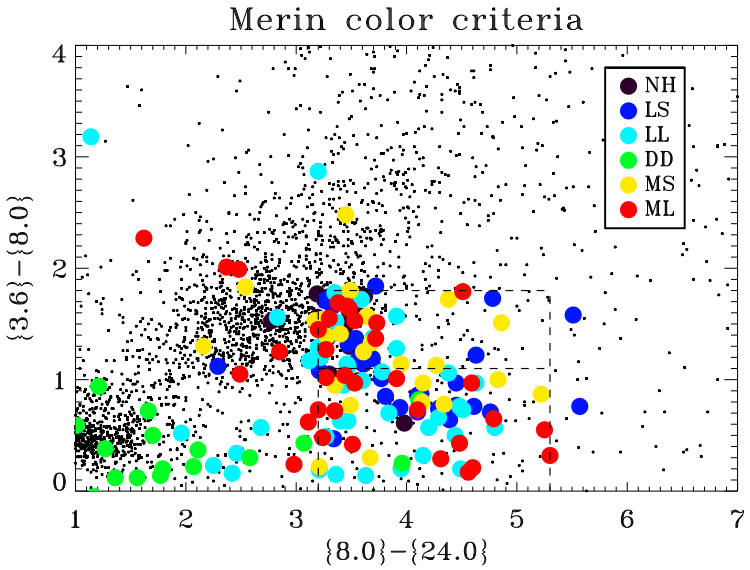


Figure 9.5: *Evaluation of the color criteria (A and B) vs the outcome of the SED modeling. The filled symbols are the targets analyzed in this study, the dots are all YSOs in the c2d, GB and Taurus catalogs. The dashed lines mark the Region B (top) and Region A (bottom) criteria.*

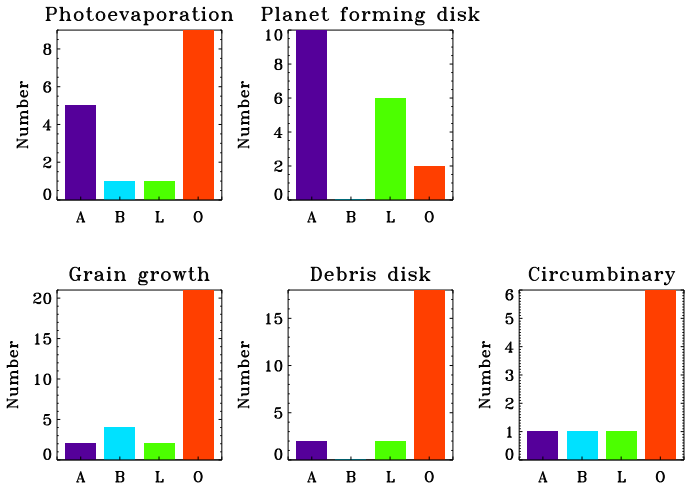


Figure 9.6: *Comparison of the categorization by the Cieza et al. studies with the color criteria used in this study applied to the Cieza sample.*

A previous large survey of transition disk candidates was performed by Cieza et al. (2010, 2012b) and Romero et al. (2012), who selected a sample of candidates using their own color criteria. Rather than SED modeling, they apply criteria based on a range of observables (disk mass, $L_{\rm disk}/L_*$, accretion, multiplicity, infrared spectral slope $\alpha_{\rm excess}$ and the wavelength where the disk emission starts to dominate, $\lambda_{\rm turnoff}$) to determine the origin of the dust deficit in their disks: circumbinary disk, photoevaporative clearing, debris disk, grain growth or planetary clearing.

Of particular interest are their planet-forming disks, which are massive, accreting disks with sharp cavities ($\alpha_{\rm excess} > 0$). Their final target list is compared with our sample, and the colors used for our color criteria have been derived for all their targets. Note that 27 of their 92 targets were already present in our sample, either selected by the color criteria or by their classification in the literature. Figure 9.6 shows how their categorization overlaps with our color criteria for these 27 targets and Figure 9.7 shows the inital color selection of Cieza et al. ([3.6]-[4.5]<0.25, [3.6]-[24.0]>1.5) in comparison with the outcome of our classification.

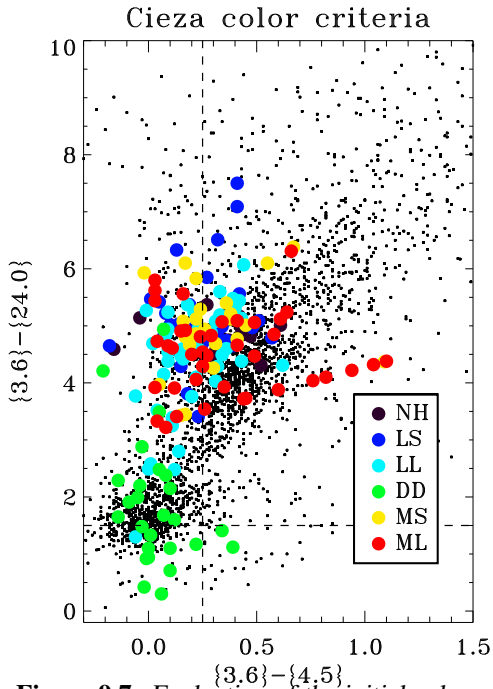


Figure 9.7: *Evaluation of the initial color criteria by the Cieza survey vs the outcome of our SED modeling. The filled symbols are the targets analyzed in our study, the dots are all YSOs in the c2d, GB and Taurus catalogs. The dashed lines mark the regions: the upper left quartile are the transition disks according to Cieza, the lower left quartile are diskless stars.*

Finally, Figure 9.8 shows how the classification of Cieza et al. compares with our classification for our targets.

Our A and L color criteria are clearly favored in the planet forming disks, while many of the less interesting disks from our perspective (grain growth, debris disks) fall in category, 'O', outside our color criteria. Several of the photoevaporation disks also follow the A criteria. This comparison confirms that our color criteria are good at selecting disks with sharp inner cavities. Inspection of the initial color criteria that Cieza et al. used for selecting targets shows only 50% of our disks with holes fall within these criteria. The DD targets fall in the same quartile as the diskless stars, as expected. Looking at the comparison of the Cieza classification with the outcome of our SED modeling in Figure 9.8, planet forming disks fall mostly within the class of massive disks with large cavities, while photoevaporation and debris disks are mostly consistent with low-mass disks. Neither of this is a surprise, considering the categorization of Cieza et al. (2010). Disks without holes all fall within the category of grain-growth disks. On the other hand, several other disks in the grain-growth category could be fit with a disk including a cavity. Note that circumbinary disks are not well-constrained for most of our sample and therefore not included.

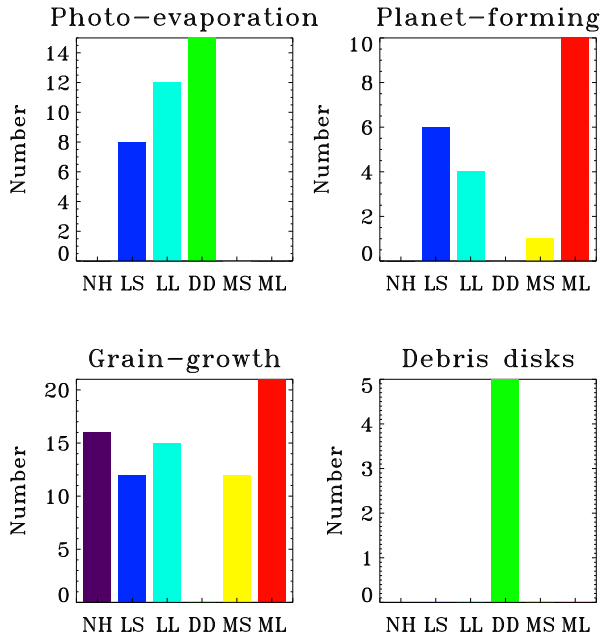


Figure 9.8: *Comparison of the categorization by the Cieza et al. studies with the classification of this study.*

9.5.6 Evolution

The $L_{\rm disk}/L_*$ ratio is generally taken as a measure of disk evolution. For the targets in this study, a clear trend is seen, with larger cavity radii and generally more non-accretors for lower $L_{\rm disk}/L_*$ (Figure 9.9a). This implies a general growth of cavity sizes with time.

A relation between disk mass and cavity radius has been noted in previous studies and interpreted as a gravitational process, where larger disk masses produce more massive planets, clearing larger cavities (Merín et al. 2010). This study shows no trend between disk mass and cavity size and generally more massive disks for accretors than for non-accretors (Figure 9.9b).

Both trends are susceptible due to the uncertainties in r_{cav} and could be biased due to the presence of many low-mass disks with large cavities in our sample, which are more likely to be debris disks than transition disks.

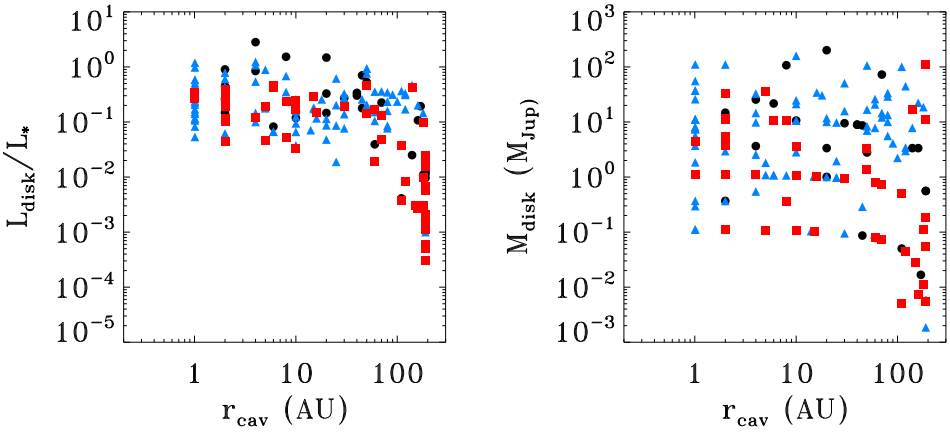


Figure 9.9: *The relation between cavity radius and L_{disk}/L_* and disk mass. Blue triangles indicate accretors, red squares non-accretors, black circles unknown.*

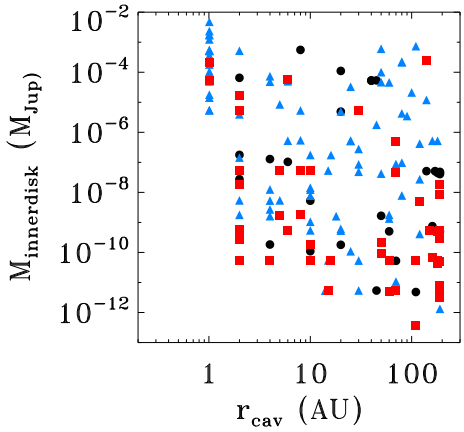


Figure 9.10: *The relation between cavity radius and inner disk mass. Blue triangles indicate accretors, red squares non-accretors, black circles unknown.*

9.5.7 Inner disk

Some transition disks are known to have an inner disk, while others have a completely empty cavity (e.g. Brown et al. 2007; Andrews et al. 2011). Some transition disk studies differentiate between these two types of disks as pre-transitional (with inner disk) and transitional disks (without inner disk), interpreting this as an evolutionary effect where the inner disk is expected to disappear with time due to accretion onto the star (Espaillat et al. 2014). However, with the measured accretion rates and inner disk masses the lifetime of the inner disk is very short (Owen et al. 2011), implying that for the inner disk to be detected it must be replenished continuously by the outer disk. Therefore, we do not distinguish between these two types of disks but use the $\delta_{\rm dust}$ value (a free parameter in our SED modeling) as a continuous parameter to fit the near infrared excess in the SEDs. Plotting the inner disk mass versus the cavity radius (Figure 9.10) reveals no significant trends (the disks with $r_{\rm cav}$=1 are disks without inner holes and there is no real inner disk) and the mass of the inner disk is spread over a large range for all cavity sizes. Accretors appear to have a slightly higher inner disk mass than non-accretors. This implies a possible division between transition disks with small cavities without inner disk and transition disks with large cavities with inner disk, each with their own origin.

9.5.8 Cavity radii and exoplanets

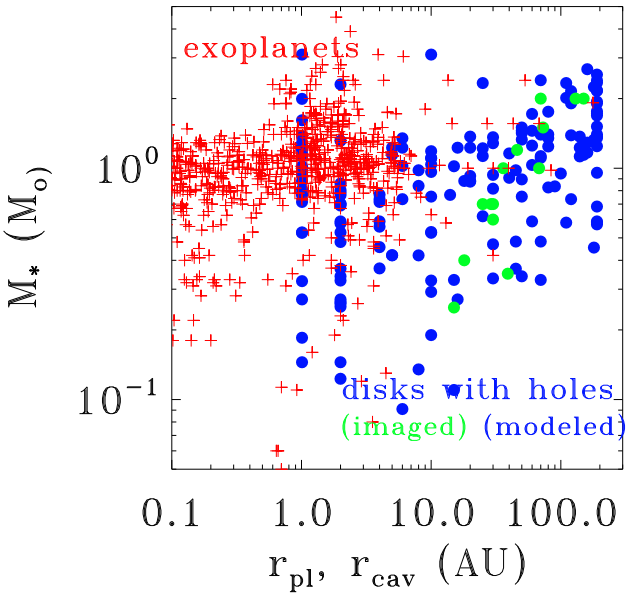


Figure 9.11: *Comparison of exoplanet orbital radii with transition disk cavity radii. Exoplanet orbital radii are indicated as red crosses, disk cavities with circles in blue (SED-modeling of this study) and green (millimeter imaging).*

If the origin of the dust cavity radii lies in forming planets, a correlation should exist between the orbital radii of exoplanets and disk cavity radii (Figure 9.11). Although both

samples are biased, a connection appears to exist, with the cavity radii several factors higher than the orbital radii. According to planet-disk interaction models, planet are expected to clear cavities up to twice their orbital radius (Pinilla et al. 2012a). A trend between cavity radius and stellar mass (blue and green points in Figure 9.11) as seen in previous work (M10) is seen as well.

9.6 Summary

The main results of this work are summarized as follows.

1. A large sample of ~200 transition disk candidates is presented and analyzed. Candidates are primarily selected from the *Spitzer* catalogs using the color criteria from Merín et al. (2010), with some additional targets from the literature.

2. The *Spitzer* data of the targets have been complemented with new submillimeter fluxes, *Herschel*-PACS archival data and optical/near infrared spectroscopy for spectral typing and accretion properties.

3. All targets are analyzed using RADMC-3D modeling with a limited number of parameters: disk mass, inner disk mass, scale height and flaring, and disk cavity radius, where the latter is the main parameter of interest.

4. The derived cavity sizes are consistent with imaging/modeling results in the literature.

5. Using the derived properties, the disks are categorized in disks without holes, large/small holes and massive/low-mass disks and very low scale height disks. The latter are likely debris disks. A large fraction of the targets falls in the category of disks with large holes, including several previously imaged disks.

6. Based on this classification, 133 targets (72% of the sample) are disks with cavities, including about 70 new transition disks that had not been identified before.

7. The color criteria are evaluated and compared for the targets in the Cieza studies (Cieza et al. 2010, 2012b; Romero et al. 2012). In general, our color criteria are a proper tool to select transition disk candidates.

8. The evolutionary parameter $L_{\rm disk}/L_*$ decreases with increasing cavity radius.

9. The cavity radius increases with stellar mass, suggesting a connection with exoplanet orbital radii.

10. The sample list provides a large number of transition disks that are suitable for follow-up observations with ALMA.

9.A Sample

Table 9.12: *Sample of transition disk candidates*

ID	Target	RA	Dec	Reg[a]	d[b] (pc)	Color[c]	Origin data	Prev.[d]	Ref
1	TCha	11 57 13.53	-79 21 31.5	ϵ Cha	108	[L]	Other	Imag.	1,2
2	RECX11	08 47 01.80	-78 59 35.2	η Cha	97	-	Other	TD	3,4
3	RECX5	08 42 27.09	-78 57 47.9	η Cha	97	[A]	Other	PF	5,4
4	CHXR22E	11 07 13.30	-77 43 49.9	ChaI	160	-	Other	TD	6,7
5	ISO52	11 04 42.58	-77 41 57.1	ChaI	160	[B]	GB	V	8
6	CSCha	11 02 25.11	-77 33 35.9	ChaI	160	[L]	c2d	V	8
7	11094742-7726290	11 09 47.27	-77 26 29.5	ChaI	160	[B]	GB		
9	T54	11 12 42.69	-77 22 23.1	ChaI	160	[L]	GB	CB	9
10	T21	11 06 15.41	-77 21 56.9	ChaI	160	-	Other	TD	6,7
11	SZCha	10 58 16.77	-77 17 17.1	ChaI	160	-	-	TD	9
12	T35	11 08 39.05	-77 16 04.2	ChaI	160	[A]	GB	TD/V	6,10
13	ISO-ChaII29	12 59 10.19	-77 12 13.7	ChaII	180	[L]	c2d		
14	T56	11 17 37.01	-77 04 38.1	ChaI	160	-	-	TD/V	6,10
15	CRCha	10 59 06.97	-77 01 40.3	ChaI	160	-	-	V	8
16	WWCha	11 10 00.11	-76 34 57.9	ChaI	160	[B]	-	V	8
17	11062554-7633418	11 06 25.47	-76 33 42.2	ChaI	160	[B]	GB		
18	T25	11 07 19.15	-76 03 04.9	ChaI	160	[A][L]	Other	V	11,7
20	MPMus	13 22 07.55	-69 38 12.2	Isol.	100	[B]	Other	TD	12,13
21	HD142527	15 56 41.89	-42 19 23.3	Isol.	140	-	-	Imag.	14
22	J16232807-4015368	16 23 28.09	-40 15 36.9	LupVI	150	[A][L]	GB		
23	Sz111	16 08 54.69	-39 37 43.1	LupIII	200	[A][L]	c2d	LU	15
24	Lup60	16 10 29.56	-39 22 14.7	LupIII	200	[A]	c2d	GG	16
25	J160830.3-390611	16 08 30.26	-39 06 11.1	LupIII	200	[B]	c2d	L	15
26	Sz104	16 08 30.80	-39 05 48.8	LupIII	200	[B]	c2d	H	15
27	Sz91	16 07 11.60	-39 03 47.7	LupIII	200	[L]	c2d	PF	16
28	J160855.5-390234	16 08 55.52	-39 02 33.9	LupIII	200	[A]	c2d	L/PE	17,18
29	Sz84	15 58 02.50	-37 36 02.8	LupI	150	[L] *	c2d	TD	19
30	16182186-3730298	16 18 21.88	-37 30 29.9	LupV	150	[L]	GB		
31	16225309-3724373	16 22 53.10	-37 24 37.4	LupV	150	[L]	GB		
32	J19002346-3712242	19 00 23.47	-37 12 24.2	CrA	150	[A]	GB		
33	HD135344	15 15 48.44	-37 09 16.0	Isol.	140	[B]	-	Imag.	20
34	CrA-466	19 01 18.95	-36 58 28.3	CrA	150	-	Other	TD	21
35	Sz76	15 49 30.80	-35 49 52.0	LupI	150	[B]	Other		22

Refs. 1) Wahhaj et al. (2010), 2) Huélamo et al. (2015), 3) Megeath et al. (2005), 4) Sicilia-Aguilar et al. (2009), 5) Bouwman et al. (2010), 6) Kim et al. (2009), 7) Luhman et al. (2008), 8) Espaillat et al. (2011), 9) Kim et al. (2009), 10) Espaillat et al. (2011), 11) Espaillat et al. (2011), 12) Cortes et al. (2009), 13) Silverstone et al. (2006), 14) Ohashi (2008), 15) Merín et al. (2008), 16) Romero et al. (2012), 17) Merín et al. (2008), 18) Romero et al. (2012), 19) Merín et al. (2010), 20) Brown et al. (2009), 21) Sicilia-Aguilar et al. (2008), 22) Padgett et al. (2006), 23) Andrews et al. (2011), 24) Rosenfeld et al. (2013), 25) Cieza et al. (2010), 26) Andrews et al. (2010), 27) van der Marel et al. (2013), 28) van Kempen et al. (2009), 29) Andrews et al. (2009), 30) McClure et al. (2010), 31) Mathews et al. (2012), 32) Harvey et al. (2007), 33) Furlan et al. (2011), 34) Andrews et al. (2011), 35) Wahhaj et al. (2010), 36) Rebull et al. (2010), 37) Cieza et al. (2012b), 38) Isella et al. (2010b), 39) Monnier et al. (2008), 40) Cieza et al. (2012b), 41) Furlan et al. (2011), 42) Isella et al. (2010a), 43) Furlan et al. (2011), 44) Piétu et al. (2005), 45) Najita et al. (2010), 46) Piétu et al. (2006), 47) Ireland & Kraus (2008), 48) Hughes et al. (2009), 49) Carpenter et al. (2008), 50) Cieza et al. (2012a)

Notes. [a] Full names of the regions: Cha = Chamaeleon, Lup = Lupus, CrA = Corona Australis, Oph = Ophiuchus, UppS = Upper Sco, Oph = Ophiuchus, Tau = Taurus, Aur = Auriga, Per = Perseus, TWH = TW Hydrae, Isol. = Isolated. [b] Distances were adopted from the literature as follows: 120 pc for Oph (Loinard et al. 2008); 150 pc for Lup I, IV, V and VI and 200 pc for LupIII (Comerón 2008; Comerón et al. 2009); 250 pc for Per (Jørgensen et al. 2006); 140 pc for Tau (Kenyon et al. 2008); 450 pc for Aur (Broekhoven-Fiene et al. 2014); 145 pc for Upp Sco (Carpenter et al. 2008); 150 pc for Corona Australis (Sicilia-Aguilar et al. 2008); 109 pc for ϵ Cha(Torres et al. 2008); 160 pc for ChaI (Kim et al. 2009); 180 pc for ChaII (Alcalá et al. 2008); 97 pc for η Cha(Mamajek et al. 1999); and 430 pc for Ser (Dzib et al. 2010). [c] An asterix (*) indicates this target was part of the M10 sample. [d] The full explanation previous classifications is as follows, according to their recording papers. 1) Cieza et al. (2010): "PF"=Planet-forming disk, "GG"=Grain-growth dominated disk, "PE"=Photoevaportive disk. 2) Merín et al. (2008); Harvey et al. (2007): "L"=low infrared excess or anemic disk, "H"=high infrared excess, "T"=T Tauri-like infrared excess. 3) Others: "PTD" = pre-transitional disk, "V" = sea-saw variability.

Table 9.12: *Sample of transition disk candidates*

ID	Target	RA	Dec	Reg[a]	d[b] (pc)	Color[c]	Origin data	Prev.[d]	Ref
36	J154508.9-341734	15 45 08.88	-34 17 33.7	LupI	150	-	Other	LU	15
38	RXJ1615.3-3255	16 15 20.23	-32 55 04.9	Lup	185	[B] *	c2d	Imag.	23
39	V4046Sgr	18 14 10.47	-32 47 34.5	Isol.	73	-	-	Imag.	24
40	J163154.7-250324	16 31 54.73	-25 03 24.0	Oph	125	[B]	c2d	GG	25
41	J163205.5-250236	16 32 05.52	-25 02 36.2	Oph	125	[A]	c2d	PF	25
43	J163023.4-245416	16 30 23.39	-24 54 16.1	Oph	125	[B]	c2d		
44	WSB63	16 28 54.06	-24 47 44.3	Oph	125	[A]	c2d	PF	25
45	SR24S	16 26 58.51	-24 45 37.0	Oph	125	-	c2d	Imag.	26
46	RXJ1633.9-2442	16 33 55.60	-24 42 05.0	Oph	125	[A]	c2d	Imag.	25,50
47	ISO-Oph43	16 26 27.53	-24 41 53.6	Oph	125	[B]	c2d		
48	WSB60	16 28 16.51	-24 36 58.3	Oph	125	[B]	c2d	Imag.	23
49	J163115.7-243402	16 31 15.74	-24 34 02.0	Oph	125	[B]	c2d	GG	25
50	J162245.4-243124	16 22 45.39	-24 31 23.8	Oph	125	[A] *	c2d	PE	25
51	IRS48	16 27 37.19	-24 30 34.8	Oph	125	-	Other	Imag.	27,28
52	DoAr44	16 31 33.46	-24 27 37.4	Oph	125	[B]	c2d	Imag.	29
53	J162435.2-242620	16 24 35.20	-24 26 20.0	Oph	125	[A]	c2d		
54	SR21	16 27 10.28	-24 19 12.5	Oph	125	-	-	Imag.	20
55	J162309.2-241705	16 23 09.22	-24 17 04.6	Oph	125	[A]	c2d	PTD	30
56	J163136.8-240420	16 31 36.77	-24 04 19.8	Oph	125	[L]	c2d		
58	J162648.6-235634	16 26 48.64	-23 56 34.1	Oph	125	[B]	c2d		
59	J162802.6-235504	16 28 02.60	-23 55 04.0	Oph	125	[A]	c2d	PE	25
60	oph62	16 25 06.92	-23 50 50.4	Oph	125	[A] *	c2d	PF	25
61	J162532.5-232626	16 25 32.50	-23 26 26.0	Oph	125	[A]	c2d		
62	J162218.5-232148	16 22 18.52	-23 21 48.1	Oph	125	[B]	c2d	GG	25
63	DoAr28	16 26 47.42	-23 14 52.2	Oph	125	-	HREL	TD	30
64	J160421.7-213028	16 04 21.70	-21 30 28.4	UppS	145	[L]	-	Imag.	31
65	18015423-0437531	18 01 54.24	-04 37 53.1	Ser	415	[L]	GB		
66	18044921-0436413	18 04 49.20	-04 36 41.5	Ser	415	[B]	GB		
67	18270980-0414297	18 27 09.79	-04 14 29.8	Ser	415	[L]	GB		
68	18272873-0406248	18 27 28.73	-04 06 24.8	Ser	415	[L]	GB		
69	18273408-0403247	18 27 34.08	-04 03 24.8	Ser	415	[L]	GB		
70	18273858-0402289	18 27 38.57	-04 02 28.9	Ser	415	[A][L]	GB		
71	18255765-0357040	18 25 57.66	-03 57 04.0	Ser	415	[L]	GB		
73	18291383-0342355	18 29 13.84	-03 42 35.5	Ser	415	[L]	GB		
74	18284156-0341507	18 28 41.56	-03 41 50.7	Ser	415	[L]	GB		
75	18283439-0339371	18 28 34.40	-03 39 37.2	Ser	415	[L]	GB		
76	18272161-0314158	18 27 21.62	-03 14 15.9	Ser	415	[L]	GB		
77	18222604-0304383	18 22 26.04	-03 04 38.3	Ser	415	[L]	GB		
78	18330328-0244021	18 33 03.30	-02 44 02.2	Ser	415	[B]	GB		
79	18324685-0243273	18 32 46.86	-02 43 27.4	Ser	415	[L]	GB		
80	18304127-0242335	18 30 41.26	-02 42 33.7	Ser	415	[L]	GB		
81	18324783-0239401	18 32 47.83	-02 39 40.1	Ser	415	[B]	GB		
82	J18321275-0222377	18 32 12.75	-02 22 37.8	Ser	415	[A][L]	GB		
83	18292883-0221157	18 29 28.84	-02 21 15.7	Ser	415	[A][L]	GB		
84	18291450-0220575	18 29 14.50	-02 20 57.5	Ser	415	[L]	GB		
85	18304121-0220189	18 30 41.20	-02 20 19.1	Ser	415	[B]	GB		
86	J18314556-0218408	18 31 45.57	-02 18 40.9	Ser	415	[A]	GB		
88	18311986-0208161	18 31 19.86	-02 08 16.1	Ser	415	[A]	GB		
89	18323005-0204130	18 32 30.06	-02 04 13.0	Ser	415	[A][L]	GB		
90	18292804-0204042	18 29 28.07	-02 04 04.7	Ser	415	[A]	GB		
91	18293961-0202414	18 29 39.60	-02 02 41.4	Ser	415	[B]	GB		
92	J18303289-0200514	18 30 32.89	-02 00 51.3	Ser	415	[A][L]	GB		
93	18311732-0200461	18 31 17.32	-02 00 46.1	Ser	415	[A]	GB		
94	18312875-0159125	18 31 28.75	-01 59 12.5	Ser	415	[A]	GB		
95	18315497-0157330	18 31 54.98	-01 57 33.1	Ser	415	[L]	GB		
96	18313657-0157320	18 31 36.57	-01 57 32.0	Ser	415	[A]	GB		

Table 9.12: *Sample of transition disk candidates*

ID	Target	RA	Dec	Reg[a]	d[b] (pc)	Color[c]	Origin data	Prev.[d]	Ref
97	18313343-0155182	18 31 33.43	-01 55 18.2	Ser	415	[A]	GB		
98	18315077-0153393	18 31 50.77	-01 53 39.3	Ser	415	[B]	GB		
99	J18303321-0152563	18 30 33.22	-01 52 56.2	Ser	415	[A][L]	GB		
100	18295741-0151541	18 29 57.41	-01 51 54.1	Ser	415	[A][L]	GB		
101	18294721-0148301	18 29 47.21	-01 48 30.2	Ser	415	[A][L]	GB		
102	18293368-0145103	18 29 33.69	-01 45 10.3	Ser	415	[B]	GB		
103	18290819-0139215	18 29 08.19	-01 39 21.5	Ser	415	[B]	GB		
104	18314110-0128035	18 31 41.10	-01 28 03.6	Ser	415	[L]	GB		
105	18290391-0115357	18 29 03.92	-01 15 35.8	Ser	415	[L]	GB		
106	18371575-0026561	18 37 15.75	-00 26 56.1	Ser	415	[L]	GB		
107	18381010-0023452	18 38 10.10	-00 23 45.2	Ser	415	[L]	GB		
108	18371444-0023261	18 37 14.45	-00 23 26.2	Ser	415	[L]	GB		
110	18385989-0008097	18 38 59.90	-00 08 09.9	Ser	415	[L]	GB		
111	J182813.5+000-249	18 28 13.51	-00 02 49.1	Ser	415	[B]	c2d	TT	32
112	J182821.6+000016	18 28 21.58	+00 00 16.4	Ser	415	[B]	c2d	L	32
113	18384257+0001324	18 38 42.59	+00 01 32.5	Ser	415	[A][L]	GB		
114	18392594+0006382	18 39 25.96	+00 06 38.4	Ser	415	[A]	GB		
115	J182850.2+000950	18 28 50.21	+00 09 49.7	Ser	415	[B]	c2d	F	32
116	183549.4+001002	18 35 49.38	+00 10 01.7	Ser	415	[L]	GB		
117	18385571+0014431	18 38 55.72	+00 14 43.1	Ser	415	[A][L]	GB		
118	18394048+0014497	18 39 40.50	+00 14 49.7	Ser	415	[B]	GB		
119	18374209+0016519	18 37 42.09	+00 16 52.0	Ser	415	[L]	GB		
120	J182911.5+002039	18 29 11.49	+00 20 38.8	Ser	415	[A] *	c2d		
121	18375663-0023253	18 37 56.63	-00 23 25.3	Ser	415	[A]	GB		
122	18381580+0024218	18 38 15.81	+00 24 21.9	Ser	415	[L]	GB		
123	J18295130+0027477	18 29 51.30	+00 27 47.9	Ser	415	[L]	c2d	LU	32
124	serp22	18 28 29.06	+00 27 56.0	Ser	415	[A] *	c2d		
125	18401205+0029276	18 40 12.06	+00 29 27.7	Ser	415	[B]	GB		
126	J182901.2+002933	18 29 01.22	+00 29 33.0	Ser	415	[B]	c2d	L	32
127	Serp127	18 29 44.10	+00 33 56.0	Ser	415	[A][L] *	c2d	LU	32
128	J182935.6+003504	18 29 35.62	+00 35 03.9	Ser	415	[A] *	c2d	LU	32
129	18381447+0035099	18 38 14.48	+00 35 09.8	Ser	415	[L]	GB		
130	18401486+0037042	18 40 14.88	+00 37 04.2	Ser	415	[A][L]	GB		
131	Serp111	18 29 36.19	+00 42 16.7	Ser	415	[A] *	c2d	LU	32
132	J182955.3+004939	18 29 55.32	+00 49 39.3	Ser	415	[A]	c2d	TT	32
133	J183008.6+005847	18 30 08.62	+00 58 46.7	Ser	415	[B]	c2d	TT	32
134	RXJ0432.8+1735	04 32 53.24	+17 35 33.7	Tau	140	-	Tau	TD	33
135	DMTau	04 33 48.73	+18 10 10.0	Tau	140	-	Tau	Imag./V	34,10
136	UXTauA	04 30 04.00	+18 13 49.3	Tau	140	[A]	Other	Imag.	34,35
137	043339.0+222720	04 33 39.00	+22 27 20.0	Tau	140	[A]	Tau		33
138	043326.2+224529	04 33 26.20	+22 45 29.0	Tau	140	[L]	Tau		36
139	J04390525+2337450	04 39 05.25	+23 37 45.0	Tau	140	[B]	GB	PTD	33
140	043649.1+241258	04 36 49.10	+24 12 58.0	Tau	140	[L]	Tau	DD	37
142	MWC758	05 30 27.53	+25 19 56.9	Isol.	200	-	Tau	Imag.	38
144	044555.7+261858	04 45 55.70	+26 18 58.0	Tau	140	[L]	Tau		
145	DHTauAB	04 29 41.50	+26 32 58.0	Tau	140	[A]	Tau		
146	043044.7+263308	04 30 44.70	+26 33 08.0	Tau	140	[L]	Tau		
147	J04214631+2659296	04 21 46.32	+26 59 29.6	Tau	140	[A]	Tau		
148	IPTau	04 24 57.08	+27 11 56.5	Tau	140	-	Tau	V	8
149	V892Tau	04 18 40.62	+28 19 15.5	Tau	140	-	Tau	CB-disk	39
150	V410X-ray6	04 19 01.10	+28 19 42.0	Tau	140	[A]	Tau	PF/TD	40,41
151	042254.6+282354	04 22 54.60	+28 23 54.0	Tau	140	[L]	Tau		
152	V819Tau	04 19 26.26	+28 26 14.3	Tau	140	-	Tau	TD	33
153	RYTau	04 21 57.41	+28 26 35.6	Tau	140	-	Tau	Imag./V	42,10
154	V410X-ray2	04 18 34.40	+28 30 30.0	Tau	140	[A]	Tau	TD	33

Table 9.12: *Sample of transition disk candidates*

ID	Target	RA	Dec	Reg[a]	d[b] (pc)	Color[c]	Origin data	Prev.[d]	Ref
155	041542.7+290959	04 15 42.78	+29 09 59.0	Tau	140	[A][L]	Tau	TD	33
156	041332.3+291726	04 13 32.30	+29 17 26.0	Tau	140	[A]	Tau		
157	J032800.1+300847	03 28 00.09	+30 08 47.0	Per	250	[B]	c2d		
158	LkCa19	04 55 36.96	+30 17 55.2	Tau	140	-	Other	TD	43,35
159	ABAur	04 55 45.85	+30 33 04.3	Tau	140	-	-	Imag.	44
160	J033341.3+311341	03 33 41.29	+31 13 41.0	Per	250	[B]	c2d		
161	ASR118	03 28 56.97	+31 16 22.3	Per	250	[B] *	c2d		
162	MBO22	03 29 29.27	+31 18 34.7	Per	250	[A] *	c2d	PF	25
163	J032856.6+311836	03 28 56.65	+31 18 35.5	Per	250	[B]	c2d		
164	J034219.3+314327	03 42 19.27	+31 43 27.0	Per	250	[B]	c2d		
165	J034227.1+314433	03 42 27.12	+31 44 32.9	Per	250	[A] *	c2d		
166	J034109.1+314438	03 41 09.13	+31 44 37.9	Per	250	[B]	c2d		
167	J034355.2+315532	03 43 55.20	+31 55 32.0	Per	250	[A]	c2d		
168	J034434.8+315655	03 44 34.81	+31 56 55.2	Per	250	[A] *	c2d		
169	IC348LRL190	03 44 29.23	+32 01 15.7	Per	250	[A] *	c2d		
171	J034520.5+320634	03 45 20.46	+32 06 34.5	Per	250	[B]	c2d		
172	IC348-67	03 43 44.63	+32 08 17.8	Per	250	[A]	c2d	PF	37
173	LkH-alpha330	03 45 48.29	+32 24 11.8	Per	250	[B]	c2d	Imag.	20
174	J04300424+3522238	04 30 04.25	+35 22 23.8	Aur	450	[A][L]	GB	PF	37
175	J04303235+3536133	04 30 32.35	+35 36 13.4	Tau	140	[L]	GB	PF	37
176	04300980+3540355	04 30 09.80	+35 40 35.6	Tau	140	[B]	GB		
177	J04304004+3542101	04 30 40.05	+35 42 10.3	Tau	140	[L]	GB	GG	37
178	J04303831+3549591	04 30 38.27	+35 49 59.3	Aur	450	[L]	GB		
179	J160044.5-415531	16 00 44.53	-41 55 31.2	LupIV	150	[B]	c2d	PF	16
180	J190058.1-364505	19 00 58.05	-36 45 05.0	UppS	145	[A]	GB	PF	16
181	03445614+3209152	03 44 56.14	+32 09 15.1	Per	250	[A]	c2d	PF	37
182	03442156+3215098	03 44 21.58	+32 15 09.7	Per	250	[A]	c2d	PE	37
183	03442257+3201536	03 44 22.58	+32 01 53.8	Per	250	[A]	c2d	PE	37
184	04330422+2921499	04 33 04.22	+29 21 50.0	Per	250	[A]	Tau	DD	37
185	J160825.76-390601.1	16 08 25.76	-39 06 01.1	LupIII	200	[B]	c2d	TT	15
186	RXJ1556.1-3655	15 56 02.10	-36 55 28.2	LupIII	150	[B]	Other		22
187	043150.5+242418	04 31 50.50	+24 24 18.0	Tau	140	[B]	Tau		
188	041413.5+281249	04 14 13.50	+28 12 49.0	Tau	140	[B]	Tau		
189	041841.3+282725	04 18 41.30	+28 27 25.0	Tau	140	[B]	Tau		
190	042025.5+270035	04 20 25.50	+27 00 35.0	Tau	140	[B]	Tau		
191	042921.6+270125	04 29 21.60	+27 01 25.0	Tau	140	[B]	Tau		
192	043249.1+225302	04 32 49.10	+22 53 02.0	Tau	140	[B]	Tau		
193	044221.0+252034	04 42 21.00	+25 20 34.0	Tau	140	[B]	Tau		
194	041539.1+281858	04 15 39.10	+28 18 58.0	Tau	140	[B]	Tau		
195	042318.2+264115	04 23 18.20	+26 41 15.0	Tau	140	[B]	Tau		
196	041414.5+282758	04 14 14.50	+28 27 58.0	Tau	140	[B]	Tau		
197	041915.8+290626	04 19 15.80	+29 06 26.0	Tau	140	[B]	Tau		
198	042155.6+275506	04 21 55.60	+27 55 06.0	Tau	140	[B]	Tau		
200	J160710.08-391103.5	16 07 10.08	-39 11 03.5	LupIII	200	[B]	c2d	L	15
201	J032741.47+302016.8	03 27 41.47	+30 20 16.8	Per	250	[B]	c2d		
202	J034345.17+320358.6	03 43 45.17	+32 03 58.6	Per	250	[A]	c2d		
203	J182815.26-000243.3	18 28 15.26	-00 02 43.3	Ser	415	[B]	c2d		
204	J162715.89-243843.2	16 27 15.89	-24 38 43.2	Oph	125	[B]	c2d		30
301	J130455.7-773949	13 04 55.74	-77 39 49.5	ChaII	180	[B] *	c2d		
303	J160115.5-415235	16 01 15.55	-41 52 35.3	LupIV	150	[B]	c2d	F	15
307	16083070-3828268	16 08 30.70	-38 28 26.8	LupIII	200	[B]	HREL	L	15
309	TWHya	11 01 51.91	-34 42 17.0	TWH	50	-	-	TD	45
310	15395742-3414567	15 39 57.42	-34 14 56.7	LupI	150	-	HREL		
314	16281385-2456113	16 28 13.85	-24 56 11.3	Oph	125	[B]	HREL		
316	16271587-2438433	16 27 15.87	-24 38 43.3	Oph	125	[B]	HREL		
317	16312019-2430009	16 31 20.19	-24 38 43.3	Oph	125	[B]	HREL		

Table 9.12: *Sample of transition disk candidates*

ID	Target	RA	Dec	Reg[a]	d[b] (pc)	Color[c]	Origin data	Prev.[d]	Ref
318	DoAr21	16 26 03.03	-24 23 36.4	Oph	125	[A] *	c2d		
319	J162740.3-242204	16 27 40.27	-24 22 04.0	Oph	125	[A]	c2d	CB	25
321	Serp48	18 28 58.08	+00 17 24.5	Ser	415	[LL] *	c2d		
322	18302986+0035004	18 30 29.86	+00 35 00.4	Ser	415	[B]	HREL		
325	LkCa15	04 39 17.78	+22 21 03.5	Tau	140	[A]	Tau	Imag./V	46,10
326	CoKu-Tau-4	04 41 16.79	+28 40 00.5	Tau	140	-	-	CB-disk	47
329	GMAur	04 55 10.98	+30 21 59.4	Tau	140	[A]	-	Imag./V	48,10
333	03370363+3039291	03 37 03.63	+30 39 29.1	Per	250	-	HREL		
334	03401579+3055047	03 40 15.79	+30 55 47.0	Per	250	[B]	HREL		
335	J033234.0+310056	03 32 34.00	+31 00 56.0	Per	250	[B] *	c2d		
348	UScoJ155837.1-225724	15 58 36.91	-22 57 15.3	UppS	145	[B]	Other		49
349	RXJ1842.9-3532	18 42 57.95	-35 32 42.7	UppS	145	[A]	Other		49
350	RXJ1852.3-3700	18 52 17.30	-37 00 11.9	UppS	145	[A]	Other		49

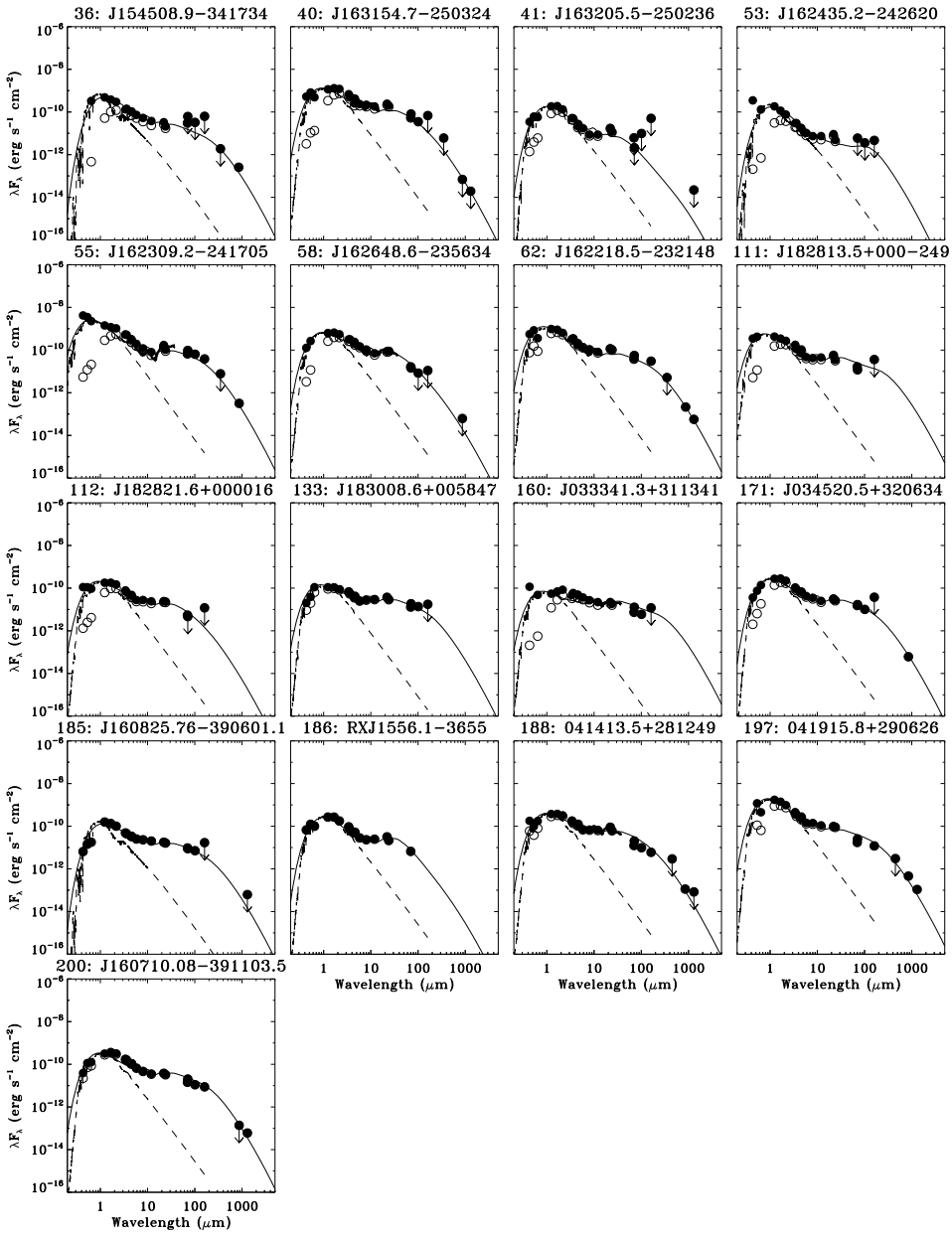


Figure 9.12: *SEDs of disks without holes. In this and subsequent Figures the dashed line indicates the stellar spectrum. Open circles denote observed fluxes before extinction correction, filled circles after extinction correction.*

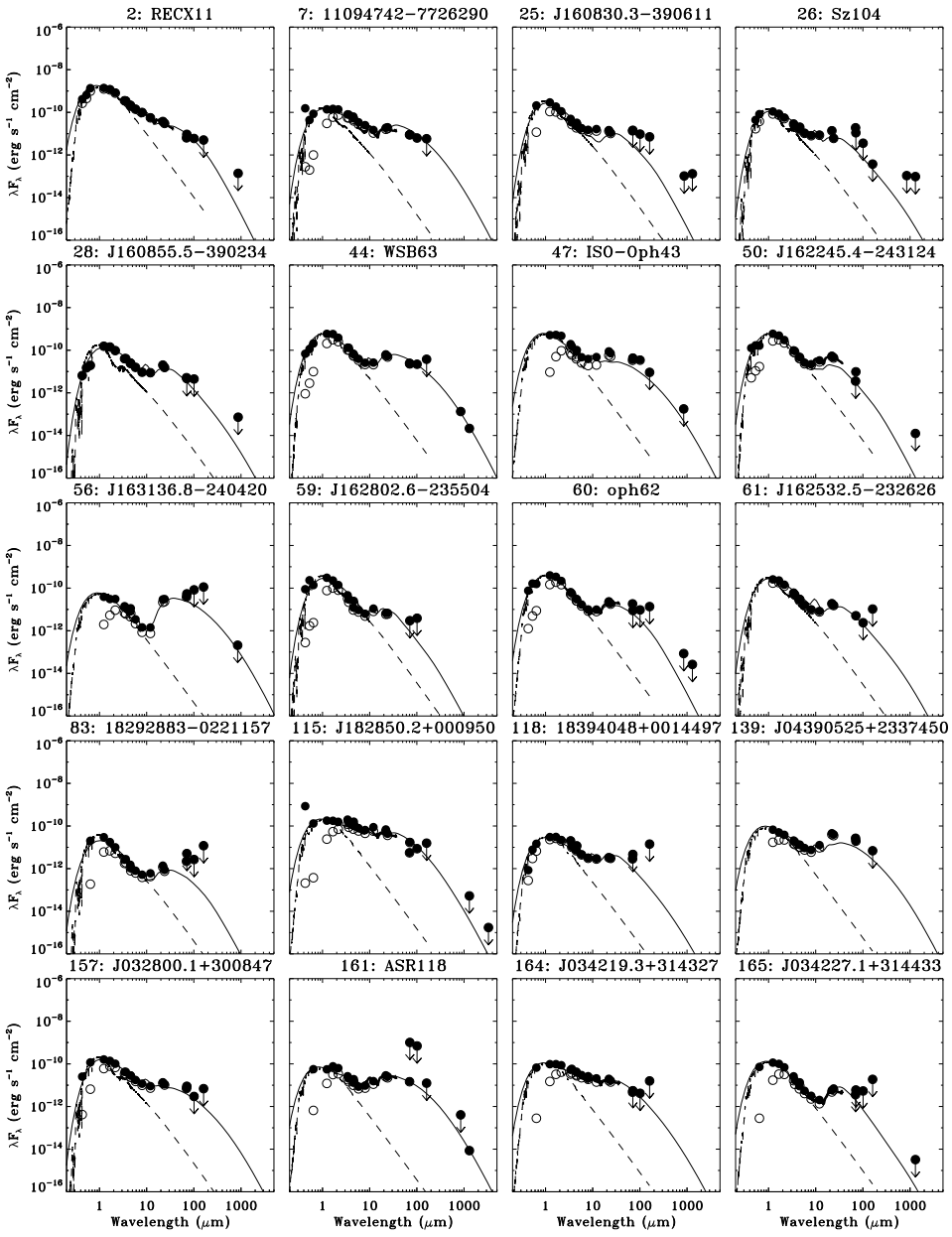


Figure 9.13: *SEDs of low-mass disks with small holes.*

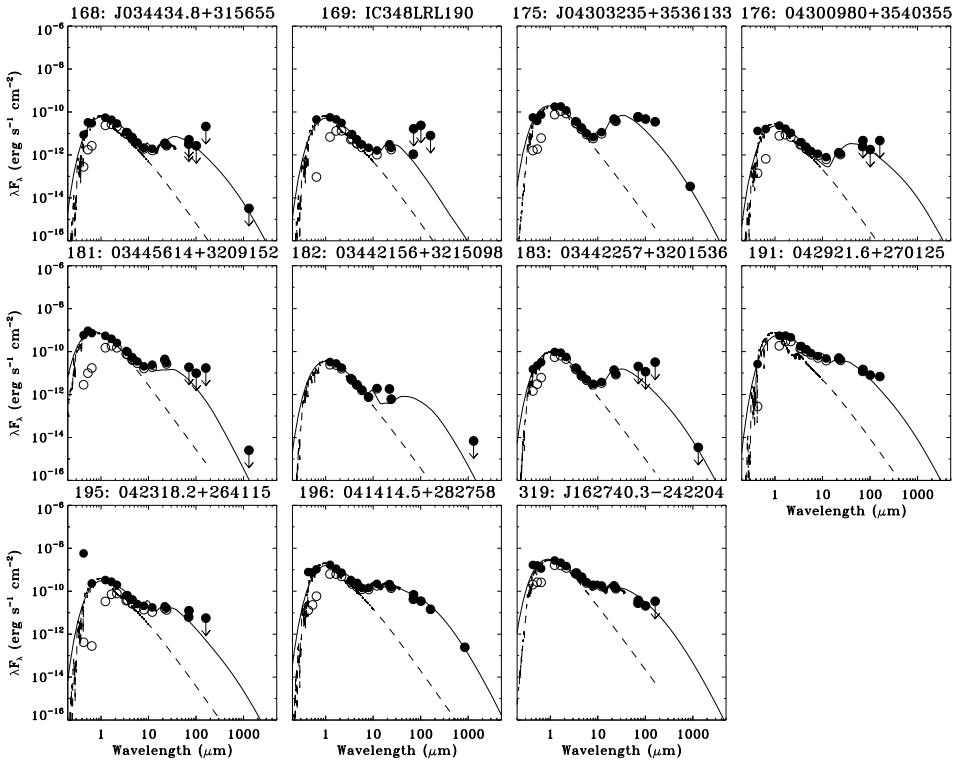


Figure 9.13: *SEDs of low-mass disks with small holes.*

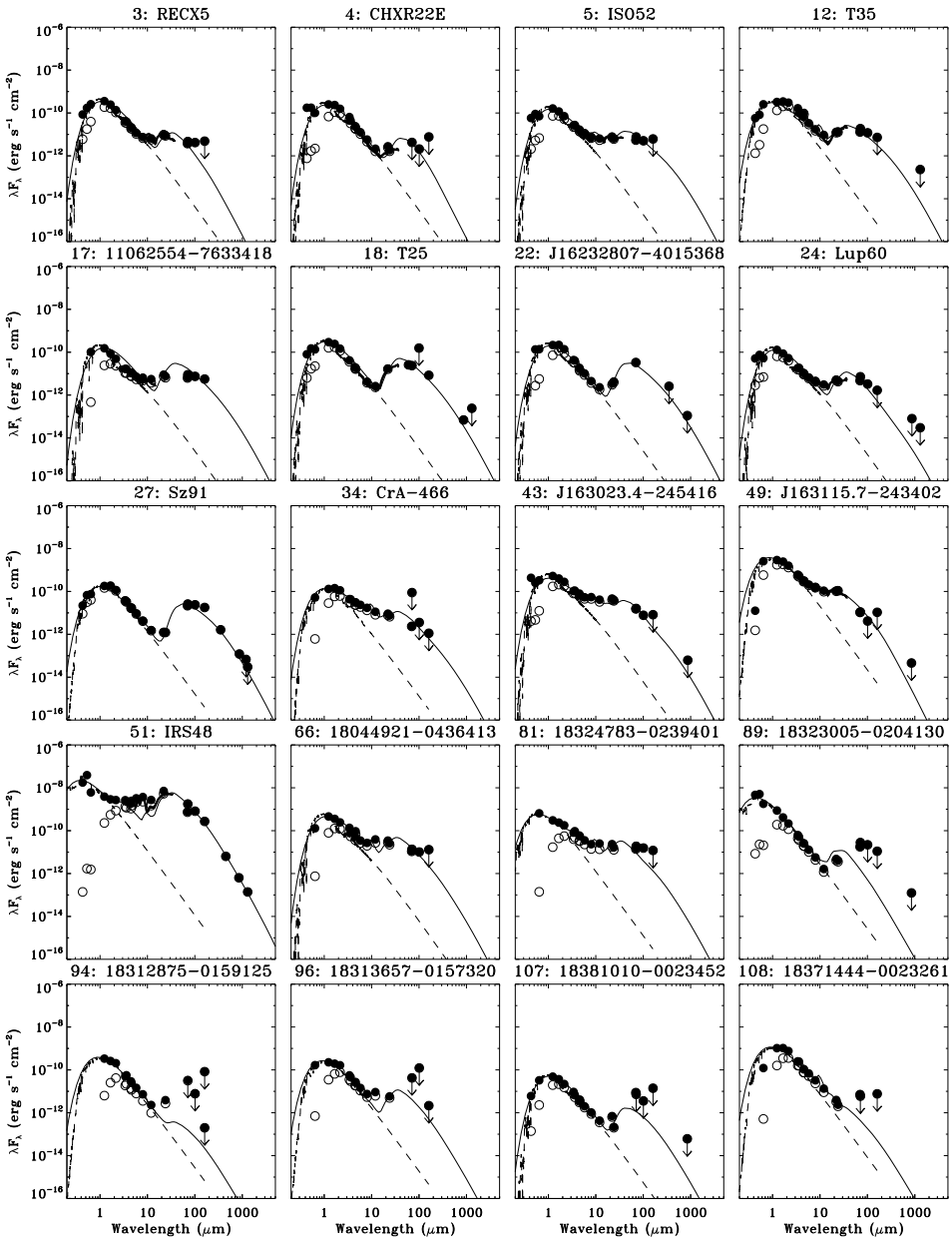


Figure 9.14: *SEDs of low-mass disks with large holes.*

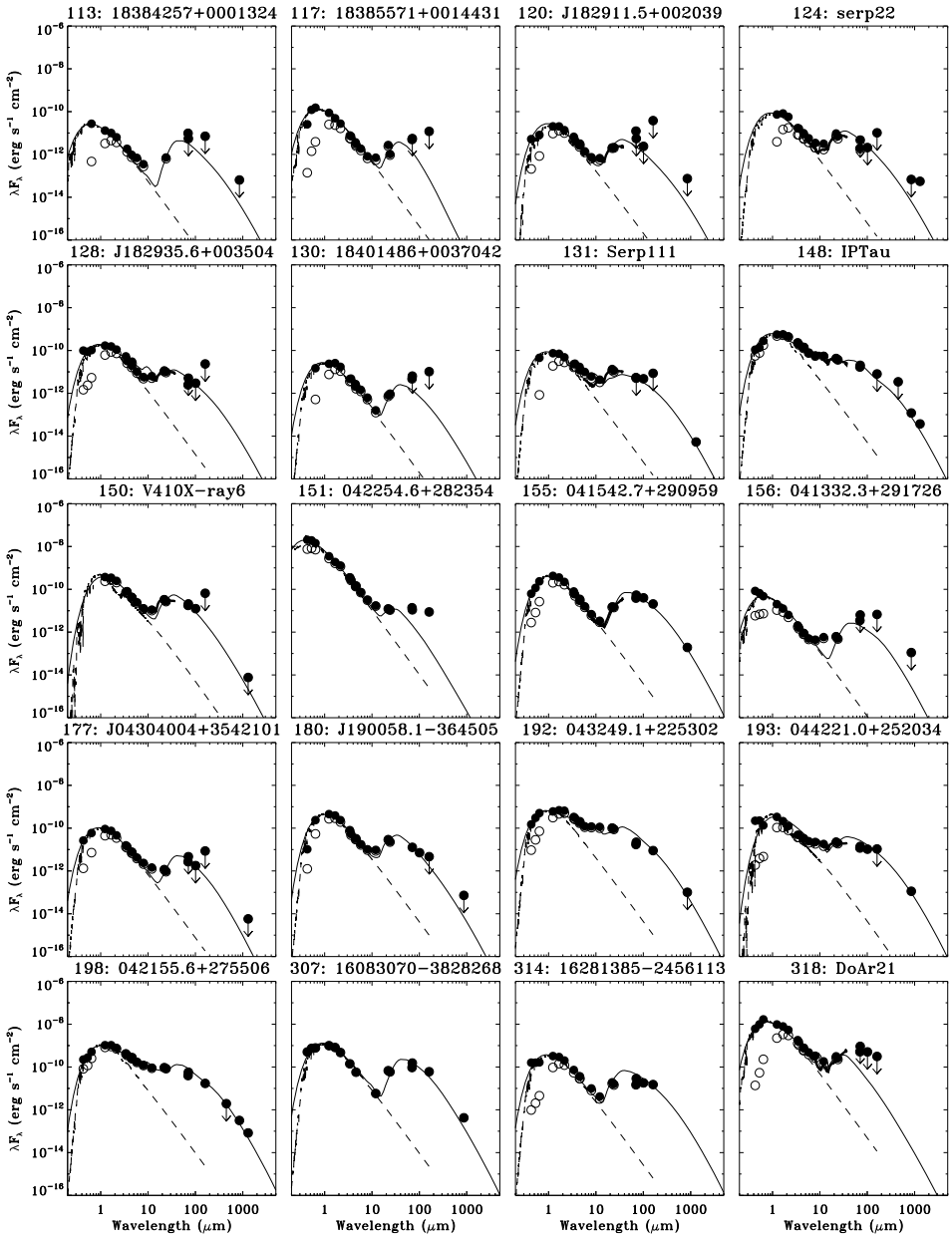


Figure 9.14: *SEDs of low-mass disks with large holes.*

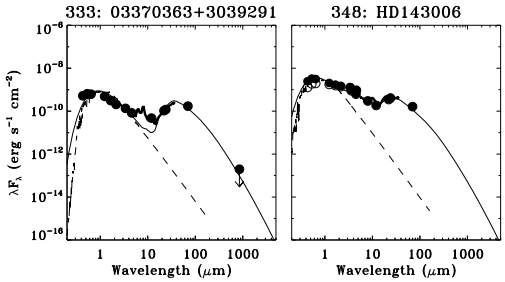


Figure 9.14: *SEDs of low-mass disks with large holes.*

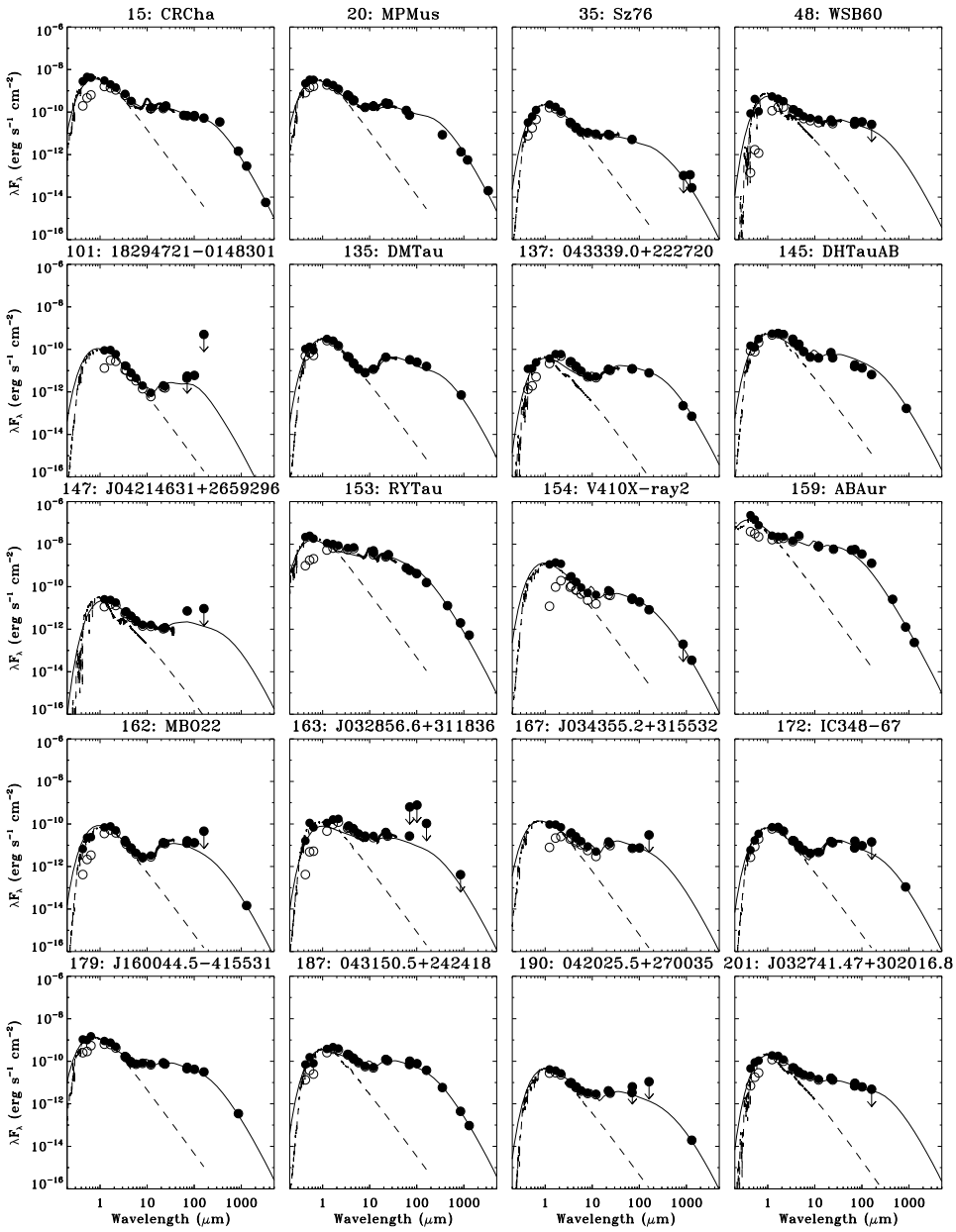


Figure 9.15: *SEDs of massive disks with small holes.*

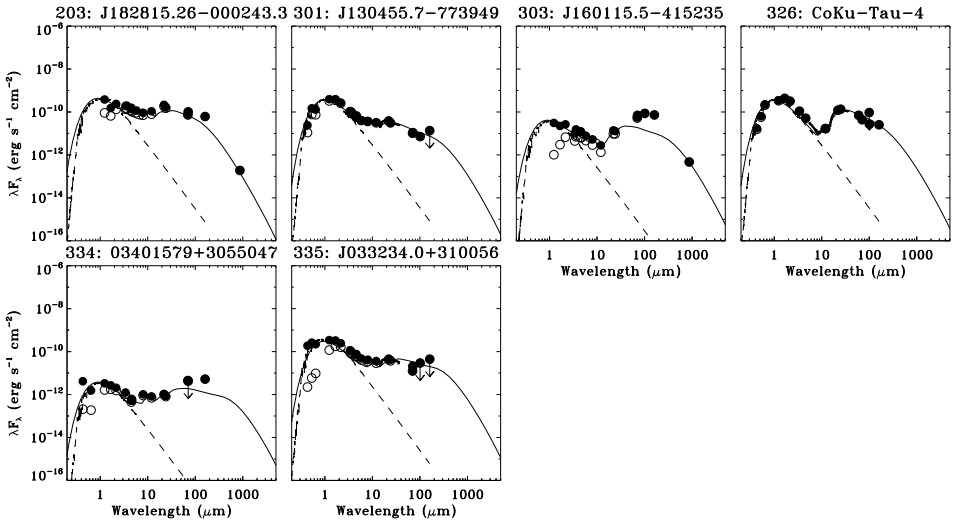


Figure 9.15: *SEDs of massive disks with small holes.*

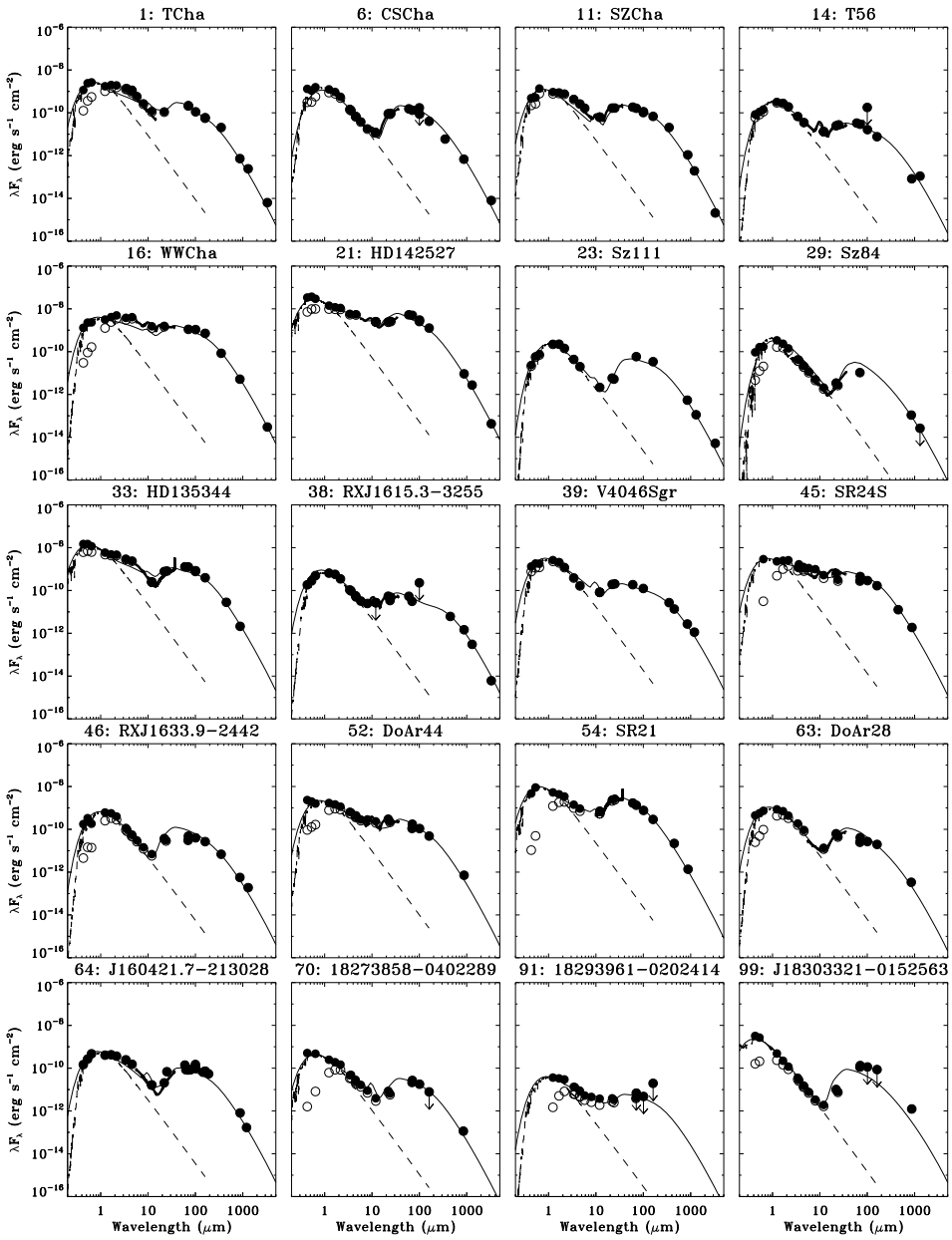


Figure 9.16: *SEDs of massive disks with large holes.*

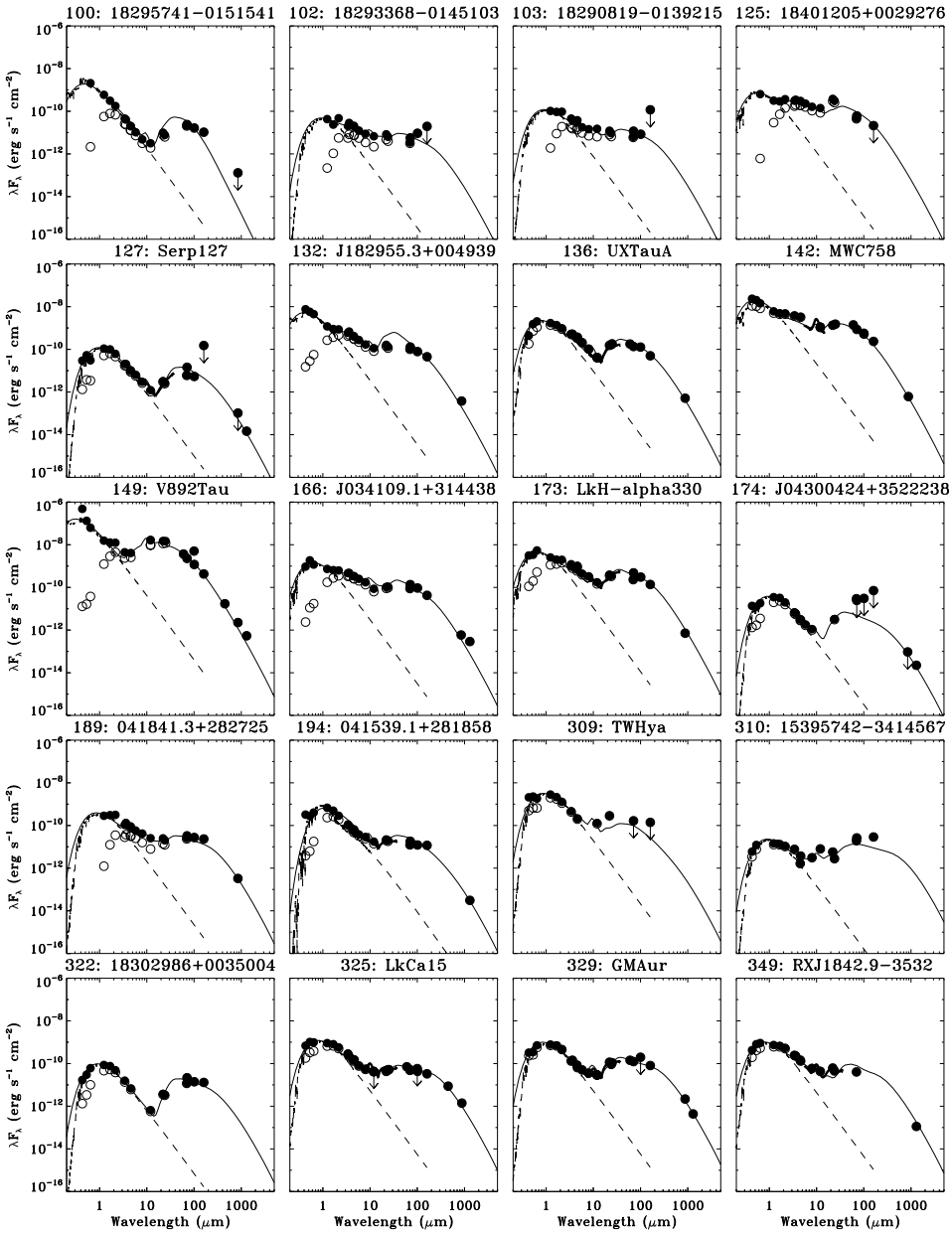


Figure 9.16: *SEDs of massive disks with large holes.*

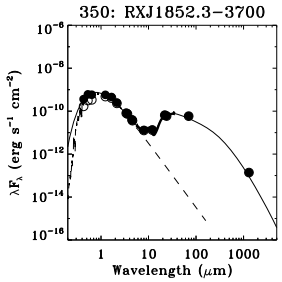


Figure 9.16: *SEDs of massive disks with large holes.*

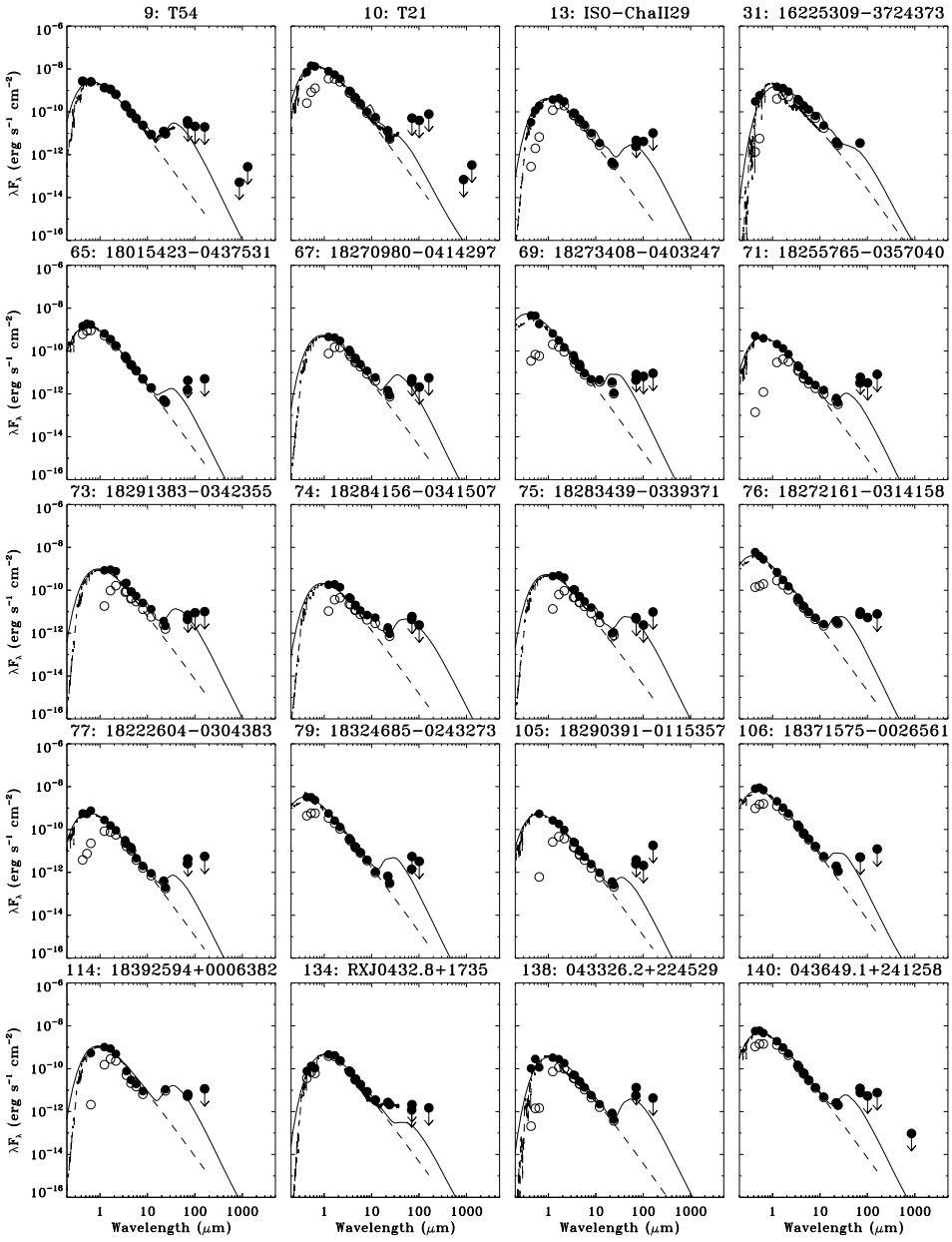


Figure 9.17: *SEDs of low scale height disks.*

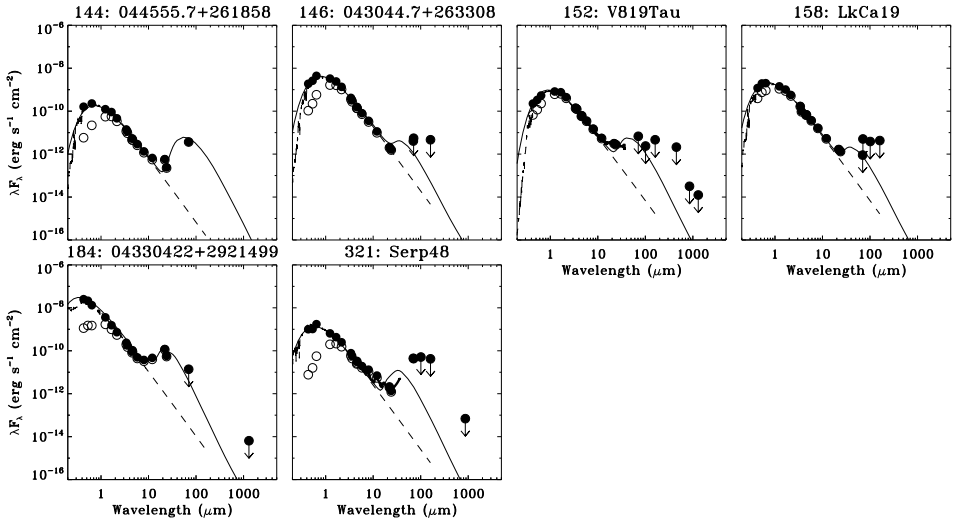


Figure 9.17: *SEDs of low scale height disks.*

9.B Flux tables

This section presents the flux tables.

Table 9.13: *Herschel photometry*

ID	PACS 70 (mJy)	PACS 100 (mJy)	PACS 160 (mJy)	ID	PACS 70 (mJy)	PACS 100 (mJy)	PACS 160 (mJy)
1	4.98±0.5	3.74±0.37	3.17±0.32	65	<0.10	-	<0.27
2	0.22±0.03	0.20±0.04	<0.27	66	0.32±0.05	0.34±0.04	<0.70[a]
3	0.11±0.03	0.14±0.03	<0.26	67	<0.12	<0.07	<0.30
4	<0.10	<0.07[a]	<0.41[a]	68	<0.13	<0.08	<0.34
5	0.18±0.05	0.17±0.03	<0.33[a]	69	<0.19	<0.22	<0.49
6	3.11±0.31	2.90±0.29	2.15±0.25	70	0.63±0.07	0.60±0.06	<0.42
7	0.21±0.04	0.21±0.03	<0.31	71	<0.14	<0.11	<0.44
9	<0.65[a]	<0.71[a]	<1.06[a]	73	<0.16	<0.30	<0.54[a]
10	<1.20[a]	<1.34[a]	<4.21[a]	74	<0.14	<0.08	<-0.02[a]
11	3.86±0.39	3.80±0.38	3.65±0.37	75	<0.11	<0.08	<0.52
12	0.44±0.05	0.40±0.05	<0.39	76	0.23±0.04	0.18±0.04	<0.42
13	<0.11	0.14±0.03	<0.55[a]	77	<0.10	-	<0.30[a]
14	0.69±0.08	0.55±0.06	0.41±0.07	78	<0.14	<0.10	<0.88
15	1.58±0.16	2.31±0.23	2.80±0.28	79	<0.13	<0.11	<-0.08[a]
16	26.06±2.92	36.06±3.9	38.45±6.0	80	<0.18	<0.24	<0.59
17	0.21±0.05	0.25±0.03	0.30±0.09	81	0.44±0.06	0.52±0.06	<0.64
18	0.56±0.07	-	0.45±0.1	82	<0.33[a]	<0.10[a]	<2.61[a]
21	117.78±11.78	100.65±10.06	67.82±6.78	83	<0.12	<0.09	<0.64
23	1.38±0.14	-	1.82±0.2	84	<0.12	<0.07	<0.42
24	0.17±0.04	0.11±0.03	<0.09[a]	85	<0.27	<0.53	<0.05[a]
25	<0.34	<0.32	<0.38[a]	86	<1.05[a]	<1.40[a]	<1.55[a]
26	<0.26	<0.12[a]	<0.02[a]	88	<32.9[a]	<26.25[a]	<59.51[a]
27	0.61±0.07	0.80±0.08	0.96±0.17	89	0.66±0.09	<0.74[a]	<0.59[a]
28	<0.11	<0.15	<-0.11[a]	90	<0.22	<0.22	<1.98
32	0.73±0.08	<1.61[a]	<2.98[a]	91	<0.16	<0.16	<1.05
33	29.8±2.98	28.3±2.83	21.13±2.11	92	<0.31[a]	<0.47[a]	<2.55[a]
34	<2.09	<0.12	<0.06[a]	93	<8.45[a]	<5.27[a]	<10.49[a]
36	<1.44	<1.09[a]	<3.36[a]	94	<0.74[a]	<0.26[a]	<4.44[a]
40	1.89±0.2	1.18±0.15	<3.65	95	<2.27[a]	<2.78[a]	<9.57[a]
41	<0.05[a]	<0.33[a]	<2.70[a]	96	<1.00[a]	<4.13[a]	<-4.57[a]
43	0.38±0.05	0.26±0.05	<0.44[a]	97	<2.49[a]	<6.83[a]	<8.58[a]
44	0.54±0.06	0.74±0.09	<2.02[a]	98	<1.46[a]	<3.07[a]	<10.72[a]
45	10.58±1.06	9.74±0.98	8.96±0.96	99	3.13±0.33	<3.84[a]	<4.62[a]
46	1.14±0.12	1.35±0.14	1.43±0.27	100	0.56±0.07	0.55±0.06	0.56±0.16
47	1.00±0.22	1.15±0.37	<0.49[a]	101	<0.13	0.20±0.05	<27.08
48	0.86±0.09	1.16±0.12	<1.41	102	0.13±0.04	0.31±0.04	<1.05
49	0.26±0.04	<0.14	<0.57[a]	103	0.27±0.06	0.28±0.08	<6.29
50	0.23±0.05	-	<-0.06[a]	104	<0.14	<0.07	<0.22
51	41.14±4.12	27.3±2.77	14.53±4.18	105	<0.09	<0.07	<0.97
52	4.10±0.41	3.66±0.37	2.60±0.5	106	<0.12	-	<0.66
53	<0.14	<0.12[a]	<0.25[a]	107	<0.17	<0.12	<0.75
54	31.58±3.16	25.75±2.58	15.61±1.88	108	<0.14	-	<0.41[a]
55	2.26±0.23	2.15±0.22	2.06±0.35	110	<0.14	-	<0.54
56	1.26±0.39	<2.78	<6.05[a]	111	0.28±0.06	-	<1.93[a]
58	0.34±0.05	<0.28	<0.59[a]	112	<0.11	-	<0.64
59	<0.07	<0.13	<-0.06[a]	113	<0.13	-	<0.38
60	<0.21[a]	<0.32	<0.73[a]	114	0.15±0.04	-	<0.62
61	0.12±0.04	<0.08	<0.56	115	0.40±0.06	0.29±0.08	<0.84
62	1.32±0.14	-	1.62±0.31	116	<0.22	-	<1.02
63	0.97±0.11	0.90±0.1	1.06±0.26	117	<0.13	-	<0.64
64	-	3.48±0.35	3.88±0.84	118	<0.11	-	<0.76

Notes. [(a)] Upper limit due to cloud confusion.

Table 9.13: *Herschel photometry*

ID	PACS 70 (mJy)	PACS 100 (mJy)	PACS 160 (mJy)	ID	PACS 70 (mJy)	PACS 100 (mJy)	PACS 160 (mJy)
119	<0.13	-	<0.02[a]	179	1.23±0.13	1.41±0.14	1.69±0.19
120	<0.13	<0.08	<2.04	180	0.30±0.04	0.24±0.03	<0.25
121	<0.59[a]	-	<0.45[a]	181	<0.44[a]	<0.33[a]	<0.92[a]
122	<0.10	-	<0.07[a]	182	<-0.07[a]	<-0.03[a]	<-0.72[a]
123	0.13±0.04	<0.07	<0.38	183	<0.48	<0.39[a]	<1.73[a]
124	<0.11	<0.07	<0.55	185	0.21±0.06	0.24±0.05	<0.91
125	1.42±0.15	-	<1.14	187	2.41±0.24	2.60±0.26	2.02±0.22
126	<16.95	<33.54	<3.04[a]	188	0.48±0.1	0.33±0.11	0.32±0.08
127	0.34±0.05	0.18±0.03	<8.11	189	0.75±0.09	0.91±0.09	1.25±0.16
128	<0.12	<0.10	<1.26	190	<0.15	-	<0.59
129	<0.12	-	<0.10[a]	191	0.35±0.07	0.27±0.04	0.37±0.11
130	<0.15	-	<0.55	192	0.52±0.09	-	0.48±0.16
131	<0.12	0.16±0.03	<0.46	193	0.33±0.05	0.35±0.04	<0.57
132	3.03±0.31	2.64±0.27	2.41±0.28	194	0.43±0.06	0.41±0.05	0.63±0.18
133	0.44±0.06	0.46±0.07	<0.94	195	0.29±0.06	-	<0.30
134	<0.05	-	<0.08	196	1.60±0.17	1.16±0.12	0.77±0.1
135	0.77±0.08	0.84±0.09	0.85±0.17	197	0.60±0.08	-	0.64±0.15
136	3.21±0.32	-	2.68±0.28	198	1.35±0.15	-	0.92±0.14
137	0.29±0.04	-	0.42±0.09	200	0.48±0.06	0.37±0.05	0.47±0.15
138	<0.31	-	<0.23[a]	201	0.22±0.05	0.21±0.03	<0.26
139	0.46±0.07	-	<0.37	202	1.73±0.3	<1.95	<1.53[a]
140	0.18±0.05	<0.18[a]	<0.41	203	2.39±0.25	-	3.30±0.38
142	20.39±2.04	17.59±1.76	12.65±2.57	204	<73.51	<60.36	<9.49[a]
145	0.44±0.06	0.45±0.05	0.35±0.09	301	0.26±0.05	0.24±0.05	<0.73
146	<0.13	-	<0.25	303	1.63±0.17	2.88±0.29	3.90±0.4
147	0.17±0.06	-	<0.50	307	3.63±0.37	-	3.24±0.33
148	0.48±0.08	-	<0.43	309	<3.93[a]	-	<7.50[a]
149	53.78±5.39	39.92±4.05	22.87±3.33	310	0.62±0.07	-	1.55±0.18
150	0.49±0.07	0.42±0.08	<3.51	314	0.68±0.07	0.61±0.08	0.81±0.26
151	0.26±0.05	-	0.47±0.12	317	1.08±0.11	0.69±0.07	<0.38
152	<0.16	<0.08	<0.25	318	<21.71[a]	<17.06[a]	<16.7[a]
153	13.82±1.38	-	8.36±0.86	319	0.89±0.1	0.70±0.12	<1.82[a]
154	0.66±0.09	0.64±0.07	0.44±0.11	321	1.02±0.11	<1.72[a]	<2.26[a]
155	1.26±0.14	1.34±0.14	1.11±0.13	322	0.51±0.07	0.47±0.05	0.70±0.14
156	<0.15	-	<0.36	325	1.20±0.13	1.45±0.15	1.77±0.38
157	0.21±0.05	<0.10	<0.37	326	1.03±0.11	0.92±0.09	1.36±0.35
158	<0.12	<0.13	<0.23	329	2.93±0.3	-	4.34±0.44
159	131.87±13.19	-	67.75±6.79	334	<0.10	-	0.28±0.09
160	0.30±0.05	0.20±0.03	<0.64	335	0.49±0.15	<0.99	<2.39
161	<23.85	<23.35	<0.67[a]	336	<0.12	0.13±0.02	<0.18
162	0.38±0.08	0.44±0.09	<2.46				
163	<14.92	<26.05	<5.67[a]				
164	<0.13	<0.14	<0.85				
165	<0.14	<0.18	<1.01				
166	3.20±0.32	3.15±0.32	2.28±0.43				
167	0.17±0.05	0.25±0.05	<1.64				
168	<0.12	<0.09	<1.14				
169	<0.39	<0.80	<0.43[a]				
171	0.40±0.06	0.34±0.07	<2.01				
172	0.37±0.06	0.32±0.05	<0.77				
173	11.41±1.14	10.25±1.03	7.38±0.74				
174	<0.58[a]	<1.03[a]	<3.80[a]				
175	1.35±0.14	1.58±0.16	1.87±0.27				
176	<0.11	<0.06	<0.25				
177	<0.11	<0.06	<0.46				
178	2.47±0.36	4.41±0.76	10.19±1.65				

Table 9.14: *Submillimeter photometry*

ID	SABOCA [350 μm] (mJy)	LABOCA [870 μm] (mJy)	SCUBA [450 μm] (mJy)	SCUBA [850 μm] (mJy)	SMA [880 μm] (mJy)	230 GHz [1.3mm] (mJy)	110 GHz [3.3mm] (mJy)	Ref
1	2400±200	210±20				105±150	7±1	1,2
2		<40						1
6	690±180	197±12.2					8.8±1.5	1,3
9		<15				<118		1,2
10		<20				<143		1,2
11	2400±500	314±12				77.5±20.3	2.3±0.4	1,4
12						<100		2
14		24±6				47.8±15.5		1,2
15	4000±200	420±50				124.9±24	6.2±1.5	1,2
16	9800±2400	1500±10					33.1±1.2	1,3
18		20±6				<105		1,2
20	1000±200	390±10				224±8	22±3.3	1,5
21					2700±270	1190±30	47±6	6,7
22	<300			<31.4				1
23				153.2±11.5		49±4.8	5.7±0.7	1,4
24		<23.2				<13		8,4
25		<30				<57		1,9
26				<30.5		<42		1,9
27	190±40	35±3				<27		1,4
28		<21						8
29				30.8±6.6		<11.4		1,10
32	<82			<36.8				1
33			4200±840		620±62			11,12
35		<30				<45		1,4
36	<220			72.6±18.5				1
38			919±184		430±43	132±3.9	6.7±0.6	13,12
39	3154±419		2042±111	770±39		451±20		14
40	<700	<20				<8.4		1,10
41						<9.6		10
43		<18						1
44				37.8±11		9.3±3		1,10
45			1900±380		550±55			13,12
46	800±200	164±14				81.8±2.7		1,10
47				<50.1				1
49				<13				10
50						<5.4		15
51			950±200	180±18		60±6		16,17
52					210±21			12
54			3300±660		400±40			13,12
55	<900	92±6						1
56				<59.1				1
58		<18						1
60				<24.2		<11.4		1,10
62	<600	62±9				24.5±3.1		1,10
63				95.2±16.4				1
64					238±24	67.5±1.4		18
70				32.4±10.7				1
82				<57.1				1

Refs. 1) This work. 2) Henning et al. (1993), 3) Lommen et al. (2007), 4) Lommen et al. (2010), 5) Gräfe & Wolf (2013), 6) Fukagawa et al. (2013), 7) Verhoeff et al. (2011), 8) Romero et al. (2012), 9) Merín et al. (2008), 10) Cieza et al. (2010), 11) Pérez et al. (2014), 12) Andrews et al. (2011), 13) van der Marel et al. (2015c), 14) Jensen et al. (1996), 15) Merín et al. (2010), 16) van der Marel et al. (2013), 17) Brown et al. (2012a), 18) Mathews et al. (2012), 19) Andrews et al. (2013), 20) Cieza et al. (2012b), 21) Andrews & Williams (2007b), 22) Andrews & Williams (2005), 23) Enoch et al. (2006), 24) Nuernberger et al. (1997), 25) Isella et al. (2009), 26) Hughes et al. (2010)

Table 9.14: *Submillimeter photometry*

ID	SABOCA [350 μm] (mJy)	LABOCA [870 μm] (mJy)	SCUBA [450 μm] (mJy)	SCUBA [850 μm] (mJy)	SMA [880 μm] (mJy)	230 GHz [1.3mm] (mJy)	110 GHz [3.3mm] (mJy)	Ref
86				<107.1				1
88				<137.3				1
89				<35.4				1
92				<79.3				1
95		49±11						1
98		63±8						1
99		360±30						1
100				<36.8				1
107				<17.3				1
113				<18.2				1
115						<22.8	<1.9	4,4
120				<21.1				1
124				<19.2		24±0.6		1,15
127				<29.2		6.3±0.6		1,15
131						2.3±0.6		15
132		109±11						1
135					210±21			12
136					150±15			12
137				63.2±18		31±2		1,19
140				<27				20
142					180±18			12
145					49±4.9			21
148			<516	34±5		16±5		22
149			2570±350	638±54		234±19		22
150						<3.3		20
152			<317	<9		<5.4		22
153			1920±160	560±30		229±17		22
154				<55.8		15±1		1,19
155				54.5±17.7				1
156				<31.4				1
159			3820±570	359±67		103±18		22
161				<115.1		3.7±0.9		1,15
162						6.3±1.1		15
163				<117.4				1
165						<1.4		15
166				166.7±14		126±12		1,23
168						<1.4		15
171				17.3±5.7				1
172				31±6				20
173					210±21			12
174				<26.9		9.7±1.5		1,20
175					10±2			20
177						<2.5		20
178				222.4±16.3				1
179		100±5						8
180		<21						8
181						<1.1		20
182						<3		20
183						<1.5		20
184						<2.8		20
185						<27		9
187	680±114			125.5±18.3		41±5		22,1
188			<442	32±8		<36		22
189				93.4±15.7				1

Table 9.14: *Submillimeter photometry*

ID	SABOCA [350 μm] (mJy)	LABOCA [870 μm] (mJy)	SCUBA [450 μm] (mJy)	SCUBA [850 μm] (mJy)	SMA [880 μm] (mJy)	230 GHz [1.3mm] (mJy)	110 GHz [3.3mm] (mJy)	Ref
190						8.4±1.4		19
192				<28.6				1
193				31.9±9.4				1
194						13.4±1.4		19
196				69.3±18.8				1
197			<456	130±7		47±0.7		22
198			<291	90±7		36±5		22
200		<40				26±9		1,24
202				<55.5				1
203		55±10						1
303		136±7						1
307		123±14						1
316		98±13						1
321		<20						1
325			1310±260		410±41			13,12
329					640±64	189±15		12,25
333				<56.1				1
349						49±9		26
350						60±8		26

Acknowledgements. The authors would like to thank C. Manara for useful discussions and M. McClure for providing the IRS spectrum on DoAr28. N.M. is supported by the Netherlands Research School for Astronomy (NOVA). Astrochemistry in Leiden is supported by the Netherlands Research School for Astronomy (NOVA), by a Royal Netherlands Academy of Arts and Sciences (KNAW) professor prize, and by the European Union A-ERC grant 291141 CHEMPLAN. This publication makes use of data products from the Wide-field Infrared Survey Explorer, which is a joint project of the University of California, Los Angeles, and the Jet Propulsion Laboratory/California Institute of Technology, funded by the National Aeronautics and Space Administration. The William Herschel Telescope is operated on the island of La Palma by the Isaac Newton Group in the Spanish Observatorio del Roque de los Muchachos of the Instituto de Astrofísica de Canarias.

Bibliography

Acke, B. & van den Ancker, M. E. 2004, A&A, 426, 151
Adams, F. C., Lada, C. J., & Shu, F. H. 1987, ApJ, 312, 788
Aikawa, Y., Momose, M., Thi, W.-F., et al. 2003, PASJ, 55, 11
Aikawa, Y., van Zadelhoff, G. J., van Dishoeck, E. F., & Herbst, E. 2002, A&A, 386, 622
Akimkin, V., Zhukovska, S., Wiebe, D., et al. 2013, ApJ, 766, 8
Alcala, J. M., Krautter, J., Schmitt, J. H. M. M., et al. 1995, A&AS, 114, 109
Alcalá, J. M., Natta, A., Manara, C. F., et al. 2014, A&A, 561, A2
Alcalá, J. M., Spezzi, L., Chapman, N., et al. 2008, ApJ, 676, 427
Alexander, R., Pascucci, I., Andrews, S., Armitage, P., & Cieza, L. 2014, Protostars and Planets VI, 475, eds. H. Beuther, R.S. Klessen, C.P. Dullemond, and T. Henning (University of Arizona Press)
Alexander, R. D. & Armitage, P. J. 2007, MNRAS, 375, 500
Alexander, R. D., Clarke, C. J., & Pringle, J. E. 2006a, MNRAS, 369, 216
Alexander, R. D., Clarke, C. J., & Pringle, J. E. 2006b, MNRAS, 369, 229
André, P., Di Francesco, J., Ward-Thompson, D., et al. 2014, Protostars and Planets VI, 27, eds. H. Beuther, R.S. Klessen, C.P. Dullemond, and T. Henning (University of Arizona Press)
Andrews, S. M., Rosenfeld, K. A., Kraus, A. L., & Wilner, D. J. 2013, ApJ, 771, 129
Andrews, S. M. & Williams, J. P. 2005, ApJ, 631, 1134
Andrews, S. M. & Williams, J. P. 2007a, ApJ, 671, 1800
Andrews, S. M. & Williams, J. P. 2007b, ApJ, 659, 705
Andrews, S. M., Wilner, D. J., Espaillat, C., et al. 2011, ApJ, 732, 42
Andrews, S. M., Wilner, D. J., Hughes, A. M., Qi, C., & Dullemond, C. P. 2009, ApJ, 700, 1502
Andrews, S. M., Wilner, D. J., Hughes, A. M., Qi, C., & Dullemond, C. P. 2010, ApJ, 723, 1241
Andrews, S. M., Wilner, D. J., Hughes, A. M., et al. 2012, ApJ, 744, 162
Armitage, P. J. 2011, ARAA, 49, 195
Artymowicz, P. & Lubow, S. H. 1996, ApJ, 467, L77
Ataiee, S. & Pinilla, P. 2015, subm. to MNRAS
Ataiee, S., Pinilla, P., Zsom, A., et al. 2013, A&A, 553, L3
Baraffe, I., Chabrier, G., Allard, F., & Hauschildt, P. H. 1998, A&A, 337, 403
Barge, P. & Sommeria, J. 1995, A&A, 295, L1
Barranco, J. A. & Marcus, P. S. 2005, ApJ, 623, 1157
Baryshev, A. M., Hesper, R., Mena, F. P., et al. 2015, A&A, 577, A129
Bast, J. E., Brown, J. M., Herczeg, G. J., van Dishoeck, E. F., & Pontoppidan, K. M. 2011, A&A, 527, A119
Batalha, N. M. 2014, Proceedings of the National Academy of Science, 111, 12647
Batalha, N. M., Rowe, J. F., Bryson, S. T., et al. 2013, ApJS, 204, 24
Beckwith, S. V. W. & Sargent, A. I. 1991, ApJ, 381, 250
Bergin, E., Calvet, N., D'Alessio, P., & Herczeg, G. J. 2003, ApJ, 591, L159
Bergin, E. A., Aikawa, Y., Blake, G. A., & van Dishoeck, E. F. 2007, Protostars and Planets V, 751, eds. B. Reipurth, D. Jewitt, and K. Keil (University of Arizona Press)
Bertout, C. 1989, ARA&A, 27, 351
Biller, B., Allers, K., Liu, M., Close, L. M., & Dupuy, T. 2011, ApJ, 730, 39
Biller, B., Lacour, S., Juhász, A., et al. 2012, ApJ, 753, L38
Birnstiel, T. & Andrews, S. M. 2014, ApJ, 780, 153
Birnstiel, T., Andrews, S. M., & Ercolano, B. 2012, A&A, 544, A79

Birnstiel, T., Dullemond, C. P., & Brauer, F. 2010, A&A, 513, A79
Birnstiel, T., Dullemond, C. P., & Pinilla, P. 2013, A&A, 550, L8
Bisschop, S. E., Fraser, H. J., Öberg, K. I., van Dishoeck, E. F., & Schlemmer, S. 2006, A&A, 449, 1297
Bisschop, S. E., Jørgensen, J. K., van Dishoeck, E. F., & de Wachter, E. B. M. 2007, A&A, 465, 913
Blum, J. & Wurm, G. 2008, ARA&A, 46, 21
Boogert, A. C. A., Hogerheijde, M. R., Ceccarelli, C., et al. 2002, ApJ, 570, 708
Boss, A. P. 1997, Science, 276, 1836
Bouwman, J., Lawson, W. A., Juhász, A., et al. 2010, ApJ, 723, L243
Brauer, F., Dullemond, C. P., & Henning, T. 2008, A&A, 480, 859
Brinch, C. & Hogerheijde, M. R. 2010, A&A, 523, A25
Brittain, S. D., Najita, J. R., & Carr, J. S. 2009, ApJ, 702, 85
Broekhoven-Fiene, H., Matthews, B. C., Harvey, P. M., et al. 2014, ApJ, 786, 37
Brown, J. M., Blake, G. A., Dullemond, C. P., et al. 2007, ApJ, 664, L107
Brown, J. M., Blake, G. A., Qi, C., Dullemond, C. P., & Wilner, D. J. 2008, ApJ, 675, L109
Brown, J. M., Blake, G. A., Qi, C., et al. 2009, ApJ, 704, 496
Brown, J. M., Herczeg, G. J., Pontoppidan, K. M., & van Dishoeck, E. F. 2012a, ApJ, 744, 116
Brown, J. M., Pontoppidan, K. M., van Dishoeck, E. F., et al. 2013, ApJ, 770, 94
Brown, J. M., Rosenfeld, K. A., Andrews, S. M., Wilner, D. J., & van Dishoeck, E. F. 2012b, ApJ, 758, L30
Bruderer, S. 2013, A&A, 559, A46
Bruderer, S., van der Marel, N., van Dishoeck, E. F., & van Kempen, T. A. 2014, A&A, 562, A26
Bruderer, S., van Dishoeck, E. F., Doty, S. D., & Herczeg, G. J. 2012, A&A, 541, A91
Bustamante, I., Merín, B., Ribas, Á., et al. 2015, A&A, 578, A23
Calvet, N., D'Alessio, P., Hartmann, L., et al. 2002, ApJ, 568, 1008
Calvet, N., D'Alessio, P., Watson, D. M., et al. 2005, ApJ, 630, L185
Calvet, N., Muzerolle, J., Briceño, C., et al. 2004, AJ, 128, 1294
Canovas, H., Schreiber, M. R., Cáceres, C., et al. 2015, ApJ, 805, 21
Carmona, A., Pinte, C., Thi, W. F., et al. 2014, A&A, 567, A51
Carpenter, J. M., Bouwman, J., Silverstone, M. D., et al. 2008, ApJS, 179, 423
Carpenter, J. M., Ricci, L., & Isella, A. 2014, ApJ, 787, 42
Casassus, S., van der Plas, G., M, S. P., et al. 2013, Nature, 493, 191
Casassus, S., Wright, C., Marino, S., et al. 2015, ArXiv e-prints
Castelli, F. & Kurucz, R. L. 2004, ArXiv Astrophysics e-prints
Ceccarelli, C., Loinard, L., Castets, A., Tielens, A. G. G. M., & Caux, E. 2000, A&A, 357, L9
Chiang, E. I. & Goldreich, P. 1997, ApJ, 490, 368
Cieza, L., Padgett, D. L., Stapelfeldt, K. R., et al. 2007, ApJ, 667, 308
Cieza, L. A., Mathews, G. S., Williams, J. P., et al. 2012a, ApJ, 752, 75
Cieza, L. A., Schreiber, M. R., Romero, G. A., et al. 2010, ApJ, 712, 925
Cieza, L. A., Schreiber, M. R., Romero, G. A., et al. 2012b, ApJ, 750, 157
Cieza, L. A., Swift, J. J., Mathews, G. S., & Williams, J. P. 2008, ApJ, 686, L115
Clarke, C. J., Gendrin, A., & Sotomayor, M. 2001, MNRAS, 328, 485
Cleeves, L. I., Adams, F. C., & Bergin, E. A. 2013, ApJ, 772, 5
Cleeves, L. I., Bergin, E. A., Bethell, T. J., et al. 2011, ApJ, 743, L2
Collings, M. P., Anderson, M. A., Chen, R., et al. 2004, MNRAS, 354, 1133
Comerón, F. 2008, The Lupus Clouds, 295, ed. B. Reipurth
Comerón, F. 2012, A&A, 537, A97
Comerón, F., Reipurth, B., Henry, A., & Fernández, M. 2004, A&A, 417, 583
Comerón, F., Spezzi, L., & López Martí, B. 2009, A&A, 500, 1045
Cortes, S. R., Meyer, M. R., Carpenter, J. M., et al. 2009, ApJ, 697, 1305

Crida, A. & Morbidelli, A. 2007, MNRAS, 377, 1324
Crida, A., Morbidelli, A., & Masset, F. 2006, Icarus, 181, 587
Cuppen, H. M., van Dishoeck, E. F., Herbst, E., & Tielens, A. G. G. M. 2009, A&A, 508, 275
Currie, T. & Kenyon, S. J. 2009, AJ, 138, 703
Cutri, R. M., Skrutskie, M. F., van Dyk, S., et al. 2003, VizieR Online Data Catalog, 2246, 0
Dahm, S. E. 2008, AJ, 136, 521
D'Alessio, P., Hartmann, L., Calvet, N., et al. 2005, ApJ, 621, 461
de Juan Ovelar, M., Min, M., Dominik, C., et al. 2013, A&A, 560, A111
de Val-Borro, M., Artymowicz, P., D'Angelo, G., & Peplinski, A. 2007, A&A, 471, 1043
Dent, W. R. F., Greaves, J. S., & Coulson, I. M. 2005, MNRAS, 359, 663
Dent, W. R. F., Wyatt, M. C., Roberge, A., et al. 2014, Science, 343, 1490
Dipierro, G., Pinilla, P., Lodato, G., & Testi, L. 2015, MNRAS, 451, 5493
Dodson-Robinson, S. E. & Salyk, C. 2011, ApJ, 738, 131
Dong, R., Rafikov, R., Zhu, Z., et al. 2012, ApJ, 750, 161
Draine, B. T. 1978, ApJS, 36, 595
Draine, B. T. 2006, ApJ, 636, 1114
Draine, B. T. & Li, A. 2007, ApJ, 657, 810
Dullemond, C. P. & Dominik, C. 2004, A&A, 417, 159
Dullemond, C. P. & Dominik, C. 2005, A&A, 434, 971
Dullemond, C. P., Dominik, C., & Natta, A. 2001, ApJ, 560, 957
Dullemond, C. P. & Monnier, J. D. 2010, ARA&A, 48, 205
Dunham, M. M., Allen, L. E., Evans, II, N. J., et al. 2015, ArXiv e-prints
Dunham, M. M., Stutz, A. M., Allen, L. E., et al. 2014, Protostars and Planets VI, 195, eds. H. Beuther, R.S. Klessen, C.P. Dullemond, and T. Henning (University of Arizona Press)
Dunkin, S. K., Barlow, M. J., & Ryan, S. G. 1997, MNRAS, 290, 165
Dutrey, A., Guilloteau, S., & Guelin, M. 1997, A&A, 317, L55
Dutrey, A., Guilloteau, S., Piétu, V., et al. 2008, A&A, 490, L15
Dzib, S., Loinard, L., Mioduszewski, A. J., et al. 2010, ApJ, 718, 610
Dzib, S., Loinard, L., Rodríguez, L. F., Mioduszewski, A. J., & Torres, R. M. 2011, ApJ, 733, 71
Dzyurkevich, N., Flock, M., Turner, N. J., Klahr, H., & Henning, T. 2010, A&A, 515, A70
Edwards, S., Cabrit, S., Strom, S. E., et al. 1987, ApJ, 321, 473
Ehrenfreund, P. & Charnley, S. B. 2000, ARA&A, 38, 427
Emprechtinger, M., Caselli, P., Volgenau, N. H., Stutzki, J., & Wiedner, M. C. 2009, A&A, 493, 89
Enoch, M. L., Young, K. E., Glenn, J., et al. 2006, ApJ, 638, 293
Erickson, K. L., Wilking, B. A., Meyer, M. R., et al. 2015, AJ, 149, 103
Espaillat, C., Calvet, N., D'Alessio, P., et al. 2007, ApJ, 670, L135
Espaillat, C., D'Alessio, P., Hernández, J., et al. 2010, ApJ, 717, 441
Espaillat, C., Furlan, E., D'Alessio, P., et al. 2011, ApJ, 728, 49
Espaillat, C., Muzerolle, J., Najita, J., et al. 2014, Protostars and Planets VI, 497, eds. H. Beuther, R.S. Klessen, C.P. Dullemond, and T. Henning (University of Arizona Press)
Evans, II, N. J., Dunham, M. M., Jørgensen, J. K., et al. 2009, ApJS, 181, 321
Fedele, D., Bruderer, S., van Dishoeck, E. F., et al. 2013, A&A, 559, A77
Finkbeiner, D. P., Davis, M., & Schlegel, D. J. 1999, ApJ, 524, 867
Flaherty, K. M. & Muzerolle, J. 2010, ApJ, 719, 1733
Flaherty, K. M., Muzerolle, J., Rieke, G., et al. 2012, ApJ, 748, 71
Flock, M., Ruge, J. P., Dzyurkevich, N., et al. 2015, A&A, 574, A68
Flower, D. R. 1999, MNRAS, 305, 651
Follette, K. B., Grady, C. A., Swearingen, J. R., et al. 2015, ApJ, 798, 132
Follette, K. B., Tamura, M., Hashimoto, J., et al. 2013, ApJ, 767, 10

Forrest, W. J., Sargent, B., Furlan, E., et al. 2004, ApJS, 154, 443
Fuchs, G. W., Cuppen, H. M., Ioppolo, S., et al. 2009, A&A, 505, 629
Fukagawa, M., Tsukagoshi, T., Momose, M., et al. 2013, PASJ, 65, L14
Fung, J., Shi, J.-M., & Chiang, E. 2014, ApJ, 782, 88
Furlan, E., Hartmann, L., Calvet, N., et al. 2006, ApJS, 165, 568
Furlan, E., Luhman, K. L., Espaillat, C., et al. 2011, ApJS, 195, 3
Gammie, C. F. 1996, ApJ, 457, 355
Gammie, C. F. 2001, ApJ, 553, 174
Garaud, P. 2007, ApJ, 671, 2091
Garcia Lopez, R., Natta, A., Testi, L., & Habart, E. 2006, A&A, 459, 837
Garrod, R., Park, I. H., Caselli, P., & Herbst, E. 2006, Faraday Discussions, 133, 51
Garufi, A., Quanz, S. P., Avenhaus, H., et al. 2013, A&A, 560, A105
Geers, V. C., Augereau, J.-C., Pontoppidan, K. M., et al. 2006, A&A, 459, 545
Geers, V. C., Pontoppidan, K. M., van Dishoeck, E. F., et al. 2007, A&A, 469, L35
Geppert, W. D., Hamberg, M., Thomas, R. D., et al. 2006, Faraday Discussions, 133, 177
Ghez, A. M., McCarthy, D. W., Patience, J. L., & Beck, T. L. 1997, ApJ, 481, 378
Gorti, U., Dullemond, C. P., & Hollenbach, D. 2009, ApJ, 705, 1237
Gorti, U. & Hollenbach, D. 2004, ApJ, 613, 424
Gorti, U. & Hollenbach, D. 2008, ApJ, 683, 287
Goto, M., Usuda, T., Dullemond, C. P., et al. 2006, ApJ, 652, 758
Grady, C. A., Schneider, G., Sitko, M. L., et al. 2009, ApJ, 699, 1822
Gräfe, C. & Wolf, S. 2013, A&A, 552, A88
Guenther, E. W., Esposito, M., Mundt, R., et al. 2007, A&A, 467, 1147
Guilloteau, S., Dutrey, A., Piétu, V., & Boehler, Y. 2011, A&A, 529, A105
Guzmán, V. V., Goicoechea, J. R., Pety, J., et al. 2013, A&A, 560, A73
Hartmann, L., Calvet, N., Gullbring, E., & D'Alessio, P. 1998, ApJ, 495, 385
Harvey, P., Merín, B., Huard, T. L., et al. 2007, ApJ, 663, 1149
Harvey, P. M., Huard, T. L., Jørgensen, J. K., et al. 2008, ApJ, 680, 495
Hatchell, J., Terebey, S., Huard, T., et al. 2012, ApJ, 754, 104
Helled, R., Bodenheimer, P., Podolak, M., et al. 2014, Protostars and Planets VI, 643, eds. H. Beuther, R.S. Klessen, C.P. Dullemond, and T. Henning (University of Arizona Press)
Helou, G. & Walker, D. W., eds. 1988, Infrared astronomical satellite (IRAS) catalogs and atlases., Vol. 7
Henning, T., Il'In, V. B., Krivova, N. A., Michel, B., & Voshchinnikov, N. V. 1999, A&AS, 136, 405
Henning, T., Pfau, W., Zinnecker, H., & Prusti, T. 1993, A&A, 276, 129
Henning, T. & Semenov, D. 2013, Chemical Reviews, 113, 9016
Herbig, G. H. 1957, in IAU Symposium, Vol. 3, Non-stable stars, 3, ed. G. H. Herbig
Herbig, G. H. 1960, ApJS, 4, 337
Herbst, E. & van Dishoeck, E. F. 2009, ARA&A, 47, 427
Herczeg, G. J. & Hillenbrand, L. A. 2014, ApJ, 786, 97
Hernández, J., Hartmann, L., Megeath, T., et al. 2007, ApJ, 662, 1067
Hernández, J., Morales-Calderon, M., Calvet, N., et al. 2010, ApJ, 722, 1226
Hidaka, H., Watanabe, N., Shiraki, T., Nagaoka, A., & Kouchi, A. 2004, ApJ, 614, 1124
Hiraoka, K., Sato, T., Sato, S., et al. 2002, ApJ, 577, 265
Høg, E., Fabricius, C., Makarov, V. V., et al. 2000, A&A, 355, L27
Hogerheijde, M. R., Bergin, E. A., Brinch, C., et al. 2011, Science, 334, 338
Holland, W. S., Bintley, D., Chapin, E. L., et al. 2013, MNRAS, 430, 2513
Hollenbach, D. J., Yorke, H. W., & Johnstone, D. 2000, Protostars and Planets IV, 401, eds. H. Beuther, R.S. Klessen, C.P. Dullemond, and T. Henning (University of Arizona Press)
Huélamo, N., de Gregorio-Monsalvo, I., Macias, E., et al. 2015, A&A, 575, L5

Huélamo, N., Lacour, S., Tuthill, P., et al. 2011, A&A, 528, L7
Hughes, A. M., Andrews, S. M., Espaillat, C., et al. 2009, ApJ, 698, 131
Hughes, A. M., Andrews, S. M., Wilner, D. J., et al. 2010, AJ, 140, 887
Hughes, A. M., Wilner, D. J., Andrews, S. M., Qi, C., & Hogerheijde, M. R. 2011, ApJ, 727, 85
Hughes, A. M., Wilner, D. J., Qi, C., & Hogerheijde, M. R. 2008, ApJ, 678, 1119
Ilgner, M. & Nelson, R. P. 2006, A&A, 445, 205
Indebetouw, R., Mathis, J. S., Babler, B. L., et al. 2005, ApJ, 619, 931
Ingleby, L., Calvet, N., Bergin, E., et al. 2009, ApJ, 703, L137
Ioppolo, S., van Boheemen, Y., Cuppen, H. M., van Dishoeck, E. F., & Linnartz, H. 2011, MNRAS, 413, 2281
Ireland, M. J. & Kraus, A. L. 2008, ApJ, 678, L59
Isella, A., Carpenter, J. M., & Sargent, A. I. 2009, ApJ, 701, 260
Isella, A., Carpenter, J. M., & Sargent, A. I. 2010a, ApJ, 714, 1746
Isella, A., Natta, A., Wilner, D., Carpenter, J. M., & Testi, L. 2010b, ApJ, 725, 1735
Isella, A., Pérez, L. M., & Carpenter, J. M. 2012, ApJ, 747, 136
Isella, A., Pérez, L. M., Carpenter, J. M., et al. 2013, ApJ, 775, 30
Jensen, E. L. N., Mathieu, R. D., & Fuller, G. A. 1996, ApJ, 458, 312
Jewitt, D. C. & Luu, J. X. 2000, Protostars and Planets IV, 1201, eds. H. Beuther, R.S. Klessen, C.P. Dullemond, and T. Henning (University of Arizona Press)
Johansen, A., Oishi, J. S., Mac Low, M.-M., et al. 2007, Nature, 448, 1022
Johansen, A., Youdin, A., & Klahr, H. 2009, ApJ, 697, 1269
Jonkheid, B., Dullemond, C. P., Hogerheijde, M. R., & van Dishoeck, E. F. 2007, A&A, 463, 203
Jonkheid, B., Faas, F. G. A., van Zadelhoff, G.-J., & van Dishoeck, E. F. 2004, A&A, 428, 511
Jonkheid, B., Kamp, I., Augereau, J.-C., & van Dishoeck, E. F. 2006, A&A, 453, 163
Jørgensen, J. K., Harvey, P. M., Evans, II, N. J., et al. 2006, ApJ, 645, 1246
Jørgensen, J. K., Schöier, F. L., & van Dishoeck, E. F. 2004, A&A, 416, 603
Joy, A. H. 1945, ApJ, 102, 168
Kamp, I. & Dullemond, C. P. 2004, ApJ, 615, 991
Kanagawa, K. D., Muto, T., Tanaka, H., et al. 2015, ApJ, 806, L15
Kastner, J. H., Zuckerman, B., Hily-Blant, P., & Forveille, T. 2008, A&A, 492, 469
Kenyon, S. J., Gómez, M., & Whitney, B. A. 2008, Low Mass Star Formation in the Taurus-Auriga Clouds, 405, ed. B. Reipurth
Kenyon, S. J. & Hartmann, L. 1987, ApJ, 323, 714
Kenyon, S. J. & Hartmann, L. 1995, ApJS, 101, 117
Kessler-Silacci, J., Augereau, J.-C., Dullemond, C. P., et al. 2006, ApJ, 639, 275
Kim, K. H., Watson, D. M., Manoj, P., et al. 2009, ApJ, 700, 1017
Kirk, J. M., Ward-Thompson, D., Di Francesco, J., et al. 2009, ApJS, 185, 198
Klahr, H. H. & Bodenheimer, P. 2003, ApJ, 582, 869
Klahr, H. H. & Henning, T. 1997, Icarus, 128, 213
Kley, W. & Nelson, R. P. 2012, ARA&A, 50, 211
Kohler, R. & Leinert, C. 1998, A&A, 331, 977
Kóspál, Á., Moór, A., Juhász, A., et al. 2013, ApJ, 776, 77
Kovács, A. 2008, in Society of Photo-Optical Instrumentation Engineers (SPIE) Conference Series, Vol. 7020, 1
Kraus, A. L. & Hillenbrand, L. A. 2009, ApJ, 703, 1511
Kraus, A. L. & Ireland, M. J. 2012, ApJ, 745, 5
Kraus, A. L., Ireland, M. J., Martinache, F., & Lloyd, J. P. 2008, ApJ, 679, 762
Kretke, K. A. & Lin, D. N. C. 2007, ApJ, 664, L55
Lafrenière, D., Jayawardhana, R., Brandeker, A., Ahmic, M., & van Kerkwijk, M. H. 2008, ApJ, 683,

844
Lagrange, A.-M., Bonnefoy, M., Chauvin, G., et al. 2010, Science, 329, 57
Lahuis, F., van Dishoeck, E. F., Blake, G. A., et al. 2007, ApJ, 665, 492
Lawson, W. A., Lyo, A.-R., & Muzerolle, J. 2004, MNRAS, 351, L39
Lazzaro, D., Sicardy, B., Roques, F., & Greenberg, R. 1994, Icarus, 108, 59
Lebouteiller, V., Barry, D. J., Spoon, H. W. W., et al. 2011, ApJS, 196, 8
Leinert, C., Henry, T., Glindemann, A., & McCarthy, Jr., D. W. 1997, A&A, 325, 159
Lesur, G. & Papaloizou, J. C. B. 2009, A&A, 498, 1
Lin, D. N. C. & Papaloizou, J. 1979, MNRAS, 188, 191
Lique, F., Spielfiedel, A., Feautrier, N., et al. 2010, J. Chem. Phys., 132, 024303
Loinard, L., Torres, R. M., Mioduszewski, A. J., & Rodríguez, L. F. 2008, ApJ, 675, L29
Lommen, D., Maddison, S. T., Wright, C. M., et al. 2009, A&A, 495, 869
Lommen, D., Wright, C. M., Maddison, S. T., et al. 2007, A&A, 462, 211
Lommen, D. J. P., van Dishoeck, E. F., Wright, C. M., et al. 2010, A&A, 515, A77
Loren, R. B. 1989, ApJ, 338, 902
Lovelace, R. V. E., Li, H., Colgate, S. A., & Nelson, A. F. 1999, ApJ, 513, 805
Lubow, S. H. & D'Angelo, G. 2006, ApJ, 641, 526
Luhman, K. L. 2004, ApJ, 602, 816
Luhman, K. L. 2007, ApJS, 173, 104
Luhman, K. L., Allen, L. E., Allen, P. R., et al. 2008, ApJ, 675, 1375
Luhman, K. L., Allen, P. R., Espaillat, C., Hartmann, L., & Calvet, N. 2010, ApJS, 186, 111
Luhman, K. L. & Muench, A. A. 2008, ApJ, 684, 654
Luhman, K. L. & Rieke, G. H. 1999, ApJ, 525, 440
Lynden-Bell, D. & Pringle, J. E. 1974, MNRAS, 168, 603
Lyo, A.-R., Ohashi, N., Qi, C., Wilner, D. J., & Su, Y.-N. 2011, AJ, 142, 151
Lyra, W., Johansen, A., Klahr, H., & Piskunov, N. 2009, A&A, 493, 1125
Lyra, W. & Lin, M.-K. 2013, ApJ, 775, 17
Lyra, W., Turner, N. J., & McNally, C. P. 2015, A&A, 574, A10
Maaskant, K. M., Honda, M., Waters, L. B. F. M., et al. 2013, A&A, 555, A64
Makarov, V. V. 2007, ApJ, 670, 1225
Mamajek, E. E., Lawson, W. A., & Feigelson, E. D. 1999, ApJ, 516, L77
Manara, C., Fedele, D., & Herczeg, G. 2015, subm. to A&A
Manara, C. F., Testi, L., Natta, A., et al. 2014, A&A, 568, A18
Marino, S., Perez, S., & Casassus, S. 2015, ApJ, 798, L44
Marois, C., Macintosh, B., Barman, T., et al. 2008, Science, 322, 1348
Masset, F. 2000, A&AS, 141, 165
Mathews, G. S., Williams, J. P., & Ménard, F. 2012, ApJ, 753, 59
Mayama, S., Tamura, M., Hanawa, T., et al. 2010, Science, 327, 306
McClure, M. K., Furlan, E., Manoj, P., et al. 2010, ApJS, 188, 75
McElroy, D., Walsh, C., Markwick, A. J., et al. 2013, A&A, 550, A36
Meeus, G., Montesinos, B., Mendigutía, I., et al. 2012, A&A, 544, A78
Megeath, S. T., Gutermuth, R., Muzerolle, J., et al. 2012, AJ, 144, 192
Megeath, S. T., Hartmann, L., Luhman, K. L., & Fazio, G. G. 2005, ApJ, 634, L113
Meheut, H., Keppens, R., Casse, F., & Benz, W. 2012, A&A, 542, A9
Meheut, H., Lovelace, R. V. E., & Lai, D. 2013, MNRAS, 1, 698
Mendigutía, I., Mora, A., Montesinos, B., et al. 2012, A&A, 543, A59
Mendoza V., E. E. 1966, ApJ, 143, 1010
Merín, B., Brown, J. M., Oliveira, I., et al. 2010, ApJ, 718, 1200
Merín, B., Jørgensen, J., Spezzi, L., et al. 2008, ApJS, 177, 551

Min, M., Dullemond, C. P., Dominik, C., de Koter, A., & Hovenier, J. W. 2009, A&A, 497, 155
Miotello, A., Bruderer, S., & van Dishoeck, E. F. 2014, A&A, 572, A96
Monnier, J. D., Tannirkulam, A., Tuthill, P. G., et al. 2008, ApJ, 681, L97
Mooley, K., Hillenbrand, L., Rebull, L., Padgett, D., & Knapp, G. 2013, ApJ, 771, 110
Mulders, G. D., Paardekooper, S.-J., Panić, O., et al. 2013, A&A, 557, A68
Müller, H. S. P., Schlöder, F., Stutzki, J., & Winnewisser, G. 2005, Journal of Molecular Structure, 742, 215
Müller, H. S. P., Thorwirth, S., Roth, D. A., & Winnewisser, G. 2001, A&A, 370, L49
Mumma, M. J. & Charnley, S. B. 2011, ARA&A, 49, 471
Murillo, N. M., Lai, S.-P., Bruderer, S., Harsono, D., & van Dishoeck, E. F. 2013, A&A, 560, A103
Muto, T., Grady, C. A., Hashimoto, J., et al. 2012, ApJ, 748, L22
Muzerolle, J., Allen, L. E., Megeath, S. T., Hernández, J., & Gutermuth, R. A. 2010, ApJ, 708, 1107
Muzerolle, J., Flaherty, K., Balog, Z., et al. 2009, ApJ, 704, L15
Najita, J., Carr, J. S., & Mathieu, R. D. 2003, ApJ, 589, 931
Najita, J. R., Carr, J. S., Strom, S. E., et al. 2010, ApJ, 712, 274
Najita, J. R., Strom, S. E., & Muzerolle, J. 2007, MNRAS, 378, 369
Natta, A., Testi, L., Muzerolle, J., et al. 2004, A&A, 424, 603
Natta, A., Testi, L., & Randich, S. 2006, A&A, 452, 245
Nguyen, D. C., Brandeker, A., van Kerkwijk, M. H., & Jayawardhana, R. 2012, ApJ, 745, 119
Nuernberger, D., Chini, R., & Zinnecker, H. 1997, A&A, 324, 1036
Öberg, K. I., Guzmán, V. V., Furuya, K., et al. 2015, Nature, 520, 198
Öberg, K. I., Qi, C., Fogel, J. K. J., et al. 2010, ApJ, 720, 480
Öberg, K. I., Qi, C., Fogel, J. K. J., et al. 2011, ApJ, 734, 98
O'Dell, C. R., Wen, Z., & Hu, X. 1993, ApJ, 410, 696
Ohashi, N. 2008, Ap&SS, 313, 101
Oke, J. B. 1990, AJ, 99, 1621
Oliveira, I., Merín, B., Pontoppidan, K. M., & van Dishoeck, E. F. 2013, ApJ, 762, 128
Oliveira, I., Merín, B., Pontoppidan, K. M., et al. 2009, ApJ, 691, 672
Oliveira, I., Pontoppidan, K. M., Merín, B., et al. 2010, ApJ, 714, 778
Olofsson, J., Benisty, M., Augereau, J.-C., et al. 2011, A&A, 528, L6
Olofsson, J., Szűcs, L., Henning, T., et al. 2013, A&A, 560, A100
Ortiz-León, G. N., Loinard, L., Mioduszewski, A. J., et al. 2015, ApJ, 805, 9
Owen, J. E. & Clarke, C. J. 2012, MNRAS, 426, L96
Owen, J. E., Ercolano, B., & Clarke, C. J. 2011, MNRAS, 412, 13
Padgett, D. L., Cieza, L., Stapelfeldt, K. R., et al. 2006, ApJ, 645, 1283
Padgett, D. L., Rebull, L. M., Stapelfeldt, K. R., et al. 2008, ApJ, 672, 1013
Partnership, A., Brogan, C. L., Pérez, L. M., et al. 2015, ApJ, 808, L3
Pascucci, I., Hollenbach, D., Najita, J., et al. 2007, ApJ, 663, 383
Pérez, L. M., Carpenter, J. M., Chandler, C. J., et al. 2012, ApJ, 760, L17
Pérez, L. M., Isella, A., Carpenter, J. M., & Chandler, C. J. 2014, ApJ, 783, L13
Perez, S., Casassus, S., Ménard, F., et al. 2015, ApJ, 798, 85
Persson, M. V., Jørgensen, J. K., & van Dishoeck, E. F. 2012, A&A, 541, A39
Peterson, D. E., Caratti o Garatti, A., Bourke, T. L., et al. 2011, ApJS, 194, 43
Pickles, A. J. 1998, PASP, 110, 863
Piétu, V., Dutrey, A., & Guilloteau, S. 2007, A&A, 467, 163
Piétu, V., Dutrey, A., Guilloteau, S., Chapillon, E., & Pety, J. 2006, A&A, 460, L43
Piétu, V., Guilloteau, S., & Dutrey, A. 2005, A&A, 443, 945
Pilbratt, G. L., Riedinger, J. R., Passvogel, T., et al. 2010, A&A, 518, L1
Pinilla, P., Benisty, M., & Birnstiel, T. 2012a, A&A, 545, A81

Pinilla, P., Benisty, M., Birnstiel, T., et al. 2014, A&A, 564, A51
Pinilla, P., Birnstiel, T., Ricci, L., et al. 2012b, A&A, 538, A114
Pinilla, P., de Juan Ovelar, M., Ataiee, S., et al. 2015a, A&A, 573, A9
Pinilla, P., van der Marel, N., Perez, L., et al. 2015b, A&A, in rev.
Pinte, C., Ménard, F., Duchêne, G., & Bastien, P. 2006, A&A, 459, 797
Poglitsch, A., Waelkens, C., Geis, N., et al. 2010, A&A, 518, L2
Pontoppidan, K. M., Blake, G. A., van Dishoeck, E. F., et al. 2008, ApJ, 684, 1323
Pott, J.-U., Perrin, M. D., Furlan, E., et al. 2010, ApJ, 710, 265
Prato, L., Greene, T. P., & Simon, M. 2003, ApJ, 584, 853
Qi, C., Öberg, K. I., & Wilner, D. J. 2013a, ApJ, 765, 34
Qi, C., Öberg, K. I., Wilner, D. J., & Rosenfeld, K. A. 2013b, ApJ, 765, L14
Quanz, S. P. 2015, Ap&SS, 357, 148
Quanz, S. P., Amara, A., Meyer, M. R., et al. 2015, ApJ, 807, 64
Quanz, S. P., Amara, A., Meyer, M. R., et al. 2013, ApJ, 766, L1
Quanz, S. P., Schmid, H. M., Geissler, K., et al. 2011, ApJ, 738, 23
Rabli, D. & Flower, D. R. 2010, MNRAS, 406, 95
Raettig, N., Klahr, H., & Lyra, W. 2015, ApJ, 804, 35
Raettig, N., Lyra, W., & Klahr, H. 2013, ApJ, 765, 115
Ratzka, T., Köhler, R., & Leinert, C. 2005, A&A, 437, 611
Raymond, S. N., Kokubo, E., Morbidelli, A., Morishima, R., & Walsh, K. J. 2014, Protostars and Planets VI, 595, eds. H. Beuther, R.S. Klessen, C.P. Dullemond, and T. Henning (University of Arizona Press)
Rebollido, I., Merín, B., Ribas, Á., et al. 2015, ArXiv e-prints
Rebull, L. M., Padgett, D. L., McCabe, C.-E., et al. 2010, ApJS, 186, 259
Regály, Z., Juhász, A., Sándor, Z., & Dullemond, C. P. 2012, MNRAS, 419, 1701
Reggiani, M., Quanz, S. P., Meyer, M. R., et al. 2014, ApJ, 792, L23
Revéret, V., André, P., Le Pennec, J., et al. 2014, in Society of Photo-Optical Instrumentation Engineers (SPIE) Conference Series, Vol. 9153, 5
Ribas, Á., Merín, B., Bouy, H., et al. 2013, A&A, 552, A115
Ricci, L., Testi, L., Natta, A., & Brooks, K. J. 2010a, A&A, 521, A66
Ricci, L., Testi, L., Natta, A., et al. 2010b, A&A, 512, A15
Rice, W. K. M., Armitage, P. J., Wood, K., & Lodato, G. 2006, MNRAS, 373, 1619
Rigliaco, E., Pascucci, I., Duchene, G., et al. 2015, ApJ, 801, 31
Rodmann, J., Henning, T., Chandler, C. J., Mundy, L. G., & Wilner, D. J. 2006, A&A, 446, 211
Romero, G. A., Schreiber, M. R., Cieza, L. A., et al. 2012, ApJ, 749, 79
Rosenfeld, K. A., Andrews, S. M., Wilner, D. J., Kastner, J. H., & McClure, M. K. 2013, ApJ, 775, 136
Rosenfeld, K. A., Chiang, E., & Andrews, S. M. 2014, ApJ, 782, 62
Rosotti, G. P., Ercolano, B., Owen, J. E., & Armitage, P. J. 2013, MNRAS, 430, 1392
Salyk, C., Blake, G. A., Boogert, A. C. A., & Brown, J. M. 2007, ApJ, 655, L105
Salyk, C., Blake, G. A., Boogert, A. C. A., & Brown, J. M. 2009, ApJ, 699, 330
Salyk, C., Herczeg, G. J., Brown, J. M., et al. 2013, ApJ, 769, 21
Sargent, A. I. & Beckwith, S. 1987, ApJ, 323, 294
Schisano, E., Covino, E., Alcalá, J. M., et al. 2009, A&A, 501, 1013
Schöier, F. L., van der Tak, F. F. S., van Dishoeck, E. F., & Black, J. H. 2005, A&A, 432, 369
Schuller, F. 2012, in Society of Photo-Optical Instrumentation Engineers (SPIE) Conference Series, Vol. 8452, 1
Semenov, D. & Wiebe, D. 2011, ApJS, 196, 25
Shakura, N. I. & Sunyaev, R. A. 1973, A&A, 24, 337
Shu, F. H., Adams, F. C., & Lizano, S. 1987, ARA&A, 25, 23
Sicilia-Aguilar, A., Bouwman, J., Juhász, A., et al. 2009, ApJ, 701, 1188

Sicilia-Aguilar, A., Henning, T., Juhász, A., et al. 2008, ApJ, 687, 1145
Siess, L., Dufour, E., & Forestini, M. 2000, A&A, 358, 593
Silverstone, M. D., Meyer, M. R., Mamajek, E. E., et al. 2006, ApJ, 639, 1138
Siringo, G., Kreysa, E., De Breuck, C., et al. 2010, The Messenger, 139, 20
Siringo, G., Kreysa, E., Kovács, A., et al. 2009, A&A, 497, 945
Smith, B. A. & Terrile, R. J. 1984, Science, 226, 1421
Spezzi, L., Alcalá, J. M., Covino, E., et al. 2008, ApJ, 680, 1295
Spezzi, L., Vernazza, P., Merín, B., et al. 2011, ApJ, 730, 65
Strom, K. M., Strom, S. E., Edwards, S., Cabrit, S., & Skrutskie, M. F. 1989, AJ, 97, 1451
Tang, Y.-W., Guilloteau, S., Piétu, V., et al. 2012, A&A, 547, A84
Testi, L., Birnstiel, T., Ricci, L., et al. 2014, Protostars and Planets VI, 339, eds. H. Beuther, R.S. Klessen, C.P. Dullemond, and T. Henning (University of Arizona Press)
Thalmann, C., Grady, C. A., Goto, M., et al. 2010, ApJ, 718, L87
Thalmann, C., Mulders, G. D., Hodapp, K., et al. 2014, A&A, 566, A51
Thi, W. F., Ménard, F., Meeus, G., et al. 2013, A&A, 557, A111
Thi, W.-F., van Zadelhoff, G.-J., & van Dishoeck, E. F. 2004, A&A, 425, 955
Tielens, A. G. G. M. & Hagen, W. 1982, A&A, 114, 245
Toomre, A. 1964, ApJ, 139, 1217
Torres, C. A. O., Quast, G. R., Melo, C. H. F., & Sterzik, M. F. 2008, Young Nearby Loose Associations, 757, ed. B. Reipurth
Troscompt, N., Faure, A., Wiesenfeld, L., Ceccarelli, C., & Valiron, P. 2009, A&A, 493, 687
Ubach, C., Maddison, S. T., Wright, C. M., et al. 2012, MNRAS, 425, 3137
Valenti, J. A., Basri, G., & Johns, C. M. 1993, AJ, 106, 2024
van Boekel, R., Dullemond, C. P., & Dominik, C. 2005, A&A, 441, 563
van der Marel, N., Pinilla, P., Tobin, J., et al. 2015a, ApJL, in press
van der Marel, N., van Dishoeck, E., Bruderer, S., et al. 2015b, subm. to A&A
van der Marel, N., van Dishoeck, E. F., Bruderer, S., et al. 2013, Science, 340, 1199
van der Marel, N., van Dishoeck, E. F., Bruderer, S., Pérez, L., & Isella, A. 2015c, A&A, 579, A106
van der Marel, N., van Dishoeck, E. F., Bruderer, S., & van Kempen, T. A. 2014, A&A, 563, A113
van der Plas, G., van den Ancker, M. E., Acke, B., et al. 2009, A&A, 500, 1137
van der Tak, F. F. S., van Dishoeck, E. F., & Caselli, P. 2000, A&A, 361, 327
van Dishoeck, E. F. & Black, J. H. 1988, ApJ, 334, 771
van Dishoeck, E. F., Jonkheid, B., & van Hemert, M. C. 2006, Faraday Discussions, 133, 231
van Kempen, T. A., van Dishoeck, E. F., Salter, D. M., et al. 2009, A&A, 498, 167
van Zadelhoff, G.-J., van Dishoeck, E. F., Thi, W.-F., & Blake, G. A. 2001, A&A, 377, 566
Varnière, P. & Tagger, M. 2006, A&A, 446, L13
Vasyunin, A. I., Wiebe, D. S., Birnstiel, T., et al. 2011, ApJ, 727, 76
Verhoeff, A. P., Min, M., Pantin, E., et al. 2011, A&A, 528, A91
Vicente, S., Merín, B., Hartung, M., et al. 2011, A&A, 533, A135
Visser, R., van Dishoeck, E. F., & Black, J. H. 2009, A&A, 503, 323
Vorobyov, E. I. & Basu, S. 2008, ApJ, 676, L139
Wahhaj, Z., Cieza, L., Koerner, D. W., et al. 2010, ApJ, 724, 835
Walsh, C., Juhász, A., Pinilla, P., et al. 2014, ApJ, 791, L6
Walsh, C., Millar, T. J., & Nomura, H. 2013, ApJ, 766, L23
Walsh, C., Nomura, H., Millar, T. J., & Aikawa, Y. 2012, ApJ, 747, 114
Walter, F. M. & Kuhi, L. V. 1981, ApJ, 250, 254
Watanabe, N. & Kouchi, A. 2002, ApJ, 571, L173
Watanabe, N., Nagaoka, A., Shiraki, T., & Kouchi, A. 2004, ApJ, 616, 638
Weidenschilling, S. J. 1977, MNRAS, 180, 57

Weingartner, J. C. & Draine, B. T. 2001, ApJ, 548, 296
Whipple, F. L. 1972, in From Plasma to Planet, 211, ed. A. Elvius, (Interscience)
White, R. J. & Basri, G. 2003, ApJ, 582, 1109
White, R. J. & Ghez, A. M. 2001, ApJ, 556, 265
Wichmann, R., Krautter, J., Covino, E., et al. 1997, A&A, 320, 185
Wilking, B. A., Meyer, M. R., Robinson, J. G., & Greene, T. P. 2005, AJ, 130, 1733
Williams, J. P. & Cieza, L. A. 2011, ARA&A, 49, 67
Wilson, T. L. & Rood, R. 1994, ARA&A, 32, 191
Windmark, F., Birnstiel, T., Güttler, C., et al. 2012, A&A, 540, A73
Winston, E., Megeath, S. T., Wolk, S. J., et al. 2009, AJ, 137, 4777
Woitke, P., Kamp, I., & Thi, W.-F. 2009, A&A, 501, 383
Wolf, S. & Klahr, H. 2002, ApJ, 578, L79
Woodall, J., Agúndez, M., Markwick-Kemper, A. J., & Millar, T. J. 2007, A&A, 466, 1197
Wright, E. L., Eisenhardt, P. R. M., Mainzer, A. K., et al. 2010, AJ, 140, 1868
Wyatt, M. C. 2003, ApJ, 598, 1321
Xie, J.-W., Payne, M. J., Thébault, P., Zhou, J.-L., & Ge, J. 2010, ApJ, 724, 1153
Yamamura, I., Makiuti, S., Ikeda, N., et al. 2010, VizieR Online Data Catalog, 2298, 0
Young, K. E., Young, C. H., Lai, S.-P., Dunham, M. M., & Evans, II, N. J. 2015, AJ, 150, 40
Zacharias, N., Monet, D. G., Levine, S. E., et al. 2005, VizieR Online Data Catalog, 1297, 0
Zhang, K., Isella, A., Carpenter, J. M., & Blake, G. A. 2014, ApJ, 791, 42
Zhu, Z., Nelson, R. P., Dong, R., Espaillat, C., & Hartmann, L. 2012, ApJ, 755, 6
Zhu, Z., Nelson, R. P., Hartmann, L., Espaillat, C., & Calvet, N. 2011, ApJ, 729, 47
Zhu, Z. & Stone, J. M. 2014, ApJ, 795, 53

Nederlandse samenvatting

Gas en stof in planeet-vormende schijven

"We leven in een heelal waarvan we de leeftijd amper kunnen berekenen, omringd door sterren waarvan we de afstanden niet weten, gevuld met materie die we niet kunnen identificeren, dat fysische wetten volgt die we niet werkelijk begrijpen." - Bill Bryson: 'Een kleine geschiedenis van bijna alles'

Sinds het begin van de mensheid hebben we omhoog gekeken naar de hemel en zich afgevraagd waar we vandaan komen. Zowel religie als filosofie hebben een belangrijke rol gespeeld om de zaken te verklaren die we niet konden begrijpen. De studie van de bewegingen en verschijnselen aan de hemel vanuit het menselijk perspectief geeft slechts een beperkt beeld van wat er in het heelal gebeurt. Het is dus al helemaal niet voor te stellen dat er een connectie bestaat tussen de aarde waarop wij leven, de zon die elke dag op- en ondergaat en de twinkelende puntjes aan de nachthemel. De rode draad in de historie van de sterrenkunde is de vraag wat de plaats van mensheid (en hun thuisplaneet) in het heelal nu eigenlijk is: van Aristarchos die voor het eerst suggereerde dat de aarde in plaats van de zon het middelpunt van het heelal was, Galileo's ontdekking van manen rond Jupiter, William Herschel die de zon definieerde als een gewone ster ergens in de buitenwijken van de Melkweg, tot exoplaneten die niet bepaald de 'perfecte' configuratie van ons zonnestelsel volgen. Met de jaren werden ideologieën en filosofische theorieën overgenomen door wetenschap en empirisch onderzoek. Ook nu nog worden nieuwe ontdekkingen continu ingehaald door de kennis van dat moment, waarbij nieuwe problemen en uitdagingen voor wetenschappers worden gecreëerd en nieuwe ideeën onderzocht.

Een van de meest noemenswaardige revoluties in de sterrenkunde was het idee dat sterren en planeten niet voor altijd bestaan, maar dat ze geboren worden, leven en sterven. Een van de aanleidingen voor dit idee was de ontdekking van kernfusie als belangrijkste energiebron voor sterren in het begin van de 20^e eeuw, waarmee direct duidelijk werd dat er een begin en einde van het fusieproces moet zijn, simpelweg door de beschikbaarheid van brandstof. De hypothese van de Zonnenevel, die stelt dat sterren en planeten op een zeker moment worden gevormd, was overigens al in de 18^e eeuw ontwikkeld, onder andere door Emanuel Swedenborg en Immanuel Kant. Het is verrassend dat het idee van een oneindig, niet-veranderlijk heelal zo lang als de standaard werd gezien, terwijl we in het dagelijks leven continu omringd zijn door bewijzen van leven en dood. Dit komt opnieuw door de beperkingen van het menselijk perspectief: de ruimte- en tijdschalen waarin gebeurtenissen plaatsvinden in het heelal, gaan ver voorbij ons voorstellingsvermogen. Zelfs als we hier getallen en eenheden aan vastplakken is het lastig om een gevoel te krijgen voor hoe het er werkelijk aan toe gaat. Daarom werd sterrenkunde voor lange tijd gedreven door de ontwikkeling van de natuurkunde.

Met de technologische ontwikkelingen en exponentiële toename van nieuwe telescopen en instrumenten in de tweede helft van de 20^e eeuw werden waarnemingen niet meer alleen een bevestiging van bestaande theorieën, maar een drijfveer voor het ontwikkelen van nieuwe theorieën. De komst van elke nieuwe telescoop onthulde nieuwe objecten, nieuwe structuren, nieuwe vooruitzichten voor ons begrip van het heelal. Ons inzicht in de vorming van sterren, schijven en planeten is enorm toegenomen met telescopen zoals *IRAS*, *Spitzer*, *Herschel* in het infrarood, en JCMT, IRAM, APEX en SMA op (sub)millimeter golflengtes, waar deze

objecten het meeste licht uitzenden.

In dit proefschrift zijn we met name geïnteresseerd in de protoplanetaire schijven van gas en stof rond jonge sterren, aangezien hierin de planeten worden gevormd. De focus ligt op zogenaamde transitieschijven: schijven met een gat in het binnenste deel van de stofschijf (zie Figuur 10.2). De belangrijkste vraag waarop een antwoord wordt gezocht is: wat is de rol van transitieschijven in het proces van planeetvorming en wat vertellen ze ons over jonge planeten?

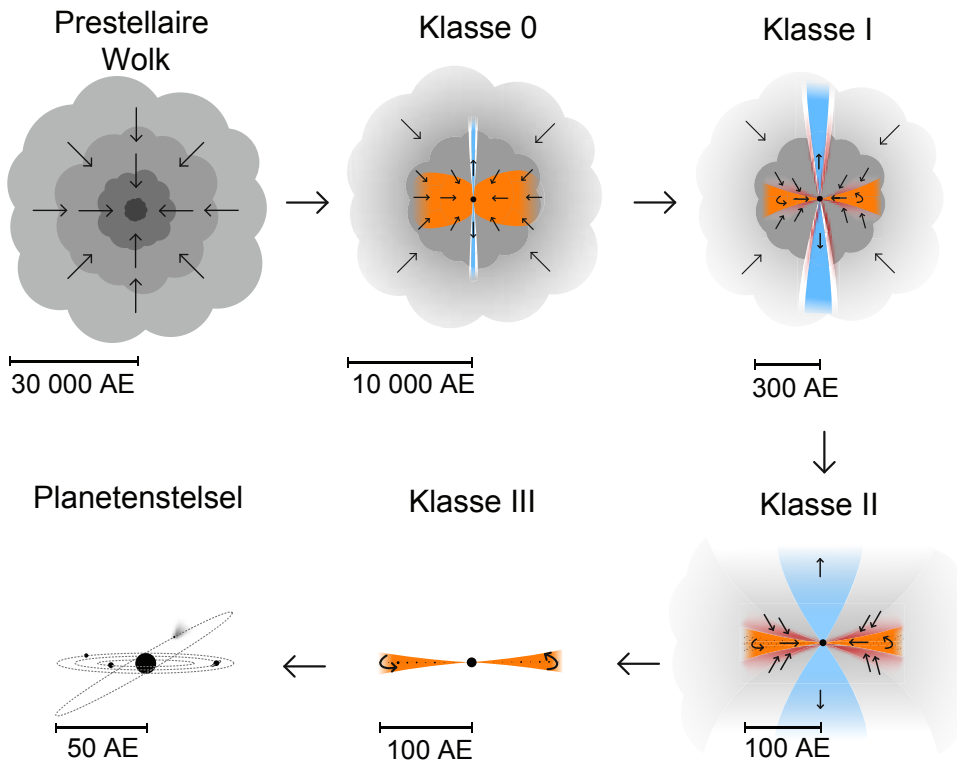
ALMA, de Atacama Large Millimeter/submillimeter Array, speelt een cruciale rol in het beantwoorden van deze vraag. ALMA komt voort uit een wereldwijd samenwerkingsproject en bestaat uit een groep van 66 telescopen werkzaam op (sub)millimeter golflengtes. De signalen van de gehele groep worden met elkaar worden verbonden in een zogenaamde synthese telescoop. Het is gebouwd op het Chajnantorplateau op 5000 meter hoogte in de Atacamawoestijn in Chili. Zowel de gevoeligheid als de spatiële resolutie zijn tot twee ordes van grootte beter dan vorige millimeter arrays. Nederland is een belangrijke partner in het ALMA-project: de ALMA Band 9 ontvangers, die op hoge frequentie opereren, zijn ontworpen en gebouwd door NOVA (Nederlandse Onderzoekschool Voor Astronomie) in samenwerking met SRON (Stichting Ruimte Onderzoek Nederland). ALMA begon haar waarnemingen in 2011 met een gedeelte van de array, en heeft in de jaren erna haar capaciteiten verder uitvergroot. ALMA geeft ons een kijkje in de kraamkamers van de planeten met scherpere details dan ooit tevoren, en stelt ons in staat om meer vragen te beantwoorden over onze oorsprong dan we ons ooit hadden kunnen voorstellen.

Sterren en schijven

Voor we ingaan op de vraagstukken van dit proefschrift volgt eerst een korte beschrijving van wat bekend is over de vorming van sterren en planeten. Planeten worden gevormd in protoplanetaire schijven rond jonge sterren. Deze schijven zijn een natuurlijk gevolg van stervorming zelf. Een ster wordt gevormd door de gravitationele instorting van een wolk van gas en stof. Er is een kleine rotatie in de wolk, en door het behoud van hoekimpuls vormt zich dan een afgeplatte, roterende structuur ('schijf') rond de ster, net als bij het ronddraaien van een deegbal voor een pizza. De wolk verdwijnt binnen een miljoen jaar en de schijf ontwikkelt zich over een tijdspanne van enkele miljoenen jaren tot een planetenstelsel rond de ster. Dit proces wordt geïllustreerd in Figuur 10.1.

Een van de grote raadsels is hoe planeten gevormd worden in de schijf. Er worden steeds meer nieuwe exoplaneten (planeten rond andere sterren) ontdekt, met name door de *Kepler* satelliet, en de teller staat nu op zo'n 2000 planeten. Dit betekent dat planeten zeker geen zeldzaamheid zijn en dus relatief eenvoudig moeten vormen. Toch hebben de huidige theorieën van planeetvorming moeite om waarnemingen te verklaren: door een lokale *gravitationele instabiliteit* in de schijf kunnen Jupiter-achtige planeten weliswaar snel worden gevormd, maar de gemeten massa's van schijven zijn niet hoog genoeg om dit proces te laten plaatsvinden. Volgens een andere theorie, waar *stofdeeltjes samenklonteren* en vervolgens groeien tot gasplaneten via *kern-accretie*, heeft planeetvorming een veel langere tijdsduur nodig dan realistisch is voor de levensduur van een schijf.

Het planeetvormingsproces is te traag om direct te volgen en objecten met groottes tussen ~10 cm en 10000 km kunnen niet direct worden waargenomen. Daarom bestuderen we in plaats daarvan de structuur van het gas en stof in de schijven waarin deze planeten gevormd worden om de relevante fysische processen beter te begrijpen. Stof kan worden waargenomen als continuum straling: thermische straling als gevolg van de opwarming van het stof door



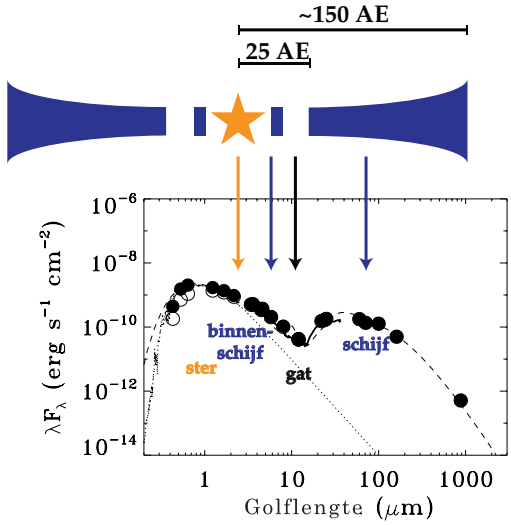
Figuur 10.1: *Het evolutieproces van ster- en planeetvorming. Een wolk van gas en stof stort in onder haar eigen zwaartekracht tot een jonge ster, waarbij ook een roterende schijf rond de ster wordt gevormd. Na het verdwijnen van de wolk evolueert de schijf tot een planetenstelsel. Figuur door Magnus Persson.*

de centrale ster, waarbij het stof dichtbij de ster heter is en dus op kortere golflengtes straalt dan het stof verder naar buiten. Gas kan worden waargenomen door middel van moleculaire lijnen, waarvoor een veel hogere gevoeligheid nodig is. Hierin ligt de kracht van ALMA: niet alleen kan ALMA in detail inzoomen op deze schijven, maar ook zowel gas als stof detecteren. De focus ligt op het materiaal dichtbij de ster, in het 'stofgat' van de transitieschijven. Een mogelijke verklaring voor de aanwezigheid voor dit gat is dat een planeet zich heeft gevormd in het binnenste deel van de schijf en daarbij zijn baan heeft schoongeveegd. Om dit scenario te bevestigen moet de structuur van zowel het gas als het stof bestudeerd worden.

Dit proefschrift

In dit proefschrift bestuderen we een aantal transitieschijven met ALMA waarnemingen in gas en stof met hoge spatiële resolutie (~0.25 boogseconden of 30 AE [4], een fractie van de totale

[4] AE = astronomische eenheid, afstand zon-aarde of 150 miljoen kilometer



Figuur 10.2: *Een schematische weergave van een transitieschijf met de verschillende onderdelen en de golflengtes waar deze licht uitstralen in een Spectraal Energie Diagram (SED). De ster straalt in het optisch en nabij-infrarood, een binnenschijf kan worden herkend als nabij-infrarode emissie bovenop de steremissie, het stofgat als een gebrek aan middel-infrarood emissie en het stof in het buitenste deel van de schijf straalt in het ver-infrarood tot millimeter golflengtes.*

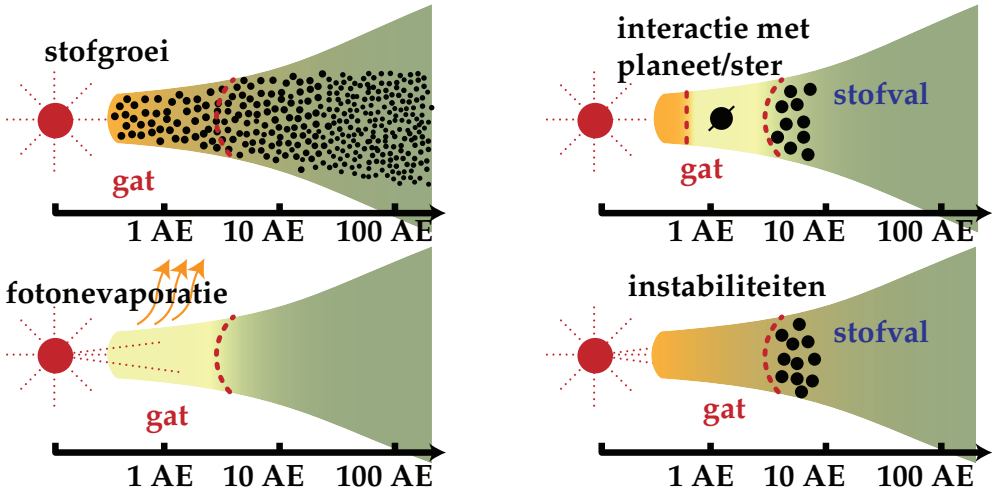
grootte van de schijf). De waarnemingen zijn genomen gedurende ALMA Early Science, de eerste jaren dat ALMA in operatie was, met een beperkt aantal basislijnen van minder dan 1 km (hoe langer de basislijnen, hoe scherper de details van de waarnemingen). De waarnemingen bestaan uit submillimeter continuum emissie van het stof en CO rotationele lijnen. De CO-emissie kon worden geïnterpreteerd als een maat van de gasdichtheid met behulp van de recent geschreven code DALI (Bruderer 2013). Met de waarnemingen van het gas binnen het gat kunnen de verschillende scenario's voor de oorsprong van het gat worden onderscheiden (Figuur 10.3).

De inhoud van de hoofdstukken kan als volgt worden samengevat.

- In Hoofdstuk 2 wordt de ontdekking van een azimuthaal asymmetrische stofval in de Oph IRS 48 schijf gepresenteerd. Het millimeterstof is geconcentreerd aan één kant van de schijf, terwijl de kleinere micrometer stofdeeltjes en het gas een ringstructuur vormen. Een stofval werd al decennia voorspeld door theoreten als een mogelijke oplossing voor het trage stofgroei probleem in schijven, maar was nog niet eerder waargenomen. De azimuthale structuur wordt gemodelleerd als stof gevangen in een vortex, die is gevormd door een Rossby instabiliteit aan de rand van een gat dat is ontstaan door een jonge planeet.

- In Hoofdstuk 3 en 4 wordt het stofvalscenario verder bestudeerd en bevestigd aan de hand van centimeter-waarnemingen in Oph IRS 48 en de combinatie van millimeter-waarnemingen van twee andere transitieschijven.

- In Hoofdstuk 5 tot en met 7 worden CO-waarnemingen van verscheidene transitieschijven gepresenteerd. Alle schijven laten zien dat er gas in het stofgat aanwezig is, waarbij de structuur suggereert dat reuzenplaneten verantwoordelijk zijn voor het gat.



Figuur 10.3: *Mechanismes voor het schoonvegen van het gat in een stofschijf. Het gas is weergegeven in geel, het stof met zwarte cirkels.* **Linksboven:** *toename stofgroei in het gat, waarbij de gasdichtheid hetzelfde blijft als in de oorspronkelijke schijf.* **Linksonder:** *fotonevaporatief schoonvegen, waarbij zowel het gas als stof tegelijkertijd van binnen naar buiten worden weggeblazen.* **Rechtsboven:** *schoonvegen door een tweede object (ster of planeet), waarbij de gasdichtheid binnen het gat lager wordt en de grote stofdeeltjes gevangen worden in een stofval aan de rand.* **Rechtsonder:** *instabiliteiten door bijvoorbeeld een viscositeit- of entropiegradiënt creëren een stofval, de gasdichtheid verandert niet ten opzichte van de oorspronkelijke schijf. Figuur gebaseerd op tekening door Simon Bruderer.*

- Hoofdstuk 8 bespreekt de chemische complexiteit van de Oph IRS 48 schijf aan de hand van een detectie van warm formaldehyde en limieten van verschillende andere moleculen.

- Ten slotte wordt in Hoofdstuk 9 een brede studie van bijna 200 transitieschijven gepresenteerd aan de hand van *Spitzer*, *Herschel* en submillimeter-waarnemingen, waarmee SEDs (Spectrale Energie Diagram) zijn samengesteld en geanalyseerd. Met dit uniforme sample worden algemene trends en eigenschappen van transitieschijven bepaald.

Toekomstperspectief

In de komende jaren zal ALMA waarnemingen gaan doen met basislijnen tot wel 16 km lengte. Dit betekent dat details in schijven tot op het niveau van enkele astronomische eenheden zichtbaar zullen worden. De verwachting is dat dit tot nog beter begrip zal leiden van de structuur van het gas en stof. Bovendien zullen transitieschijven met kleinere gaten kunnen worden bestudeerd, die wellicht een andere oorsprong hebben dan planeten. Ook zal het mogelijk zijn om exoplaneten in wording direct waar te nemen als ze een circumplanetaire schijf om zich heen hebben. De hogere gevoeligheid van de volledige array van ALMA zal ons in staat stellen om meer complexe moleculen waar te nemen, die de bouwstenen vormen van leven hier en op andere planeten.

Ook andere (toekomstige) telescopen en instrumenten zullen naar verwachting belangrijke bijdragen leveren aan de studies van protoplanetaire schijven en de studie van de vorming van planeten: de EVLA geeft inzicht in de verdeling van grotere stofdeeltjes, VLT-SPHERE in die van de kleinere stofdeeltjes, wat cruciaal is voor het begrijpen van de rol van stofvallen in schijven. Infraroodwaarnemingen met onder andere de *James Webb Space Telescope*, de *European Extremely Large Telescope* en de *Thirty Meter Telescope* geven verder inzicht in het hete, binnenste deel van de schijven, waar men verwacht dat de meeste planeten zich vormen.

List of publications

Refereed Publications

1. **van der Marel, N.**; van Dishoeck, E.F.; Bruderer, S.; Andrews, S.M.; Pontoppidan, K.M.; Herczeg, G.J.; van Kempen, T.; Miotello, A. *Resolved gas cavities in transitional disks inferred from CO isotopologues with ALMA.* subm. to A&A. **(Chapter 7)**

2. Pinilla, P.; **van der Marel, N.**; Pérez, L.M.; van Dishoeck, E.F.; Andrews, S.M.; Birnstiel, T.; Herczeg, G.J.; Pontoppidan, K.M.; van Kempen, T. *Testing particle trapping in transition disks with ALMA.* A&A, in revision. **(Chapter 4)**

3. **van der Marel, N.**; Pinilla, P.; J. Tobin; T. van Kempen; S. Andrews; L. Ricci; T. Birnstiel. *A concentration of centimeter-sized grains in the Oph IRS 48 dust trap.* ApJL, in press (arXiv: 1508.01003). **(Chapter 3)**

4. Rapson, V. A.; Sargent, B.; Sacco, G.; Kastner, J. H.; Wilner, D.; Rosenfeld, K.; Andrews, S.; Herczeg, G.; **van der Marel, N.**. *A Combined Spitzer and Herschel Infrared Study of Gas and Dust in the Circumbinary Disk Orbiting V4046 Sgr.* ApJ, in press (arXiv: 1507.05574).

5. van Kempen, T. A.; Hogerheijde, M. R.; van Dishoeck, E. F.; Kristensen, L. E.; Belloche, A.; Klaassen, P. D.; Leurini, S.; San Jose-Garcia, I.; Aykutalp, A.; Choi, Y.; Endo, A.; Frieswijk, W.; Harsono, D.; Karska, A.; Koumpia, E.; **van der Marel, N.**; Nagy, Z.; Pérez-Beaupuits, J. P.; Risacher, C.; van Weeren, R. J.; Wyrowski, F.; Yildiz, U. A.; Güsten, R.; Boland, W.; Baryshev, A. *Outflow forces in intermediate mass star formation.* A&A, in press (arXiv: 1507.01973).

6. **van der Marel, N.**; van Dishoeck, E. F.; Bruderer, S.; Perez, L. M.; Isella, A. *Gas density drops inside dust cavities of transitional disks around young stars observed with ALMA.* 2015, A&A, 579, 106. **(Chapter 6)**

7. Yildiz, U. A.; Kristensen, L. E.; van Dishoeck, E. F.; Hogerheijde, M. R.; Karska, A.; Belloche, A.; Endo, A.; Frieswijk, W.; Güsten, R.; van Kempen, T. A.; Leurini, S.; Nagy, Z.; Pérez-Beaupuits, J. P.; Risacher, C.; **van der Marel, N.**; van Weeren, R. J.; Wyrowski, F. *APEX-CHAMP+ high-J CO observations of low-mass young stellar objects. IV. Mechanical and radiative feedback.* 2015, A&A, 576, 109Y

8. Follette, K. B.; Grady, C. A.; Swearingen, J. R.; Sitko, M. L.; Champney, E. H.; **van der Marel, N.**; Takami, M.; Kuchner, M. J.; Close, L. M.; Muto, T.; and 53 coauthors. *SEEDS Adaptive Optics Imaging of the Asymmetric Transition Disk Oph IRS 48 in Scattered Light.* 2015, ApJ, 798, 132F

9. **van der Marel, N.**; van Dishoeck, E. F.; Bruderer, S.; van Kempen, T. A. *Warm formaldehyde in the Ophiuchus IRS 48 transitional disk.* 2014, A&A, 563, 113V **(Chapter 8)**

10. Bruderer, S.; **van der Marel, N.**; van Dishoeck, E. F.; van Kempen, T. A. *Gas structure inside dust cavities of transition disks: Ophiuchus IRS 48 observed by ALMA.* 2014, A&A, 562, 26B **(Chapter 5)**

11. **van der Marel, N.**; Kristensen, L. E.; Visser, R.; Mottram, J. C.; Yildiz, U. A.; van Dishoeck, E. F. *Outflow forces of low-mass embedded objects in Ophiuchus: a quantitative comparison of analysis methods.* 2013, A&A, 556, 76V

12. **van der Marel, N.**; van Dishoeck, E. F.; Bruderer, S.; Birnstiel, T.; Pinilla, P.; Dullemond, C. P.; van Kempen, T. A.; Schmalzl, M.; Brown, J. M.; Herczeg, G. J.; Mathews, G. S.; Geers, V. *A Major Asymmetric Dust Trap in a Transition Disk.* 2013, Science, 340, 1199V **(Chapter 2)**

13. Yildiz, U. A.; Kristensen, L. E.; van Dishoeck, E. F.; Belloche, A.; van Kempen, T. A.; Hogerheijde, M. R.; Güsten, R.; **van der Marel, N.**. *APEX-CHAMP+ high-J CO observations of low-mass young stellar objects. III. NGC 1333 IRAS 4A/4B envelope, outflow, and ultraviolet heating.* 2012, A&A, 542, 86Y

14. Cuppen, H. M.; Penteado, E. M.; Isokoski, K.; **van der Marel, N.**; Linnartz, H. *CO ice mixed with CH_3OH: the answer to the non-detection of the 2152 cm-1 band?* 2011, MNRAS, 417, 2809C

15. Öberg, K. I.; **van der Marel, N.**; Kristensen, L. E.; van Dishoeck, E. F. *Complex Molecules toward Low-mass Protostars: The Serpens Core.* 2011, ApJ, 740, 14O

Conference Proceedings

1. **van der Marel, N.**; van Dishoeck, E. F.; Bruderer, S.; Perez, L. M.; Isella, A. *Gas cavities inside dust cavities inferred from ALMA observations* IAUS, 314, in press (2015), ed. J. Kastner

2. van Dishoeck, E. F.; **van der Marel, N.**; Bruderer, S.; Pinilla, P. *Quantifying the gas inside dust cavities in transitional disks: implications for young planets* 'Revolution in Astronomy with ALMA: the 3rd year' (2015)

3. **van der Marel, N.**; van Dishoeck, E. F.; Bruderer, S.; Birnstiel, T.; Pinilla, P.; Dullemond, C. P.; van Kempen, T. A.; Schmalzl, M.; Brown, J. M.; Herczeg, G. J.; Mathews, G. S.; Geers, V. *Planet formation in action: resolved gas and dust images of a transitional disk and its cavity* IAUS, 299, 90 (2014), ed. M. Booth, B.C. Matthews, J.R. Graham

Curriculum Vitae

I was born on February 2nd, 1986, in Groningen. Six months later my parents moved to the south of the Netherlands, to a village in the neighbourhood of Eindhoven, where I spent my childhood. With my father being a physicist, I was introduced early on to funny consequences of physics and scientific experiments. I was addicted to books, and spent almost all my time on reading about a large variety of topics, including volcanoes, dinosaurs, animals, mountains, ancient history and of course: stars and planets. With all those interests, who could have known that I would end up studying astronomy? I went to the gymnasium called Christiaan Huygens College when I was 12, choosing the scientific track with mathematics, physics and chemistry, but also Latin and Greek, which kept my interest for the full six years. Analyzing and translating classical texts was the same for me as solving a mathematical or physics puzzle, and I graduated with the highest marks for both the scientific and the classical courses. My dreams for the future floated between becoming a (children's) book writer, a teacher and 'completely clueless'. The job perspectives convinced me to look into studying physics at university rather than classical languages. During one of the university days I heard about the possibility of studying astronomy on the side, and my childhood memories of the beautiful star images returned.

I decided to study physics and astronomy at Leiden University, starting Fall 2004. Unlike most of my fellow students, who disliked either the lab experiments at physics or the large uncertainties in astronomy, I continued being fascinated by both disciplines and was unable to make a choice between the two. In my second year I joined the observing trip to the Isaac Newton Telescope at La Palma for a week of learning how to operate a telescope, and I was gripped: being on top of a mountain with state of the art technology, looking at data that nobody else had seen before, was the most exhillarating feeling I had ever had. In my bachelor research project in the third year I got introduced to astrochemistry, doing laboratory infrared spectroscopy on interstellar ice mixtures in the Sackler Laboratory. In addition to my course work I became very active in the study society De Leidsche Flesch, as member of several committees, main editor of Eureka! magazine and board member. The lessons I have learnt during those years on social interaction, networking, organization and writing form an indispensable part of my development, and as a scientist I am still taking the advantages of those years.

For my master studies I chose the new master program Astronomy & Instrumentation, a collaboration between Leiden University and Delft University, as a way to continue working on topics in both astronomy and physics. I did a minor research project on molecular outflow observations with Ewine van Dishoeck, Lars Kristensen and Ruud Visser; a major research project on polarization effects in infrared interferometry with Walter Jaffe and Remko Stuik in the optical laboratory; and an observing project at the IRAM 30m telescope on complex organic molecules in young protostars with Karin Öberg and Lars Kristensen. Observational research became my passion, and when I got the opportunity to work as PhD student with Ewine van Dishoeck on an entirely new project on transitional disks with the recently commissioned ALMA telescsope I took it without further doubt.

As PhD student I discovered the real world of astronomical research: the stress of ALMA and ESO proposal deadlines, the large numbers of papers to read, the telescope and instrument manuals, the enormous amounts of data, the frustrations of data analysis, but also the excitement about new discoveries, the joy of solving puzzles, the relief of finishing a paper

and the interaction with astronomers all over the world. I presented my work at conferences in Toledo, Washington, Grenoble, Hamilton, Puerto Varas, Hawaii, Victoria, Heidelberg, Santiago, Bonn, Cambridge, Kiel and Atlanta, and visited institutes of MPE, ESAC, ETH, ESO Munich and Santiago, Beijing University, Harvard CfA, Ann Arbor, IAC La Palma, Caltech, IfA Hawaii, PUC Chile and NRC Canada. I also went observing at some of the most beautiful locations in the world at CARMA, William Herschel Telescope and APEX. Back in Leiden I was teaching assistant of Bernhard Brandl's course on Observing techniques, main organizer of the Astronomy Olympiad for high school students, member of the social committee and I organized a Lorentz Center workshop on the link between theory and observations of transitional disks together with Paola Pinilla. I gave public talks in many places in the Netherlands on astrochemistry, planet formation and ALMA during these years. I also had the privilege of (co)supervising three master students (Sierk Terwisga, Roman Tatch and Bart Verhaar), and I feel very proud that Sierk will start as PhD student in Leiden at my departure, continuing on the topic of my research, the transitional disks. After my PhD defense I will start my next job as Beatrice Watson Parrent Fellow at the University of Hawaii in Honolulu.

Acknowledgements

The years as a member of the Leiden Observatory have been a truly exciting experience and I feel extremely lucky that I had the opportunity to work here as PhD student. I owe the joy of these years and the success of my PhD to many more people than I can thank in these few pages, but I would like to point out a few people that were of particular importance for me.

First of all I would like to thank my supervisors, both before and during my PhD: without you I would never have started or finished. Lars, you were the first person giving me the confidence that I would be smart enough for a PhD position and I can not thank you enough for your praising and encouraging words that have led to me continuing in research. Simon, your never-ending patience in explaining me basic physics and radiative transfer were truly incredible. Paola, thank you so much for endlessly clarifying the details of theoretical modeling, I really enjoyed all of our discussions on interpreting the models and the observations (and the uncertainties in both). Bruno and Joanna, thank you for your help with getting started on radiative transfer modeling. Geoff M., you demonstrated your teaching skills during the year you were in Leiden, guiding me into disk and dust analysis and leaving me confident with the remark that you had taught me all you knew. I owe most of all to the person who pushed me but left me all the freedom to find my own limits, who always told me to enjoy the weekend or my holidays when I sent e-mails outside working hours and who gave me a desk full of inspiration: thank you for the wonderful years together.

I would not have been half as successful if it had not been for the amazing environment of Leiden Observatory. I will truly miss the Kaiser lounge, the coffee breaks, the borrels, the social events and all the other things that made this such a stimulating work place. A big thank you goes to the computer group: Erik, David, Aart, Niels, Leonardo: I could always knock at your door with the most trivial computer questions. Equally important is the work from the secretaries: Liesbeth, Anita, Alexandra, Jacqueline, Els, Jeanne, Debbie: thank you for making everything run so smoothly. Also special thanks to the Allegro group in Leiden for all the help with ALMA: Michiel, Tim, Pamela, Markus, Attila, Remo, Luke and Ian.

I have had the privilege of working in a fantastic group, which has expanded over the years that I was here. From being the only person 'not in WISH' to being amongst a mix of astrochemists, disk observers, star formation experts and modelers: there would always be somebody around to ask questions, discuss the life and the universe over lunch, enjoy brain storm sessions and sports during our legendary group retreats and have a beer after work. Many thanks to my current and former group members: Catherine, Paola, Magnus, Alan, Anna, Agata, Irene, Mihkel, Maria, Daniel, Christian, Niels, John, Vianney, Xiaohu, Nadia, Joe, Davide, Kenji, Koju, Umut, Jeanette, Lars and Ruud. Many other people in the Observatory have contributed to fantastic times here: my former office mate Edith (the hamster, the light sabre and our crazy holiday in northern Italy), Matthew (always time for a discussion with a beer), Nico (still impossible to practice Spanish with you) and all the other people I was hanging out with: Tiffany, Marissa, Matteo, Andra, Berenice, Renske, Heather, Anton, Gustavo, Wendy, Maria, Francisco, Sylvia, Edwin, Henry, Remco, Allison, Mason, Nicola, Marco, Mattia, Grainne, Lucie, Jayne, Steven and Jesse and many many more.

None of the work in this thesis would have been possible without the help of my collaborators. Kees, your drive and enthusiasm for problems ('That is so cool!') is infectious, and I feel honored that you were willing to become my second promotor. Greg, I always enjoyed our conversations, your 'minor' comments, my visit in Beijing and our observing run at La

Palma ('Let's observe it again to make sure'). Laura and Andrea, sharing our transitional disk ALMA data has been really insightful and I hope to continue working together on ALMA observations. Sean and Klaus, I really appreciate your critical view on several of my papers ('I am a stickler on titles'). Luca, you were not only a great teacher in dust observations, but also a wonderful friend ('Italians always complain about everything'). Til, thank you for explaining me countless times about the consequences of the dust evolution. Geoff B., many thanks for our useful discussions during ALMA deadline and for helping me to continue working in astronomy in the United States. Jonathan, I can't wait to get started in Hawaii.

One of the most rewarding experiences during my PhD was public outreach: telling non-astronomers about my work truly was the best test of my knowledge or in the words of Einstein: *"If you can't explain it simply, you don't understand it well enough"*. Therefore, I thank all the audiences I have had during public talks for their stimulating questions. My deepest gratitude for Marieke Baan, Richard Hook and Luis Calçada for all their help on the press release on the IRS 48 dust trap. Special thanks also to the co-organizers of the Astronomy Olympiad: Jens, Renske, Berenice and Irene, it was a pleasure to work with you.

During the years I have made many amazing friends amongst astronomers all around the world. Ilse, I can only say: you rock! I am so glad we became such good friends while climbing the PhD ladder together, and now both continuing in fellowships in the United States, solving planet formation together as we promised each other. Stefano A., I will never forget our epic hike to the volcanoe in Chile. Mihkel and Matteo, thank you for driving me around in Hawaii. Tiffany and Demerese, I owe you for showing me around in beautiful California. And so many more people that I have met over the years: Carlo, Giovanni, Rosina, Wlad, Melissa, Agnes, Ciro, Rafael, Rosina, Antonio, Sascha, Thayne, Mark, Marco T., Sebastian P., Gijs, Sarah, James, Giuseppe, Ruobing, Zhaohuan, Andres and Stefano F.

Also outside astronomy I have been fortunate to be surrounded by good friends. Mesa and Magda, I am so happy that years after our time at the Vrijheidslaan we are still in touch. I owe a lot to the study society De Leidsche Flesch. Special thanks to my dear fellow board members: Marinus, Ilse, Anton, Frank and Gonny, for all the good times that we have had. Jelmer, Guus and Mette, thank you for all the good times together after our 'SPIN' years. Several other friends: Marina, Adrienn, Erica, Babak, it is great to have met you! Jarno, even though we are no longer together, I thank you for the support you have given me over the years. My dearest Dita, getting to know you is one of the best things happening to me in 2014: thank you for all the evenings together, the laughs and cries we shared, the motivation you gave me to start running and most of all that you are always there for me.

Farhad, eshgham, *"Aani ke malek ba to dar ayad be tarab"* (Rumi). Life with you is one big adventure. I can not thank you enough for your eternal optimism, for introducing me to Iranian culture, for supporting me and keeping me sane at stressful times and all the happiness that you have given me in the last year, and I hope we can continue our journey together.

Finally, I would not have been anywhere without my wonderful family. My grandmother Dolly, even though she did not make it to this day, I know she is with me as she has always been. My aunts, uncles and cousins: Harry, Marjan, Sjoerd, Rion, Willem, Imma, Dick, Rosemarie, Bert, Piet, Suzanne, Wouter, Reinier, Alba, Manuel, Eva, Daniel and Fareeda; thank you for being part of our family.

My dear brothers, Floris and Ivo, you have followed your hearts looking for adventure all over the world and I am so proud of what you have accomplished. I am also really happy that you are joining me at the defence as my paranymphs. Special thanks to Floris and Killian for the beautiful cover design! Most of all I thank my parents for their eternal love and support for any decision that I have made in my life. You have made me the way that I am and I am truly grateful for that. Pappa en mamma, ik hou van jullie.